

Copyright
by
Harish Subbaraman
2009

The Dissertation Committee for Harish Subbaraman Certifies that this is the approved version of the following dissertation:

Highly Dispersive Photonic Crystal Fibers for Optical True Time Delay (TTD) Based X-Band Phased Array Antenna

Committee:

Ray T. Chen, Supervisor

Gary A. Hallock

Roger D. Bengtson

Seth R. Bank

Maggie Yihong Chen

Edward J. Powers

**Highly Dispersive Photonic Crystal Fibers for Optical True Time Delay
(TTD) Based X-Band Phased Array Antenna**

by

Harish Subbaraman, B.E.; M.S.E.

Dissertation

Presented to the Faculty of the Graduate School of

The University of Texas at Austin

in Partial Fulfillment

of the Requirements

for the Degree of

Doctor of Philosophy

The University of Texas at Austin

August, 2009

Dedicated to my Parents, Brother, Sister-in-Law and my Fiancée

Acknowledgements

I am greatly indebted to my supervisor Professor Ray T. Chen for providing me with an excellent platform to learn things and for the invaluable advice and support rendered during every aspect of my research work. This thesis also holds a great debt of gratitude to Dr. Maggie Yihong Chen for closely monitoring my progress and providing me with timely and important advice. I would also like to thank Dr. Gary A. Hallock, Dr. Roger D. Bengtson, Dr. Seth R. Bank, and Dr. Edward J. Powers for their valuable time and interest in this research. I also extend my special thanks to my colleagues and friends at the Optical Interconnects Group for their help, assistance and advice especially Xiaonan Chen, YongQiang Jiang, Lanlan Gu, Alan Wang, Xinyuan Dou, Beom-Suk Lee, Jian Zhang, and Stephen Hsu. I also owe a great load of thanks to the staff at the Microelectronics Research Center, especially Jean Toll, Joyce Kokes, Gerlinde Sehne and Jackie Srnensky for their help with purchasing and procurement.

Finally, I want to thank my parents, brother and sister-in-law for always believing in my abilities and for always showering their invaluable love and support. Most of all, I want to thank my Fiancée Nirmala for her love, patience, support and encouragement which made everything look doable and within reach.

Highly Dispersive Photonic Crystal Fibers for Optical True Time Delay (TTD) Based X-Band Phased Array Antenna

Publication No. _____

Harish Subbaraman, Ph. D

The University of Texas at Austin, 2009

Supervisor: Ray T. Chen

Phased array antenna (PAA) is a key component in many of the modern military and commercial radar and communication systems requiring highly directional beams with narrow beam widths. One of the advantages that this technology offers is a physical movement-free beam steering. Radar and communication technologies also require the PAA systems to be compact, light weight, demonstrate high bandwidth and electromagnetic interference (EMI) free performance. Conventional electrical phase shifters are inherently narrowband. This calls for technologies that have a larger bandwidth and high immunity to electromagnetic interference. Optical true-time-delay (TTD) technique is an emerging technology that is capable of providing these features along with the ability to provide frequency independent beam steering. Photonic crystal fiber (PCF) based optical TTD lines are capable of providing precise and continuous time delays required for PAA systems.

Photonic crystal fibers are a new class of optical fibers with a periodic arrangement of air-holes around a core that can be designed to provide extraordinary optical characteristics which are unrealizable using conventional optical fibers. In this dissertation, highly dispersive photonic crystal fiber structures based on index-guidance and bandgap-guidance were designed. Designs exhibiting dispersion coefficients as large as -9500ps/nm/km and 4000ps/nm/km at 1550nm were presented. A TTD module utilizing a fabricated highly dispersive PCF with a dispersion coefficient of -600ps/nm/km at 1550nm was formed and characterized. The module consisted of 4 delay lines employing highly dispersive PCFs connected with various lengths of non-zero dispersion shifted fibers. By employing PCFs with enhanced dispersion coefficients, the TTD module size can be proportionally reduced. A 4-element linear X-band PAA system using the PCF-TTD module was formed and characterized to provide continuous time delays to steer radio-frequency (RF) beams from -41 degrees to 46 degrees by tuning the wavelength from 1530nm to 1560nm .

Using the PCF-TTD based X-Band PAA system, single and simultaneous multiple beam transmission and reception capabilities were demonstrated. Noise and distortion performance characteristics of the entire PAA system were also evaluated and device control parameters were optimized to provide maximum spurious-free-dynamic range. In order to alleviate computational and weight requirements of practical large PAA systems, a sparse array instead of a standard array needs to be used. X-Band sparse array systems using PCF and dispersive fiber TTD technique were formed and RF beam steering was demonstrated. As an important achievement during the research work, the design and fabricated structure of a PCF currently reported to have the highest dispersion coefficient of -5400ps/nm/km at 1549nm , along with its limitations was also presented. Finally, other

interesting applications of highly dispersive PCFs in the areas of pulse compression and soliton propagation were explored.

2.2.2	Highly dispersive structures based on air-guiding PCF.....	43
2.2.3	Other highly dispersive PCF structures	51
2.3	Fabrication of photonic crystal fibers	53
2.3.1	Stack and Draw Technique	53
2.3.2	Fabrication difficulties	54
2.4	Summary	57
2.5	References	57
Chapter 3	Photonic crystal fibers based true-time delay modules for X-band phased array antennas	61
3.1	Practical design of a highly dispersive photonic crystal fiber	61
3.2	Experimental characterization of true-time-delay (TTD) modules	65
3.2.1	Time delay interval measurement.....	67
3.2.2	Phase-frequency curve measurement.....	69
3.3	Summary	73
3.4	References	74
Chapter 4	1x4 X-band phased array antenna subsystem for single beam transmission/reception.....	75
4.1	Demonstration of single RF beam transmission of PCF-TTD based X-band PAA.....	75
4.1.1	Principle of single RF beam transmission	76
4.1.2	Experimental setup.....	78
4.1.3	Results and discussion	83
4.2	Demonstration of single RF beam reception of PCF-TTD based X-band PAA.....	86
4.2.1	Principle of single RF beam reception.....	86
4.2.2	Experimental setup.....	87
4.2.3	Results and discussion	89
4.3	Summary	91
4.4	References	91

Chapter 5	Simultaneous multiple-beam transmission and reception of a PCF	
	TTD-based X-band phased array antenna	94
5.1	Principle of simultaneous multiple RF beam transmission.....	94
5.2	Demonstration of simultaneous multiple beam transmission of a PCF-TTD based X-band PAA	97
5.2.1	Experimental setup.....	97
5.2.2	Results and discussion	98
5.3	Principle of simultaneous multiple RF beam reception.....	100
5.4	Demonstration of simultaneous multiple beam reception of a PCF-TTD based X-band PAA	102
5.4.1	Experimental setup.....	102
5.4.2	Results and discussion	107
5.5	Summary	109
5.6	References.....	109
Chapter 6	Characterization and RF performance evaluation of PCF-TTD analog	
	subsystem	111
6.1	Noise in analog links.....	111
6.1.1	Noise sources	112
6.1.2	Noise figure (NF) measurement.....	115
6.2	Distortion in analog links.....	118
6.2.1	Harmonic distortion	119
6.2.2	Intermodulation distortion	120
6.3	Sources of distortion	121
6.4	Harmonic distortion measurement.....	122
6.5	Intermodulation distortion measurement	124
6.5.1	Spurious-Free Dynamic Range (SFDR)	124
6.5.2	SFDR measurement	125
6.6	Improving SFDR using high power Erbium-doped fiber amplifier.....	129
6.6.1	Principle of operation.....	129

6.6.2	Experimental results.....	130
6.7	Summary	133
6.8	References.....	133
Chapter 7	X-band Sparse Array Antenna Demonstration	135
7.1	Why do we require sparse array?.....	135
7.1.1	Simulation results.....	136
7.2	Sparse Array Antenna.....	139
7.3	Highly dispersive PCF based sparse array.....	141
7.4	Highly dispersive fiber – based sparse array antenna.....	144
7.4.1	Time delay measurement	145
7.4.2	Experimental setup.....	146
7.4.3	Far-field radiation pattern	148
7.5	Summary	150
7.6	References.....	151
Chapter 8	Other important achievements.....	152
8.1	PCF with highest dispersion coefficient	152
8.1.1	Structural design of the PCF.....	152
8.1.2	Dispersion coefficient	156
8.1.3	Limitations of the PCF.....	158
8.2	Pulse Compression.....	159
8.2.1	Principle of operation.....	159
8.2.2	Experimental setup and results	161
8.3	Summary	164
8.4	References.....	164
Chapter 9	Recommendations for Future work	166
9.1	2-D continuously tunable photonic crystal fiber true-time delay modules for standard and sparse phased array antenna systems	166
9.2	Other applications of highly dispersive PCF	167
9.2.1	Soliton propagation.....	167

9.3 Summary	169
Chapter 10 Summary	171
Appendix Publications of Harish Subbaraman	174
Bibliography	176
Vita.....	190

List of Tables

Table 3.1 Measured time delay (in ps) from four true-time-delay lines	71
Table 7.1 Measured dispersion coefficient of the DCF	146

List of Figures

Fig. 1.1 Schematic diagram of a linear antenna array.....	2
Fig. 1.2 Schematic diagram of a Phased-Array Antenna (PAA)	5
Fig. 1.3 Radiation pattern dependence on single element pattern	7
Fig. 1.4 Radiation pattern of an 8 element PAA with grating lobes.....	9
Fig. 1.5 (a) Beam-Squint effect of a phased array antenna controlled by electrical phase shifters (b) Nature of a phased array antenna controlled by true-time-delay network	10
Fig. 1.6 Fiber-Optic Prism true-time-delay feed network [6]	13
Fig. 1.7 Schematic of the Highly Dispersive PCF-TTD based PAA. MZM: Mach-Zehnder modulator; EDFA: Erbium-doped fiber amplifier, TTD: true time delay, LNA: low noise amplifier. (PCF is represented with red dots and non-zero dispersion shifted fibers is represented with blue dots)	17
Fig. 2.1 SEM cross-sections of (a) Index-guiding PCF [1] (b) Photonic bandgap guiding PCF [13].....	26
Fig. 2.2 Schematic cross section of the designed dual concentric core PCF.....	34
Fig. 2.3 Mode profile of the dual concentric-core PCF at (a) $\lambda < \lambda_p$ (b) $\lambda \approx \lambda_p$ and (c) $\lambda > \lambda_p$	35
Fig. 2.4 Variation of $dn/d\lambda$ with respect to the period (Λ) for the inner core (filled squares) and outer core (empty squares).....	36
Fig. 2.5 Calculation result (stars) and its curve fit (circles) for the relationship between T and Period (Λ).....	37
Fig. 2.6 Effect of coupling on the effective refractive index	39
Fig. 2.7 Relationship between the dispersion value D and wavelength and comparison of Plane Wave Expansion (filled squares) and Coupled-Mode Theory (empty circles) results	40
Fig. 2.8 Variation of the dispersion value and the shift observed due to (a) variation in the pitch, (b) variation of d_1 , (c) variation of d_2 , and (d) variation of d_3 , while keeping all the other parameters as in the given design in each case.....	42
Fig. 2.9 Variation of dispersion with number of air hole rings between the inner and the outer core	43
Fig. 2.10 Schematic cross section of the designed photonic bandgap fiber	45
Fig. 2.11 (a) Frequency versus propagation constant relation for the cladding showing forbidden regions (gap) within which no solution to Maxwell's equations exists (b) The gap edges are plotted showing the light line (frequency = propagation constant)	46
Fig. 2.12 Computed transverse mode profiles of the designed highly dispersive bandgap fiber showing (a) Fundamental mode (b) and (c) higher order modes	48
Fig. 2.13 Calculated effective refractive index of the fundamental guided mode (n_{eff}) as a function of wavelength	48
Fig. 2.14 Dispersion curve of the simulated highly dispersive photonic bandgap fiber... ..	49
Fig. 2.15 Effect of change of period (P) on the dispersion curve for $3.85\mu\text{m}$ (black curve), $3.86\mu\text{m}$ (red curve), and $3.87\mu\text{m}$ (green curve)	50
Fig. 2.16 Dispersion coefficient for PCF structure with a small air-hole at the center (cross section of the designed fiber is also shown).....	51
Fig. 2.17 Dispersion coefficient for PCF structure with doping-induced refractive index change of the cores.....	52

Fig. 2.18 Schematic of stack and draw method for fabricating photonic crystal fibers [36]	53
Fig. 2.19 D_{max} -FWHM product plotted as a function of PCF parameters. The solid lines are only to aid the human eye. The data points are marked with solid squares.....	56
Fig 3.1(a) Scanning electron microscope (SEM) images of the fabricated high dispersion PCF [1-2] (b) Schematic cross section of the PCF	62
Fig. 3.2 Simulated transverse mode profiles of the highly dispersive photonic crystal fiber when (a) $\lambda < \lambda_p$ (b) $\lambda > \lambda_p$ and (c) $\lambda \approx \lambda_p$	63
Fig. 3.3 Simulated dispersion coefficient of the designed highly dispersive photonic crystal fiber	64
Fig. 3.4 Schematic representation of connection between NZ-DSF and PCF using UHNA fiber (only connections at one end of PCF are shown).....	66
Fig. 3.5 Measured dispersion coefficient of the fabricated highly dispersive photonic crystal fiber	67
Fig. 3.6 Schematic of the time delay interval measurement setup using femtosecond laser source	68
Fig. 3.7 Time delayed pulse traces of 4 TTD lines measured on the digital communication analyzer.....	69
Fig. 3.8 Schematic of Phase versus Frequency measurement setup.....	70
Fig. 3.9 Phase versus Frequency plots for (a) TTD line consisting of 3.5m PCF and 7.0m NZ-DSF, (b) TTD line consisting of 7.0m PCF and 3.5m NZ-DSF, (c) TTD line consisting of 10.5m PCF and 0m NZ-DSF.....	71
Fig. 3.10 Calculated steering angle of X-band PAA with antenna element spacing $d = 1.3cm$	72
Fig. 4.1 Schematic of the Highly Dispersive PCF-TTD based PAA setup for single RF beam transmission (PCF is represented with red dots and non-zero dispersion shifted fibers is represented with blue dots)	76
Fig. 4.2 Experimental setup of the PAA in transmitting mode (a) Overall setup along with an expanded view of the antenna array is shown. (b) The four TTD lines are shown. The inset shows the composition of each line. (c) The receiving horn antenna and the microwave spectrum analyzer are shown	81
Fig. 4.3 Measured normalized element pattern of the patch antenna at 9GHz.....	82
Fig. 4.4 Simulated and measured far field patterns for (a) RF signal with frequency = 8.4GHz at a wavelength of 1547.72nm. (b) RF signal with frequency = 12GHz at a wavelength of 1552.52nm.....	84
Fig. 4.5 Beam squint-free demonstration of the PCF-TTD based phased array antenna system	85
Fig. 4.6 Schematic of the Highly Dispersive PCF-TTD based PAA system for single RF beam reception. MZM: Mach-Zehnder modulator; TTD: true time delay, LNA: low noise amplifier, MSA: Microwave spectrum analyzer (PCF is represented with red dots and non-zero dispersion shifted fibers is represented with blue dots).....	88
Fig. 4.7 Measured received power versus wavelength for (a) 8.4GHz RF signal impinging on the antenna array from -7.4° (b) 12GHz RF signal impinging on the antenna array from -21.2°	90

Fig. 5.1 Schematic setup for simultaneous transmission of multiple beams, EOM: electro-optic modulator, EDFA: Erbium doped fiber amplifier, TTD: true-time-delay. The cross sectional schematic view of the PCF is also shown	95
Fig. 5.2 Experimental setup for simultaneous dual RF beam steering, EDFA: Erbium doped fiber amplifier, TTD: true-time-delay, LNA: low noise amplifier, TDL: tunable delay line.....	98
Fig. 5.3 Simulated and Measured Far Field Patterns of two RF signals with frequencies 8.4GHz and 12GHz steered simultaneously to angles of 7.4 and 21.2 degrees respectively	99
Fig. 5.4 Structure of the receiving mode with multiple incoming beams, WDM: wavelength division multiplexer, LNA: low noise amplifier, EOM: electro-optic modulator, TTD: true-time-delay, DEMUX: demultiplexer	101
Fig.5.5 Schematic of simultaneous dual beam operation setup and photograph of actual (a) RF reception and electro-optical conversion setup (b) True-Time-Delay lines and signal processing setup; the output from the modulators in (a) are connected to the inputs of EDFAs in (b). (The RF sources and the transmitting horn antennas of the setup are not shown in the figure)	105
Fig. 5.6 Signal power measured at the photodetector vs. wavelength. The signal power peaks appear at 1547.72nm for 8.4GHz and 12GHz signals placed at -7.4 degrees and at 1552.52nm for 8.4GHz and 12GHz signals placed at -21.2 degrees	106
Fig. 6.1 Schematic of the setup used for noise figure measurement.....	116
Fig. 6.2 Noise Figure versus Modulator bias measurement for PCF-TTD system at 20mW optical input power	118
Fig 6.3 Spectrum plot of output RF signals from a component having a nonlinear transfer function	119
Fig. 6.4 Measured fundamental (black curve), second harmonic (red curve) and third harmonic (green) powers as a function of modulator bias.....	123
Fig. 6.5 Experimental setup for spurious-free dynamic range measurement. EDFA: Erbium-Doped Fiber Amplifier; MZM: Mach-Zehnder Modulator; TTD: True-Time-Delay; MSA: Microwave Spectrum Analyzer; LNA: Low-Noise Amplifier.....	126
Fig. 6.6 Fundamental and IMD-3 output powers as observed on a microwave spectrum analyzer	127
Fig. 6.7 Fundamental (red squares) and IMD-3 (blue circles) RF output powers as a function of input RF power. Optical input power of 20mW and modulator bias angle of 90 degrees are used. Extrapolated straight line fits to the data points are also shown. The extrapolated lines intersect at a point whose corresponding RF input power gives IIP3	128
Fig. 6.8 Measured link noise figure as a function of modulator bias angle for different optical input powers	130
Fig. 6.9 Fundamental (red squares) and IMD-3 (blue circles) RF output powers as a function of input RF power. Optical input power of 200mW and modulator bias angle of 153 degrees are used. Extrapolated straight line fits to the data points are also shown. The extrapolated lines intersect at a point whose corresponding RF input power gives IIP3	132
Fig. 7.1 Array factor simulation of a 100 element standard array with inter-element spacing $d = \frac{\lambda}{2}$ at 12.5GHz	136

Fig. 7.2 Array factor simulation of an 8 element sparse array with inter-element spacing $d = 14 * \frac{\lambda}{2}$ at 12.5GHz	137
Fig. 7.3 X-band sparse array antenna consisting of three periodically spaced horn antennas spaced 0.168m apart, equivalent to a 29-element standard array (precision rotation stage is also shown)	139
Fig. 7.4 Measured S_{11} parameter of three antenna elements.....	140
Fig. 7.5 Measured normalized patterns of 3 antenna elements at a frequency of (a) 9GHz and (b) 10GHz.....	141
Fig. 7.6 Simulated and Measured far-field radiation patterns of the sparse array antenna at an optical wavelength of (a) 1559.9nm corresponding to +3degree beam steering and (b) 1529.9nm corresponding to -3degree beam steering (blue arrows indicate the desired beam, dashed red arrows at 0degree indicate the beam steering angle at center wavelength of 1545nm).....	143
Fig. 7.7 Experimental setup for sparse array antenna demonstration, LNA: low-noise amplifier; MZM: Mach-Zehnder modulator; TTD: true-time-delay	147
Fig. 7.8 Simulated (dashed curve) and Measured (curve marked with data points) far-field radiation patterns of the sparse array antenna at an optical wavelength of 1558.65nm corresponding to +11degree beam steering of a 9GHz RF signal (blue arrow indicates the desired beam). Measured pattern at central wavelength of 1555nm is also shown as a dashed red curve with peak at 0 degrees indicated by a red arrow	148
Fig. 7.9 Simulated (dashed smooth curves) and Measured (curves marked with data points) far-field radiation patterns of the sparse array antenna at an optical wavelength of 1550nm corresponding to -15degree beam steering of a 9GHz (red curves) and a 10GHz RF signal (green curves)	150
Fig. 8.1 Cross section of the designed photonic crystal fiber. The periodicity of the structure is given by Λ . A high index central core (d_1) is surrounded by an inner cladding (d_2) consisting of air holes. Outer core (d_3) has slightly lower refractive index compared to the central core. All other air holes (d_4) form the outer cladding region.....	153
Fig. 8.2 Scanning electron microscope (SEM) picture of the cross section of the fabricated highly dispersive PCF (Enlarged views of the highlighted sections are also shown).....	154
Fig. 8.3 Simulated dispersion coefficient for the designed high dispersion PCF with selective injecting into the inner core (red curve) and with random injection (black curve)	155
Fig. 8.4 System setup to measure dispersion value of PCF using phase-shift method...	156
Fig. 8.5 Simulated dispersion curves for selective injection (dashed red curve), random injection (dashed green curve) and measured dispersion curve (green curve with marked circles) of the PCF	158
Fig. 8.6 Experimental setup for demonstrating pulse compression	162
Fig. 8.7 Pulse compression demonstration with (a) Input pulse launched into the PCF (FWHM = 2898fs, pulse width = 1.848ps) (b) Output pulse as measured on the autocorrelator (FWHM = 630fs, pulse width = 401.94fs)	163
Fig. 9.1 Schematic setup of TTD based 2-D Phased Array Antenna, MZM: Mach-Zehnder modulator; TTD: true-time-delay; WC: wavelength convertor; PD: photodetector; LNA: low-noise amplifier.....	166

Fig. 9.2 Measured pulse traces of soliton from the PCF at different pump current levels
..... 169

Chapter 1 Introduction

1.1 Overview of Phased Array Antennas (PAA)

An *antenna* is a device that can transmit and receive electromagnetic wave energy. It forms the basic component for electronic systems based on free space propagation such as satellite communication, mobile communication, radar, air traffic control etc. Antennas can be classified based on bandwidth into *narrow band antennas* and *broad band antennas* and they can also be classified based on their radiation pattern into *directional antennas* and *isotropic antennas*. It is possible to create a highly directional antenna by arranging individual antenna elements in linear, circular, rectangular etc patterns. Directional antennas have a very high signal-to-noise (S/N) ratio compared to individual radiating elements. A phased array antenna (PAA) is a special kind of an array antenna wherein the beam pointing direction can be changed without mechanically moving the antenna head. The principle behind the working of a PAA can be understood by first understanding the working of an antenna array. Therefore, this section begins with the development of theory for an antenna array, followed by an extension of the theory to phased array antennas.

1.1.1 ARRAY ANTENNA

In order to understand the working principle of a phased array antenna (PAA), a simple linear antenna array is explained first, followed by development of theory for PAA in the next section. A linear array consisting of K identical antenna elements with a separation between elements given by d is shown in Fig. 1.1. It is mathematically convenient to assume the antenna array to be working in the receiving mode. This is not a

restriction on the antenna, because by the virtue of reciprocity theorem, the transmission characteristics are similar to the receiving characteristics [1]. The incoming electromagnetic beam from an angle theta (θ) impinges on the array in such a way that the wavefront first reaches element K, and due to the additional distance traveled by the wavefront to reach every element, a different phase is received by each element.

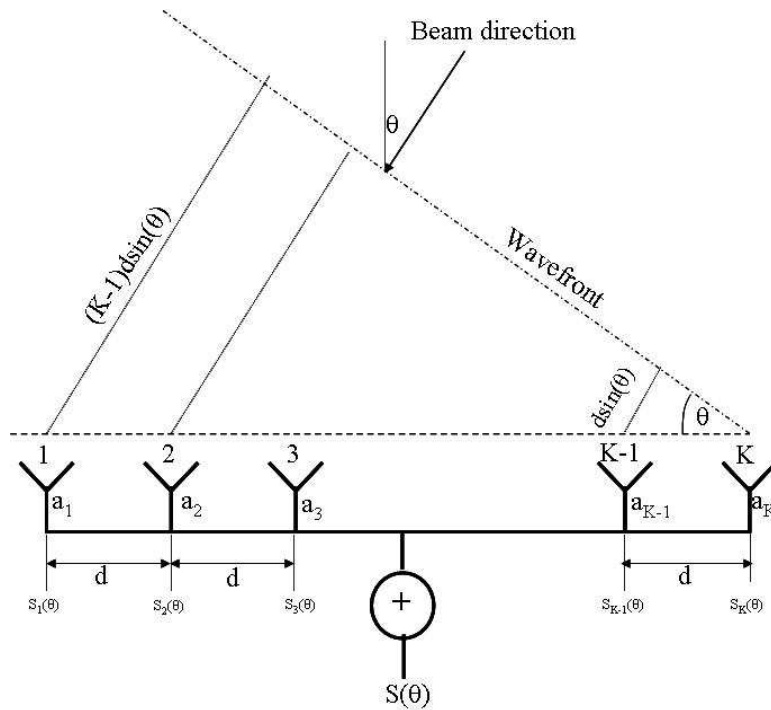


Fig. 1.1 Schematic diagram of a linear antenna array

The phase of all other elements (ϕ_i) with respect to element K can be obtained by multiplying the path length difference with the free-space wave number k_0 [1]

$$\phi_i = k_0 (K - i) d \sin(\theta) \quad (1.1)$$

where $k_0 = \frac{2\pi}{\lambda_0}$ and λ_0 is the free-space wavelength and $i = 1, 2, 3 \dots K$

If a_i is the amplitude received by each antenna element and $S_{el}(\theta)$ is the complex radiation pattern of each antenna element, then the complex signal received by each element can be written as:

$$S_i(\theta) = S_{el}(\theta)a_i e^{jk_0(K-i)d \sin(\theta)} \quad (1.2)$$

Without introducing any additional phase shifts, the signals from all the elements can be combined and the overall received signal $S(\theta)$ can be written as:

$$S(\theta) = S_{el}(\theta) \sum_{i=1}^K a_i e^{jk_0(K-i)d \sin(\theta)} \quad (1.3)$$

Here, $S_{el}(\theta)$ is assumed to be the same for all the elements. This is a reasonable assumption because, in a practical antenna array, the antenna elements are very identical. Let us also assume that the amplitudes received by the individual antenna elements are equal, i.e. $a_i = 1$.

$$S(\theta) = S_{el}(\theta) \sum_{i=1}^K e^{jk_0(K-i)d \sin(\theta)} \quad (1.4)$$

and,

$$S(\theta) = S_{el}(\theta)S_a(\theta) \quad (1.5)$$

where $S_a(\theta) = \sum_{i=1}^K e^{jk_0(K-i)d \sin(\theta)}$ is called the array factor.

From equation (1.4) we see that $S(\theta)$ is maximum for $\theta = 0$ degrees. This is called the broadside of the array. The above expressions are derived assuming far-field approximations. A far field is the region wherein the angular distribution of the radiating

fields is independent of the distance to the antenna. The required distance R where one can safely use far-field approximations is given by [1]

$$R = \frac{2D^2}{\lambda_{RF}} \quad (1.6)$$

where, D is the largest dimension of the array and λ_{RF} is the radio frequency (RF) signal wavelength.

1.1.2 PHASED ARRAY ANTENNA (PAA)

Using the results from section 1.1.1 on array antennas, let us examine what would happen if we intentionally added additional phase terms (ψ_i) to each antenna element as shown in Fig. 1.2. The array factor from the previous section changes and incorporates this additional phase term to become:

$$S_a(\theta) = \sum_{i=1}^K e^{j\{k_0(K-i)d \sin(\theta) + \psi_i\}} \quad (1.7)$$

Depending on the value of ψ_i , the following three cases are encountered:

Case 1:

If $\psi_i = 0$, then equation (1.7) becomes:

$$S_a(\theta) = \sum_{i=1}^K e^{j\{k_0(K-i)d \sin(\theta)\}} \quad (1.7 a)$$

This is just the case of an array antenna wherein the maximum occurs at $\theta = 0$ degrees. This is the broadside of the array.

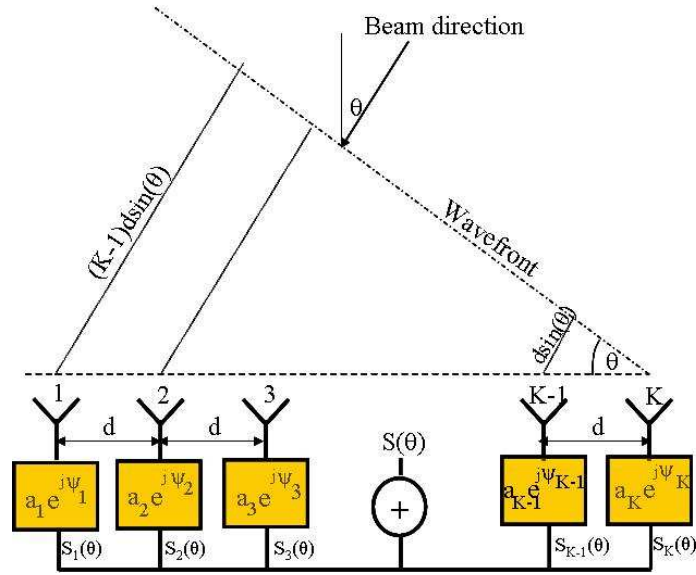


Fig. 1.2 Schematic diagram of a Phased-Array Antenna (PAA)

Case 2:

If $\psi_i = (-K - i)k_0 d$, then equation (1.7) becomes:

$$S_a(\theta) = \sum_{i=1}^K e^{j\{k_0(K-i)d \sin(\theta) - (K-i)k_0 d\}} \quad (1.7 \text{ b})$$

In this case, the maximum of the array factor is obtained when the exponent becomes zero, or $\theta = 90$ degrees. This is called the end-fire direction.

Case 3:

If $0 < \psi_i < \{-(K - i)k_0 d\}$, then the maximum of the array factor occurs between 0 and 90 degrees.

Therefore, by changing the relative phase difference between adjacent elements, the direction of maximum can be changed. Such antenna systems wherein the beam can

be steered by changing the phase are called Scanned-Beam Array Antenna or Phase-Steered Antenna or Phased-Array Antenna (PAA)

Phased Array Antennas are getting more and more important in present-day communications. One primary advantage that such PAA systems offer over other antenna systems is that in order to transmit/receive an electromagnetic field to/from any direction, mechanical movement of the antenna body is not necessary. Also, these antennas have low visibility which means that such antenna arrays cannot be detected as there are no moving parts. Quick steering of beams is possible either by using electrically or optically controlled networks. These systems are also small in terms of size and weight. Furthermore, they can be used for multi-mode operation, having simultaneous multiple steering beams that cover a large area [2, 3]. Due to so many advantages over a single antenna, phased array antennas are widely used in both civilian operations, such as air traffic control and mobile communication, satellite communications, and in the military operations, such as radar, missile guidance, trajectory determination, and satellite communications etc.

1.1.2.1 Features of phased array antennas

Till this point, emphasis has been on the characteristics of the array factor and how the phase fed to the individual antenna elements changes the beam pointing direction or the steering angle. Although the beam pointing direction strictly depends on the antenna factor, the overall radiation pattern depends both on the element radiation pattern $S_{el}(\theta)$ and the array factor $S_a(\theta)$ according to equation (1.5).

If we write down the complex radiation pattern in the logarithmic form, then

$$S(\theta)dB = 20\log|S_{el}(\theta)| + 20\log|S_a(\theta)| \quad (1.8)$$

Fig. 1.3 shows the radiation pattern of an 8 element linear array with inter-element spacing = 1.25cm working at 12GHz and with phase information provided such that the maximum occurs at 20 degrees. The voltage radiation pattern of the individual elements is assumed to be of the form $S_{el}(\theta) = \cos(\theta)$. The dashed red pattern, the dotted blue pattern and the solid green pattern correspond to element, array factor and overall radiation patterns respectively.

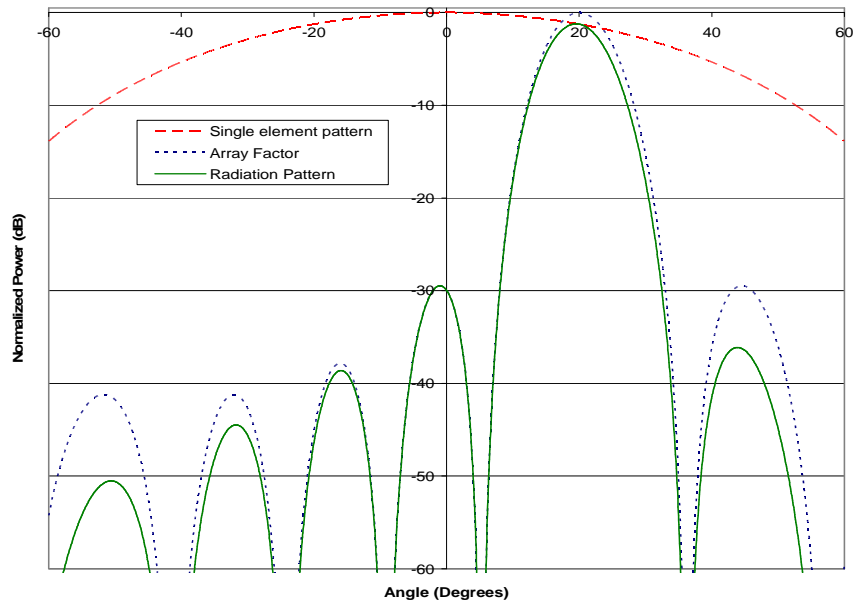


Fig. 1.3 Radiation pattern dependence on single element pattern

The part of the radiation pattern with the highest power is called the main beam. All other lobes are called side lobes. It can be seen from the figure that the element pattern only acts as a filter at larger angles and the peak radiation direction is still determined by the array factor. Due to this filtering effect, there is a small error in the

beam pointing direction at larger angles and is slightly less than that given by the array factor.

1.1.2.2 Grating Lobes

We can rewrite equation (1.7) by inserting $\psi_i = -(K-i)k_0 \sin(\theta_0)$ for a general value of θ_0 lying in between -90 and 90 degrees as

$$S_a(\theta) = \sum_{i=1}^K e^{jk_0(K-i)d\{\sin(\theta) - \sin(\theta_0)\}} \quad (1.9)$$

From the above equation, we see that whenever $k_0 d \{\sin(\theta) - \sin(\theta_0)\} = 2n\pi$, where n is an integer, the array factor repeats itself, i.e. the lobes reoccurs in the angular space as long as $\frac{2\pi}{\lambda_0} d \{\sin(\theta) - \sin(\theta_0)\} = 2n\pi$ or $\frac{d}{\lambda_0} = \frac{1}{\{\sin(\theta) - \sin(\theta_0)\}}$. The lobe at n=0 is called the main lobe and all other lobes are called grating lobes. For $-90^\circ \leq \theta \leq 90^\circ$, $\sin(\theta)$ value lies between -1 and 1. In order to avoid grating lobes, the pitch of the antenna array must be chosen in such a manner that

$$\frac{d}{\lambda_0} < \frac{1}{1 + |\sin(\theta)_{\max}|} \quad (1.10)$$

Therefore, for a maximum scan angle of $\pm 90^\circ$, the grating lobes can be avoided as long as

$$\frac{d}{\lambda_0} \leq \frac{1}{2} \quad (1.11)$$

The effect of antenna element spacing on the array factor is shown in Fig. 1.4. Similar parameters as chosen for Fig. 1.3 are chosen, but the spacing between elements is

set as 5cm. It can be seen from the figure that the grating lobes occur for a 12GHz signal at -41.1 degrees, -9 degrees, and 57.3 degrees with the main lobe occurring at 20 degrees.

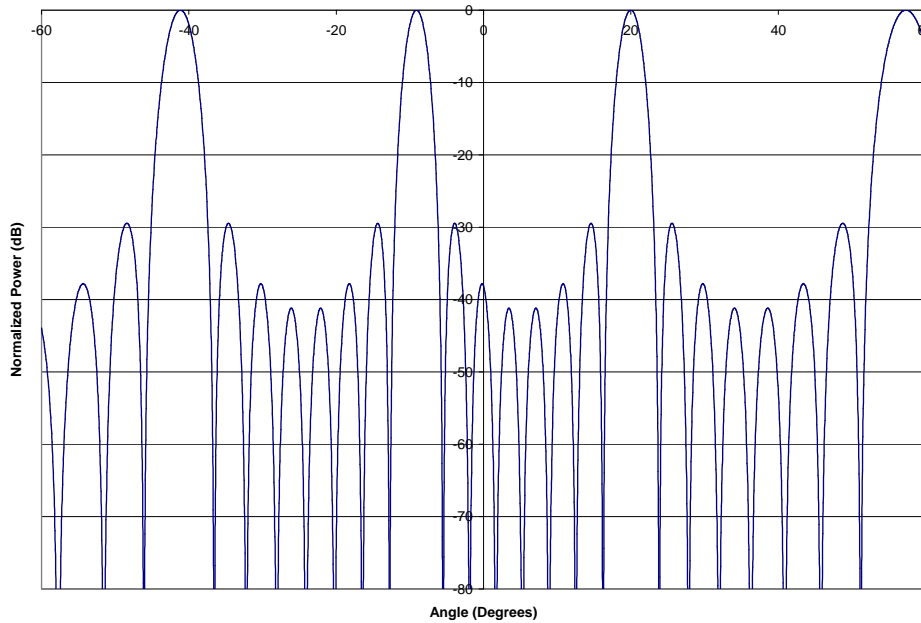


Fig. 1.4 Radiation pattern of an 8 element PAA with grating lobes

1.1.3 METHODS OF PHASE CONTROL

Since controlling phase in PAA systems is of paramount importance, it is worthwhile to introduce the techniques of phase control in this section. Primarily, there are two ways to control the phase of individual elements in the array

1. Using Electrical Phase Shifters
2. Using True Time Delay (TTD)

Conventional electrical phase shifters or phase trimmers are inherently narrow band and they add a constant phase in the frequency range of interest. Therefore, the radiation peak angle changes with frequency according to the relation:

$$\Delta\theta_0 = -\tan(\theta_0)\frac{\Delta\omega}{\omega} \quad (1.12)$$

Therefore, there is a change in the beam pointing direction due to a change in the operating frequency. This effect is called *beam squint* and is highly undesirable in various military and civilian applications. The beam squint effect is illustrated in Fig. 1.5(a). The radiation pattern simulation is performed for a 16 element linear PAA with separation between adjacent elements equal to 1.5cm and the beam pointing direction is chosen as 30 degrees. It can be seen from the figure that as the operating frequency is changed from 8GHz to 12GHz, the beam pointing direction changes from 38.6 degrees to 24.6 degrees. Therefore, an extremely narrow range of frequencies around the center frequency can be used in the system operation.

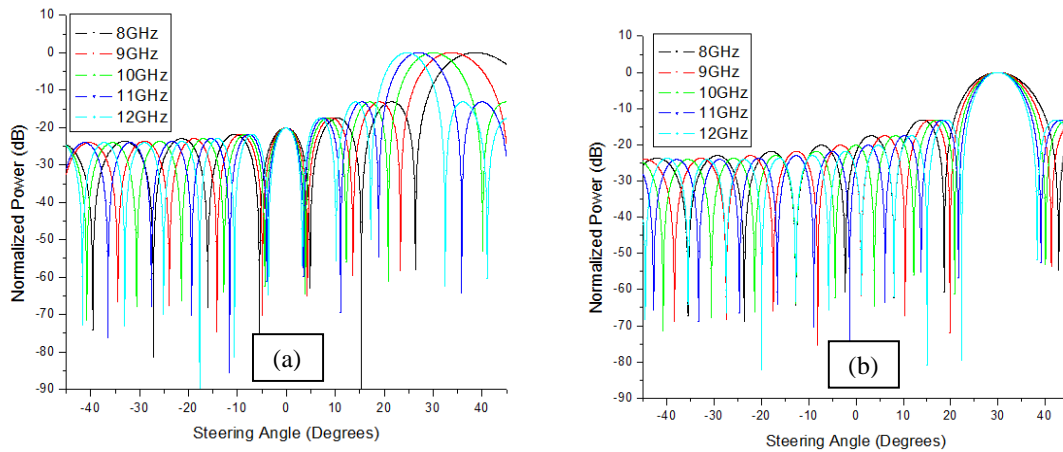


Fig. 1.5 (a) Beam-Squint effect of a phased array antenna controlled by electrical phase shifters (b) Nature of a phased array antenna controlled by true-time-delay network

Modern day PAA applications demand a broad bandwidth and a squint-free operation with characteristics as shown in Fig. 1.5(b). Irrespective of the frequency used, all the main lobes point to 30 degrees. Therefore, instead of providing a constant phase at all frequencies, the system should be able to provide phase that linearly changes with frequency. Such systems are called *true-time-delay (TTD)* systems wherein the time delay is independent of the frequency of operation.

1.2 Overview of true-time-delay (TTD) techniques

In this section, an overview of the various true-time-delay techniques will be covered. The TTD techniques can be further classified into electrical-TTD and optical-TTD. The electrical TTD technique is a very mature technique. Electrical TTD mainly includes the binary path selection TTD technique and the length tunable waveguide TTD technique [4]. The binary path selection technique is highly efficient for large phased array antenna configurations. The length tunable waveguide TTD technique suffers from inherent disadvantages of error in time delay with increasing frequency of operation and a very small maximum time delay value leads to a small angular range in beam steering. Nonetheless, it is relatively easier to configure the electrical TTDs compared to optical TTD networks. One major disadvantage that the electrical TTD suffers from is that the modules are prone to electromagnetic interference (EMI). Although optical TTD is not as easily configurable as its electrical counterpart, there has been a growing interest in this technique due to features such as large time delay with squint-free beam steering, wide bandwidth, reduced system weight and size, and low electromagnetic interference (EMI) when compared with electrical TTD techniques [5-9]. However, most of the optical TTD techniques require a large number of electro-optical elements such as lasers, optical modulators, photodiodes, etc resulting in a complex system design that may also suffer

from large power losses and may require specialized components. Sometimes, it also becomes cumbersome to extend these systems to 2-D arrays.

Optical TTD techniques can be further divided into *discrete* and *continuously tunable techniques*. Examples of discrete optical TTD techniques are bulk optical TTD technique [10-14], optical non-dispersive fiber TTD technique [15], wavelength-division-multiplexer TTD technique [16-21], holographic-grating based TTD technique [8, 22], wavelength-selective waveguide TTD technique [23], acoustic-optic TTD technique [24-27]. Examples of continuously tunable optical TTD techniques are optical dispersion based TTD technique [7], dispersive fiber prism based TTD technique [6, 28, 29, 30], chirped fiber grating based TTD technique [31, 32], and holographic-grating based TTD technique [33-35]. The dispersive fiber prism TTD technique involves using conventional dispersion compensating fiber which have a relatively small dispersion coefficient, $D = -100\text{ps/nm/km}$, and therefore long fiber lengths are required in the TTD module to achieve the required time delay. Therefore, by increasing the dispersion coefficient, the module size can be decreased proportionally.

1.3 Dispersive Fiber Prism Technique

The highly dispersive photonic crystal fiber true-time-delay (TTD) network presented in this work is based on a method called the dispersive fiber prism technique [6, 28, 29, 30]. This technique was first proposed and demonstrated by Esman et al in the year 1992. The schematic of the setup used by Esman et al is shown in Fig. 1.6 [6].

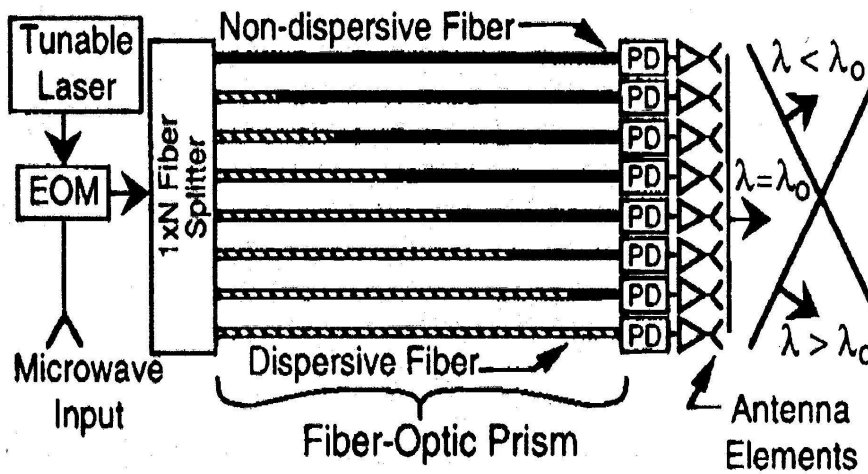


Fig. 1.6 Fiber-Optic Prism true-time-delay feed network [6]

A microwave input signal is modulated onto an optical carrier generated by a tunable laser source using an electro-optic modulator (EOM). This modulated optical carrier is split to N channels via a 1 -to- N splitter. These N output channels feed a dispersive fiber prism true-time-delay network consisting of a series of N delay lines. Each delay line consists of a highly dispersive fiber (HDF) connected to a non-dispersive fiber (NDF) with an overall length approximately equal between adjacent lines. After passing through the dispersive fiber prism, each optical signal is converted to an electrical signal at the photodetector (PD) and is fed to each element in the antenna array. The lengths of the dispersive and the non-dispersive fibers in each line are carefully chosen such that at a central optical wavelength λ_0 , the delay through all the lines are equal, i.e. all the signal arrive in phase at the output. Since there is no phase difference between adjacent elements at λ_0 , the RF beam is radiated broadside. For a wavelength greater or lesser than the central wavelength, the time delays between adjacent elements provide a

constant non-zero phase for the antenna array and the beam is steered to a different angle depending on the time delay difference between adjacent elements.

Dispersion is a property of a medium wherein the refractive index depends on the wavelength of light. The dispersion coefficient is given by [36]

$$D = -\frac{\lambda}{c} \frac{d^2 n_{eff}}{d\lambda^2} \quad (1.13)$$

where, n_{eff} is the effective refractive index of the guided mode inside the fiber. D is usually expressed in the units of ps/nm/km. Let us assume L to be the length of the fiber with a dispersion coefficient D , then the time delay generated (τ_i) when the wavelength is changed from λ_0 to λ_i can be written as

$$\tau_i = L \int_{\lambda_0}^{\lambda_i} D(\lambda).d\lambda \quad (1.14)$$

Applying the above principle to the dispersive fiber prism technique, and assuming the length of high dispersion fiber as L_i and the length of non dispersive fiber as $(L-L_i)$, we see that the time delay τ_i generated by changing the wavelength from λ_0 to λ_1 consists of contributions from both the highly dispersive and the non dispersive fibers and equation (1.14) can be modified as

$$\tau_i = L_i \int_{\lambda_0}^{\lambda_1} D_{HDF}(\lambda).d\lambda + (L-L_i) \int_{\lambda_0}^{\lambda_1} D_{NDF}(\lambda).d\lambda \quad (1.15)$$

$D_{HDF}(\lambda)$ is the dispersion coefficient of the highly dispersive fiber and

$D_{NDF}(\lambda)$ is the dispersion coefficient of the non-dispersive fiber

Therefore, the time delay difference $\Delta\tau_1$ between adjacent delay lines i and $i-1$ can be written as

$$\Delta\tau_1 = \tau_i - \tau_{i-1} = (L_i - L_{i-1}) \cdot \int_{\lambda_0}^{\lambda_1} D_{HDF}(\lambda) \cdot d\lambda - (L_i - L_{i-1}) \cdot \int_{\lambda_0}^{\lambda_1} D_{NDF}(\lambda) \cdot d\lambda \quad (1.16)$$

The dispersion coefficient of the high dispersion fiber is $\sim -100\text{ps/nmm/km}$ and that of the non-dispersive fiber is $\sim 3\text{ps/nm/km}$. Since the contribution from the non dispersive fiber is negligible, the second term on the right hand side of the above equation can be neglected and equation (1.16) can therefore be rewritten as

$$\Delta\tau_1 = \tau_i - \tau_{i-1} \cong (L_i - L_{i-1}) \cdot \int_{\lambda_0}^{\lambda_1} D_{HDF}(\lambda) \cdot d\lambda \quad (1.17)$$

The above integral depends on the length difference of highly dispersive fibers between adjacent elements and the integral. If $(L_i - L_{i-1})$ is chosen to be a constant, then $\Delta\tau_1$ depends on the integral alone. For a known deviation in the optical wavelength from the center wavelength, the integral is a constant. Therefore, for a wavelength λ_1 , $\Delta\tau_1$ between adjacent elements is constant. Similarly, for wavelength λ_2 , $\Delta\tau_2$ between adjacent elements is constant ($\Delta\tau_1 \neq \Delta\tau_2$).

The above constant time delay difference between adjacent elements leads to a constant phase difference between adjacent elements given by

$$\Delta\phi = 2\pi f_{RF} \Delta\tau \quad (1.18)$$

Recall from equation (1.1) that the phase difference between adjacent elements ($\Delta\phi$) required to transmit a signal to the θ direction is given by

$$\Delta\phi = \phi_i - \phi_{i-1} = k_0 d \sin(\theta) \quad (1.19)$$

Equating equations (1.18) and (1.19), we can write

$$\Delta\tau = \frac{d \sin \theta}{c} \quad (1.20)$$

Equation (1.20) is independent of the RF frequency used. Therefore, any RF frequency can be steered to a particular angle without any beam squint effect.

1.4 Highly dispersive Photonic Crystal Fiber (PCF) TTD based PAA

We see from equation (1.17) that a large time delay difference can be achieved if either or both of the length difference of the dispersion fiber is large between adjacent elements and the dispersion coefficient is large. Modern day PAA systems demand compact and small weight TTD networks. Therefore, one way of making the system compact is by utilizing very high dispersion coefficient fibers. The fibers used by Esman et al have a coefficient of $\sim -100\text{ps/nm/km}$ [6]. Photonic crystal fibers can be designed to achieve very high dispersion coefficients [37-42]. Therefore, the size of the TTD network can be reduced considerably.

A schematic of the PAA system utilizing the highly dispersive PCF-TTD is shown in Fig. 1.7. The TTD network consists of 4 delay, each with a different length of high dispersion PCF (red squares) and a non-zero dispersion shifted fiber (blue squares) such that at a central wavelength of 1545nm, the RF beam is radiated broadside.

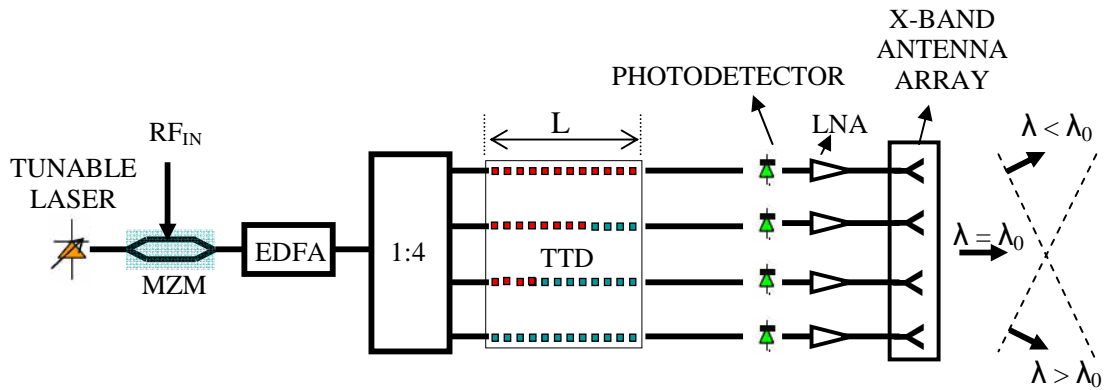


Fig. 1.7 Schematic of the Highly Dispersive PCF-TTD based PAA. MZM: Mach-Zehnder modulator; EDFA: Erbium-doped fiber amplifier, TTD: true time delay, LNA: low noise amplifier. (PCF is represented with red dots and non-zero dispersion shifted fibers is represented with blue dots)

Due to very high dispersion coefficients attainable in photonic crystal fibers compared to conventional dispersion compensation fibers, the required time delay difference for large scanning angle can be obtained within a short length of the fiber.

1.5 Objectives of the dissertation

The objectives of this dissertation are:

- To design photonic crystal fibers exhibiting very high dispersion coefficients for use as delay elements in a phased array antenna systems. Particular research emphasis is placed on designing highly dispersive structures using index guiding and photonic bandgap type photonic crystal fiber structures.
- To form a true time delay network employing fabricated highly dispersive photonic crystal fibers and demonstrate single beam transmission and reception of RF signals using an X-band antenna array.

- To demonstrate the feasibility of expanding the PAA system to transmit and receive multiple RF beams and perform an experiment to show simultaneous dual RF beam transmission and reception of RF signals.
- To evaluate the RF characteristics the X-band PAA system employing highly dispersive PCF based TTD network by performing harmonic and intermodulation distortion measurements and to measure the noise figure (NF) and the spurious-free-dynamic range (SFDR). Efforts are made to improve the SFDR of the system by employing a high power Erbium-doped fiber amplifier (EDFA).
- To provide an understanding of the difficulties of forming large practical antenna arrays and to introduce the concept of sparse arrays. A sparse array is designed and its working is demonstrated using highly dispersive conventional dispersion compensation fiber based true-time-delay network.
- To explore the applications of highly dispersive photonic crystal fibers in other important fields such as pulse compression, soliton propagation etc.

1.6 Dissertation Layout

This dissertation is divided into ten chapters. In Chapter 1, basic concepts of phased array antennas, phase control methods and an overview of different true-time-delay techniques are provided. A dispersive fiber prism technique is introduced and the use of highly dispersive photonic crystal fibers as true-time-delay elements is briefly discussed. Chapter 2 begins with a brief introduction of photonic crystal fibers. The central focus of the chapter is on designing highly dispersive photonic crystal fiber structures. Highly dispersive photonic crystal fiber designs based on index-guidance and photonic-bandgap guidance mechanisms are presented. The PCF fabrication procedure

and the difficulties encountered during the fabrication of such fibers are also briefly discussed. In Chapter 3, true-time-delay modules formed using a highly dispersive photonic crystal fiber is presented. The characterization of the highly dispersive photonic crystal fibers is performed and time delay measurement results of the modules are presented. In Chapter 4, the formation of a 1x4 X-band phased-array antenna utilizing the photonic crystal fiber time delay modules is presented in detail. The results for the demonstration of a single RF beam transmission and reception are presented and discussed. In Chapter 5, the principle of operation of multiple beam transmission and reception of the X-band phased-array antenna is introduced. Using the highly dispersive photonic crystal fiber based true-time-delay modules, simultaneous dual beam transmission and reception of the phased array antenna system is demonstrated. In Chapter 6, the effects of noise and distortion on the system performance are briefly discussed. The Noise Figure (NF), harmonic distortion and intermodulation distortion of the phased array antenna system are measured. An important parameter describing the non-linear effects of the system, namely the spurious-free dynamic range (SFDR) is measured and a method to improve the SFDR is also presented. In Chapter 7, the practical limitations on the implementation of large phased-array antennas will be briefly discussed. The concept of a sparse array will be introduced and the feasibility of using the dispersive fiber prism technique for such systems will be presented and demonstrated using a true-time-delay network formed using dispersion compensation fibers. In Chapter 8, other important achievements along the way of my research are presented. As a major achievement, a designed and fabricated photonic crystal fiber exhibiting the highest dispersion coefficient so far is presented and the practical issues with the fiber are discussed. The second achievement is the demonstration of the effect of pulse compression using highly dispersive photonic crystal fiber presented in Chapter 3 by

making use of the interplay between dispersive and non-linear effects inside the photonic crystal fiber. The highly dispersive photonic crystal fiber presented in Chapter 3 is used in conjunction with a pulsed laser source to demonstrate the effect of pulse compression. Recommendations for future work such as extending the single and multiple beam transmission and reception to 2 dimensional phased-array antennas and using highly dispersive photonic crystal fibers to demonstrate soliton propagation are briefly discussed in Chapter 9. Finally, in Chapter 10, a summary of the dissertation is given.

1.7 References

- [1] H. J. Visser, *Array and Phased Array Antenna Basics*, John Wiley and Sons Ltd (2005)
- [2] C. A. Balanis, *Antenna theory: Analysis and design, 3rd Edition*, John Wiley & Sons (2005)
- [3] R. C. Hansen, *Phased array antennas*, Wiley-Interscience (1998)
- [4] S. Barker and G. M. Rebeiz, "Distributed MEMS true-time delay phase shifters and wide-band switches," *IEEE. Trans. Microwav. Theory. Techniq.* vol. **46**, pp. 1881 - 1890 (1998)
- [5] W. Ng, A. A. Walston, G. L. Tangonan, J. J. Lee, I. L. Newberg, and N. Bernstein, "The first demonstration of an optically steered microwave phased array antenna using true-time-delay," *IEEE. J. Lightwav. Technol.* vol. **9**, pp. 1124- 1131 (1991)
- [6] R. D. Esman, M. Y. Frankel, J. L. Dexter, L. Goldberg, M. G. Parent, D. Stilwell, and D. G. Cooper, "Fiber-optic prism true time-delay antenna feed," *IEEE Photon. Technol. Letts.* vol. **11**, pp. 1347-1349 (1993)
- [7] R. Soref, "Optical dispersion technique for time-delay beam steering," *Appl. Opt.* vol. **31**, pp. 7395-7397 (1992)
- [8] Y. Chen and R. T. Chen, "A fully packaged true time delay module for a K-band phased array antenna system demonstration," *IEEE. Photon. Technol. Letts.* vol. **14**, pp. 1175 – 1177 (2002)

- [9] S. Yegnanarayanan and B. Jalali, "Wavelength-selective true time delay for optical control of phased-array antenna," *IEEE. Photon. Technol. Letts.* vol. **12**, pp. 1049 – 1051 (2000)
- [10] D. Dolfi, J. P. Huignard, and M. Baril, "Optically controlled true-time delays for phased array antenna," *Proc. SPIE.* vol. **1102**, pp. 152 (1989)
- [11] D. Dolfi, F. Michel-Gabriel, S. Bann, and J. P. Huignard, "Two-dimensional optical architecture for true-time-delay beam forming in a phased-array antenna," *Opt. Letts.* vol. **16**, pp. 255-257 (1991)
- [12] D. Dolfi, P. Joffre, J. Antoine, J. P. Huignard, D. Philippet, and P. Granger, "Experimental demonstration of a phased-array antenna optically controlled with phase and time delays," *Appl. Opt.* vol. **35**, pp. 5293-5300 (1996)
- [13] N. A. Riza, "Transmit/receive time-delay beam-forming optical architecture for phased-array antennas," *Appl. Opt.* vol. **30**, pp. 4594-4595 (1991)
- [14] N. A. Riza, "Liquid crystal-based optical time delay control system for wideband phased arrays," *Proc. SPIE.* vol. **1790**, pp. 171-183 (1992)
- [15] A. M. Levine, "Use of fiber optic frequency and phase determining element in radar," in *Proceedings of the 33rd Annual Symposium on Frequency Control*, IEEE, 436-443 (1979)
- [16] P. M. Freitag and S. R. Forrest, "A coherent optically controlled phased array antenna system," *IEEE. Microwav. Guided. Wav. Letts.* vol. **3**, pp. 293-295 (1993)
- [17] L. Xu, R. Taylor, and S. R. Forrest, "True-time delay phased array antenna feed system based on optical heterodyne techniques," *IEEE. Photon. Technol. Letts.* vol. **8**, pp. 160-162 (1996)
- [18] D. K. T. Tong, and M. C. Wu, "A novel multiwavelength optically controlled phased array antenna with a programmable dispersion matrix," *IEEE. Photon. Technol. Letts.* vol. **8**, pp. 812-814 (1996)
- [19] P. Goutzoulis and D. K. Davies, "Hardware-compressive 2-D fiber-optic delay line architecture for time steering of phased-array antennas," *Appl. Opt.* vol. **29**, pp. 5353-5359 (1990)
- [20] P. Goutzoulis and D. K. Davies, "All-optical hardware-compressive wavelength multiplexed fiber optic architecture for true-time delay steering of 2-D phased array antenna," *Proc. SPIE.* vol. **1703**, pp. 604-614 (1992)

- [21] P. Goutzoulis and D. K. Davies, J. Zomp, P. Hrycak, and A. Johnson, "Development and field demonstration of a hardware-compressive fiber-optic true time delay steering system for phased array antennas," *Appl. Opt.* vol. **33**, pp. 8173-8185 (1994)
- [22] Z. Fu and R. T. Chen, "Highly packing density optical true-time delay lines for phased array antenna applications," *Recent Research Developments Series*, pp. 1, Dec. 1998
- [23] S. Yegnanarayanan, P. D. Trinh, and B. Jalali, "Recirculating photonic filter: a wavelength-selective time delay for phased array antennas and wavelength code division multiple access," *Opt. Letts.* vol. **21**, pp. 740-742 (1996)
- [24] W. D. Jemison and P. R. Herczfeld, "Acousto-optically controlled true-time delay," *IEEE. Microwav. Guided Wav. Letts.* vol. **3**, pp. 72-75 (1993)
- [25] L. H. Gesell, R. E. Feinleib, J. L. Lafuse, and T. M. Turpin, "Acousto-optic control of time delays for array beam steering," *Proc. SPIE.* vol. **2155**, 194 (1994)
- [26] E. N. Toughlian and H. Zmuda, "A photonic variable RF delay line for phased array antennas," *IEEE. J. Lightwav. Technol.* vol. **8**, pp. 1824-1828 (1990)
- [27] E. H. Monsay, K. C. Baldwin, and M. J. Caucitto, "Photonic true-time delay for high-frequency phased array systems," *IEEE. Photon. Technol. Letts.* vol. **6**, pp. 118-120 (1994)
- [28] R. D. Esman, M. J. Monsma, J. L. Dexter, and D. G. Cooper, "Microwave True Time-Delay Modulator Using Fibre-Optic Dispersion," *Electron. Letts.* vol. **28**, pp. 1905-1907 (1992)
- [29] M. Y. Frankel and R. D. Esman, "True time-delay fiber-optic control of an ultra wideband array transmitter/receiver with multibeam capability," *IEEE. Trans. Microwav. Theory. Techniq.* vol. **43**, pp. 2387-2394 (1995)
- [30] S. T. Johns, D. A. Norton, C. W. Keefer, R. Erdmann, and R. A. Soref, "Variable time delay of microwave signals using high dispersion fibre," *Electron. Letts.* vol. **29**, pp. 555-556 (1993)
- [31] J. L. Cruz, B. Ortega, M. V. Andres, B. Gimeno, D. Pastor, J. Capmany, and L. Dong, "Chirped fiber gratings for phased array antenna," *Electron. Letts.* vol. **33**, pp. 545-546 (1997)
- [32] J. L. Corral, J. Marti, S. Regidor, J. M. Fuster, R. Laming, and M. J. Cole, "Continuously variable true time-delay optical feeder for phased-array antenna employing chirped fiber gratings," *IEEE. Trans. Microwav. Theory. Techniq.* vol. **45**, pp. 1531-1536 (1997)

- [33] Z. Shi, Y. Jiang, B. Howley, Y. Chen, F. Zhao, and R. T. Chen, "Continuously delay time tunable-waveguide hologram module for X-band phased-array antenna," *IEEE. Photon. Technol. Letts.* vol. **15**, pp. 972-974 (2003)
- [34] Z. Shi, L. Gu, B. Howley, Y. Jiang, Q. Zhou, R. T. Chen, M. Y. Chen, X. Wang, H. R. Fetterman, and G. Brost, "True-time-delay modules based on single tunable laser in conjunction with waveguide-hologram for phased-array antenna," *Opt. Engineering.* vol. **44**, 084301, (2005)
- [35] X. Chen, Z. Shi, L. Gu, B. Howley, Y. Jiang, and R. T. Chen, "Miniaturized Delay time-enhanced Photopolymer Waveguide Hologram Module for Phased-Array Antenna," *IEEE. Photon. Technol. Letts.* vol. **17**, pp. 2182-2184, (2005)
- [36] G. P. Agrawal, *Nonlinear Fiber Optics*, Academic Press (1995)
- [37] K. Thyagarajan, R. K. Varshney, P. Palai, A. K. Ghatak, and I. C. Goyal, "A Novel Design of a Dispersion Compensating Fiber," *IEEE. Photon. Technol. Letts.* vol. **8**, pp. 1510-1512 (1996)
- [38] J. -L. Auguste, R. Jindal, J. -M. Blondy, M. Clapeau, J. Marcou, B. Dussardier, G. Monnom, D. B. Ostrowsky, B. P. Pal, and K. Thyagarajan, "-1800ps/(nm.km) chromatic dispersion at 1.55 μ m in dual concentric core fibre," *Electron. Letts.* vol, pp. 1689-1690 (2000)
- [39] Y. Ni, L. Zhang, L. An, J. Peng, and C. Fan, "Dual-Core Photonic Crystal Fiber for Dispersion Compensation," *IEEE. Photon. Technol. Letts.* vol. **16**, pp. 1516-1518 (2004).
- [40] F. Gerome, J. -L. Auguste, and J. -M. Blondy, "Design of dispersion-compensating fibers based on a dual-concentric-core photonic crystal fiber," *Opt. Letts.* vol. **29**, pp. 2725-2727 (2004)
- [41] A. Huttunen, P. Torma, "Optimization of dual-core and microstructure fiber geometries for dispersion compensation and large mode area," *Opt. Express.* vol. **13**, pp. 627-635 (2005)
- [42] P. J. Roberts, B. J. Mangan, H. Sabert, F. Couny, T. A. Birks, J. C. Knight, and P. St. J. Russell, "Control of dispersion in photonic crystal fibers," *J. Opt. Fiber. Commun. Rep.* **2**, pp. 435-461 (2005)

Chapter 2 Highly dispersive photonic crystal fibers

In this chapter, a relatively new kind of fiber called the photonic crystal fiber (PCF) will be introduced. In such fibers, the structural parameters can be controlled to tune the dispersion coefficient, which is difficult to achieve in conventional optical fibers. Two different types of photonic crystal fibers – one having a core made up of solid silica and the other having an air core will be designed to achieve very high dispersion coefficients with a potential to be used as true-time-delay (TTD) elements in phased-array antenna (PAA) systems. Finally, the fabrication method of PCFs will be explained and difficulties encountered in fabrication will be briefly discussed.

2.1 Photonic Crystal Fiber (PCF)

Photonic crystal fibers (PCF) were first demonstrated by Knight et al. in 1996 [1]. PCFs are very different compared to the conventional single mode fibers. In the conventional single mode fibers, there is a high refractive index core surrounded by a low index cladding and light is guided in the core via the principle of total internal reflection at the core-cladding interface. In a PCF, the uniform cladding of the conventional fibers is replaced with an array of microscopic air holes that run down the entire length of the fiber [2, 3]. A defect, usually one or multiple missing holes, acts as core. Due to the presence of such a cladding, a photonic crystal fiber provides excellent flexibility in controlling the characteristics of the fiber such as the number of modes, numerical aperture, dispersion properties, nonlinearity etc by controlling the structural parameters [1-6]. For example, the dispersion of the PCFs can be flexibly tailored by tuning the pitch (Λ) of the periodic array, the air-hole diameter (d) or the refractive index (n) of silica.

Highly dispersive PCFs have been proposed for the application of broadband dispersion compensation in telecommunication [6]. PCFs can also be designed to achieve very high dispersion coefficients [7-12]. Such highly dispersive photonic crystal fibers have a great potential for use in phased array antenna systems because they can reduce the size and weight of the system considerably. The PCFs are also called microstructured fibers, holey fibers, and photonic bandgap fibers.

2.1.1 TYPES OF PHOTONIC CRYSTAL FIBERS

Depending on the type of guidance in the fibers, PCFs can be classified into [3]

1. Index-guiding PCF
2. Photonic-bandgap PCF

The light guidance mechanism in the index-guiding PCF is very similar to that in conventional optical fibers, wherein a high index core is surrounded by a relatively lower index cladding. The scanning electron microscope (SEM) cross section of a fabricated index-guiding PCF is shown in Fig. 2.1(a) [1]. The core is made up of solid silica and the cladding is composed of an array of microscopic air holes that run along the axis of the fiber. The presence of such an air-hole matrix reduces the effective index of the cladding region. Therefore, similar to the guidance mechanism in conventional optical fibers, the guidance in this kind of a PCF is due to total internal reflection. By changing the periodicity (also called pitch) of the air-hole array or the size air-holes in the cladding, the effective index can be modified and the fiber can exhibit many interesting characteristics [1-6].

In a photonic-bandgap PCF whose cross sectional SEM shown in Fig. 2.1(b), the central solid silica core is missing [13]. This forms a structure with a low index core (usually air) surrounded by a high effective index cladding. Therefore, light cannot be guided in this fiber by the principle of total internal reflection.

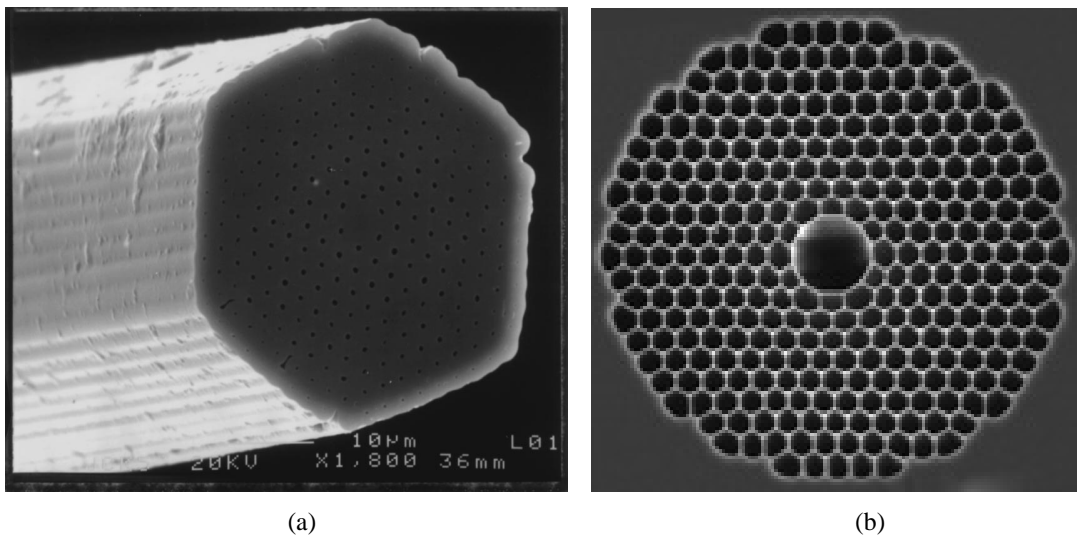


Fig. 2.1 SEM cross-sections of (a) Index-guiding PCF [1] (b) Photonic bandgap guiding PCF [13]

However, light can be guided in this structure using the phenomenon of photonic-bandgap guidance. In this kind of guidance, the periodic array of air-holes creates forbidden bands of frequencies (photonic bandgaps) within which light cannot penetrate the periodic cladding. The defect (large air-hole at the center), creates modes within the photonic bandgaps and light can be guided through the large central low index core. A mathematical explanation of the physics behind this phenomenon is provided in section 2.1.2.

2.1.2 MAXWELL'S EQUATIONS AND BLOCH THEOREM

The set of Maxwell's electromagnetic equations form the basis for the development of the theory for photonic bandgap guidance in photonic crystal fibers. The macroscopic Maxwell's equation in a dielectric medium under charge-free and current-free conditions can be written as [3, 14, 15]

$$\begin{aligned}
 \nabla \times \vec{E}(\vec{r}, t) &= \frac{\partial(\mu_0 \vec{H}(\vec{r}, t))}{\partial t} \\
 \nabla \times \vec{H}(\vec{r}, t) &= \varepsilon_0 \varepsilon(\vec{r}) \frac{\partial(\vec{E}(\vec{r}, t))}{\partial t} \\
 \nabla \cdot (\varepsilon_0 \varepsilon(\vec{r}) \vec{E}(\vec{r}, t)) &= 0 \\
 \nabla \cdot \vec{H}(\vec{r}, t) &= 0
 \end{aligned} \tag{2.1}$$

where \vec{E} and \vec{H} are the electrical and magnetic fields, ε is the permittivity, μ is the permeability, t is time, and r is the displacement to origin.

The time harmonic mode at the steady state is

$$\begin{aligned}
 \vec{H}(\vec{r}, t) &= \vec{H}(\vec{r}) e^{-i\omega t} \\
 \vec{E}(\vec{r}, t) &= \vec{E}(\vec{r}) e^{-i\omega t}
 \end{aligned} \tag{2.2}$$

By substituting equation (2.2) into equation (2.1), Maxwell equation for the steady state can be obtained

$$\begin{aligned}
 \nabla \times \vec{H}(\vec{r}) + i\omega(\varepsilon(\vec{r})\varepsilon_0 \vec{E}(\vec{r})) &= 0 \\
 \nabla \times \vec{E}(\vec{r}) - i\omega(\mu_0 \vec{H}(\vec{r})) &= 0
 \end{aligned} \tag{2.3}$$

It is possible to provide a master equation that fully describes the propagation of electromagnetic waves. By expressing the equation in magnetic field \vec{H} -field alone, full-vector wave equation is [14, 15]

$$\vec{\nabla} \times \left(\frac{1}{\mathcal{E}(\vec{r})} \vec{\nabla} \times \vec{H}(\vec{r}) \right) = -\frac{\omega^2}{c^2} \vec{H}(\vec{r}) \quad (2.4)$$

The eigen values are given by $(\omega/c)^2$. For a periodic lattice with period = a, the permittivity can be expressed as

$$\mathcal{E}(\vec{r}) = \mathcal{E}(\vec{r} + \vec{a}) \quad (2.5)$$

By employing Bloch theorem, we can express $\vec{H}(\vec{r})$ as a plane wave modulated with a periodic envelope

$$\vec{H}(\vec{r}) = e^{i\vec{k} \cdot \vec{r}} u_k(\vec{r}) \quad (2.6)$$

It is usually convenient to work in the reciprocal space. The wave equation of equation (2.4) can also be expressed in the reciprocal space as [15]

$$(i\vec{k} + \vec{\nabla}) \times \frac{1}{\mathcal{E}(\vec{r})} (i\vec{k} + \vec{\nabla}) \times u_k(\vec{r}) = \left(\frac{\omega_n}{c} \right)^2 u_k(\vec{r}) \quad (2.7)$$

$u_k(\vec{r})$ is a periodic function and can be expanded in terms of its Fourier coefficients [14, 15]

$$u_k(r) = \sum_G c_G(k) e^{i\vec{G} \cdot \vec{r}} \quad (2.8)$$

The transversality condition requires $(\vec{k} + \vec{G}) \bullet c_{\vec{G}} = 0$. We can express $c_{\vec{G}}$ as the sum of two components along unit vectors \hat{e}_1 and \hat{e}_2 which are orthogonal to $(\vec{k} + \vec{G})$ i.e. $(c_{\vec{G}} = c_{1,\vec{G}}\hat{e}_1 + c_{2,\vec{G}}\hat{e}_2)$ [3]. By substituting equation (2.8) in equation (2.7) and taking the Fourier transform on both sides, we get [15]

$$\sum_G \left[-\epsilon_{G',-G}^{-1} \cdot (k + G') \times (k + G) \right] c_G = \frac{\omega^2}{c^2} c_G \quad (2.9)$$

Equation (2.9) can be solved using Fast Fourier Transform techniques and compute the set of c_G 's by using a finite and a large number of plane waves. The eigensolutions are periodic functions of Bloch wavevector k . This method of solving is also called the plane wave expansion (PWE) [3]

2.2 Design of highly dispersive photonic crystal fibers

Conventional fibers designed for dispersion compensation in optical communication have shown that high values of dispersion coefficients ($D \sim -100$ ps/nm/km) can be achieved [5, 16]. However, the dispersion cannot be changed significantly in such fibers due to the small index variation across the transverse cross section of the fiber from doping.

Due to the presence of an array of periodic air holes running down the length in a photonic crystal fiber, index variations across the transverse cross section by changing the structural parameters such as air-hole diameter, periodicity etc is highly feasible. Therefore, PCFs have gained increasing popularity over the recent years due to their unique properties such as endless single mode operation [17], high nonlinearity [18], and

ultralow loss [19, 20] etc. It has been shown that photonic crystal fibers, unlike conventional dispersion compensation fibers (DCF) can be designed to exhibit extremely high dispersion coefficients [6, 8, 9, 10, 11, 12, 21, 22, 23]. Extreme values of dispersion coefficient as large as -59000ps/nm/km have been predicted [8] for geometries based on dual-core structure using a doped core. However, this comes at the expense of extremely narrow bandwidth. Although such highly dispersive photonic crystal fibers can be used for phased array antenna application, due to their extremely narrow bandwidth, the steering angle becomes extremely difficult to control. Therefore, there is a need to fabricate highly dispersive PCF structures that exhibit high dispersion and modest bandwidth (high dispersion-bandwidth product) for use as true-time-delay modules in phased array antenna systems. As stated earlier in section 1.4, the employment of such highly dispersive PCFs helps in reducing the size and weight of the system when used in a true-time-delay network, leading to compact device structures suitable for air-borne and space-borne applications.

2.2.1 HIGHLY DISPERSIVE STRUCTURE BASED ON INDEX-GUIDING PCF

It is possible to design highly dispersive structures based on index-guiding PCFs. The structure of the highly dispersive photonic crystal fiber is based on dual concentric-core design as proposed by Thyagarajan et al. in the year 1996 [9]. The working principle of this structure is similar to that of a directional coupler [24]. In this section, the working principle of a dual concentric-core photonic crystal fiber and design results demonstrating very high dispersion and bandwidth will be presented.

2.2.1.1 Working principle of a highly dispersive PCF based on a dual concentric-core design

The working mechanism of a dual concentric-core PCF is very similar to that of a directional coupler which can support two supermodes [24]. First, we introduce the coupled mode theory on the dual core PCFs [22]. The central core and the outer core behave like two parallel waveguides and the high dispersion is from the coupling between the two waveguides. We can expand the propagation constants, β , of the modes in the isolated waveguides around the phase matched frequency using Taylor's series and neglect higher order terms to get [24]

$$\beta_i(\omega) \approx \beta(\omega_p) + (\omega - \omega_p) \left. \frac{d\beta_i}{d\omega} \right|_{\omega=\omega_p} + \frac{(\omega - \omega_p)^2}{2} \left. \frac{d^2\beta_i}{d\omega^2} \right|_{\omega=\omega_p} \quad (2.10)$$

where $i = 1, 2$ represents the inner and the outer waveguide respectively and ω_p represents the phase matched frequency.

The coupled mode theory tells us that the coupling of individual modes can generate two supermodes, whose propagation constants can be written as [24, 25]

$$\begin{aligned} B_{\pm} &= \beta_0 + \gamma_n = \beta_0 \pm \sqrt{\kappa^2 + \delta^2} \\ \delta &= (\beta_1 - \beta_2)/2 \\ \beta_0 &= (\beta_1 + \beta_2)/2 \\ \Rightarrow B_{\pm} &= (\beta_1 + \beta_2)/2 \pm \sqrt{\kappa^2 + (\beta_1^2 - \beta_2^2)^2/4} \end{aligned} \quad (2.11)$$

where κ is the coupling constant between the two waveguides. β_1 and β_2 are the propagation constants of the inner and outer cores respectively.

Let us now insert equation (2.10) into equation (2.11) and differentiate the result twice with respect to angular frequency. Supposing that the two waveguides' $\left. \frac{d^2 \beta}{d\omega^2} \right|_{\omega=\omega_p}$ are all very small numbers (this term is mainly determined by the material dispersion of waveguide, and so it must be a very small term), we get the group velocity dispersion as

$$\frac{d^2 B_{+/-}}{d\omega^2} = \pm \frac{1}{4\kappa} \left(\frac{d\beta_1}{d\omega} - \frac{d\beta_2}{d\omega} \right)^2 \times \left[\frac{(\omega - \omega_p)^2}{4\kappa^2} \left(\frac{d\beta_1}{d\omega} - \frac{d\beta_2}{d\omega} \right)^2 + 1 \right]^{\frac{3}{2}} \quad (2.12)$$

The dispersion parameter is normally written as [24]

$$D = -\frac{\lambda}{c} \frac{d^2 n_{eff}}{d\lambda^2} = -\frac{2\pi c}{\lambda^2} \frac{d^2 B}{d\omega^2} \quad (2.13)$$

Therefore, equations (2.12) and (2.13) can be combined to get the dispersion coefficient (D)

$$D = \mp \frac{\pi}{2c\kappa} \left(\frac{dn_1}{d\lambda} - \frac{dn_2}{d\lambda} \right)^2 \times \left[\frac{\pi^2}{\kappa^2} \frac{(\lambda - \lambda_p)^2}{\lambda_p^2} \left(\frac{dn_1}{d\lambda} - \frac{dn_2}{d\lambda} \right)^2 + 1 \right]^{-3/2} \quad (2.14)$$

From the above equation, we see that the D reaches its maximum value when $(\lambda - \lambda_p) = 0$. Therefore, equation (2.14) changes into

$$D_{Max} = \mp \frac{\pi}{2c\kappa} \left(\frac{dn_1}{d\lambda} - \frac{dn_2}{d\lambda} \right)^2 \quad (2.15)$$

The full width at half maximum (FWHM) can be derived from equations (2.14) and (2.15) as [26]

$$\Delta\lambda = 0.766 \times \frac{2\kappa\lambda_p}{\pi} \left| \left(\frac{dn_1}{d\lambda} - \frac{dn_2}{d\lambda} \right)^{-1} \right| \quad (2.16)$$

From equations (2.15) and (2.16) we see that the dispersion coefficient and the FWHM, both mainly depend on the coupling constant κ and the difference of $dn/d\lambda$ between the inner and the outer core. The dependence also suggests that there is a trade off between the maximum dispersion coefficient (D_{Max}) and FWHM ($\Delta\lambda$). If we multiply equation (2.15) with equation (2.16), we can get a dispersion-bandwidth product that is independent of the coupling constant (κ). This product can be defined as a figure of merit for our structure [26]

$$|D_{Max} \times \Delta\lambda| = 0.766 \times \frac{\lambda_p}{c} \left| \frac{dn_1}{d\lambda} - \frac{dn_2}{d\lambda} \right| \quad (2.17)$$

Equation (2.17) shows that the product depends on the phase match wavelength and we further define $T = \left| \frac{dn_1}{d\lambda} - \frac{dn_2}{d\lambda} \right|$ which is the difference of $dn/d\lambda$ between the inner and the outer core. If our interest is around a specific wavelength, say $\lambda_p = 1.56 \mu\text{m}$, then the product just depends on the value of T . In order to maximize the dispersion-bandwidth product, we need to increase T as much as possible.

2.2.1.2 Highly dispersive dual concentric-core PCF structure

A schematic cross section of the designed dual concentric-core highly dispersive photonic crystal fiber is shown in Fig. 2.2 [26]. The white region is the silica background and the pink region represents air-holes. The periodicity of the air-holes is given by Λ . d_1 , d_2 denote the diameters of the first and second air hole rings which form the inner cladding; The area at the center, determined by the first air hole ring diameter and the

period, forms the center core; d_3 denotes the diameter of the third air hole ring which forms the second core. The rest of the air hole rings (fourth-tenth rings) form the outer cladding region. The research work presented herein has the highest value dispersion-bandwidth product reported thus far [26]. It also has high dispersion value which is an improvement by a factor of 5 over previous designs and is a promising candidate for applications requiring compact systems for broadband phased array antennas.

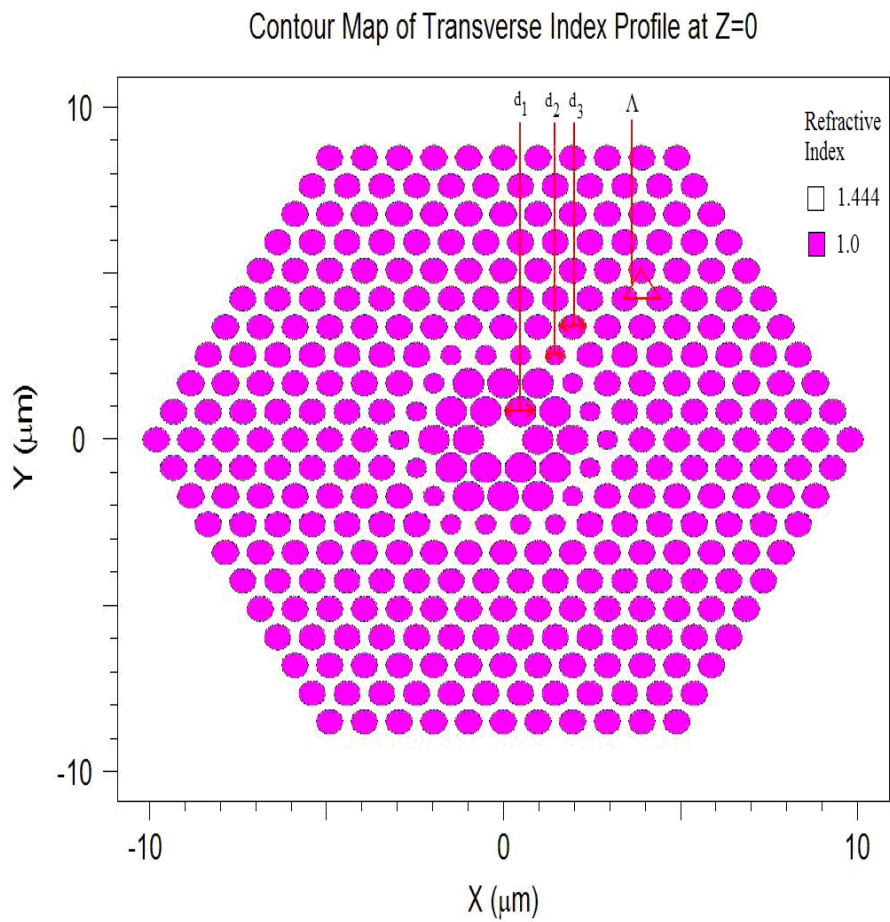


Fig. 2.2 Schematic cross section of the designed dual concentric core PCF

The parameters of the fiber are carefully chosen to make the respective modes have a phase match at a wavelength (λ_p) close to 1.56 μm . The redistribution of modal fields with a variation in wavelength is shown in Fig. 2.3. When the wavelength is shorter than phase match wavelength ($\lambda < \lambda_p$) the field is essentially confined in the inner core (Fig. 2.3(a)). Around the phase match wavelength ($\lambda \approx \lambda_p$), a part of the field is in the inner core and a part is in the outer core (Fig. 2.3(b)). When the wavelength is longer than phase match wavelength ($\lambda > \lambda_p$), most of the power spreads to the outer core and is effectively guided in the outer core (Fig. 2.3(c)).

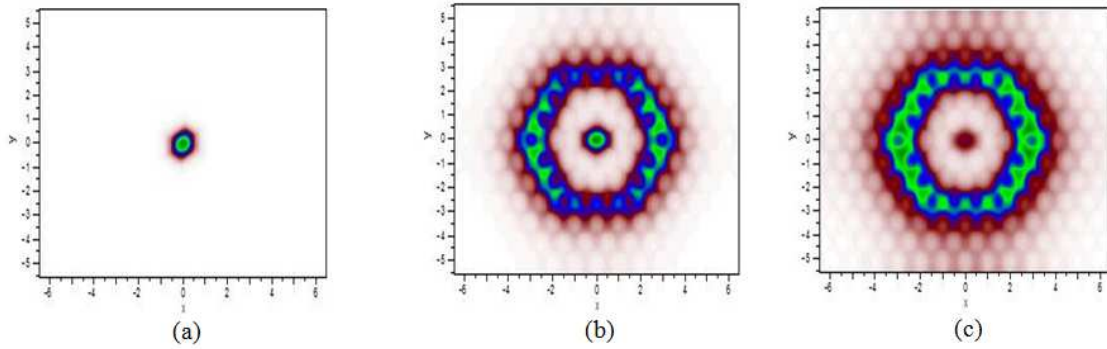


Fig. 2.3 Mode profile of the dual concentric-core PCF at (a) $\lambda < \lambda_p$ (b) $\lambda \approx \lambda_p$ and (c) $\lambda > \lambda_p$

This kind of modal field redistribution makes the effective index change greatly with the wavelength and thus, near the phase match wavelength, the dispersion coefficient of the dual concentric core PCF is very large.

At the phase match wavelength around 1.56 μm , the effect of varying the period (A) on $dn/d\lambda$ and dispersion-bandwidth product is carefully studied using fully vectorial plane wave expansion (PWE) method [27], wherein, the solutions to Maxwell's equations are found by expanding the fields in terms of plane waves and applying Bloch's theorem,

along with the principle of orthogonality of modes. Fully vectorial PWE method is extremely accurate for perfect periodic structures without defects, and it is only approximately accurate for periodic structures with defects – provided that a proper supercell containing the defect is selected for calculations. A more detailed explanation can be found in a paper by Ho et al. [27]. All simulations are performed using commercially available RSoft BandSOLVETM software that is based on fully vectorial PWE method [28]. For our design, a supercell of size 10 x 10, instead of a unit cell is implemented for periodic boundary conditions. In Fig. 2.4, the curve marked with filled squares shows the $dn/d\lambda$ change of the inner core with respect to change in the period and the curve marked with the empty squares shows the same variation for the outer core around the wavelength 1.56 μm .

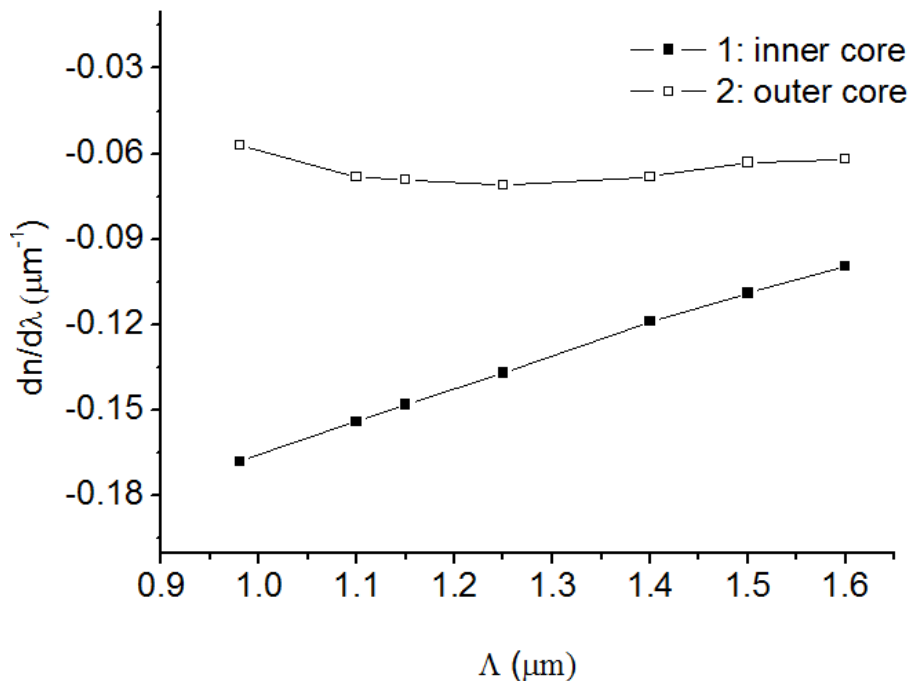


Fig. 2.4 Variation of $dn/d\lambda$ with respect to the period (Λ) for the inner core (filled squares) and outer core (empty squares)

It can clearly be seen from the figure that the inner core $dn/d\lambda$ changes linearly with a change in the period and a smaller period gives a larger $dn/d\lambda$ value. This is because a smaller period gives a smaller inner core and thus the confinement in the inner core will become weaker. This makes the effective index in inner core more sensitive to the wavelength change, which means that the absolute value of $dn/d\lambda$ increases significantly when the period is decreased. For outer core, the $dn/d\lambda$ value changes very little with the period. This is because the outer core has a ring like structure and this kind of structure's confinement ability is stronger compared to the inner core's rod structure. So, we can see that $dn/d\lambda$ of the outer core guided mode is almost unchanged and the value is around $-0.065\mu\text{m}^{-1}$. Using the results from Fig. 2.4, the value of T is derived and shown in Fig. 2.5.

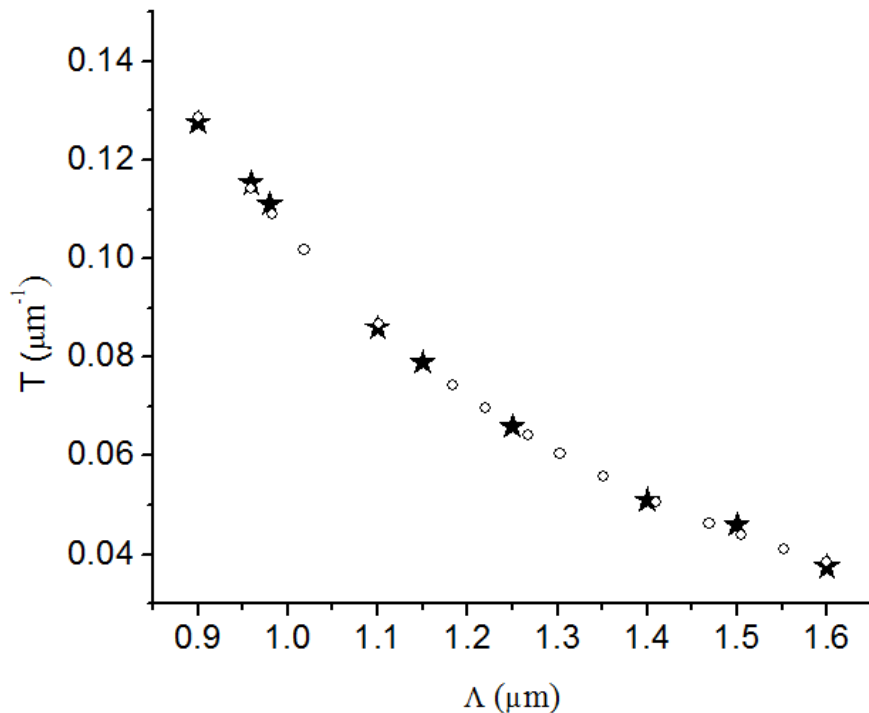


Fig. 2.5 Calculation result (stars) and its curve fit (circles) for the relationship between T and Period (Λ)

It can be seen from the figure that the value of T decreases with an increase in the value of the period and this is mainly contributed by the inner core's $dn/d\lambda$ change. The curve marked with stars is the calculation result and the curve marked with circles is a fit to the calculation result. It is found that the value of T decays exponentially with an increase in the period of the holes and the decay constant is about $0.431\mu\text{m}$. This result combined with equation (2.17) also means that the dispersion-bandwidth product decays exponentially as the period is increased.

From the above discussion we find that the period (Λ) plays a vital role in achieving broadband operation along with a very high dispersion value. By designing PCF structures with very small air-hole pitch, we can achieve very high dispersion-bandwidth products. However, it becomes very difficult, in practice, to control the diameter of the air holes over such small dimensions. As will be discussed in section 2.3.2, by choosing a value of period as $0.98\ \mu\text{m}$, we are almost hitting the limits of manufacturability. In order to satisfy the high dispersion-bandwidth requirement and manufacturing feasibility simultaneously, a dual concentric-core pure silica PCF with $\Lambda = 0.98\ \mu\text{m}$ is designed to have a maximum dispersion value of about $-9500\ \text{ps}/\text{nm}/\text{km}$ and bandwidth of about $55\ \text{nm}$. The inner core is made of pure silica, surrounded by an inner cladding made of two air hole rings with of diameter d_1 , followed by an outer core with diameter d_2 , and then by an outer cladding with diameter d_3 . Since we are hitting the limit of manufacturability at a period of $0.98\ \mu\text{m}$, we choose this value for period and simulate structures with various parameter values. The fabrication difficulties are discussed later in this chapter. A structure with values of $d_1/\Lambda = 0.90$, $d_2/\Lambda = 0.59$, and $d_3/\Lambda = 0.76$, is chosen in order to provide a maximum dispersion coefficient

around 1.56 μm [26]. These values are obtained after many trial values are simulated and each parameter can be used independently to tune the dispersion curve.

The variation in the effective index of the fundamental mode with wavelength is studied by using the plane wave expansion method [27]. In Fig. 2.6, the curves marked with – and + show the effective refractive index change with the wavelength in the inner and the outer core, respectively. The curve marked with stars is due to the combined effect of the concentric cores and it connects the inner core's $dn/d\lambda$ and outer core's $dn/d\lambda$ and is mainly dependent on the coupling constant between the inner and the outer core.

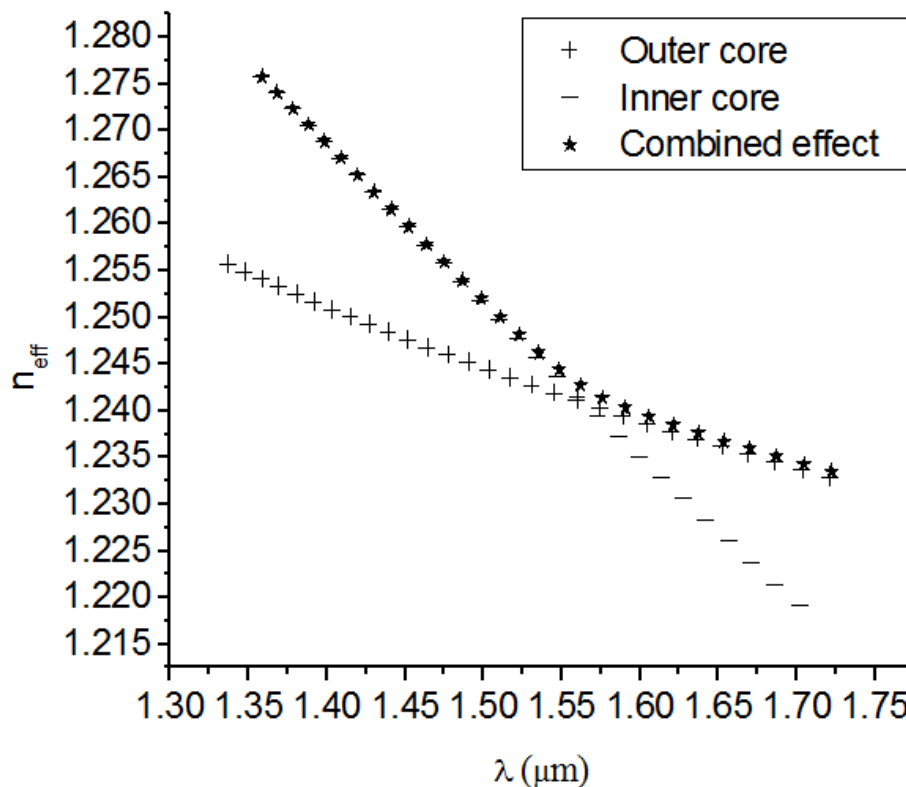


Fig. 2.6 Effect of coupling on the effective refractive index

This curve predominantly controls the shape of the resulting dispersion curve. We can also see that the two individual core curves are like the asymptotes to the combined curve. This means that, for a wavelength greater than the phase match wavelength, the mode is just like being confined in the outer core and can not feel any effect from the inner core and vice versa. In order to use equation (2.13) to calculate the net chromatic dispersion of the structure, we perform a second differential on the curve marked with stars with respect to the wavelength and multiply the by $-\lambda c$. The result of our calculation is shown in Fig. 2.7 as a curve marked with solid squares. From the figure, we see that the maximum value of dispersion achieved is around -9500ps/nm/km and the FWHM is about 55nm near a wavelength of $1.56\mu\text{m}$.

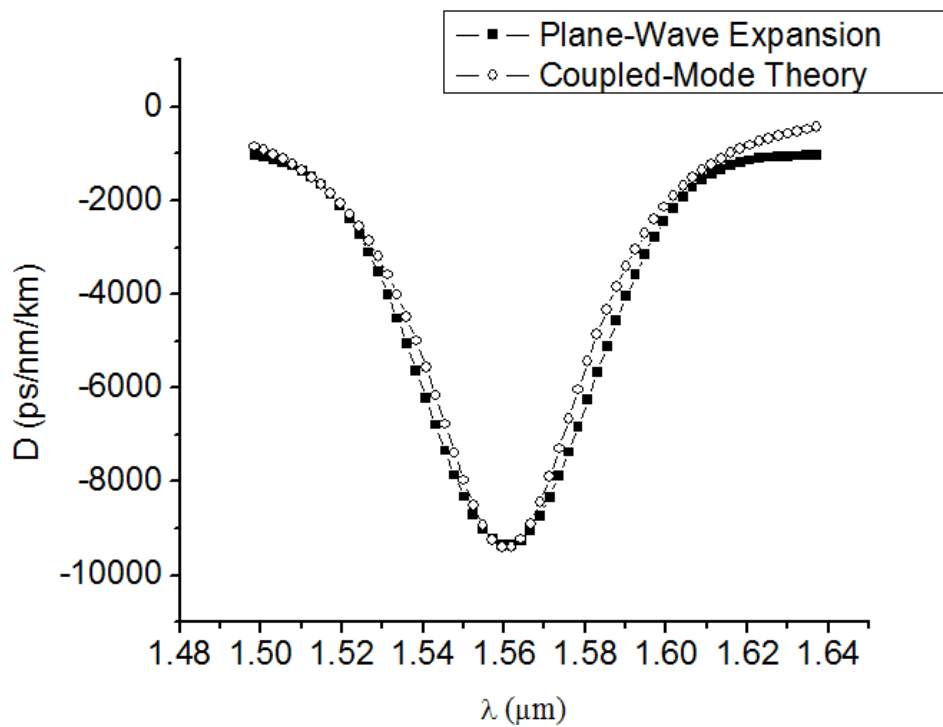


Fig. 2.7 Relationship between the dispersion value D and wavelength and comparison of Plane Wave Expansion (filled squares) and Coupled-Mode Theory (empty circles) results

Finite Difference Beam Propagation Method (BPM) [28-30] is used to calculate the two mode patterns in the inner and the outer core and an overlap integral method is used to calculate the coupling constant between the two cores. All the simulations performed above are done using RSoft BeamPROPTM software package [28]. The software can compute the mode patterns, given a refractive index profile and an input field. The coupling factor is also computed and is found to be, $\kappa=2\pi*0.00167/\lambda_p=0.00673 \mu\text{m}^{-1}$. Coupled mode theory is employed to obtain the curve between the dispersion and the wavelength. The plane wave expansion [27] is compared with that of the coupled mode theory [29] in Fig. 2.7 and the results are found to be in good agreement with each other. This kind of broadband, highly negative dispersion fiber can be used in radar applications.

In order to see the effect of these parameters on the dispersion curve, each parameter is varied independently, while keeping the remaining parameters at the above mentioned values and the results are shown in Fig. 2.8. The dependence of dispersion on Λ is shown in Fig. 2.8(a). As discussed previously, it can be seen that the value of dispersion decreases as the period is increased. The dip also changes its position on the wavelength scale. The dependence of the position and magnitude of the dispersion curve on d_1 , d_2 , and d_3 are shown in Figs. 2.8(b), 2.8(c) and 2.8(d) respectively. It can be seen from these figures that the position and magnitude of the dispersion curve is extremely sensitive to the parameter values, therefore the parameters need to be strictly controlled while drawing the fibers making fabrication even more challenging. This issue also sets a limit on the manufacturability.

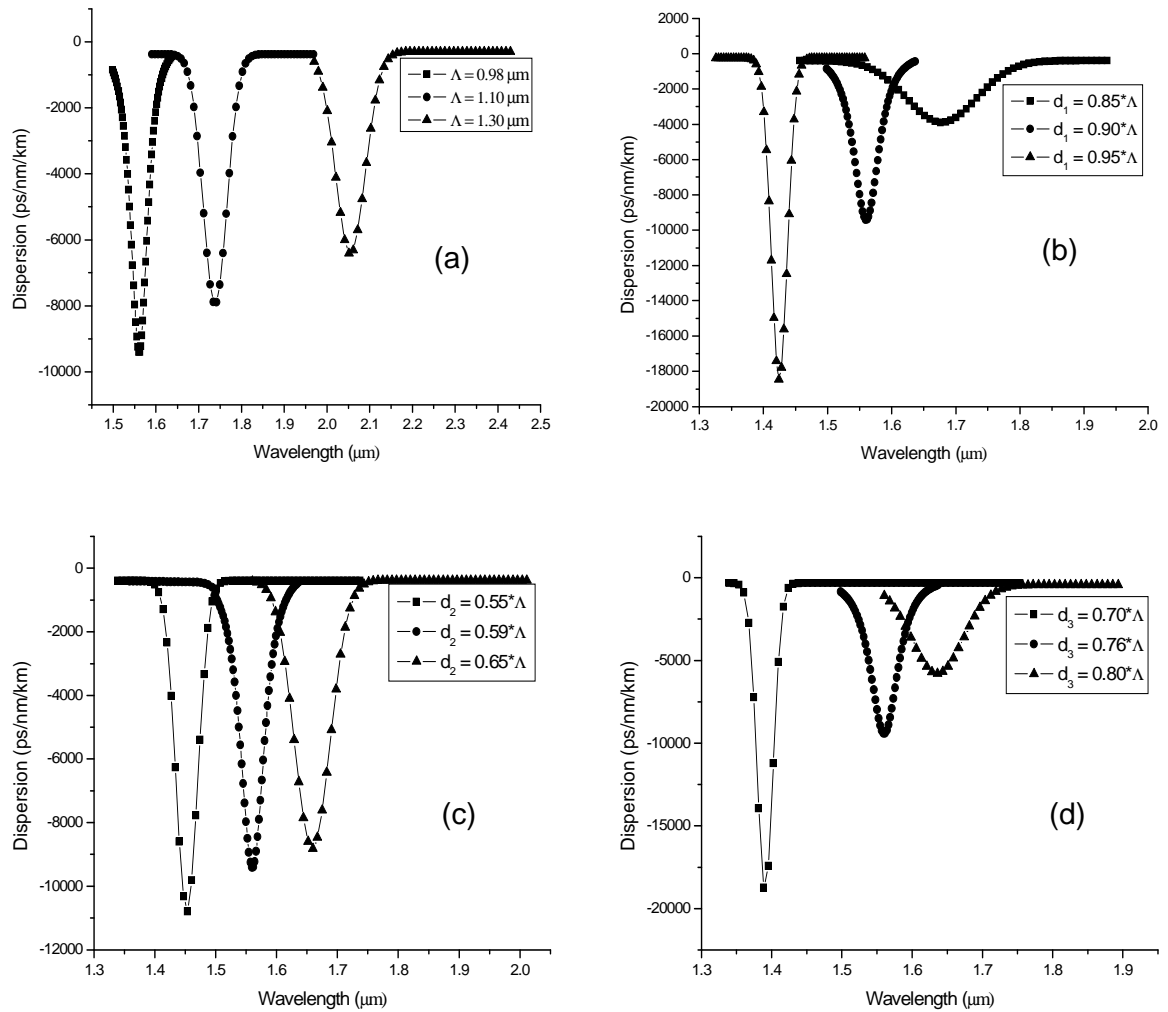


Fig. 2.8 Variation of the dispersion value and the shift observed due to (a) variation in the pitch, (b) variation of d_1 , (c) variation of d_2 , and (d) variation of d_3 , while keeping all the other parameters as in the given design in each case

In our design, we have used two air hole rings between the inner and the outer core instead of one as given by G er ome et al [11]. As the number of air hole rings increase between the two cores, the value of dispersion gets larger, but the bandwidth gets narrower as shown in Fig. 2.9.

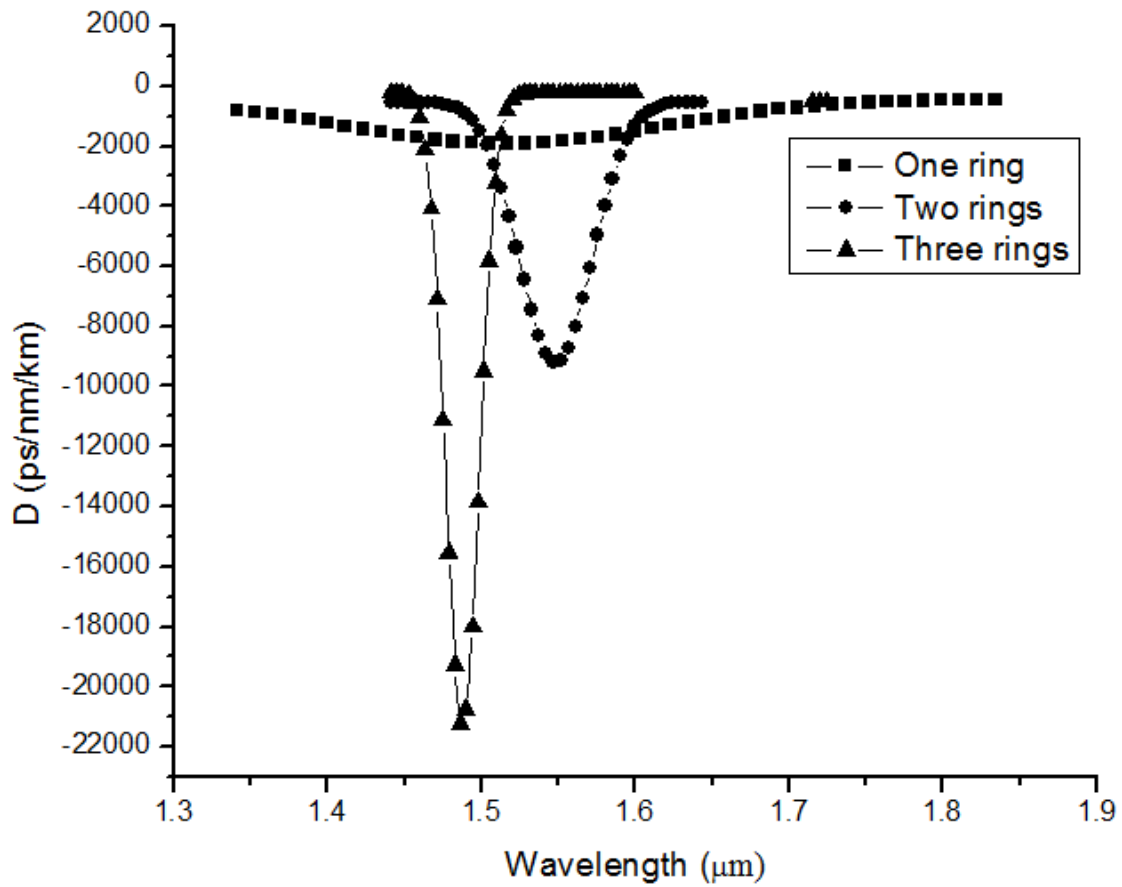


Fig. 2.9 Variation of dispersion with number of air hole rings between the inner and the outer core

We choose two air hole rings as it gives a high value of dispersion, along with a reasonable bandwidth of operation suitable for our application.

2.2.2 HIGHLY DISPERSIVE STRUCTURE BASED ON AIR-GUIDING PCF

Air-guiding PCFs, which have an air-core, can also be designed to achieve very high dispersion coefficients. Light in these fibers is guided via the principle of photonic bandgap guidance. Equation (2.9) is solved by Plane Wave Expansion method and the effective index as a function of wavelength is computed. One advantage with this kind of

a structure is that very high power light can be guided through these fibers as there is very little interaction of light with glass. Therefore, the damage threshold of the fibers is very high. Such photonic bandgap fibers also exhibit very high dispersion coefficient values near the band edges as a consequence of Kramers-Kronig relation. The dispersion coefficient of such fibers is negative at shorter wavelengths, passes through zero and then assumes positive values at higher wavelengths within the bandgap.

A photonic bandgap fiber with a hexagonal lattice is very easy to fabricate. Such a structure provides a very high air-filling fraction. A high air-filling fraction opens the band gap even more, thus increasing the bandwidth of the fiber. By introducing a defect, such as an air-core in an otherwise perfectly periodic lattice, defect modes are created inside the photonic bandgap. Light satisfying the defect mode criterion cannot propagate into the periodic cladding as it is within the photonic bandgap (forbidden frequency band) of the periodic cladding. Therefore, light propagates through the defect (air-core) without much interaction with the surrounding silica lattice. Near the band edges, the transmission abruptly drops and light is no longer within the forbidden region of the periodic cladding. There is a sudden change in the effective refractive index of the mode, and hence, a steep increase in the dispersion coefficient is observed near the band edges.

The schematic of the cross section of the designed photonic bandgap fiber structure exhibiting a very high value of dispersion coefficient near 1550nm is shown in Fig. 2.10. The red region is the silica background and the white regions denote air. It can be seen from the figure that the structure consists of a periodic cladding made up of closely packed hexagonal shaped holes.

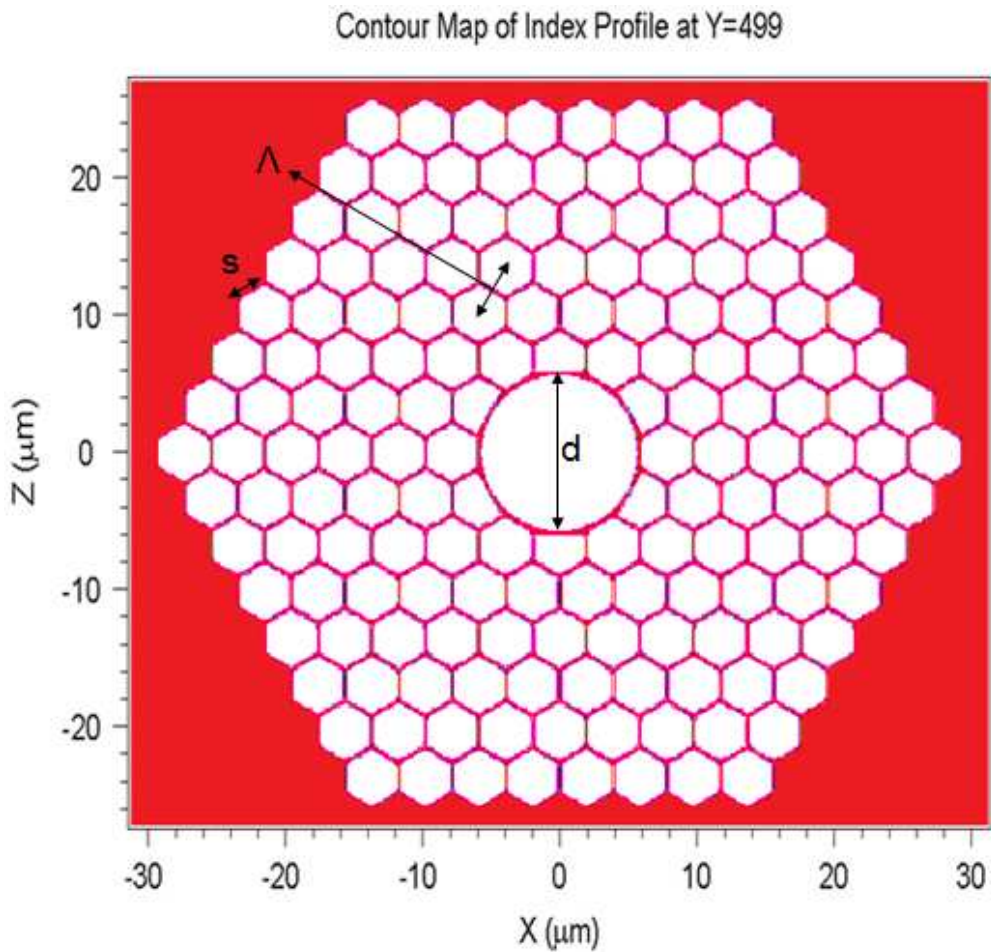


Fig. 2.10 Schematic cross section of the designed photonic bandgap fiber

In a practical draw procedure, a hollow glass tube is inserted into the center and the structure is drawn by maintaining sufficient pressure inside the tube and preventing it from collapsing. This technique produces a circular center core, but modifying the nearby holes as required to give a combination of hexagonal and pentagonal shaped holes. A thin annular silica ring surrounding the air-core is formed due to the finite thickness of the inserted glass tube. Such features can be clearly observed in Fig. 2.10. The period (Λ), hexagon side length (s) and central air-core diameter (d) are chosen as $3.86\mu m$, $2.14\mu m$ and $11.35\mu m$ respectively.

Using the formalism in section 2.1.2, the periodic boundary valued problem can be solved using PWE method. RSoft BandSOLVE™ software is used to compute the bandgaps exhibited by the periodic cladding. The solutions to the periodic cladding problem are plotted (blue) on the frequency versus propagation constant as shown in Fig. 2.11(a).

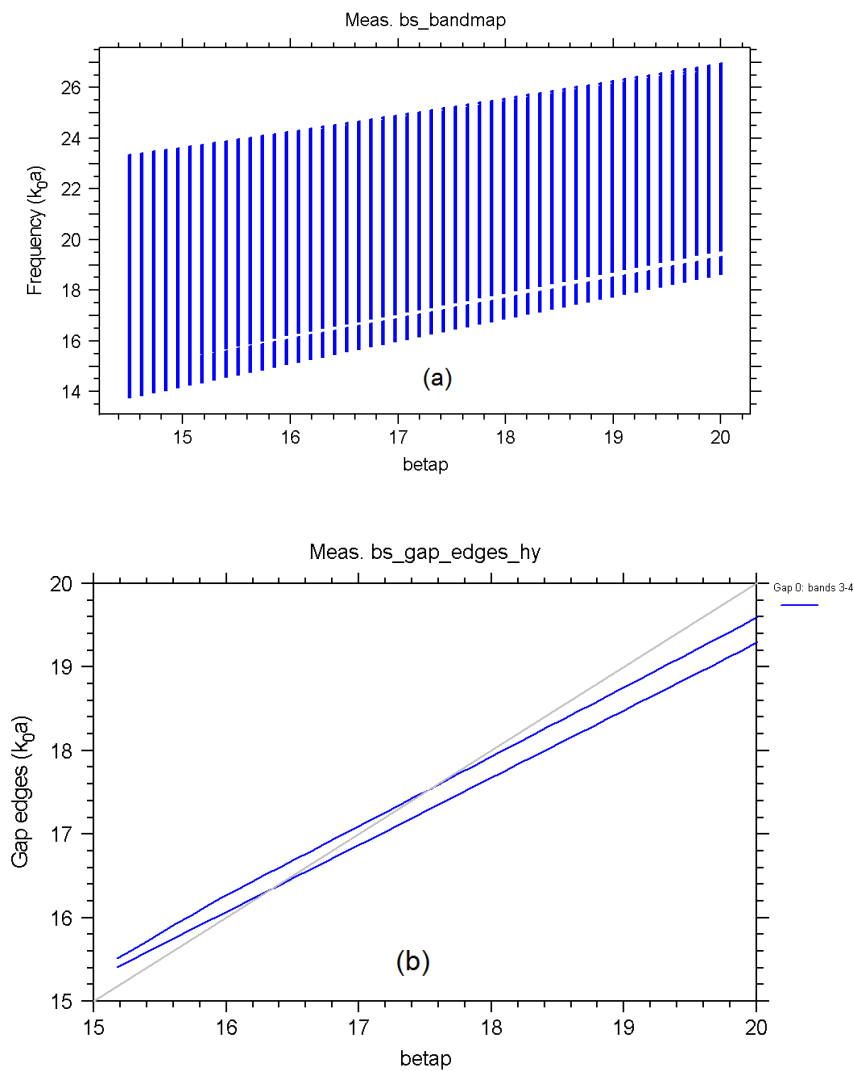


Fig. 2.11 (a) Frequency versus propagation constant relation for the cladding showing forbidden regions (gap) within which no solution to Maxwell's equations exists (b) The gap edges are plotted showing the light line (frequency = propagation constant)

The discrete lines are due to discrete steps used in defining the propagation constant in the software. It can be seen from the figure that there is a frequency range for certain propagation constants within which no solutions to Maxwell's equations exist. These forbidden frequency ranges, also called bandgaps, are regions within which light cannot propagate through the cladding. The bandgap edges along with the light line (slope = unity) is also shown in Fig. 2.11(b). The light line is important for our application because the central core (defect) is made of air. Due to the inclusion of such a defect, thousands of defect modes (solutions to Maxwell's equations) exist within the bandgap. It becomes necessary to filter out the unnecessary modes and only extract the useful modes. We know that since the light mode propagates through air-core, the modal index is very close to unity. Therefore, the probability of finding a useful mode very close to the light line becomes very high. Using such a condition, the software can be used to extract useful modes and provide solutions.

As was in the previous case of index guiding PCF fiber, in order to simulate the dispersion curves of such a structure, a super cell needs to be chosen as the structure has a defect (central air-core). A 10 x 10 supercell satisfies the periodic boundary conditions. The fiber supports fundamental modes which have a near-Gaussian profile as shown in Fig. 2.12 (a). The higher order modes are also shown in Fig. 2.12 (b) and Fig. 2.12 (c). The calculated effective refractive index of the fundamental mode as a function of wavelength is shown in Fig. 2.13.

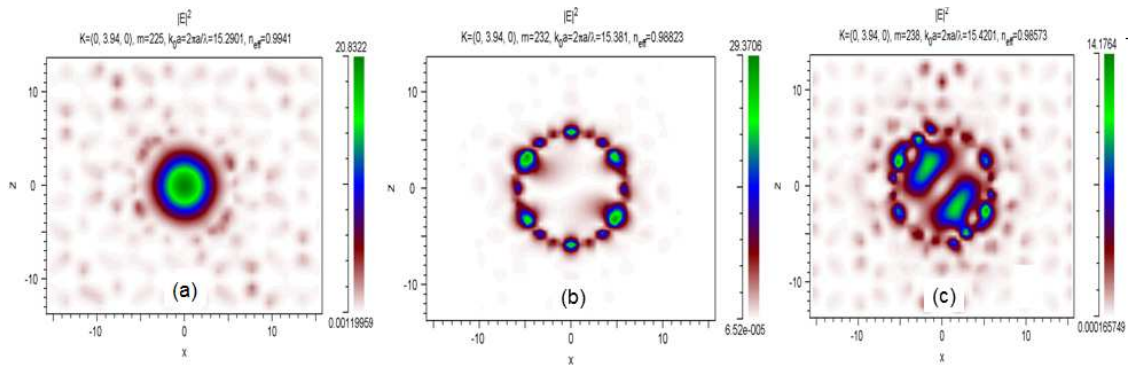


Fig. 2.12 Computed transverse mode profiles of the designed highly dispersive bandgap fiber showing (a) Fundamental mode (b) and (c) higher order modes

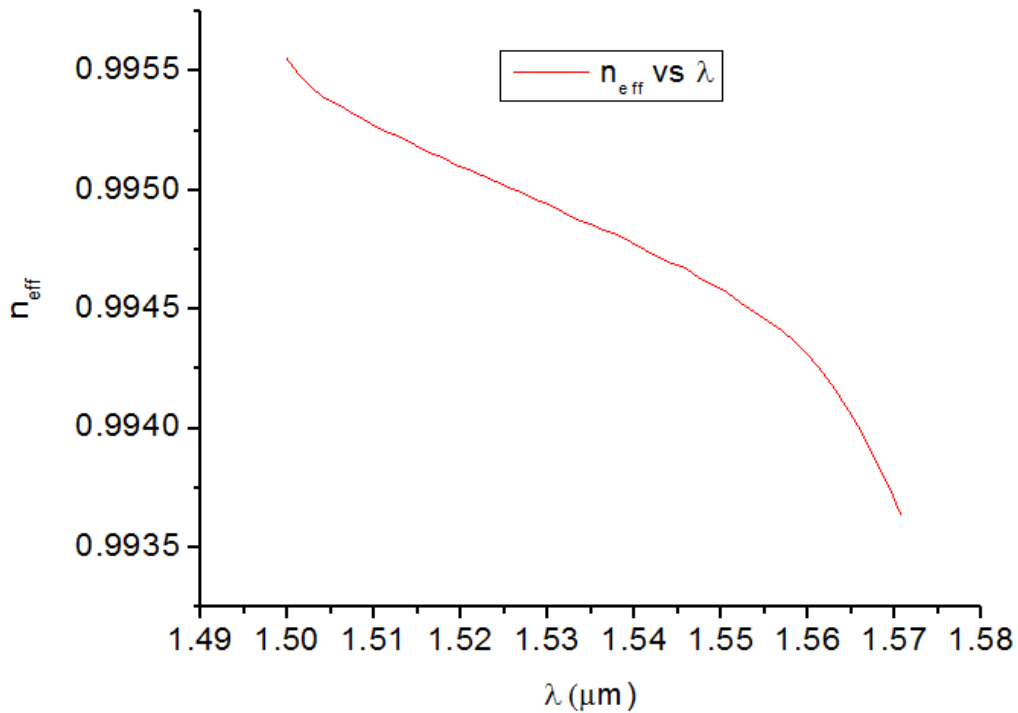


Fig. 2.13 Calculated effective refractive index of the fundamental guided mode (n_{eff}) as a function of wavelength

Employing equation (2.13), the dispersion coefficient of the photonic bandgap fiber is obtained. The derived dispersion coefficient curve is shown in Fig. 2.14. The fiber

exhibits the characteristic dispersion curve with high negative values at shorter wavelengths, passing through zero near 1517nm and rising to high positive values at longer wavelengths. The simulated photonic bandgap fiber can achieve dispersion coefficients larger than 4000ps/nm/km near 1550nm. Such a fiber finds great application in phased array antenna systems as the true-time-delay units can be compact and light weight.

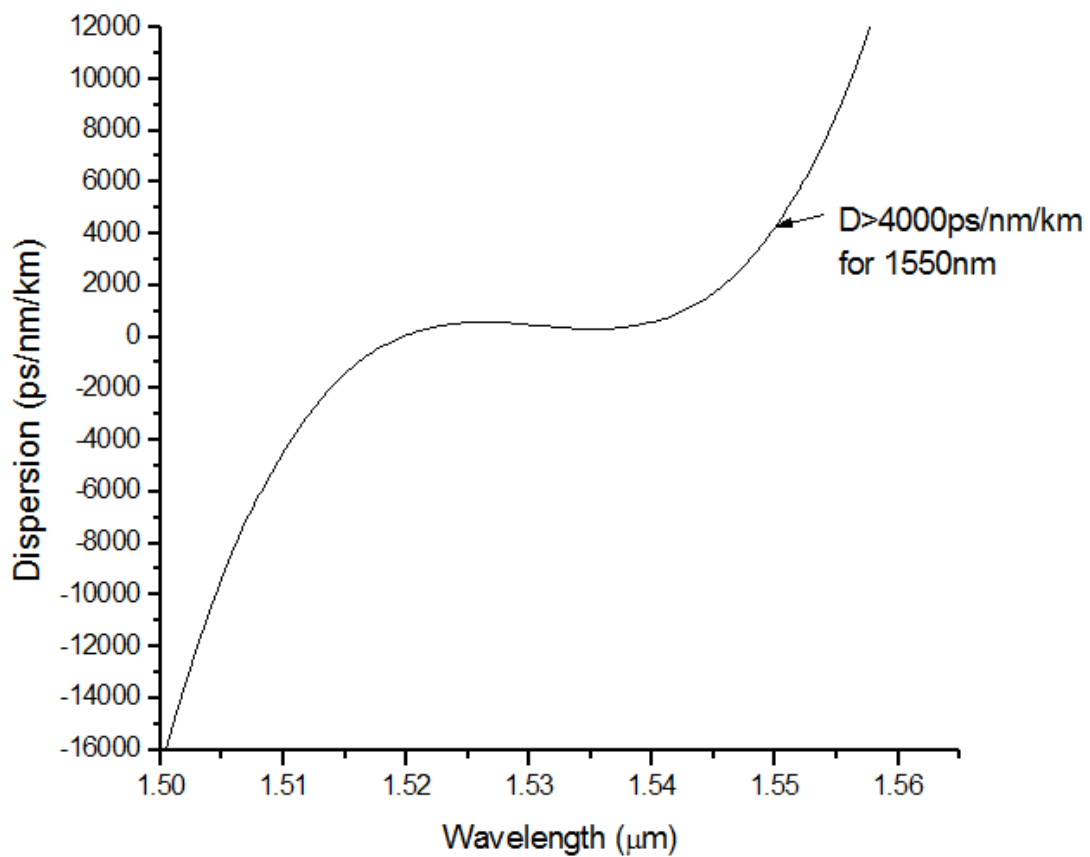


Fig. 2.14 Dispersion curve of the simulated highly dispersive photonic bandgap fiber

In order to determine the sensitivity of fabrication techniques on the dispersion curve, the period is changed around the central value of $3.86\mu\text{m}$ to within $\pm 0.01\mu\text{m}$ and its effect on the dispersion curve is observed.

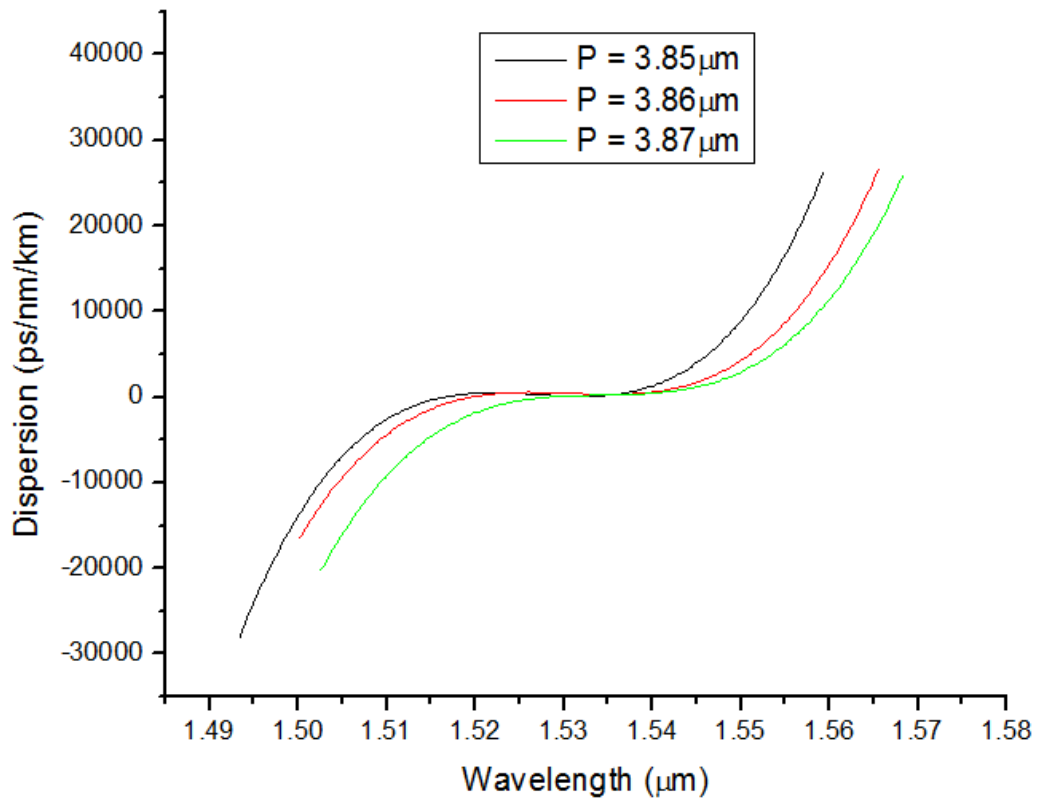


Fig. 2.15 Effect of change of period (P) on the dispersion curve for $3.85\mu\text{m}$ (black curve), $3.86\mu\text{m}$ (red curve), and $3.87\mu\text{m}$ (green curve)

It can be seen from Fig. 2.15 that as the period is changed, the dispersion curve moves to the left (right) for a decrease (increase) in the pitch value. This shift greatly influences the dispersion coefficient and thus the fabrication procedure must strictly be controlled.

2.2.3 OTHER HIGHLY DISPERSIVE PCF STRUCTURES

By introducing an additional air hole at the center with diameter d_4 , it is possible to tune the refractive index of the central core. By choosing simulation parameters as $\Lambda = 1.1\mu\text{m}$, $\frac{d_1}{\Lambda} = 0.94$, $\frac{d_2}{\Lambda} = 0.64$, $\frac{d_3}{\Lambda} = 0.76$, and $\frac{d_4}{\Lambda} = 0.2$, it is possible to obtain a broader bandwidth dispersion curve as shown in Fig. 2.16 (cross section of the designed fiber is also shown). However, this structure exhibits a lower dispersion coefficient compared to the structure described in section 2.1. The structure exhibits a dispersion coefficient as large as $-2500\text{ps}/\text{nm}/\text{km}$ at 1550nm and has a FWHM of $\sim 200\text{nm}$.

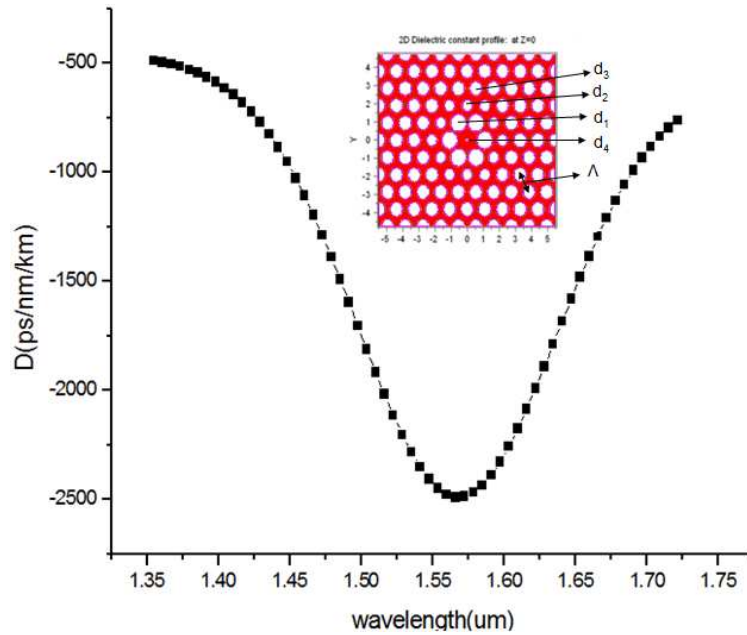


Fig. 2.16 Dispersion coefficient for PCF structure with a small air-hole at the center (cross section of the designed fiber is also shown)

Apart from using an all-silica photonic crystal fiber structure to achieve high dispersion bandwidth, the inner and outer cores can be doped to increase (Germanium Dioxide doping) or decrease (Fluorine doping) the refractive index with respect to

background silica. A higher refractive index contrast between the inner and outer core provides a larger dispersion coefficient. By properly choosing the parameters as $\Lambda = 2.51$ microns, $\frac{d_1}{\Lambda} = 0.85$, $\frac{d_2}{\Lambda} = 0.73$, $\frac{d_3}{\Lambda} = 0.80$, $\frac{d_4}{\Lambda} = 0.40$ and doping the inner and outer cores to achieve change in refractive index (Δn) as 1.35% and -0.7% respectively, a very high dispersion coefficient of -5500 ps/nm/km at 1553nm is achieved as shown in Fig. 2.17. The FWHM of the structure is $\sim 20\text{nm}$. However, introducing dopants to increase or decrease the refractive index creates more scattering locations and this greatly affects the performance of the system in terms of loss.

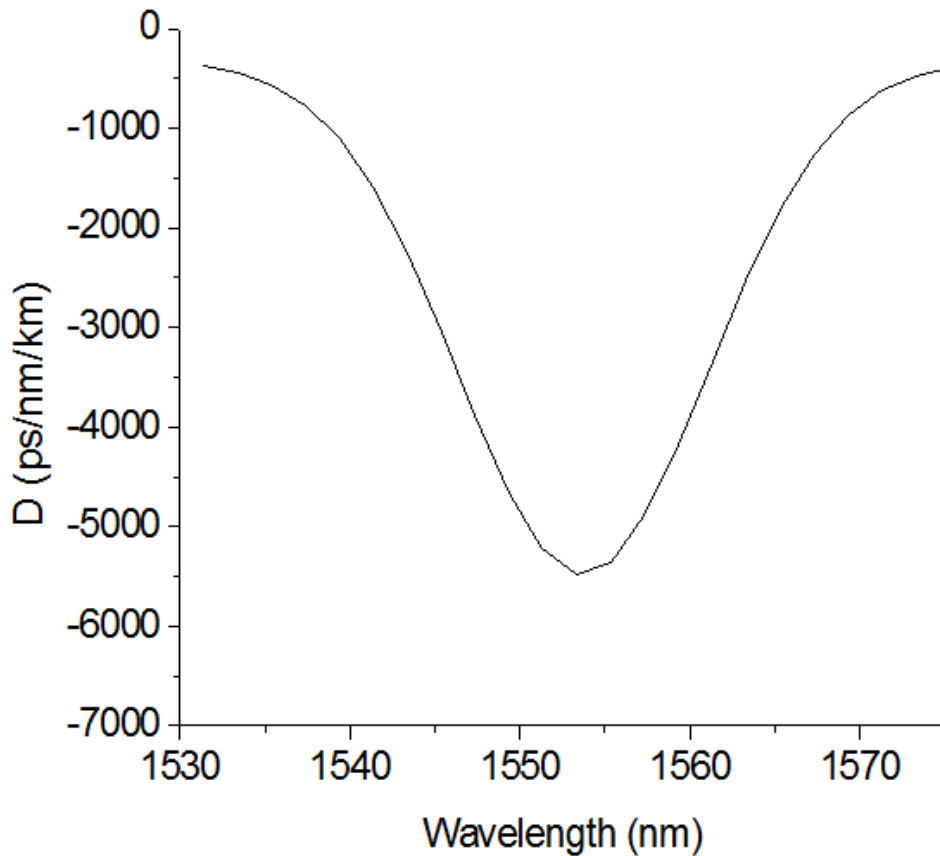


Fig. 2.17 Dispersion coefficient for PCF structure with doping-induced refractive index change of the cores

2.3 Fabrication of photonic crystal fibers

In this section, the fabrication technique of photonic crystal fibers is described. Difficulties encountered during fabrication and practical design considerations are also discussed.

2.3.1 STACK AND DRAW TECHNIQUE

PCFs can be fabricated using stack and draw [3, 31, 32], extrusion [34, 35] and drilling [33] techniques. Extrusion and drilling techniques are used for soft glasses and polymers. The stack and draw technique is the most widely used method, and hence will be described in this section. The fabrication of PCF is similar to that of a conventional fiber fabrication method. A schematic of the fabrication procedure is shown in Fig. 2.18 [36].

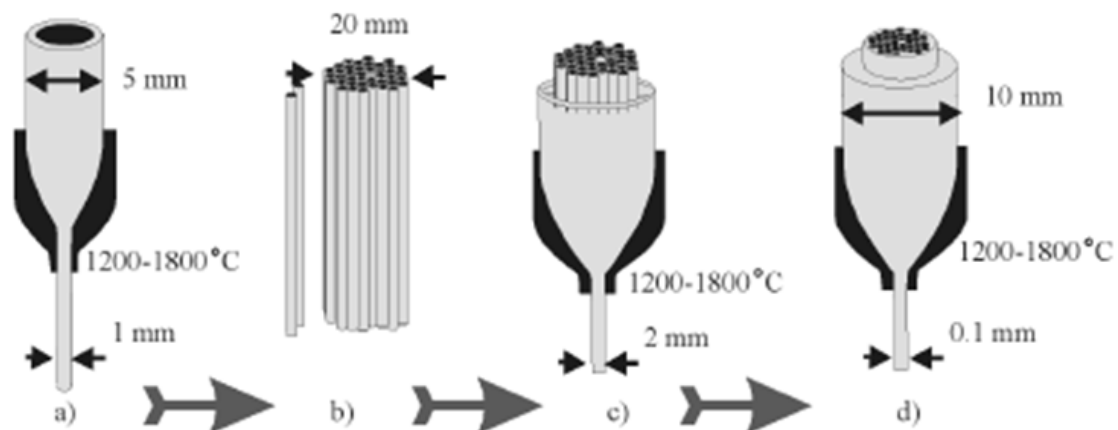


Fig. 2.18 Schematic of stack and draw method for fabricating photonic crystal fibers [36]

High purity silica tubes with different diameters and thicknesses can be used to determine the pitch and diameter of air holes. These tubes, which have an initial diameter

of about 5mm, are heated to temperatures between 1200⁰-1800⁰C and drawn down to capillaries with a diameter of about 1mm as shown in Fig. 2.18(a). In the next step, multiple individual capillaries are stacked by hand to create a preform with the required structure as shown in Fig. 2.18(b). The center core is usually a solid rod (for index-guiding PCF) or air-hole with suitable diameter at the center (for photonic bandgap PCF). It is also possible to create additional defect locations using the stack technique. Once the structure is realized, the stack is fused and drawn down to an overall diameter of about 2mm to kilometer lengths in a fiber draw tower at high temperatures as shown in Fig. 2.18(c). Finally, a polymer coating is added to increase the strength and drawn down to a final diameter of about 0.1mm as shown in Fig. 2.18(d). In the entire process, the draw parameters (like pressure, speed etc) are carefully controlled to prevent the air-holes from deforming or collapsing. The size and shape of air-holes are closely monitored as the fiber is drawn. This method provides a great deal of design flexibility, since the core size, air-hole diameters, shape and the index profile throughout the fiber can be controlled.

2.3.2 FABRICATION DIFFICULTIES

The main problems that are encountered during fabrication are presence of deformed air-holes, generation of additional holes, and changes in the structure's symmetry [37]. During fabrication, a number of factors contribute to the deviation of the final PCF structure from the desired one. Such deviations can greatly influence the properties of the resulting PCF. As the capillary stack is drawn to form the PCF structure, the walls of capillaries also shrink. If however, the wall thickness is small, then surface tension (usually exerted due to outer coating) and high viscosity of glass at low temperature acts to deform the circular shape. The thin walls, under the influence of neighboring capillaries adopt a shape that corresponds to the symmetry of the cladding

region and deform away from a circle. For example, if the wall thickness is too thin in a hexagonal cladding lattice, then the individual circular holes deform and assume a hexagonal shape. Although this is advantageous for certain kinds of desired photonic bandgap fibers, it is not a desirable effect for other structures. Therefore, it is not practically feasible to control the shape of air holes when the ratio of air-hole diameter to pitch (d/Λ) is greater than 0.8. The shape of the air holes can also be well controlled when the pitch is at least greater than or equal to $0.98\mu m$, although pitch greater than $2\mu m$ is highly recommended.

It is also difficult to control the shape of the air-holes because the effects of surface tension and viscosity of glass tend to collapse the air-holes. The large interstitial holes are avoided by fusion and inclusion of fine fibers in the interstices before drawing. The shape of the air-holes depends on temperature distribution, which has a radial profile. This causes outer holes to be more deformed compared to the inner holes. Therefore, extra rings of capillaries need to be added to prevent this. The additional rings do not affect the optical mode guided in the core [37]. During the fabrication process, microscopic sized holes are controlled by adjusting the temperature and drawing rate. In order to alleviate the effects of air-hole closure, the air-holes can be pressurized [38]. It is possible to control the shape of air holes by controlling the pressure. In structures requiring more than 3 different air-hole sizes, it becomes very difficult to control the diameters as three different sized capillaries with different wall thicknesses are stacked to form the perform. Also, it is difficult to obtain an optimum operating point when a large number of air-hole sizes are required.

We have simulated various structures and determined the product of D_{max} and $FWHM$ as shown in Fig. 2.19 [39]. It can be seen from the figure that although various designs exhibit extremely high dispersion-bandwidth products, only few designs that satisfy manufacturability criteria can be used. Unfortunately, these designs provide a relatively lower dispersion-bandwidth product (8 to 10 times lower) compared to currently non-realizable designs shown inside the red box. It can be expected that with the advances made in the fabrication technology in the recent years, the currently difficult design criterion can be met in the near future.

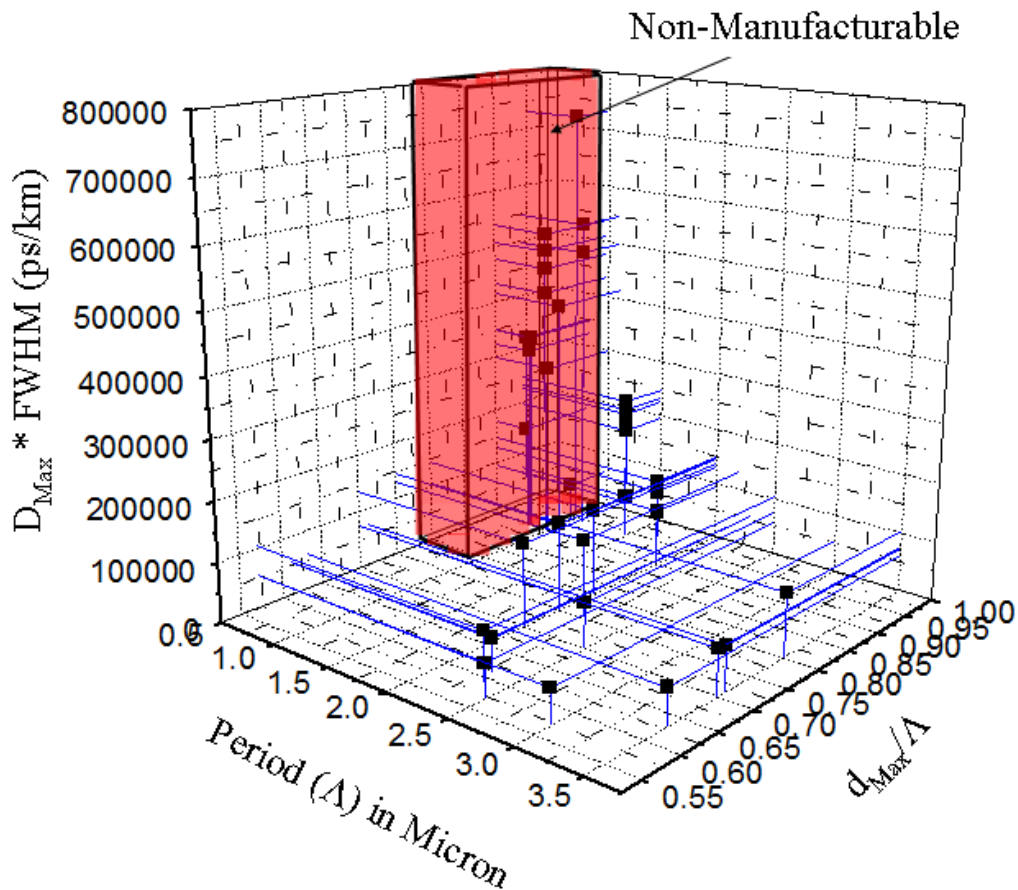


Fig. 2.19 D_{max} - $FWHM$ product plotted as a function of PCF parameters. The solid lines are only to aid the human eye. The data points are marked with solid squares

2.4 Summary

In this chapter, photonic crystal fibers were introduced and the working principle of two kinds of photonic crystal fibers was explained. Working principle of a highly dispersive photonic crystal fiber with a dual concentric-core was presented and a PCF structure was designed to exhibit a very high dispersion coefficient of -9500 ps/nm/km close to 1550nm and a FWHM of 55nm. Another photonic crystal fiber based on photonic bandgap guidance was also designed to achieve dispersion coefficient greater than 4000 ps/nm/km around 1550nm. Few other structures exhibiting very high dispersion coefficients were also presented. Such fibers show great potential for use as true-time-delay elements in phased array antenna systems. Finally fabrication technique of PCFs based on stack and draw technique was explained and the difficulties encountered during such fabrication were also briefly discussed.

2.5 References

- [1] J. C. Knight, T. A. Birks, P. St. J. Russell, and D. M. Atkin, "All-silica single-mode optical fiber with photonic crystal cladding," *Opt Letts.* vol. **21**, pp. 1547-1549 (1996); Also "errata," vol. **22**, 484 (1997)
- [2] J. Broeng, D. Mogilevstev, S. E. Barkou, and A. Bjarklev, "Photonic crystal fibres : A new class of optical waveguides," *Opt. Fiber. Tech.* vol. **5**, pp. 305-330 (1999)
- [3] Bjarklev, J. Broeng, A. S. Bjarklev, *Photonic crystal fibers*, Kluwer Academic Publishers (2003)
- [4] P. St J. Russell, "Photonic crystal fibers," *Science.* vol. **299**, pp. 358-362 (2003)
- [5] T. A. Birks, D. Mogilevtsev, J. C. Knight, P. St. J. Russell, "Dispersion compensation using single-material fibers," *IEEE Photon. Technol. Letts.* vol. **11**, pp. 674 – 676 (1999)

- [6] L. P. Shen, W. P. Huang, G. X. Chen, S. S. Jian, "Design and optimization of photonic crystal fibers for broad-band dispersion compensation," *IEEE. Photon. Technol. Letts.* vol. **15**, pp. 540-542 (2003)
- [7] A. Huttunen and P. Torma, "Optimization of dual-core and microstructure fiber geometries for dispersion compensation and large mode area," *Opt. Express.* vol. **13**, pp. 627-635 (2005)
- [8] Y. Ni, L. Zhang, L. An, J. Peng, and C. Fan, "Dual-Core Photonic Crystal Fiber for Dispersion Compensation," *IEEE. Photon. Technol. Letts.* vol. **16**, pp. 1516-1518 (2004)
- [9] K. Thyagarajan, R. K. Varshney, P. Palai, A. K. Ghatak, and I. C. Goyal, "A Novel Design of a Dispersion Compensating Fiber," *IEEE. Photon. Technol. Letts.* vol. **8**, pp. 1510-1512 (1996)
- [10] J. -L. Auguste, R. Jindal, J. -M. Blondy, M. Clapeau, J. Marcou, B. Dussardier, G. Monnom, D. B. Ostrowsky, B. P. Pal, and K. Thyagarajan, "-1800ps/(nm.km) chromatic dispersion at 1.55 μ m in dual concentric core fibre," *Electron. Letts.* vol. **36**, pp. 1689-1690 (2000)
- [11] F. G er ome, J. -L. Auguste, and J. -M. Blondy, "Design of dispersion-compensating fibers based on a dual-concentric-core photonic crystal fiber," *Opt. Letts.* vol. **29**, pp. 2725-2727 (2004)
- [12] P. J. Roberts, B. J. Mangan, H. Sabert, F. Couny, T. A. Birks, J. C. Knight, and P. St. J. Russell, "Control of dispersion in photonic crystal fibers," *J. Opt. Fiber. Commun. Rep.* vol. **2**, pp. 435-461 (2005)
- [13] R. Amezcua-Correa, F. G er ome, S. G. Leon-Saval, N.G. R. Broderick, T. A. Birks, and J. C. Knight, "Control of surface modes in low loss hollow-core photonic bandgap fibers," *Opt. Express.* vol. **16**, pp. 1142-1149 (2008)
- [14] J. D. Joannopoulos, R. D. Meade, and J. N. Winn, *Photonic Crystals*, Princeton University Press (1995)
- [15] J. D. Joannopoulos, S. G. Johnson, J. N. Winn, and R. D. Meade, *Photonic Crystals: Molding the flow of light*, Princeton University press, 2nd ed. (2008)
- [16] B. Jopson and A. Gnauck, "Dispersion compensation for optical fiber systems," *IEEE. Comm. Mag.* vol. **33**, pp. 96-102 (1995)
- [17] T. A. Birks, J. C. Knight, and P. St J. Russell, "Endlessly single-mode photonic crystal fiber," *Opt. Letts.* vol. **22**, pp. 961-963 (1997)

- [18] Z. Yusoff, J. H. Lee, W. Belardi, T. M. Monro, P. C. Teh, and D. J. Richardson, "Raman effects in a highly nonlinear holey fiber: amplification and modulation," *Opt. Letts.* vol. **27**, pp. 424-426 (2002)
- [19] K. Tajima, J. Zhou, K. Nakajima, and K. Sato, "Ultralow Loss and Long Length Photonic Crystal Fiber," *J. Lightwav. Technol.* vol. **22**, pp. 7-10 (2004)
- [20] M. Koshiba and K. Saitoh, "Simple evaluation of confinement losses in holey fibers," *Opt. Comm.* vol. **253**, pp. 95-98 (2005)
- [21] S. K. Varshney, K. Saitoh, and M. Koshiba, "A Novel Design for Dispersion Compensating Photonic Crystal Fiber Raman Amplifier," *IEEE. Photon. Technol. Letts.* vol. **17**, pp. 2062-2064 (2005)
- [22] S. K. Varshney, T. Fujisawa, K. Saitoh, and M. Koshiba, "Design and analysis of a broadband dispersion compensating photonic crystal fiber Raman amplifier operating in S-band," *Opt. Express.* vol. **14**, pp. 3528-3540 (2006)
- [23] B. J. Mangan, F. Couny, L. Farr, A. Langford, P. J. Roberts, D. P. Williams, M. Banham, M. W. Mason, D. F. Murphy, E. A. M. Brown, and H. Sabert, "Slope-matched dispersion-compensating photonic crystal fibre," *Lasers and Electro-Optics, 2004. (CLEO). (Conference on Vol. 2, 16-21 May 2004)*, pp. 1069-1070.
- [24] U. Peschel, T. Peschel, and F. Lederer, "A compact device for highly efficient dispersion compensation in fiber transmission," *Appl. Phys. Letts.* vol. **67**, pp. 2111-2113 (1995)
- [25] V. M. Schneider and J. A. West, "Analysis of wideband dispersion slope compensating optical fibres by supermode theory," *Electron. Letts.* vol. **38**, pp. 306-307 (2002)
- [26] H. Subbaraman, T. Ling, Y. Q. Jiang, M. Y. Chen, P. Y. Cao, and R. T. Chen, "Design of a broadband highly dispersive pure silica photonic crystal fiber," *Appl. Opt.* vol. **46**, pp. 3263 – 3268 (2007)
- [27] K. M. Ho, C. T. Chan, and C. M. Soukoulis, "Existence of a Photonic Gap in Periodic Dielectric Structures," *Phy. Rev. Letts.* vol. **65**, pp. 3152-3155 (1990)
- [28] RSoft Photonics CAD Suite, Version 5.1.7
- [29] R. Scarmozzino, A. Gopinath, R. Pregla, and S. Helfert, "Numerical Techniques for Modeling Guided-Wave Photonic Devices," *J. Selected Topics in Quantum Electronics.* vol. **6**, pp. 150-162 (2000)

- [30] R. Scarmozzino and R. M. Osgood, Jr, "Comparison of finite-difference and Fourier-transform solutions of the parabolic wave equation with emphasis on integrated-optics applications," *J. Opt. Soc. Amer. A.* vol. **8**, 724-731 (1991)
- [31] J. C. Knight, T. A. Birks, P. St J. Russell, and D. M. Atkin, "All-silica single-mode optical fiber with photonic crystal cladding," *Opt. Letts.* vol. **21**, pp. 1547–1549 (1996)
- [32] P. Kaiser, and H. W. Astle, "Low loss single material fibers made from pure fused silica," *J. Bell Syst. Tech.* vol. **53**, pp. 1021–1039 (1974)
- [33] M. van Eijkelenborg, M. Large, A. Argyros, J. Zagari, S. Manos, N. Issa, I. Bassett, S. Fleming, R. McPhedran, C. M. de Sterke, and N. A. Nicorovici, "Microstructured polymer optical fiber," *Opt. Express.* vol. 9, pp. 319–317 (2001)
- [34] K. Kiang, K. Frampton, T. Monro, R. Moore, J. Tucknott, D. Hevak, N. Broderick, D. Richardson, H. Rutt, "Extruded singlemode non-silica glass holey optical fibres," *Electron. Letts.* vol. **38**, pp. 546-547 (2002)
- [35] D. C. Allan et al. Photonic crystal fibers: effective index and band gap guidance. In *Photonic Crystals and Light Localization in the 21st Century* (ed. C. M. Soukoulis) pp. 305–320 (Kluwer, Netherlands, 2001).
- [36] R. Buczynski, "Photonic Crystal Fibers," *Acta Physica Polonica A*, vol. **106**, pp. 141-167 (2004)
- [37] D. Pysz, R. Stepien, P. Szarniak, R. Buczynski, and T. Szoplik, "Comparing characteristics and prospects of fabrication of multicomponent photonic crystal fibers with different lattice structures," *Proc. SPIE*, vol. **5576**, pp. 74-80 (2004)
- [38] T. Guo, S. Lou, H. Fang, and S. Jian, "Research on the fabrication of photonic crystal fiber," *Proc. SPIE*. vol. **6352**, 63523C (2006)
- [39] H. Subbaraman, M. Yihong Chen, Y. Jiang, and R. T. Chen, "Reply to Comment on Design of a broadband highly dispersive pure silica photonic crystal fiber," *Appl. Opt.* vol. **44**, pp. 3330-3332 (2008)

Chapter 3 Photonic crystal fibers based true-time-delay modules for X-band phased array antennas

This chapter will present the design of a practically realized highly dispersive photonic crystal fiber. Characterization of the highly dispersive fiber in terms of time delay achievable for use in an X-band phased array antenna system will be performed. A true-time-delay (TTD) module consisting of 4 delay lines will be formed using these PCFs and two methods to independently measure the time delay through the dispersive fibers will be presented. The implications of such TTD modules for use in X-band phased array systems will also be discussed briefly.

3.1 Practical design of a highly dispersive photonic crystal fiber

In section 2.3.2, we briefly discussed the difficulties in fabricating photonic crystal fibers. By keeping the fabrication constraints in mind, PCF structures with high dispersion coefficients can be practically realized. The SEM and the schematic cross section of a practically realized high dispersion PCF are shown in Figs. 3.1(a) and 3.1(b) respectively [1-2].

The PCF has a pitch (Λ) = 3.5 μm , $d_0 = 1.72\mu\text{m}$, $d_1 = 1.45\mu\text{m}$, $d_2 = 1.08\mu\text{m}$, $d_3 = 0.86\mu\text{m}$. The inner core (red region) consists of a doped silica rod such that the refractive index of the rod is higher than background silica (white region) by 1.9%. The outer core is made up of 12 doped silica rods (wine red region) such that the refractive index of the rods is higher than background silica by 1.2% [1-2]. As previously discussed in section 2.2.1.1, such a structure is similar to a directional coupler and can support two

supermodes [3]. The design parameters are chosen to have a phased matched wavelength (λ_0) near 1550 nm.

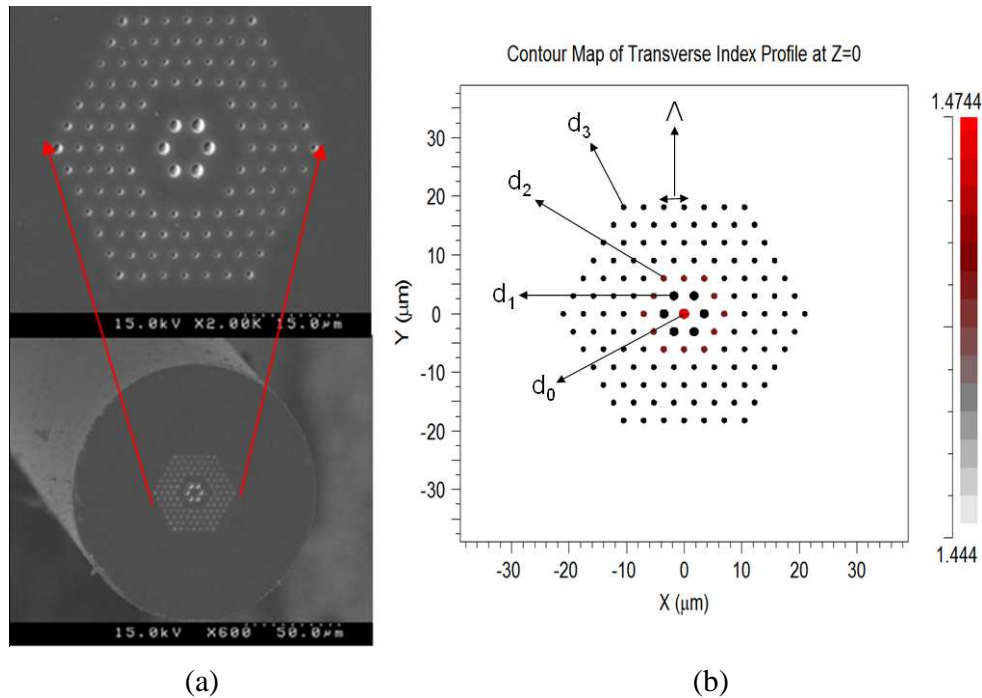


Fig 3.1(a) Scanning electron microscope (SEM) images of the fabricated high dispersion PCF [1-2] (b) Schematic cross section of the PCF

When the wavelength is shorter than phase match wavelength ($\lambda < \lambda_0$), the field is essentially confined in the inner core. Around the phase match wavelength ($\lambda \approx \lambda_0$), a part of the field is in the inner core and a part is in the outer core. When the wavelength is longer than phase match wavelength ($\lambda > \lambda_0$), most of the power spreads to the outer core and is effectively guided in the outer core. This kind of modal field redistribution makes the effective index change greatly with the wavelength and thus, near the phase match wavelength, the dispersion coefficient of the dual concentric core PCF is very large.

The dispersion of PCFs is simulated using commercially available RSoft BandSOLVETM software [4] that is based on fully vectorial plane wave expansion (PWE) method [5]. Since the PCF structure is not a perfect crystal without defects due to the presence of inner and outer cores, a supercell having a size of $N \times N$ instead of a natural unit cell is implemented in order to satisfy periodic boundary conditions. An 8×8 supercell is used for simulation purposes as it meets the simulation convergence compared with a 9×9 supercell or a 7×7 supercell.

The group velocity dispersion (GVD), given by $D(\lambda)$ can be directly calculated from the modal effective index $n_{\text{eff}}(\lambda)$ of the fundamental mode over a range of wavelengths using [3]

$$D(\lambda) = -\frac{\lambda}{c} \frac{d^2 n_{\text{eff}}(\lambda)}{d\lambda^2} \quad (3.1)$$

The two supermodes that correspond to the guided mode in the inner core and in the outer core are shown in Figs. 3.2(a) and 3.2(b) respectively.

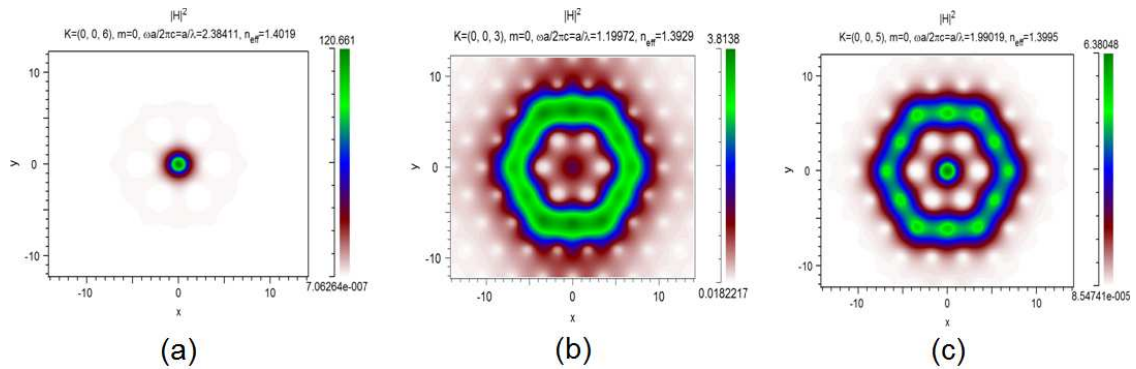


Fig. 3.2 Simulated transverse mode profiles of the highly dispersive photonic crystal fiber when (a) $\lambda < \lambda_p$ (b) $\lambda > \lambda_p$ and (c) $\lambda \approx \lambda_p$

Near the phase matched wavelength, there is a strong coupling between these two modes and the mode is partly guided in the inner core and partly guided in the outer core as shown in Fig. 3.2(c). This leads to a change in the refractive index of the fundamental mode near the phase matched wavelength. This redistribution of the modal index, as discussed in Chapter 2, leads to a high value of dispersion coefficient near the phase matched wavelength. The simulated dispersion curve of the fabricated fiber is shown in Fig. 3.3 [1-2].

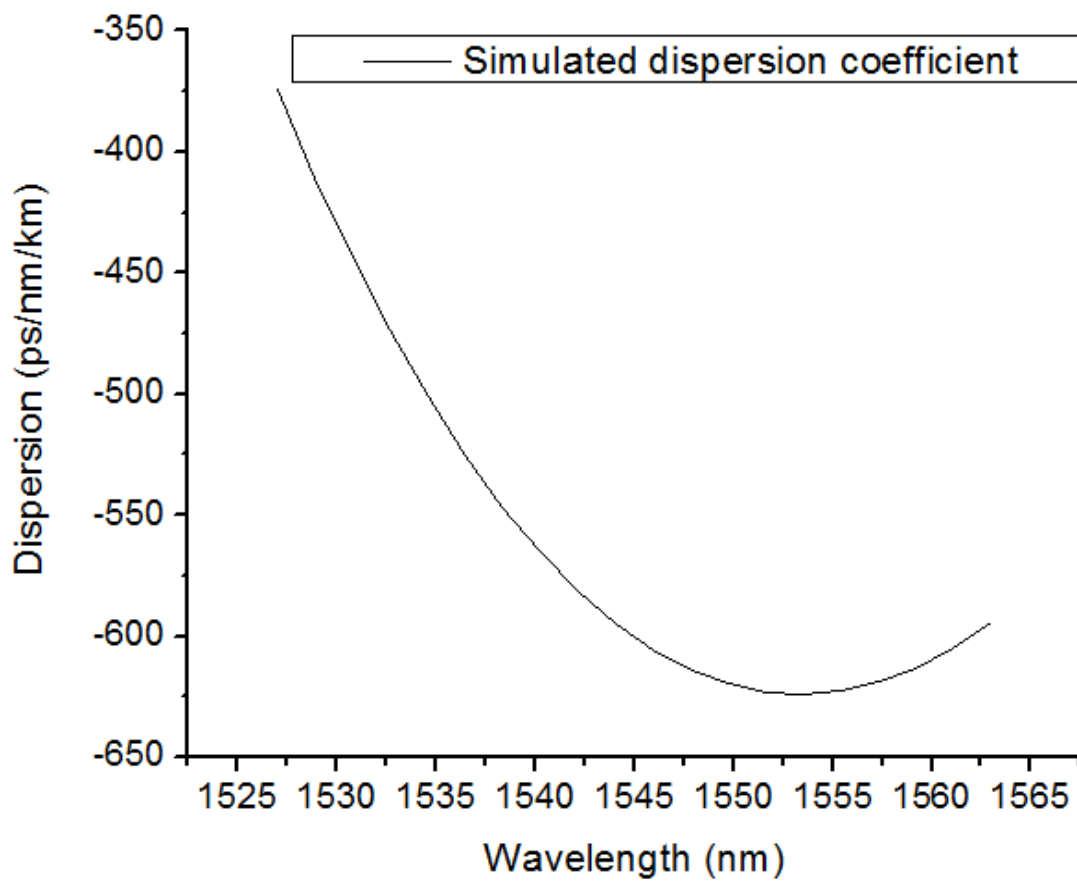


Fig. 3.3 Simulated dispersion coefficient of the designed highly dispersive photonic crystal fiber

It can be seen from the figure that very high dispersion coefficients (exceeding -600 ps/nm/km) can be achieved in this structure. This value is greater than the dispersion coefficient of conventional single mode fibers, SMF-28 ($D_{SMF} = 18\text{ ps/nm/km}$) by a factor of 33, and larger by a factor of 6 compared to dispersion compensation fibers.

3.2 Experimental characterization of true-time-delay (TTD) modules

The highly dispersive PCF is used to form a true-time-delay (TTD) module for an X-band phased array antenna. The TTD module consists of 4 delay lines. Each delay line consists of a length of the highly dispersive PCF connected to Lucent TrueWave SMF non-zero dispersion shifted fiber (NZ-DSF), with dispersion coefficient $\sim 3\text{ ps/nm/km}$ from 1530nm to 1560nm. The total length L , of each delay line is 10.5 meters, and the lengths of PCF segments used in the 4 delay lines are 0m, 3.5m, 7m, and 10.5m respectively [1-2]. Usually, there is a mode field diameter mismatch between the NZ-DSF and the PCF. Therefore, at each of the ends of the PCF segments, a very short length of ultra high numerical aperture (UHNA) fiber is spliced between the NZ-DSF and the PCF as shown in Fig. 3.4 [6]. The UHNA also ensures selective injection of light into the central core. The splices are protected with splice sleeves.

A wavelength of 1545nm is chosen as the central wavelength. The NZ-DSF lengths in all the delays lines are trimmed such that the delay through each line at the central wavelength is the same. The maximum insertion loss added due to the delay lines is 11dB [7].

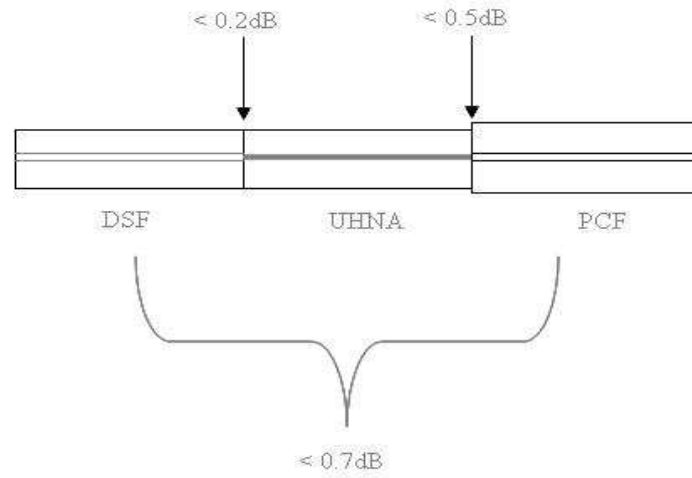


Fig. 3.4 Schematic representation of connection between NZ-DSF and PCF using UHNA fiber (only connections at one end of PCF are shown)

In order to obtain the chromatic dispersion of the fabricated highly dispersive PCFs, the time delay difference (ΔT) between optical wavelengths of $\lambda \pm 0.1 \text{ nm}$ is measured at each wavelength according to the setup explained in [8]. In order to measure the time delay difference, the phase difference as a function of microwave frequency is measured at optical wavelengths of $(\lambda + 0.1 \text{ nm})$ and $(\lambda - 0.1 \text{ nm})$. The slope of the phase versus frequency curve gives the time delay. The dispersion coefficient (D) is calculated using

$$D = \Delta T / (\Delta \lambda \cdot L) \quad (3.2)$$

where $\Delta \lambda = 0.2 \text{ nm}$ is the wavelength difference and L is the length of PCF (contribution to time delay difference from NZ-DSF is negligible). The measured group velocity dispersion curve as a function of wavelength is shown in Fig. 3.5 [9]. It can be seen from the figure that the dispersion coefficient is as high as $\sim -600 \text{ ps/nm/km}$ near 1550 nm . The simulated dispersion coefficient curve is also shown in the same figure.

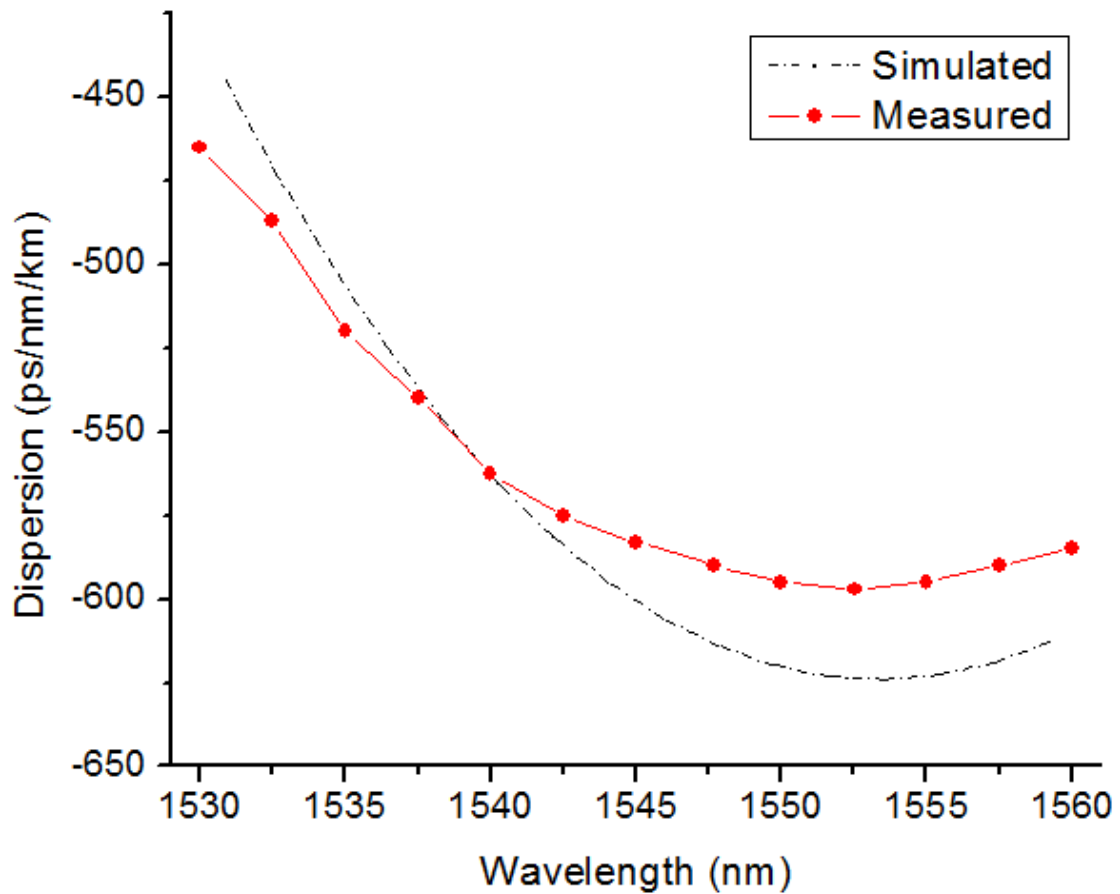


Fig. 3.5 Measured dispersion coefficient of the fabricated highly dispersive photonic crystal fiber

3.2.1 TIME DELAY INTERVAL MEASUREMENT

The time delay interval between adjacent delay lines is measured using the setup as shown in Fig. 3.6. A femtosecond laser source (FPL-01T femtosecond Erbium doped fiber laser from Calmar Optcom Inc.) generates the optical carrier with a wavelength of 1550nm, and with an average power of 10mW. The pulse width is about 0.08ps and the repetition rate is 19MHz. This optical signal is split to three channels using a 1-to-4 optical power splitter.

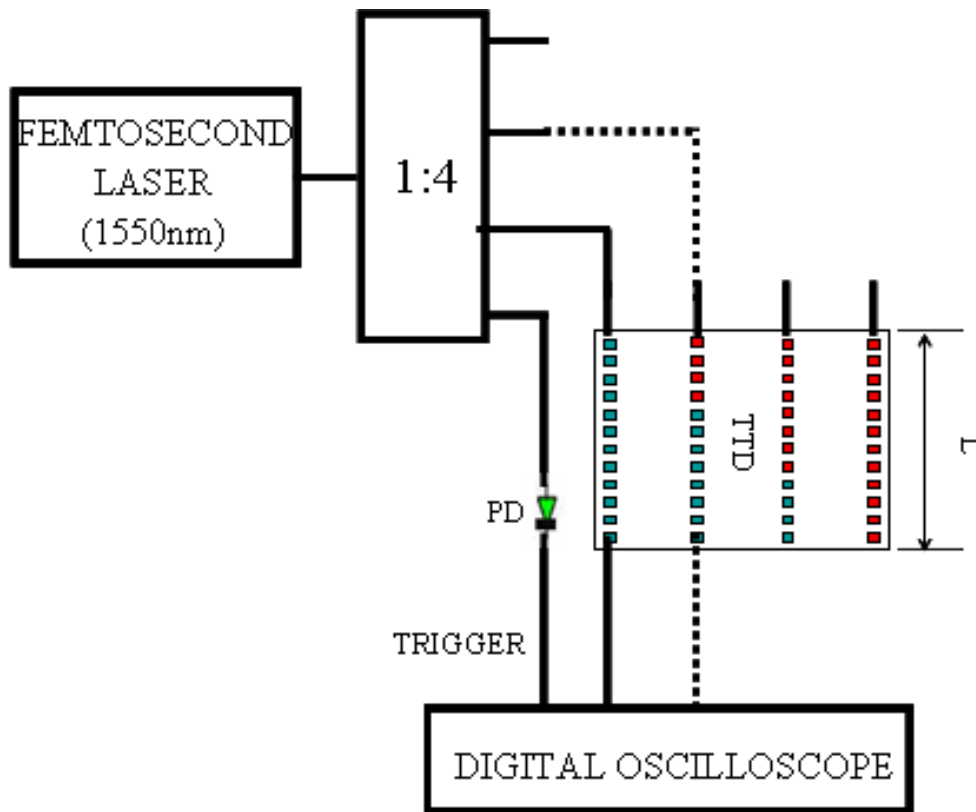


Fig. 3.6 Schematic of the time delay interval measurement setup using femtosecond laser source

One arm serves a trigger for the digital communication analyzer and two other arms pass through adjacent delay lines in the TTD network. The pulse traces measured through all the delay lines are shown in Fig. 3.7. The wavelength of 1550nm creates different delays for the pulses through the delay lines. The pulse traces corresponding to delays lines consisting of PCF lengths 0m, 3.5m, 7.0m, and 10.5m respectively are numbered from 0 through 3 respectively [10]. The broad output pulses are due to the limitation from the speed of the photodetector. It can be seen from the figure that time delay difference values obtained between adjacent lines, say between line # 0 and line # 1 is 11.04ps, and the time delay differences between any two adjacent delay lines is

constant. This is a requirement for phased array antenna systems. Since using this method only time delay differences at a wavelength of 1550nm can be obtained, another method is used to determine the time delay differences at other wavelengths.

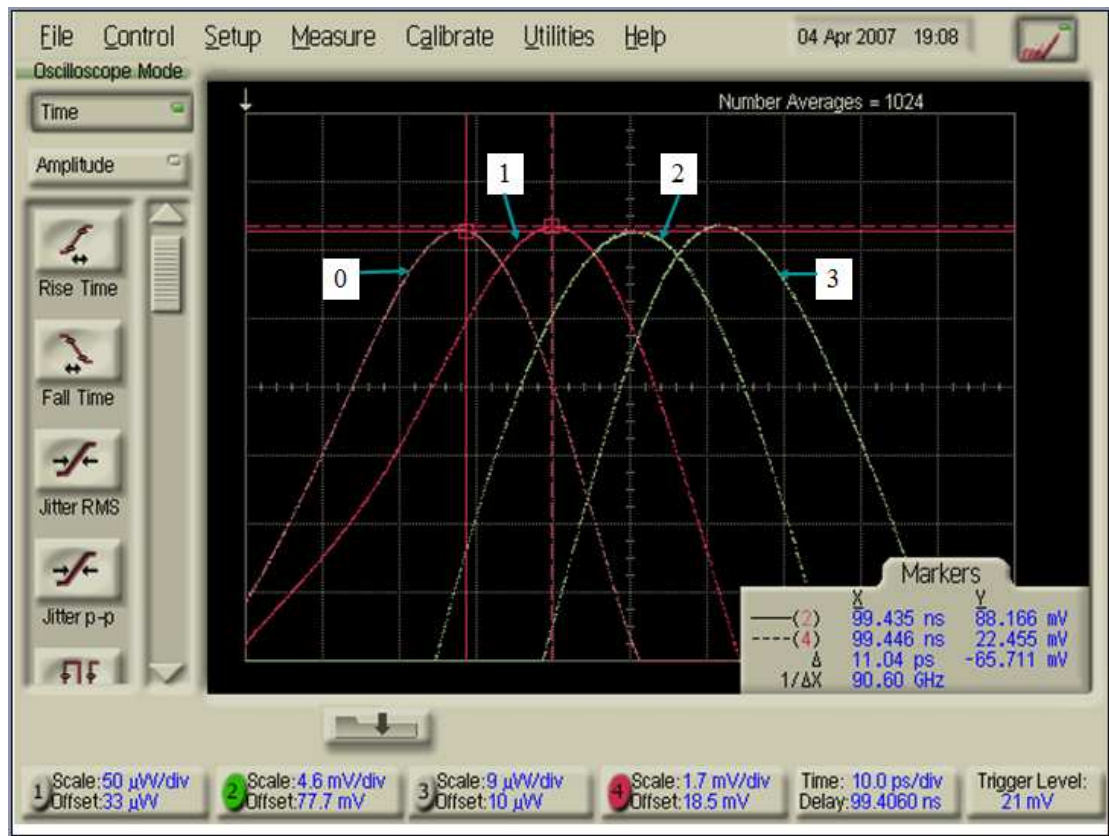


Fig. 3.7 Time delayed pulse traces of 4 TTD lines measured on the digital communication analyzer

3.2.2 PHASE VERSUS FREQUENCY MEASUREMENT

In order to show the true-time-delay nature and measure the time delay difference at different wavelengths between adjacent delay lines of the module consisting of highly dispersive PCF, a phase versus frequency measurement is performed. The schematic of the phase versus frequency measurement setup is shown in Fig. 3.8. The microwave

signal in the X-band (8-12.5GHz) from an HP8510C vector network analyzer is modulated onto an optical carrier generated by an external cavity tunable laser source (Santec ECL-200) using a Lithium Niobate (LiNbO_3) Mach-Zehnder Modulator (MZM). The modulated carrier is split into two channels using 1-to-2 optical power splitter. One output arm of the splitter feeds a reference TTD line consisting of 10.5m NZ-DSF, and the other output arm is fed to the TTD line under test. After passing through the TTD lines, the optical signals are converted back to electrical signals at the photodetector (PD). The phase of the output electrical signal is measured with respect to the reference arm on the network analyzer. An external tunable delay line (not shown in the schematic) is used as an initial calibration step to equalize the phase difference between adjacent delay lines to zero at a wavelength of 1545nm.

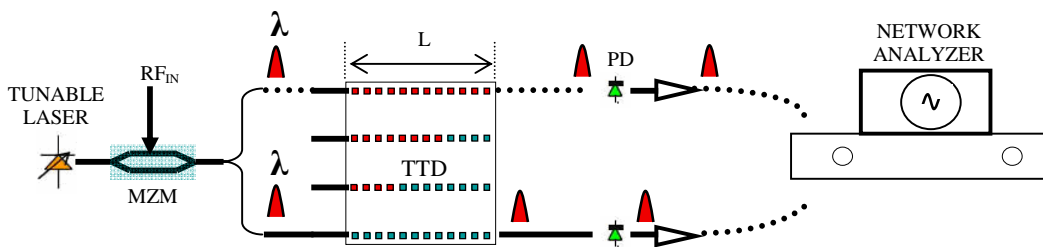


Fig. 3.8 Schematic of Phase versus Frequency measurement setup

At a fixed optical wavelength, the frequency of the microwave signal is changed from 8GHz to 12GHz in steps of 0.5GHz. At each frequency, the phase difference between the TTD line under test and the reference arm is measured using the network analyzer and the values are noted down carefully. This procedure is repeated at different wavelengths by tuning the laser wavelength. The measured phase versus frequency curves for the three TTD lines are shown in Fig. 3.9 [6]. It can be seen from the figure that the phase versus frequency plots are straight lines, which is a characteristic of true

time delay networks. The time delay values can be obtained from the slopes of these straight lines and the time delay values thus obtained are also provided in Table 3.1. Since the NZ-DSF sections are trimmed for all the TTD lines to have the same delay value at 1545nm, the phase versus frequency plot is a straight line with slope = 0 for all the lines at 1545nm. It can be seen that by changing the wavelength from 1530nm to 1560nm, continuous time delays from -28.3ps to 31.3ps are achievable.

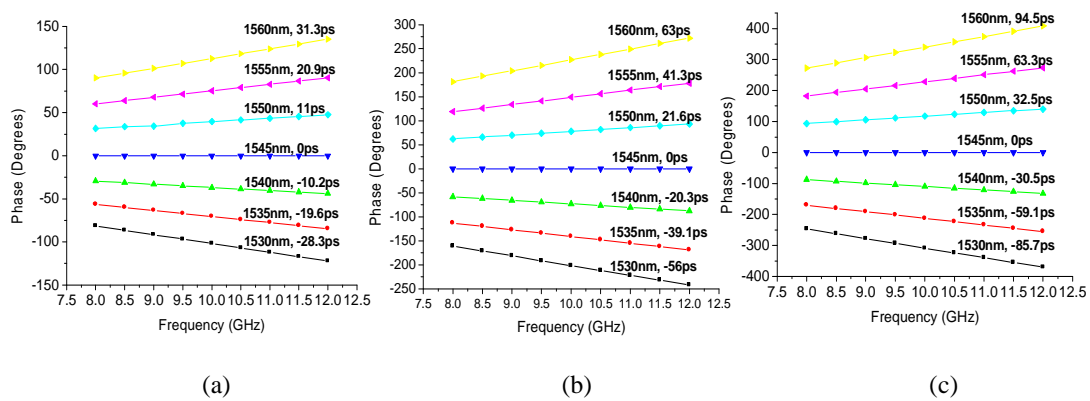


Fig. 3.9 Phase versus Frequency plots for (a) TTD line consisting of 3.5m PCF and 7.0m NZ-DSF, (b) TTD line consisting of 7.0m PCF and 3.5m NZ-DSF, (c) TTD line consisting of 10.5m PCF and 0m NZ-DSF

Table 3.1 Measured time delay (in ps) from four true-time-delay lines

Wavelength \star	1530nm	1535nm	1540nm	1545nm	1550nm	1555nm	1560nm
NZ-DSF: PCF \downarrow							
10.5m : 0m	0	0	0	0	0	0	0
7.0m : 3.5m	-28.3	-19.6	-10.2	0	11	20.9	31.3
3.5m : 7.0m	-56	-39.1	-20.3	0	21.6	41.3	63
0m : 10.5m	-85.7	-59.1	-30.5	0	32.5	63.3	94.5

It can also be observed from Table 3.1 that for any given wavelength, the time delay difference between adjacent delay lines is almost constant. The time delay difference values from table 3.1 can be used to calculate the steering angle using equation (1.20). The calculated steering angle of X-band PAA system with antenna element spacing = 1.3 cm is shown in Fig. 3.10 [9].

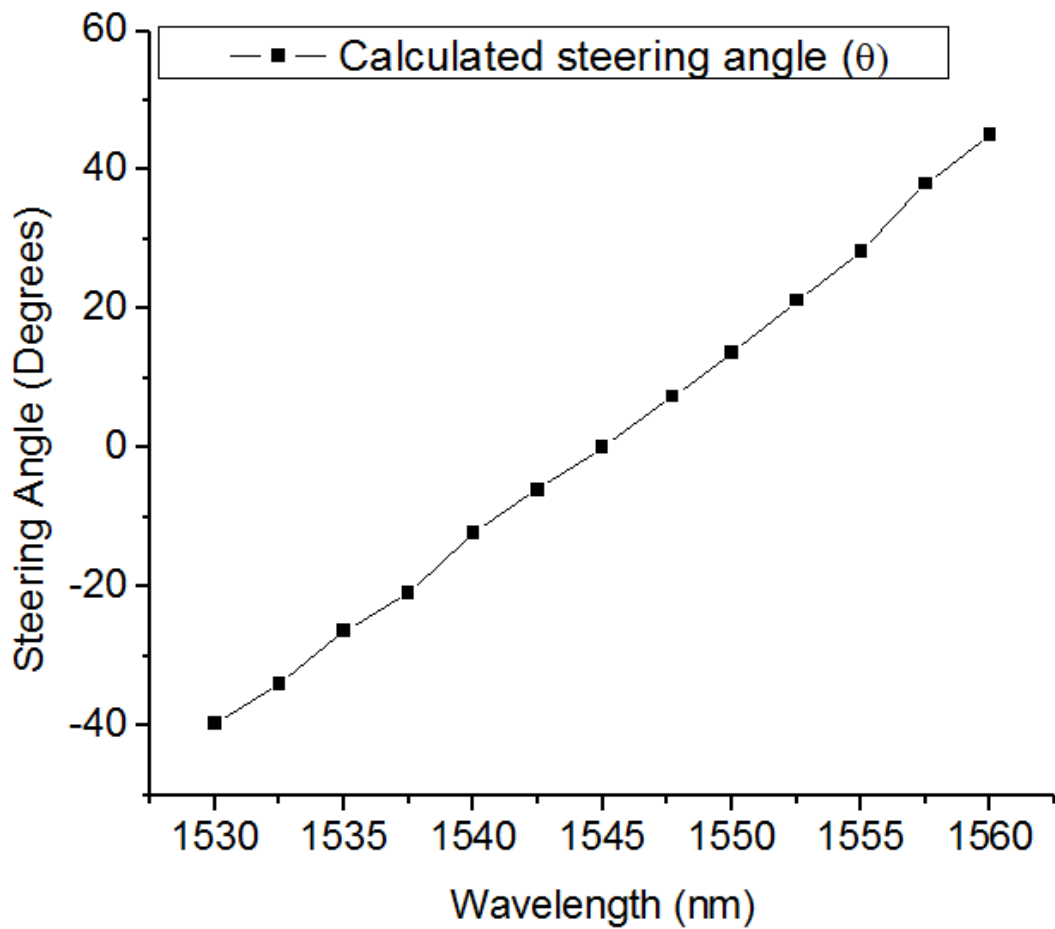


Fig. 3.10 Calculated steering angle of X-band PAA with antenna element spacing $d = 1.3\text{cm}$

It can be seen from the figure that as the wavelength of the optical carrier is changed from 1530nm to 1560nm, the X-band PAA can steer the beam continuously

from -41° to $+46^{\circ}$. This TTD network is used to demonstrate single and simultaneous multiple RF beam transmission and reception in the subsequent chapters.

3.3 Summary

In this chapter, a practical design of a highly dispersive photonic crystal fiber was presented. Chromatic dispersion of highly dispersive photonic crystal fiber was theoretically simulated and experimentally measured. The dispersion of the fabricated photonic crystal fiber, which is based on a dual concentric-core structure, was measured to be as high as -600 ps/nm/km at 1550 nm. A true-time-delay network consisting of four delay lines was formed using the fabricated highly dispersive PCF. Each delay line in the module consisted of a length of highly dispersive PCF connected to a length of NZ-DSF. The PCF length segment difference between adjacent delay lines in the module was 3.5m and the overall length of each delay line including PCF and NZ-DSF was 10.5m. Time delay interval was measured using a femtosecond laser source operating at 1550nm and a digital oscilloscope. Finally, true-time-delay nature of the TTD module was verified by performing phase versus frequency measurements and showing linearity of the phase-frequency plots. Time delay values at each wavelength were deduced by calculating the slope of phase-frequency lines. The derived time delay values showed the feasibility of steering an RF beam from -41° to $+46^{\circ}$ by tuning the wavelength from 1530nm to 1560nm for a 4-element X-band antenna array with inter-element spacing = 1.3cm.

3.4 References

- [1] Y. Jiang, B. Howley, Z. Shi, Q. Zhou, R. T. Chen, M. Y. Chen, G. Brost, C. Lee, "Dispersion-Enhanced Photonic Crystal Fiber Array for A True-Time-Delay Structured X-band Phased Array Antenna," *IEEE. Photon. Technol. Letts.* vol. **17**, pp. 187-189 (2005)
- [2] Y. Jiang, Z. Shi, B. Howley, X. Chen, M. Y. Chen, and R. T. Chen, "Delay Time Enhanced Photonic Crystal Fibers Array for Wireless Communications using 2-D X-band Phased Array Antennas," *Opt. Engineering.* vol. **44**, (2005)
- [3] U. Peschel, T. Peschel, and F. Lederer, "A compact device for highly efficient dispersion compensation in fiber transmission," *Appl. Phys. Letts.* vol. **67**, pp. 2111-2113 (1995)
- [4] RSoft Photonics CAD Suite, Version 5.1.7
- [5] K. M. Ho, C. T. Chan, and C. M. Soukoulis, "Existence of a Photonic Gap in Periodic Dielectric Structures," *Phy. Rev. Letts.* vol. **65**, pp. 3152-3155 (1990)
- [6] H. Subbaraman, M. Y. Chen, and R. T. Chen, Packaging and system demonstration of an X-band phased array antenna utilizing highly dispersive photonic crystal fiber based true-time-delay, in *Proc. SPIE*, vol. **7221**, pp. 722107-1 (2009)
- [7] H. Subbaraman, M. Y. Chen, and R. T. Chen, "Photonic dual RF beam reception of an X band phased array antenna using a photonic crystal fiber-based true-time-delay beamformer," *Appl. Opt.* vol. **7**, pp. 6448-6452 (2008)
- [8] B. Howley, Z. Shi, Y. Jiang, and R. T. Chen, "Thermally tuned optical fiber for true time delay generation," *Opt. Laser Technol.* vol. **37**, pp. 29-32, (2004)
- [9] H. Subbaraman, M. Y. Chen, and R. T. Chen, "Photonic Crystal Fiber-Based True-Time-Delay Beamformer for Multiple RF Beam Transmission and Reception of an X-Band Phased-Array Antenna," *J. Lightwav. Technol.* vol. **26**, pp. 2803-2809 (2008)
- [10] M. Y. Chen, H. Subbaraman, and R. T. Chen, "Photonic Crystal Fiber Beamformer for Multiple X-band Phased-Array Antenna Transmissions," *IEEE. Photon. Technol. Letts.* vol. **5**, pp. 375-377 (2008)

Chapter 4 1x4 X-band phased array antenna subsystem for single beam transmission/reception

The PCF-TTD module described in Chapter 3 forms a continuously tunable time delay system which can provide continuous beam steering capabilities apart from advantages of compact size and low weight features over other optical TTD techniques such as bulk optical TTD technique [1-5], optical non-dispersive fiber TTD technique [6], wavelength-division-multiplexer TTD technique [7-12], holographic-grating based TTD technique [13-14], wavelength-selective waveguide TTD technique [15], acoustic-optic TTD technique [16-19], optical dispersion based TTD technique [20], chirped fiber grating based TTD technique [21-22], and holographic-grating based TTD technique [23-25] etc. In this chapter, the principle of operation and demonstration of single beam transmission and reception of RF signals in the X-band using four true-time-delay lines consisting of highly dispersive photonic crystal fibers and non-zero dispersion shifted fibers will be described. By tuning the wavelength of the optical carrier, the transmission and reception of two different RF signals will be demonstrated.

4.1 Demonstration of single RF beam transmission of PCF-TTD based X-band PAA

In this section, the principle of operation of the highly dispersive photonic crystal fiber true-time-delay (TTD) based X-band phased array antenna system for transmitting a single RF beam is described. Experiment is set up to transmit an RF signal with frequency 8.4GHz to 7.4 degrees by tuning the wavelength to 1547.72nm. Similarly, another RF signal with frequency 12GHz is transmitted to 21.2 degrees by tuning the wavelength to 1552.52nm, thus showing the capability of the system to transmit RF

beams in the X-band. The experimental setup and the results are also explained in this section.

4.1.1 PRINCIPLE OF SINGLE RF BEAM TRANSMISSION

Using the PCF based TTD module, single beam transmission can be realized by using the schematic as shown in Fig. 4.1 [26]. A single set of PCF-TTD lines generates the required time delay values for each element in the antenna array.

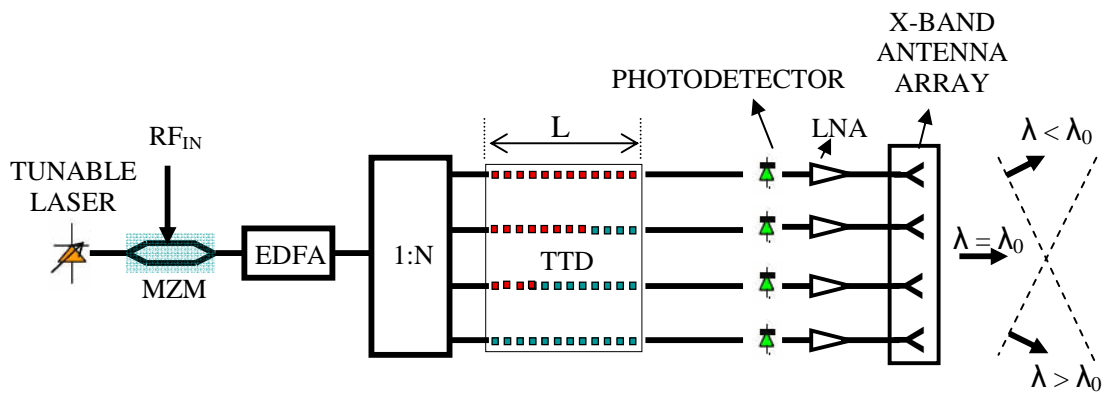


Fig. 4.1 Schematic of the Highly Dispersive PCF-TTD based PAA setup for single RF beam transmission (PCF is represented with red dots and non-zero dispersion shifted fibers is represented with blue dots)

An external cavity tunable laser is used to provide an optical carrier wave. An RF signal from a network analyzer is modulated onto the optical carrier wave using Lithium Niobate Mach-Zehnder modulators (MZM). After passing through the MZM, the optical carrier wave is amplified using an Erbium Doped Fiber Amplifier (EDFA). A 1-to-N optical power splitter divides the amplified optical signal to N true-time-delay (TTD) lines. As described in the previous chapter, each TTD line has consists of different lengths of PCF and NZ-DSF segments, with overall length equal to L for each line. The

lengths are chosen in such a way that at a wavelength λ_0 , the nominal delay through each TTD line is the same and the beam is radiated broadside at the antenna array.

For wavelengths greater than or less than λ_0 , different time delays are induced in each TTD line, with a constant time delay difference between adjacent channels at each wavelength, and the beam is steered at an angle ' θ ' given by [27]

$$\tau = \frac{d \cdot \sin \theta}{c} \quad (4.1)$$

where τ is the time delay difference between adjacent delay lines, d is the antenna element spacing, and c is the speed of light in free space.

Suppose there are N true time delay lines having PCF segments of lengths L_1, L_2, L_3, \dots and L_N respectively, then the additional time delay generated in a delay line having PCF segment of length L_i is given by

$$T_{delay,i} = L_i \int_{\lambda_0}^{\lambda_1} D_{PCF}(\lambda) d\lambda + (L - L_i) \int_{\lambda_0}^{\lambda_1} D_{NZ-DSF}(\lambda) d\lambda \quad i = 1, 2, 3 \dots N \quad (4.2)$$

The first term is contributed by the PCF section and the second term by the NZ-DSF. If we consider the difference of delay time τ , between the i^{th} and the $(i+1)^{\text{th}}$ delay line, we have

$$\tau = (L_i - L_{i+1}) \cdot \int_{\lambda_0}^{\lambda} [D_{PCF}(\lambda) - D_{NZ-DSF}(\lambda)] \cdot d\lambda \quad i = 1, 2, 3 \dots (N-1) \quad (4.3)$$

Since the dispersion coefficient of the PCF ($\sim -600 \text{ ps/nm/km}$ at 1550nm) is much larger compared to that of the NZ-DSF (Lucent TrueWave SMF with dispersion

coefficient $\sim 3\text{ps}/\text{nm}/\text{km}$ from 1530nm to 1560nm), for a fixed wavelength λ , the difference of time delays between different channels are only determined by the lengths of the PCF segments. Therefore, by making the lengths of the PCF an arithmetic sequence, we can achieve equal time delay differences between adjacent TTD lines at any given wavelength, thus, forming a wavelength-tuned TTD line. After the optical signals pass through the TTD lines, they are converted back to electrical signals at the photodetector bank. These electrical signals now provide the phase information for the antenna array. Since for a fixed optical wavelength, the time delay is only related to the lengths of PCF segments, the delay time of the each output electrical signal is controlled continuously by tuning the optical wavelengths. Each optical wavelength creates a time delay set corresponding to a specific steering angle as given by equation (4.1).

4.1.2 EXPERIMENTAL SETUP

Using the PCF-TTD module described in Chapter 3 in the X-band PAA setup, a single RF beam can be transmitted and steered in space using an array antenna. The phase control required to steer the beam is provided by wavelength tuning the TTD modules. From the phase versus frequency measurements provided in Chapter 3, it is seen that continuous time delay intervals from -28.3ps to 31.3ps can be achieved by tuning the wavelength from 1530nm to 1560nm and using equation (4.1), the steering angle can be obtained. Using the highly dispersive photonic crystal fiber TTD network, the RF beam can be steered from -41 degrees to 46 degrees by tuning the wavelength from 1530nm to 1560nm.

In the setup, the lengths of the NZ-DSF segments in each delay line are trimmed such that the delay difference between adjacent lines at 1545nm is zero. By tuning the

laser wavelength to λ_1 , the time delay difference ($\Delta\tau$) from equation (1.17) can be rewritten as

$$\Delta\tau = \tau_i - \tau_{i-1} = \frac{3.5}{1000} \cdot \int_{\lambda_0}^{\lambda_1} D_{PCF}(\lambda).d\lambda \quad \text{picoseconds} \quad (4.4)$$

where $(L_i - L_{i-1})$ in equation 1.17 is the length difference of the PCF segments between adjacent elements (=3.5m) and $D_{PCF}(\lambda)$ is the dispersion coefficient of the photonic crystal fiber expressed in $ps/nm/km$.

The actual experimental setup used for demonstrating single RF beam transmission in Fig 4.2(a) [26]. Optical carrier from an external cavity tunable laser source (Santec ECL-200) is modulated with an X-band RF signal generated by HP 8510C vector network analyzer, using a high speed Lithium Niobate ($LiNbO_3$) modulator. The modulated optical signal is amplified using an Erbium-doped fiber amplifier (EDFA) which provides a maximum output power of 13dBm. The amplified signal is split into 4 channels using a 1-to-4 optical power splitter and distributed to the four TTD lines. The total length L , of each delay line is 10.5 meters, and the lengths of PCF segments used in the 4 delay lines are 0m, 3.5m, 7m, and 10.5m respectively. The 4 delay lines are shown in Fig. 4.2(b). The compositions of the lines are also shown in the inset [26].

The lengths are chosen such that at a wavelength of 1545nm, the nominal delay through each TTD line is the same. This implies that at 1545nm, the RF signal is radiated broadside at the X-band (8-12.5GHz) antenna array. At any other wavelength, the beam is steered to a different direction depending on the time delay differences between

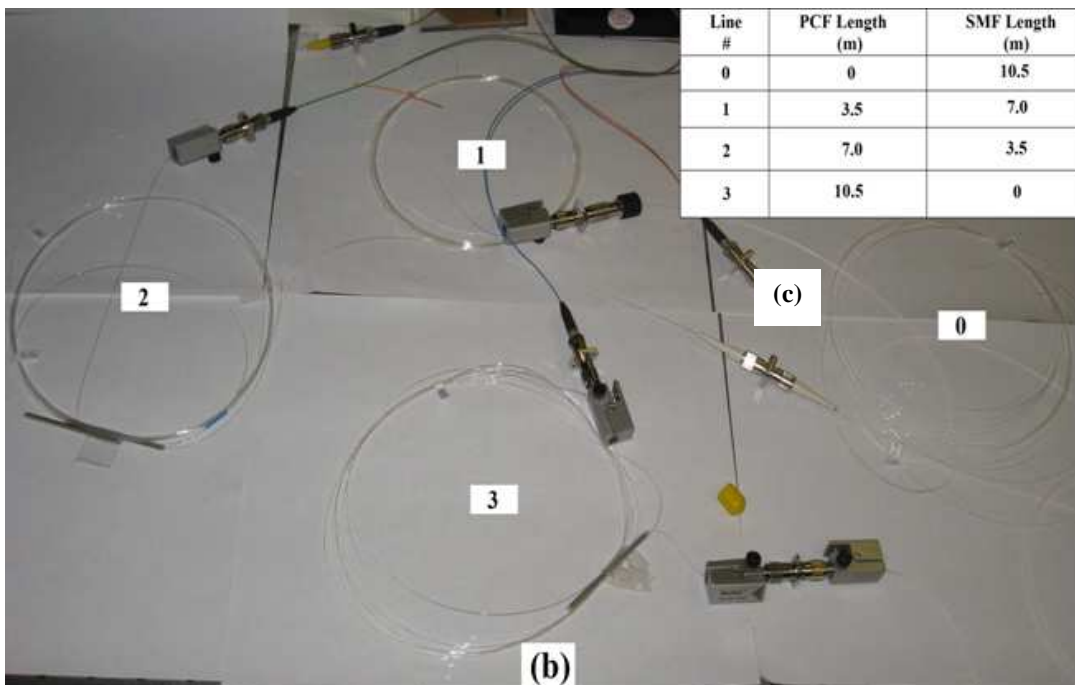
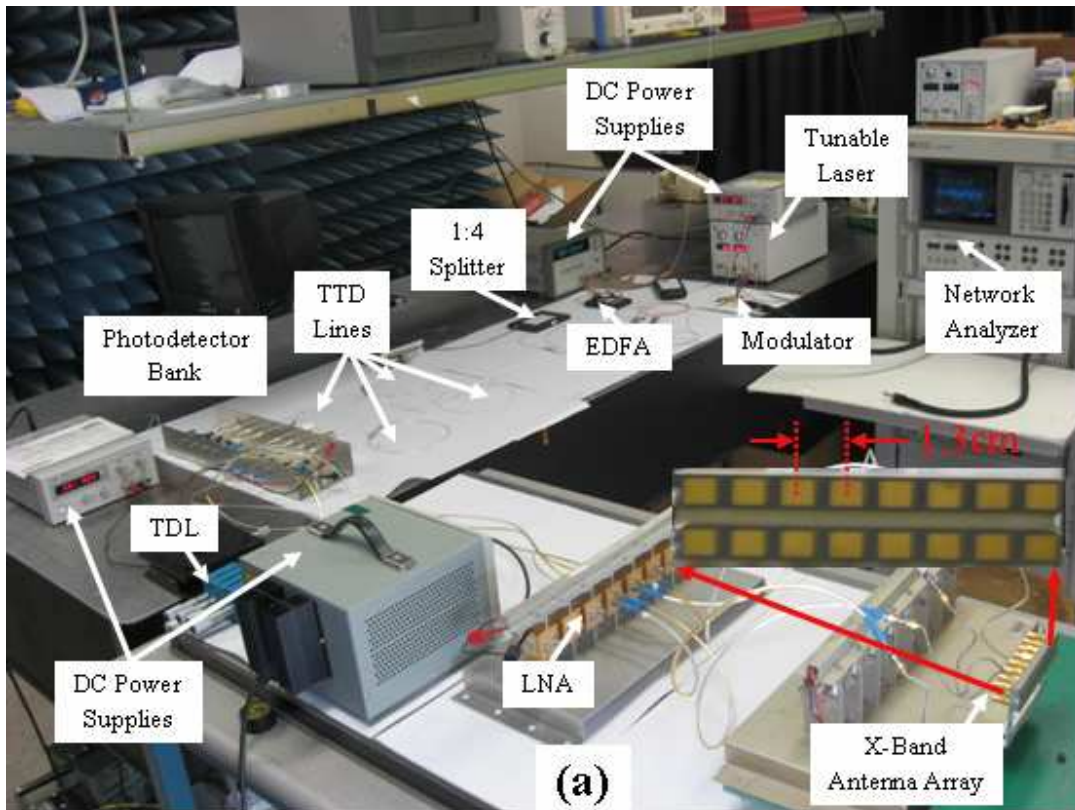




Fig. 4.2 Experimental setup of the PAA in transmitting mode (a) Overall setup along with an expanded view of the antenna array is shown. (b) The four TTD lines are shown. The inset shows the composition of each line. (c) The receiving horn antenna and the microwave spectrum analyzer are shown

adjacent delay lines. A photodetector bank converts the optical signals into electrical signals. Electrical tunable delay lines are used to fine tune the delays such that the delay through all TTD lines are equal at a wavelength of 1545nm. These signals are then amplified by an X-band low noise amplifier (LNA). After amplification, the electrical signals are fed to the center 4 adjacent elements of an antenna array, which has an element spacing of 1.3cm. An enlarged picture of the antenna array is also shown in the inset of Fig. 4.2(a). The far field radiation pattern of the X-band PAA is measured by fixing the antenna array on an accurate positioner and measuring the received power by a fixed standard horn antenna connected to a microwave spectrum analyzer (MSA). The receiving horn antenna and the microwave spectrum analyzer are shown in Fig. 4.2(c).

The X-band antenna array shown in Fig. 4.2(a) is made up of patch antenna elements spaced 1.3cm apart. Since the overall radiation pattern depends on the array factor and the element pattern, the element pattern of the patch elements is measured. The element patterns of the patch antennas are measured at different RF frequencies. As an example, the measured element pattern at a frequency of 9GHz is shown in Fig. 4.3. It can be seen from the figure that the element pattern is relatively flat for a wide range of steering angles, and therefore, the array factor is dominant and determines the shape of the overall far-field radiation pattern.

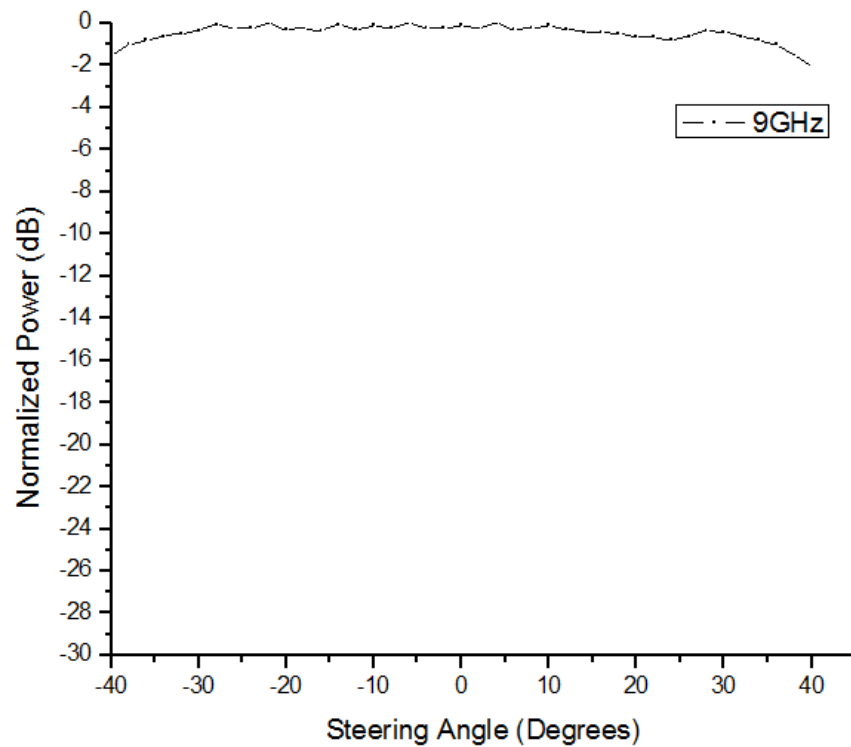


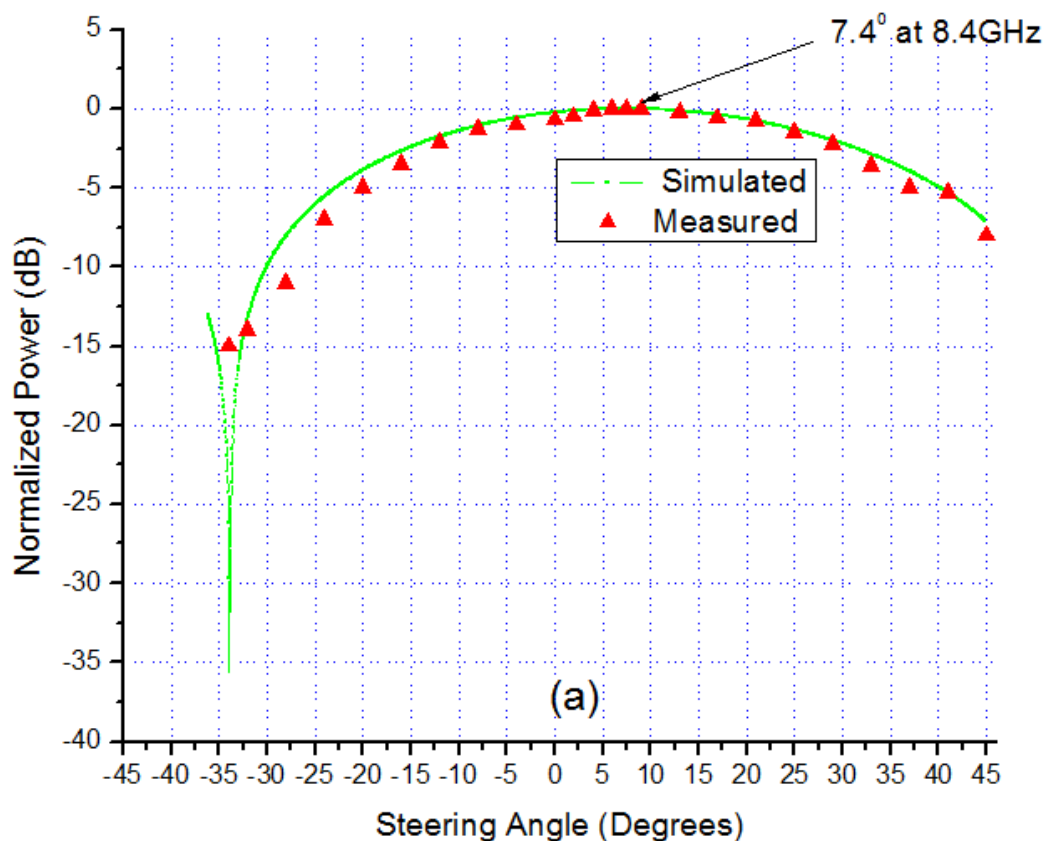
Fig. 4.3 Measured normalized element pattern of the patch antenna at 9GHz

In the experiment, an 8.4GHz RF signal is modulated on an optical carrier with a wavelength 1547.72nm. The transmitted RF signal from the X-band antenna array is

received by the receiving horn antenna, which is placed at a distance greater than the far-field distance (~ 4 meters). The antenna head is rotated on a precision micro-rotation stage and the received power at the horn antenna is measured as a function of the steering angle on the microwave spectrum analyzer. Similarly, the experiment is also performed for a 12GHz signal using an optical carrier wavelength of 1552.52nm.

4.1.3 RESULTS AND DISCUSSION

Figs. 4.4(a) and 4.4(b) show the measured far-field radiation pattern of the 8.4GHz signal (curve marked as solid triangles) and the 12GHz signal (curve marked as solid squares) at optical carrier wavelengths of 1547.72nm and 1552.52nm respectively [26].



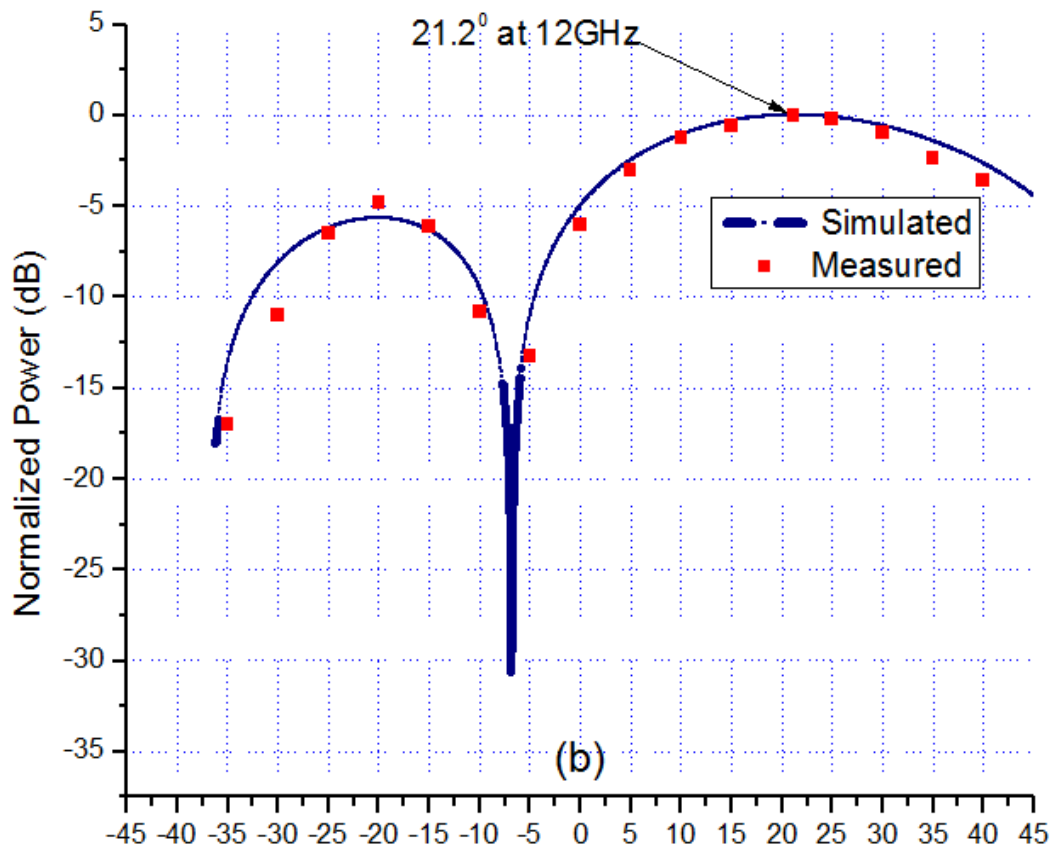


Fig. 4.4 Simulated and measured far field patterns for (a) RF signal with frequency = 8.4GHz at a wavelength of 1547.72nm. (b) RF signal with frequency = 12GHz at a wavelength of 1552.52nm

The simulated far field radiation patterns are shown in both the figures as continuous solid curves. It can be seen from the figures that the maximum received powers occur at 7.4 degrees and 21.2 degrees for 8.4GHz and 12GHz respectively. These angles are also shown as data points on Fig. 3.10. It can also be seen from the figures that the measured patterns agree well with the simulated results, thus showing the capability of single beam transmitting capability of the system. Therefore, by tuning the optical wavelength of the carrier, the RF beam can be steered in space.

In order to beam squint-free nature of the PCF-TTD network, far field radiation patterns of two RF signals at 8.4GHz and 10.3GHz respectively are measured by using an optical carrier wavelength of 1523nm and the measured far-field radiation patterns are shown in Fig. 4.5. It can be seen from the figure that the maximum transmitted power for both 8.4GHz (curve marked with solid circles) and 10.3GHz (curve marked with solid triangles) occur at -23 degrees. The measured and simulated results agree well with each other. This result shows that the PCF-TTD has a frequency independent steering angle capability and thus has a beam squint-free operation.

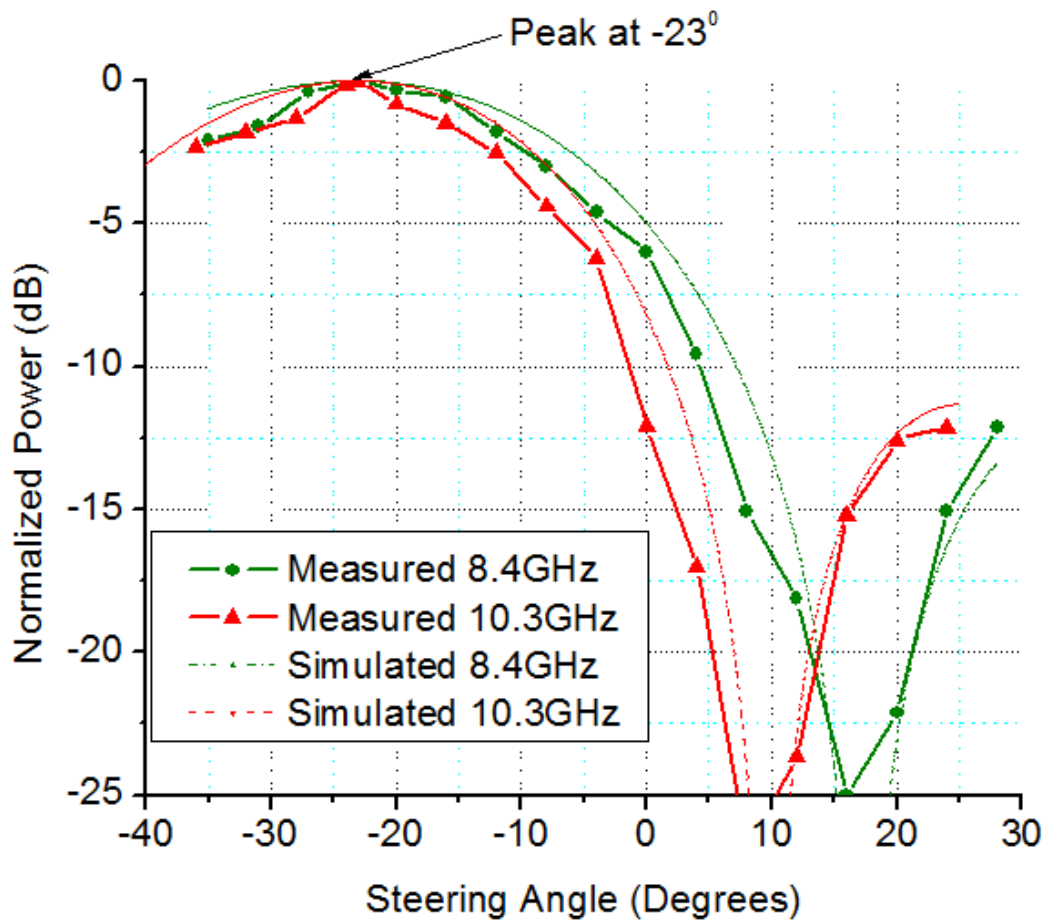


Fig. 4.5 Beam squint-free demonstration of the PCF-TTD based phased array antenna system

4.2 Demonstration of single RF beam reception of PCF-TTD based X-band PAA

The PCF-TTD based PAA architecture can also be used to receive an incoming RF signal and determine the angle of arrival accurately. In this section, the principle of operation of the highly dispersive photonic crystal fiber true-time-delay (TTD) based X-band phased array antenna system for receiving a single RF beam is described. Experiment is set up to receive an RF signal with frequency 8.4GHz from -7.4 degrees by tuning the wavelength to 1547.72nm. Similarly, another RF signal with frequency 12GHz is received from -21.2 degrees by tuning the wavelength to 1552.52nm, thus showing the capability of the system to receive RF beams in the X-band. The experimental setup and the results are also explained in this section.

4.2.1 PRINCIPLE OF SINGLE RF BEAM RECEPTION

Since the incoming RF beam travels a different path length in order to reach each of the two antenna elements, a phase difference between the two signals is created. These received RF signals from the antenna elements are amplified using LNAs and modulated onto the optical carrier. The optical signal feeding each MZM is obtained by splitting the optical carrier from a tunable laser source using a *1-to-N* optical power splitter. Depending on the wavelength of the optical carrier, the TTD lines also induce additional phase shifts to the original signals. Therefore, if the additional phase shift has a sign opposite to the one created by the incoming beams, then the two signals coming out of the TTD lines will be in phase and they will add up at the *N-to-1* power combiner and produce a maximum power on the microwave spectrum analyzer. Thus, if the incoming beam is arriving from a direction ' θ ', then the optical wavelength that can cancel the phase difference is the one that would direct a beam at an angle of ' $-\theta$ ' in the

transmitting mode. Therefore, there is a peak on the plot of the combined power at the photodetector versus wavelength. The wavelength at which the peak occurs can be used in conjunction with steering angle data as shown in Fig. 3.10 to accurately determine the angle of arrival.

Using the highly dispersive photonic crystal fiber TTD network, the incoming RF beam can be detected from 41 degrees to -46 degrees by tuning the wavelength from 1530nm to 1560nm and its angle of arrival can be determined accurately.

4.2.2 EXPERIMENTAL SETUP

The beam receiving and angle of arrival determining capability of the PCF-TTD based PAA system can be demonstrated by slightly modifying the single beam transmission setup. A schematic of the setup used to detect and determine the angle of arrival of the incoming RF beam is shown in Fig. 4.6 [26]. In the case of single beam transmission, only one modulator is required to modulate the RF signal onto the optical carrier. In the case of receiving mode operation however, since each element receives the RF signal, one modulator per antenna element is required. Since we are limited by the available hardware in the laboratory, the receiving mode experiment is performed using center two adjacent antenna elements.

The RF signal impinging on the antenna array is generated by a HP 8620C sweep oscillator. A horn antenna is used to transmit the signal towards the X-band antenna array. The horn antenna is placed at an angle with respect to the antenna array. The incoming signal is received by the two adjacent center antenna elements on the lower line of X-band antenna array shown in the inset of Fig. 4.2(a).

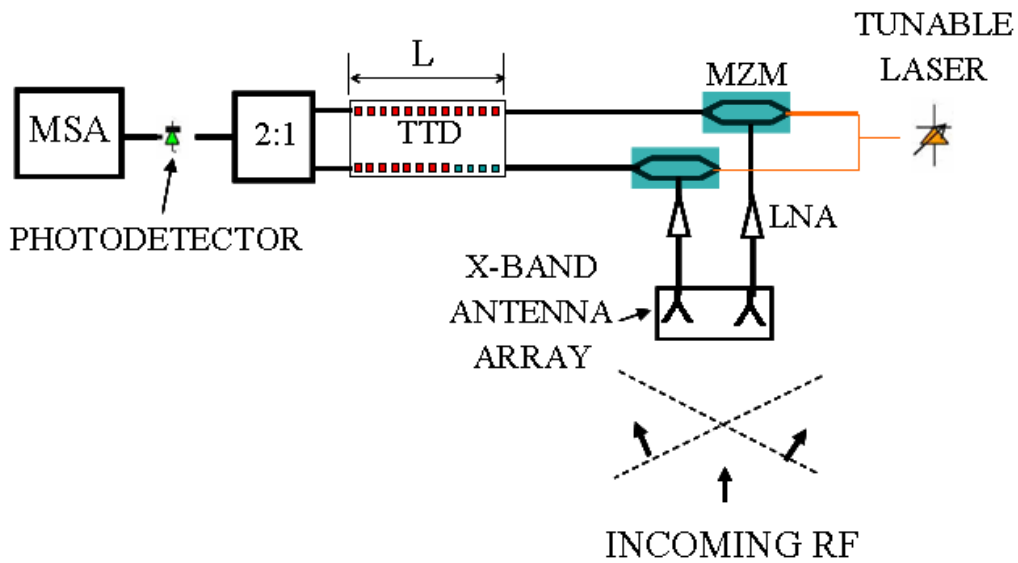


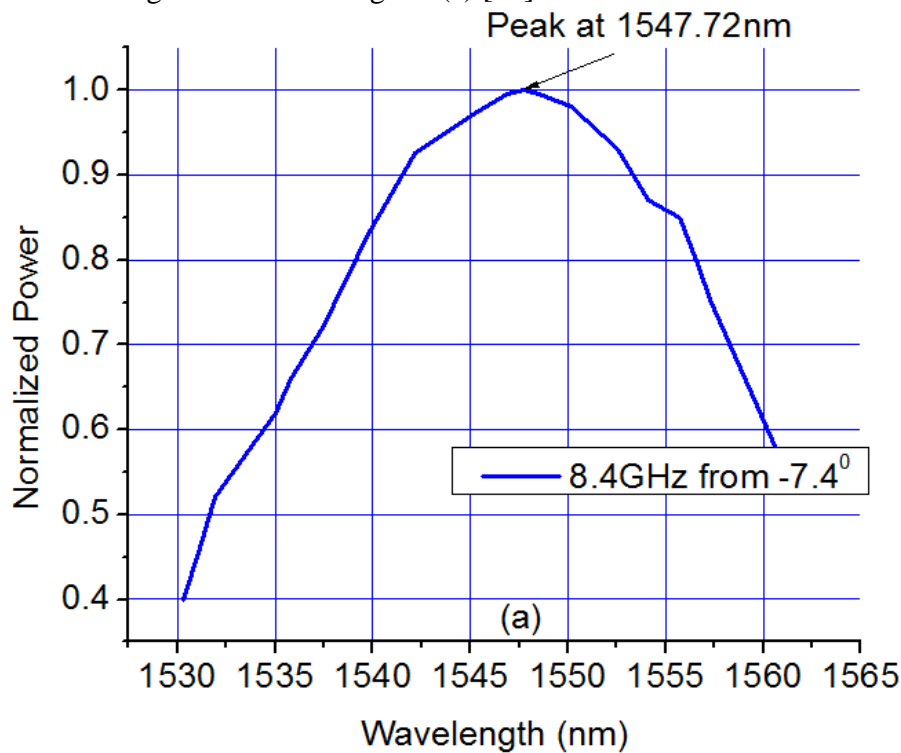
Fig. 4.6 Schematic of the Highly Dispersive PCF-TTD based PAA system for single RF beam reception. MZM: Mach-Zehnder modulator; TTD: true time delay, LNA: low noise amplifier, MSA: Microwave spectrum analyzer (PCF is represented with red dots and non-zero dispersion shifted fibers is represented with blue dots)

Since the RF beam travels a different path length in order to reach each of the two antenna elements, a phase difference between the two signals is created. These received RF signals from the X-band antenna elements are amplified using LNAs and modulated onto the optical carrier. The optical signal feeding each MZM is obtained by splitting the optical carrier from a tunable laser source (Santec ECL-100) using a 1-to-2 optical power splitter. After modulation, the optical carriers pass through two adjacent PCF-TTD lines consisting of 0m of PCF : 10.5m NZ-DSF and 3.5m of PCF : 7.0m of NZ-DSF. The signals from the two delay lines are combined using a 2-to-1 power combiner. The optical signal is converted into electrical signal at the photodetector. The wavelength on the tunable laser source is changed from 1530nm to 1560nm and the RF power at the photodetector is measured on the microwave spectrum analyzer.

In order for the receiving mode experiment results to be consistent with transmitting mode experiment results, the incoming RF beams are chosen to have frequencies of 8.4GHz and 12GHz. The sweep oscillator is set to provide an 8.4GHz signal and the horn antenna is placed at an angle of -7.4 degrees with respect to the X-band antenna array. The wavelength on the tunable laser source is varied from 1530nm to 1560nm and the power of the received 8.4GHz RF signal at the photodetector is measured on the MSA as a function of the wavelength of the optical carrier. Similarly, the measurement is also performed for another RF signal with frequency 12GHz impinging on the array from -21.2 degrees.

4.2.3 RESULTS AND DISCUSSION

A plot showing the power measured on the MSA for the 8.4GHz signal as a function of wavelength is shown in Fig. 4.7(a) [26].



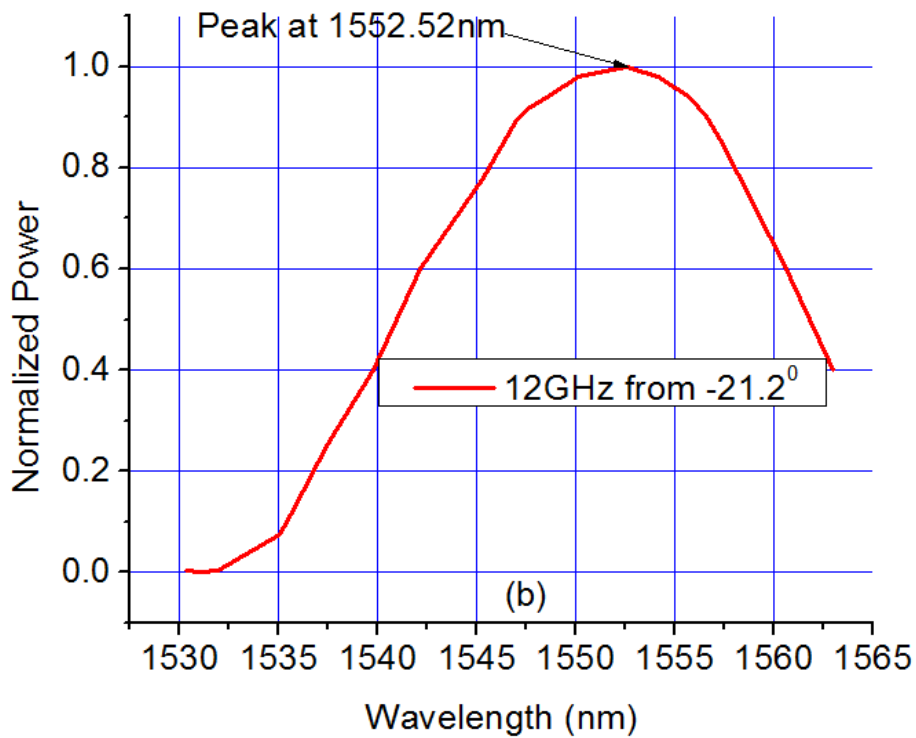


Fig. 4.7 Measured received power versus wavelength for (a) 8.4GHz RF signal impinging on the antenna array from -7.4° (b) 12GHz RF signal impinging on the antenna array from -21.2°

It can be seen from the figure that a peak in the power at the photodetector is obtained at a wavelength of 1547.72nm. The wavelength at which the peak occurs can be used in conjunction with steering angle data as shown in Fig. 3.10 to accurately determine the angle of arrival. The peak wavelength in Fig. 4.7(a) corresponds to a complementary angle of 7.4 degrees in the transmitting mode. Similarly, for the 12GHz signal placed at an angle of -21.2 degrees with respect to the antenna array normal, the plot of the measured power as a function of wavelength is shown in Fig. 4.7(b). It can be seen from the figure that a peak in the power at the photodetector is obtained at a wavelength of 1552.52nm. This corresponds to a complementary angle of 21.2 degrees in

the transmitting mode. These results prove the feasibility of using the PCF-TTD based X-band PAA in the receiving mode.

4.3 Summary

In this chapter, the principle of operation and demonstration of single beam transmission and reception of PCF-TTD based X-band PAA system was explained. By tuning the optical wavelength, transmission of two RF signals with frequencies 8.4GHz and 12GHz to 7.4 degrees and 21.2 degrees respectively was observed by tuning the wavelengths respectively to 1547.72nm and 1552.52nm. Single RF beam receiving capability was demonstrated by receiving two RF signals with frequencies 8.4GHz and 12GHz from -7.4 degrees and -21.2 degrees respectively by detecting peak in the received power by tuning the optical wavelengths to 1547.72nm and 1552.52nm respectively. Thus, the capability of the PAA system to transmit and receive single RF beams was successfully demonstrated.

4.4 References

- [1] D. Dolfi, J. P. Huignard, and M. Baril, "Optically controlled true-time delays for phased array antenna," Proc. SPIE. vol. **1102**, pp. 152 (1989)
- [2] D. Dolfi, F. Michel-Gabriel, S. Bann, and J. P. Huignard, "Two-dimensional optical architecture for true-time-delay beam forming in a phased-array antenna," Opt. Letts. vol. **16**, pp. 255-257 (1991)
- [3] D. Dolfi, P. Joffre, J. Antoine, J. P. Huignard, D. Philippet, and P. Granger, "Experimental demonstration of a phased-array antenna optically controlled with phase and time delays," Appl. Opt. vol. **35**, pp. 5293-5300 (1996)
- [4] N. A. Riza, "Transmit/receive time-delay beam-forming optical architecture for phased-array antennas," Appl. Opt. vol. **30**, pp. 4594-4595 (1991)

- [5] N. A. Riza, "Liquid crystal-based optical time delay control system for wideband phased arrays," *Proc. SPIE*. vol. **1790**, pp. 171-183 (1992)
- [6] A. M. Levine, "Use of fiber optic frequency and phase determining element in radar," in *Proceedings of the 33rd Annual Symposium on Frequency Control*, IEEE, 436-443 (1979)
- [7] P. M. Freitag and S. R. Forrest, "A coherent optically controlled phased array antenna system," *IEEE. Microwav. Guided. Wav. Letts.* vol. **3**, pp. 293-295 (1993)
- [8] L. Xu, R. Taylor, and S. R. Forrest, "True-time delay phased array antenna feed system based on optical heterodyne techniques," *IEEE. Photon. Technol. Letts.* vol. **8**, pp. 160-162 (1996)
- [9] D. K. T. Tong, and M. C. Wu, "A novel multiwavelength optically controlled phased array antenna with a programmable dispersion matrix," *IEEE. Photon. Technol. Letts.* vol. **8**, pp. 812-814 (1996)
- [10] P. Goutzoulis and D. K. Davies, "Hardware-compressive 2-D fiber-optic delay line architecture for time steering of phased-array antennas," *Appl. Opt.* vol. **29**, pp. 5353-5359 (1990)
- [11] P. Goutzoulis and D. K. Davies, "All-optical hardware-compressive wavelength multiplexed fiber optic architecture for true-time delay steering of 2-D phased array antenna," *Proc. SPIE*. vol. **1703**, pp. 604-614 (1992)
- [12] P. Goutzoulis and D. K. Davies, J. Zomp, P. Hrycak, and A. Johnson, "Development and field demonstration of a hardware-compressive fiber-optic true time delay steering system for phased array antennas," *Appl. Opt.* vol. **33**, pp. 8173-8185 (1994)
- [13] Y. Chen and R. T. Chen, "A fully packaged true time delay module for a K-band phased array antenna system demonstration," *IEEE. Photon. Technol. Letts.* vol. **14**, pp. 1175 – 1177 (2002)
- [14] Z. Fu and R. T. Chen, "Highly packing density optical true-time delay lines for phased array antenna applications," *Recent Research Developments Series*, pp. 1, Dec. 1998
- [15] S. Yegnanarayanan, P. D. Trinh, and B. Jalali, "Recirculating photonic filter: a wavelength-selective time delay for phased array antennas and wavelength code division multiple access," *Opt. Letts.* vol. **21**, pp. 740-742 (1996)
- [16] W. D. Jemison and P. R. Herczfeld, "Acousto-optically controlled true-time delay," *IEEE. Microwav. Guided Wav. Letts.* vol. **3**, pp. 72-75 (1993)

- [17] L. H. Gesell, R. E. Feinleib, J. L. Lafuse, and T. M. Turpin, "Acousto-optic control of time delays for array beam steering," *Proc. SPIE*. vol. **2155**, 194 (1994)
- [18] E. N. Toughlian and H. Zmuda, "A photonic variable RF delay line for phased array antennas," *IEEE. J. Lightwav. Technol.* vol. **8**, pp. 1824-1828 (1990)
- [19] E. H. Monsay, K. C. Baldwin, and M. J. Caucitto, "Photonic true-time delay for high-frequency phased array systems," *IEEE. Photon. Technol. Letts.* vol. **6**, pp. 118-120 (1994)
- [20] R. Soref, "Optical dispersion technique for time-delay beam steering," *Appl. Opt.* vol. **31**, pp. 7395-7397 (1992)
- [21] J. L. Cruz, B. Ortega, M. V. Andres, B. Gimeno, D. Pastor, J. Capmany, and L. Dong, "Chirped fiber gratings for phased array antenna," *Electron. Letts.* vol. **33**, pp. 545-546 (1997)
- [22] J. L. Corral, J. Marti, S. Regidor, J. M. Fuster, R. Laming, and M. J. Cole, "Continuously variable true time-delay optical feeder for phased-array antenna employing chirped fiber gratings," *IEEE. Trans. Microwav. Theory. Techniq.* vol. **45**, pp. 1531-1536 (1997)
- [23] Z. Shi, Y. Jiang, B. Howley, Y. Chen, F. Zhao, and R. T. Chen, "Continuously delay time tunable-waveguide hologram module for X-band phased-array antenna," *IEEE. Photon. Technol. Letts.* vol. **15**, pp. 972-974 (2003)
- [24] Z. Shi, L. Gu, B. Howley, Y. Jiang, Q. Zhou, R. T. Chen, M. Y. Chen, X. Wang, H. R. Fetterman, and G. Brost, "True-time-delay modules based on single tunable laser in conjunction with waveguide-hologram for phased-array antenna," *Opt. Engineering.* vol. **44**, 084301, (2005)
- [25] X. Chen, Z. Shi, L. Gu, B. Howley, Y. Jiang, and R. T. Chen, "Miniaturized Delay time-enhanced Photopolymer Waveguide Hologram Module for Phased-Array Antenna," *IEEE. Photon. Technol. Letts.* vol. **17**, pp. 2182-2184, (2005)
- [26] H. Subbaraman, M. Y. Chen, and R. T. Chen, "Packaging and system demonstration of an X-band phased array antenna utilizing highly dispersive photonic crystal fiber based true-time-delay," in *Proc. SPIE*, vol. **7221**, pp. 722107-1 (2009)
- [27] W. Ng, A. A. Walston, G. L. Tangonan, J. J. Lee, I. L. Newberg, and N. Bernstein, "The first demonstration of an optically steered microwave phased array antenna using true-time-delay," *IEEE. J. Lightwav. Technol.* vol. **9**, pp. 1124- 1131 (1991)

Chapter 5 Simultaneous multiple-beam transmission and reception of a PCF TTD-based X-band phased array antenna

In the previous chapter, the results of the demonstration of single beam transmission and reception of RF beams using the photonic crystal fiber true-time-delay based X-band phased array antenna system was presented. In this chapter, application of the TTD network will be extended to show simultaneous multiple RF beam transmission and reception capability of the X-band phased antenna array utilizing PCF-TTD for the first time. The principle of simultaneous multiple RF beam transmission and reception will be described and experimental results of simultaneous dual RF beam transmission and reception capability of the PAA system will be demonstrated.

5.1 Principle of simultaneous multiple RF beam transmission

Using the PCF based TTD module, multiple-beam transmission can be realized by using the scheme as shown in Fig. 5.1 [1, 2]. A general system is shown in which a multiple number (M) of RF signals are transmitted simultaneously using an X-band antenna array having N elements.

External cavity tunable lasers are used to generate a multiple number of optical carrier waves with wavelengths λ_1 to λ_M . RF signals with different frequencies are modulated onto these optical carrier waves using Lithium Niobate Mach-Zehnder modulators (MZMs). After passing through the MZMs, the optical carrier waves are combined together using an M -to-1 power combiner and these optical signals are amplified using an Erbium Doped Fiber Amplifier (EDFA). A 1-to- N optical power splitter divides the amplified optical signal to N true-time-delay (TTD) lines. Each TTD

line has consists of different lengths of PCF and NZ-DSF segments, with overall length equal to L for each line. As described earlier, the lengths are chosen in such a way that at a wavelength λ_0 , the nominal delay through each TTD line is the same and the beam is radiated broadside at the antenna array. Transition to multiple beam capability from single beam setup is straightforward as only a single set of PCF-TTD lines generates the required time delay values for each element in the antenna array and for all multiple beams.

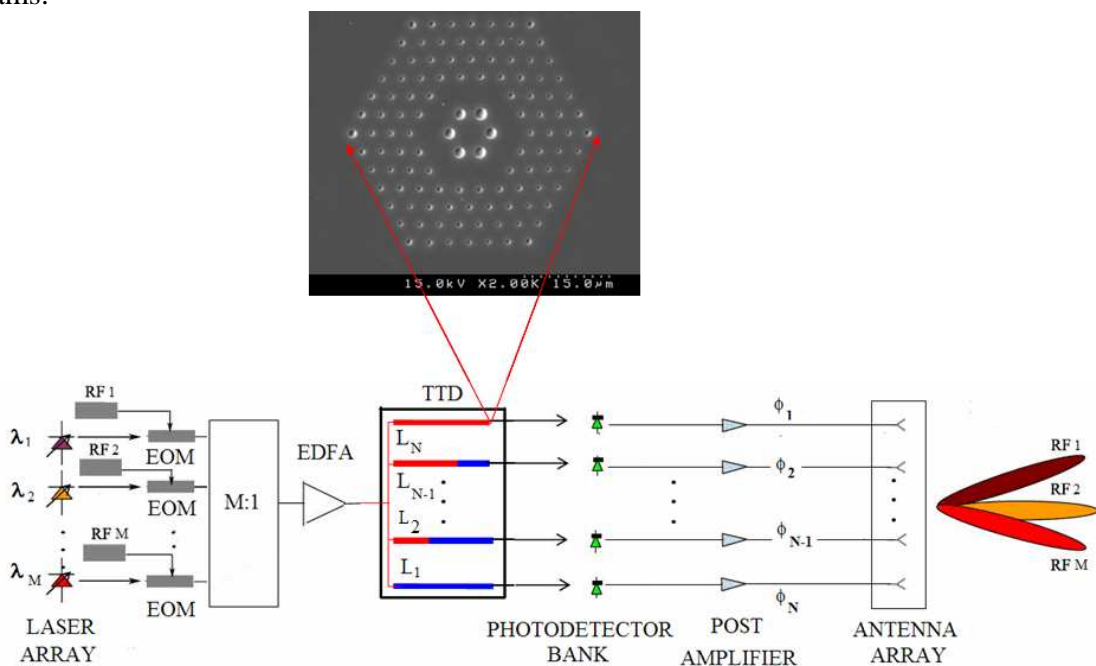


Fig. 5.1 Schematic setup for simultaneous transmission of multiple beams, EOM: electro-optic modulator, EDFA: Erbium doped fiber amplifier, TTD: true-time-delay. The cross sectional schematic view of the PCF is also shown

From the previous chapter we know that the additional time delay generated in a delay line having PCF segment of length L_i by changing the wavelength from λ_0 to λ_1 is given by

$$T_{delay,i} = L_i \int_{\lambda_0}^{\lambda_i} D_{PCF}(\lambda) d\lambda + (L - L_i) \int_{\lambda_0}^{\lambda_i} D_{NZ-DSF}(\lambda) d\lambda \quad i = 1, 2, 3 \dots N \quad (5.1)$$

where, the first term is contributed by the PCF section and the second term by the NZ-DSF and the time delay difference (τ), between the i^{th} and the $(i+1)^{\text{th}}$ delay line is given by

$$\tau = (L_i - L_{i+1}) \cdot \int_{\lambda_0}^{\lambda} [D_{PCF}(\lambda) - D_{NZ-DSF}(\lambda)] \cdot d\lambda \quad i = 1, 2, 3 \dots (N-1) \quad (5.2)$$

We see from equation (5.2) that the time delay difference is independent of the RF frequency. The steering angle given by $\theta = \sin^{-1}\left(\frac{c \times \tau}{d}\right)$ is also independent of the RF frequency used [3]. Therefore, by modulating one RF signal on one optical carrier, the different RF beams can be independently and simultaneously transmitted and steered. Therefore, in order to simultaneously transmit N RF beams, N electro-optic modulators and N tunable laser sources need to be used. After the optical signals pass through the TTD lines, they are converted back to electrical signals at the photodetector bank. Since for a fixed optical wavelength, the time delay is only related to the lengths of PCF segments, the delay time of the each output electrical signal is controlled continuously by tuning the optical wavelengths. Each optical wavelength creates a time delay set corresponding to a specific steering angle as given by equation (5.1). Since different RF signals are modulated on separate optical carriers, by injecting these multiple wavelengths simultaneously, one can generate equivalent number of independently steered RF far field patterns at the same time due to the squint-free nature of the TTD lines.

5.2 Demonstration of simultaneous multiple beam transmission of a PCF-TTD based X-band PAA

Due to the limitation on the availability of hardware in the laboratory, a simultaneous dual RF beam transmission experiment is performed. This section describes the experimental setup and provides the results of simultaneous dual RF beam transmission using PCF-TTD based X-band PAA system for the first time.

5.2.1 EXPERIMENTAL SETUP

The experimental setup used for the demonstration of simultaneous dual-beam steering is shown in Fig. 5.2 [2]. Two tunable laser sources (Santec ECL-100) are used to generate two optical carriers with different wavelengths. The tunable lasers have an output power of 8dBm. An HP8620C sweep oscillator and an HP8510C network analyzer generate two RF signals with frequencies 8.4GHz and 12GHz respectively, which are independently modulated onto the two optical carriers using two high speed LiNbO₃ modulators. A maximum of 7dB loss is encountered after passing through the modulator. The optical signals are first combined through an optical combiner and amplified using an EDFA. The EDFA has a maximum output of 13dBm. The amplified signal is split into 4 channels using a 1:4 optical power splitter and distributed to the four TTD lines. The power splitting creates fan-out loss of 6dB for each delay line path. The maximum insertion loss added due to the delay lines is 11dB. The photodetector bank converts the optical signals into electrical signals. Tunable delay lines are used to fine tune the delays as an initial calibration step such that the delay through the TTD lines are equal at 1545nm. These electrical signals are then amplified by the X-band low noise amplifiers (LNA) that have a gain of 35dB. After amplification, the electrical signals are fed to a 4-element X-band antenna array, which has an element spacing of 1.3cm.

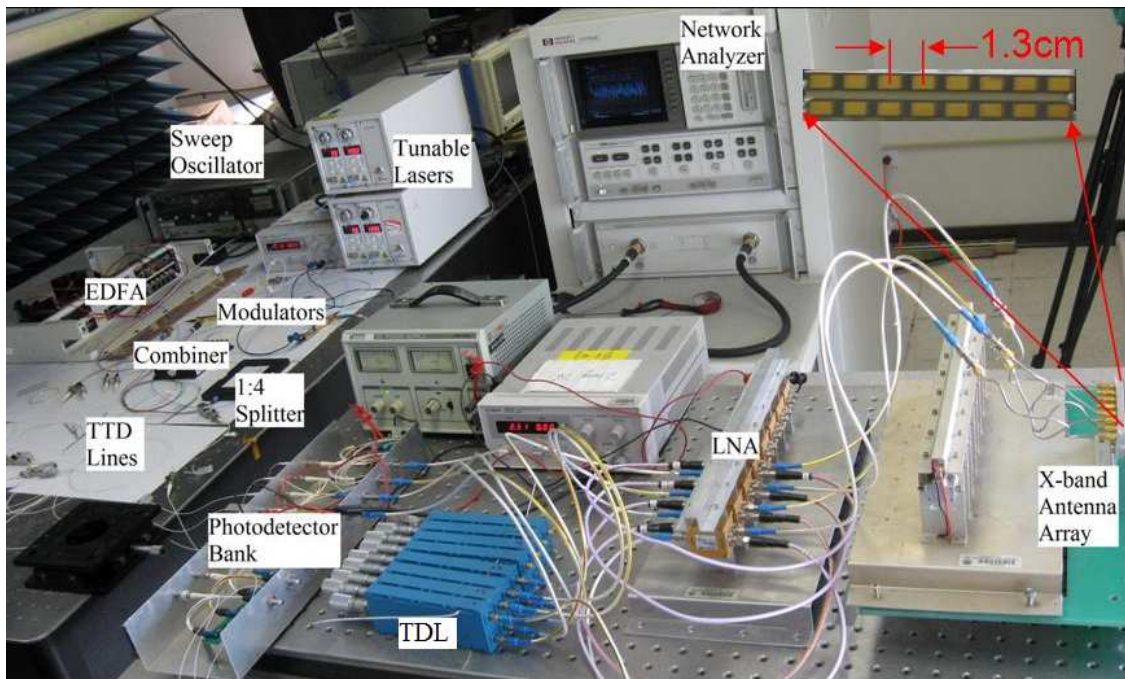


Fig. 5.2 Experimental setup for simultaneous dual RF beam steering, EDFA: Erbium doped fiber amplifier, TTD: true-time-delay, LNA: low noise amplifier, TDL: tunable delay line

5.2.2 RESULTS AND DISCUSSION

The far field radiation pattern of the phased antenna array (PAA) is measured by fixing the X-band antenna array on an accurate micro-rotation stage and measuring the power received by a standard horn antenna connected to a microwave spectrum analyzer (MSA) placed at a distance greater than the far-field distance (~5 meters). The received power at the MSA is measured as a function of antenna array rotation angle for the two frequencies. The simulated and measured far field patterns are shown in Fig. 5.3 for the two beam operation at RF frequencies of 8.4GHz and 12GHz. It can be seen from the figure that the beam pointing direction of the 8.4GHz signal is 7.4 degrees for a wavelength of 1547.72nm, and is 21.2 degrees at a wavelength of 1552.52nm for the

12GHz signal. From Fig. 5.3, it can also be seen that the measured patterns agree well with the simulated results, showing the capability of multiple beam transmitting capability of our system. In simulating the radiation pattern, the measured patch antenna element patterns are taken into account. This data can further be used to verify the results of the dual beam receiving experiment which will be explained in detail in the sections 5.3 and 5.4.

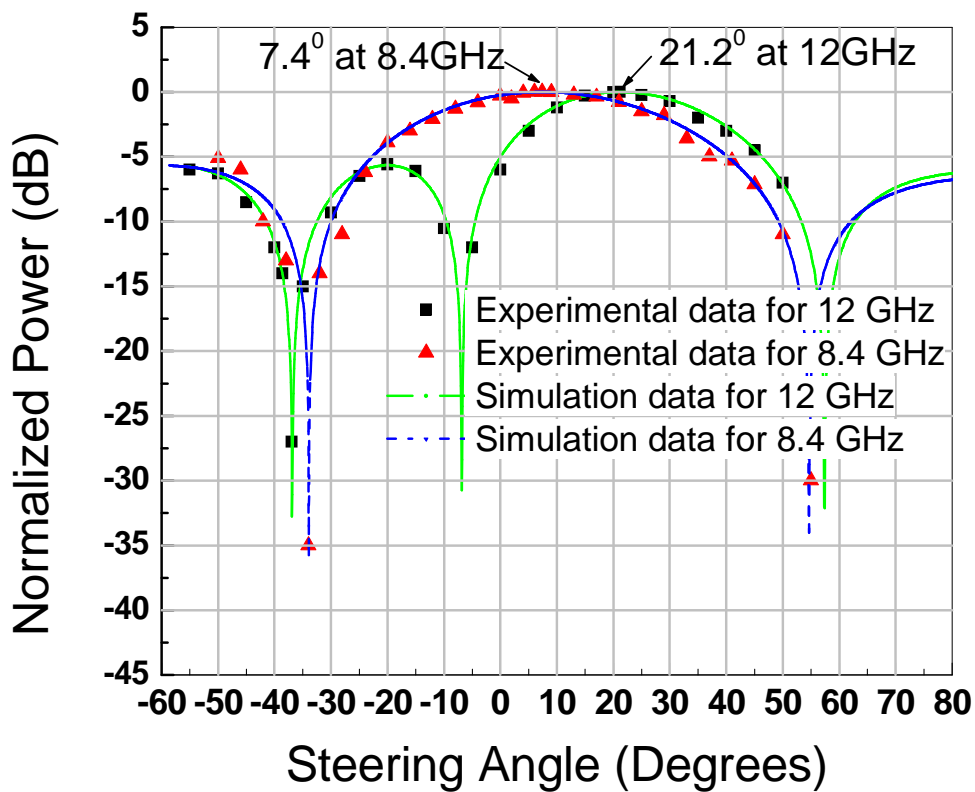


Fig. 5.3 Simulated and Measured Far Field Patterns of two RF signals with frequencies 8.4GHz and 12GHz steered simultaneously to angles of 7.4 and 21.2 degrees respectively

Therefore, by independently tuning the optical wavelength of the carrier on each tunable laser source, each of the two RF beams can be simultaneously and independently steered in space.

5.3 Principle of simultaneous multiple beam reception

The schematic diagram of the receiving mode for simultaneously receiving multiple number (M) of RF beams is shown in Fig. 5.4 [4]. This configuration can be achieved by slightly modifying the setup of the transmitting mode. In this structure, multiple received RF signals from external sources impinge upon the X-band PAA from different directions. At each antenna element, any arbitrary RF signal arrives with a slightly different time delay due to angle between the incoming RF signal and antenna array, and due to the fact that the antenna elements are spatially separated. Therefore, there is a phase difference between the adjacent element signals for each RF signal, which represents the signature of the angle of incoming RF signals.

A multiple N number of electrical signals are produced at the output of the N element antenna array. These received electrical signals at each antenna element are amplified using LNAs. Each amplified signal modulates the optical signals coming from the output of a wavelength division multiplexer (WDM) having a multiple number (M) of independent optical wavelengths, such that one optical carrier can be used for each incoming RF signal. The output signal from each modulator passes through a TTD line, and gets delayed time-reversely in reference to the transmission mode, according to the dispersion value and length of the PCF in that line.

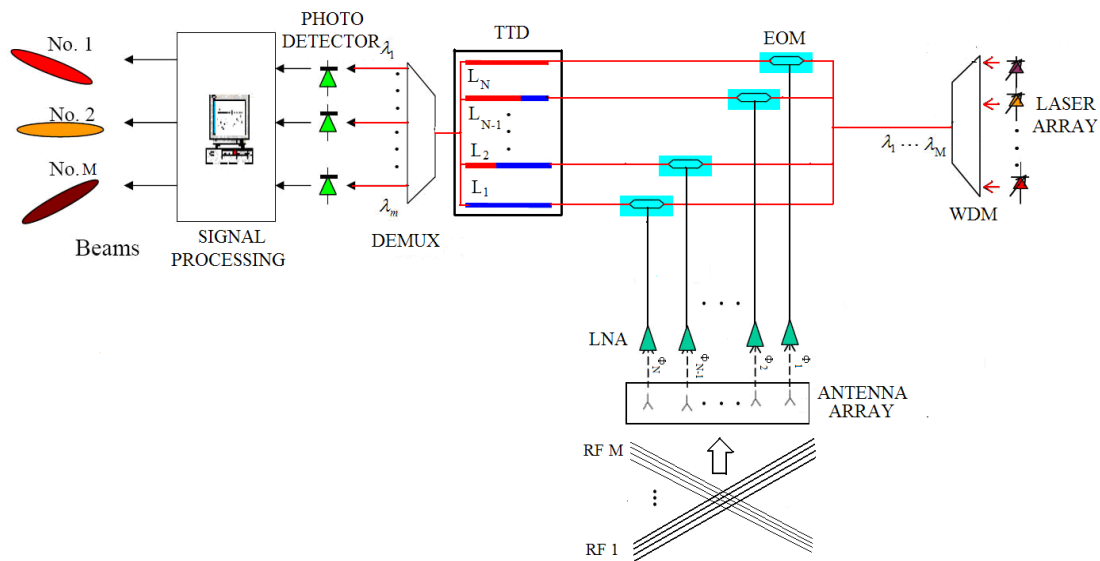


Fig. 5.4 Structure of the receiving mode with multiple incoming beams, WDM: wavelength division multiplexer, LNA: low noise amplifier, EOM: electro-optic modulator, TTD: true-time-delay, DEMUX: demultiplexer

The delayed output optical signals from the TTD lines are then fed to a wavelength division demultiplexer (WDM), where different optical wavelengths are separated into their respective M wavelengths. At any photodetector, say P_M , the signals corresponding to wavelength λ_M coming from all delay lines add up. In order for all the signals to add up constructively for the corresponding direction, the delay lines should alter the phase of signals in such a way that all signals arrive in phase at the corresponding photodetector.

Since every wavelength generates one set of time delay values in the delay lines, for a given angle of arrival, θ only one wavelength would be able to compensate phase differences between adjacent elements and deliver maximum power at the photodetector output. The wavelength at which maximum power is detected at the photodetector output

corresponds to one angle of arrival. The angle of arrival can thus be determined for any RF signal of interest due to the squint-free nature of the true-time delay lines.

5.4 Demonstration of simultaneous multiple beam reception of a PCF-TTD based X-band PAA

As was in the case of simultaneous dual RF beam transmission, hardware limitation in the laboratory limits the demonstration of simultaneous multiple RF beam reception to two beams. An experiment is performed to simultaneously receive and determine the angle of arrival of two incoming RF signals. This section describes the experimental setup and provides the results of simultaneous dual RF beam reception using PCF-TTD based X-band PAA system for the first time.

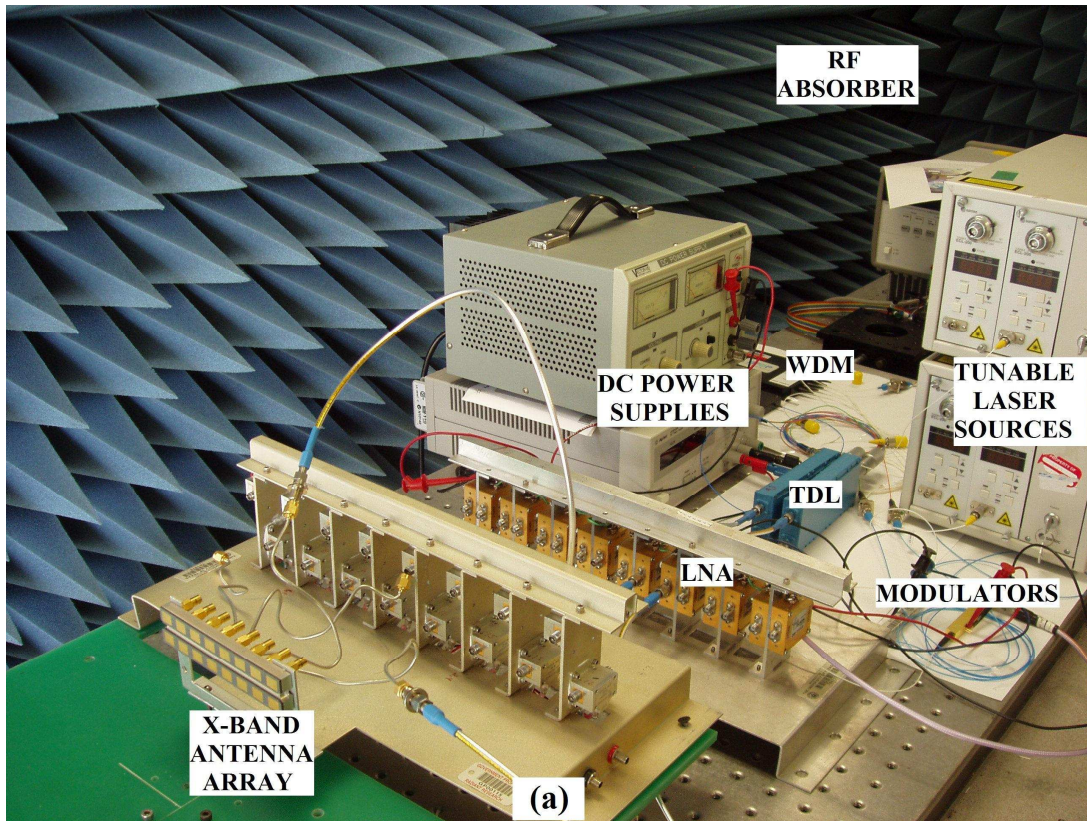
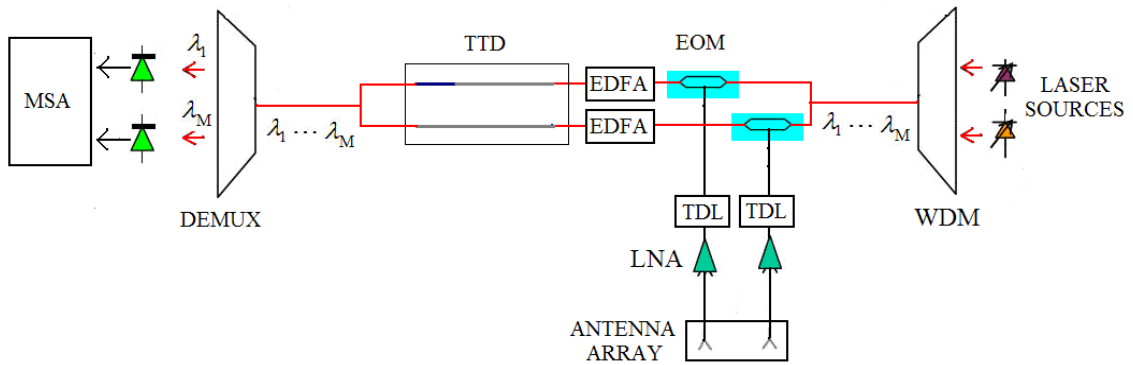
5.4.1 EXPERIMENTAL SETUP

An experiment is performed in order to receive two RF beams simultaneously and determine the angle of arrival of each incoming signal. The experimental setup used in the demonstration is shown in Fig. 5.5 [4]. A schematic of the simultaneous dual beam setup is also shown for clarity.

In order to perform the experiment, center two adjacent elements of the X-band antenna array, two LiNbO₃ modulators and two adjacent delay lines in the setup are used. The 2 delay lines consist of 0 meters of PCF : 10.5 meters of NZ-DSF and 3.5 meters of PCF : 7 meters of NZ-DSF respectively. As discussed previously, the lengths of the NZ-DSF sections are trimmed such that at 1545nm, the delays in each of the delay lines are equal. That is, for an RF signal incident normally on the antenna array, modulating a

wavelength of 1545nm, the signal detected at the photodetector will be a maximum. Therefore, different angle of arrival of RF signal will require a different wavelength to equalize the phase difference between adjacent elements in the TTD lines and generate a maximum at the photodetector output. In order to receive a beam from positive ' θ ' direction, the experiment must be set up such that in the transmitting mode, the beam is steered in the negative ' θ ' direction. The steering angle versus the wavelength is calculated for our setup and the result is shown in Fig. 3.10. This calculated result is later experimentally verified by detecting two beams impinging upon the X-band antenna array from two different angles.

The 8.4GHz and 12GHz signals are generated using a HP 8620C sweep oscillator and 8510C HP network analyzer respectively. In order to show consistency with the transmitting mode experiment results, the 8.4GHz and 12GHz signals emitted by standard horn antennas are placed at -7.4 degrees and -21.2 degrees respectively with respect to the antenna array normal. These external RF signals impinge on the antenna array and the signals received by the center low adjacent antenna elements are amplified using two low noise amplifiers (LNAs). The tunable delay lines (TDL) are used to fine tune the delay through the lines for initial calibration of the setup at 1545nm. The amplified signals modulate the output signal of WDM, comprising of two optical wavelengths coming from two external cavity tunable laser sources. The modulated optical signals are amplified using Erbium doped fiber amplifiers (EDFA) and fed to two adjacent delay lines. After passing through the TTD lines, the wavelengths are demultiplexed at the output of the delay lines and fed to a photodetector bank. A microwave spectrum analyzer (MSA) is used to monitor the detected RF output power from the photodetectors.



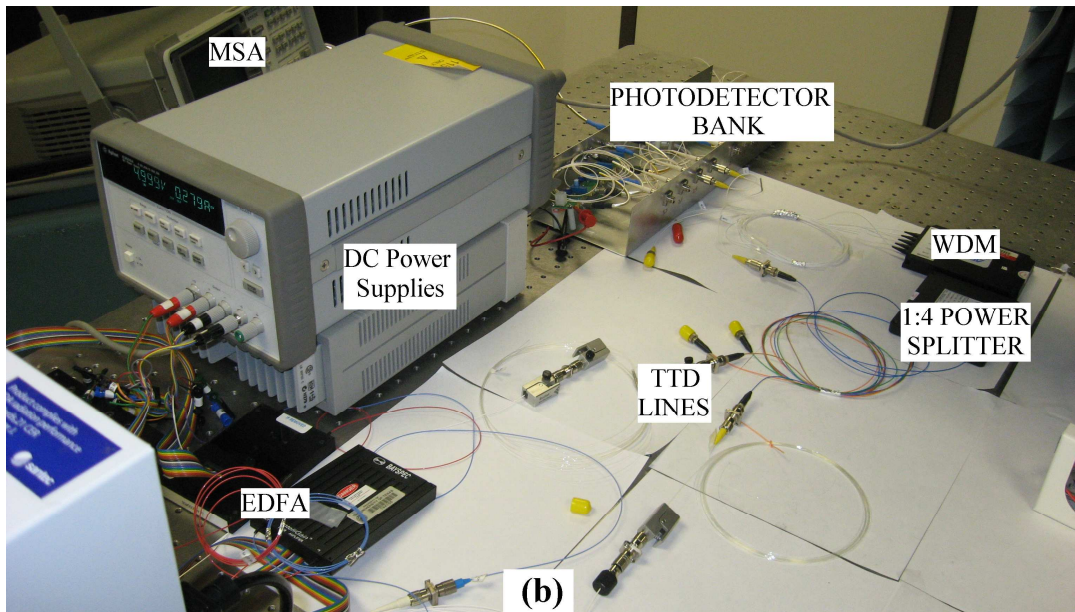


Fig.5.5 Schematic of simultaneous dual beam operation setup and photograph of actual (a) RF reception and electro-optical conversion setup (b) True-Time-Delay lines and signal processing setup; the output from the modulators in (a) are connected to the inputs of EDFAs in (b). (The RF sources and the transmitting horn antennas of the setup are not shown in the figure)

Although one tunable laser source is sufficient to detect all of the impinging RF signals, one tunable laser source per RF signal will enable us to lock one signal with one tunable laser source while scanning for another RF signal using the other laser source. Therefore, we use two tunable lasers for locking and detecting the 8.4GHz and 12GHz signals independently. The wavelengths on the tunable lasers are tuned from 1530nm to 1560nm, and the outputs from the photodetectors are measured. The data is first measured for 8.4GHz and 12GHz signal sources placed at -7.4 degrees and -21.2 degrees respectively and then measured for 8.4GHz and 12GHz signal sources placed at -21.2 degrees and -7.4 degrees respectively. The four measured data curves are shown in Fig.

5.6 [4]. Note that the true-time delay (TTD) setup provides squint-free steering covering the whole RF spectrum of interest.

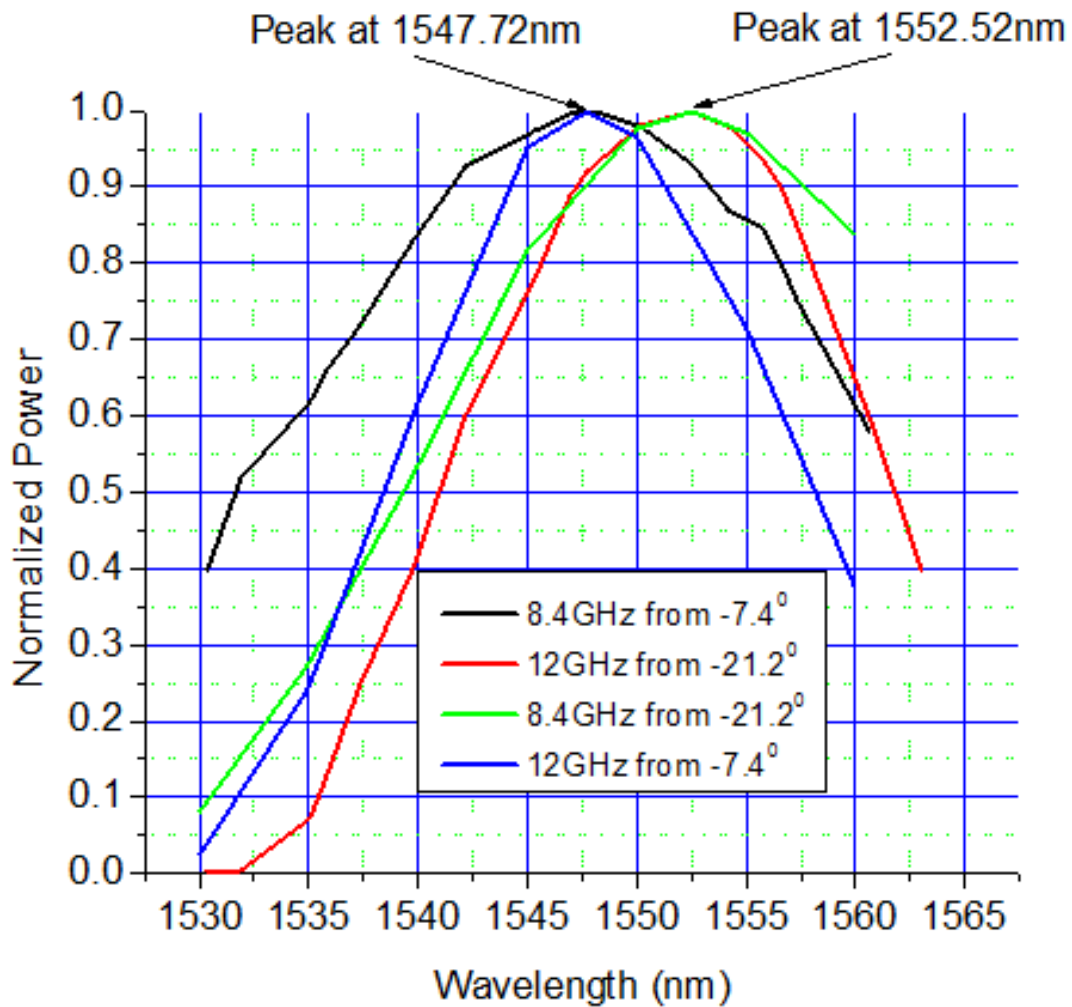


Fig. 5.6 Signal power measured at the photodetector vs. wavelength. The signal power peaks appear at 1547.72nm for 8.4GHz and 12GHz signals placed at -7.4 degrees and at 1552.52nm for 8.4GHz and 12GHz signals placed at -21.2 degrees

5.4.2 RESULTS AND DISCUSSION

It can be seen clearly from the figure that at a wavelength of 1547.72nm, there is a peak in the detected output power for 8.4GHz and 12GHz signals arriving from -7.4 degrees, and at a wavelength of 1552.52nm, there is a peak in the detected power for 8.4GHz and 12GHz signals arriving from -21.2 degrees. These wavelengths correspond to complementary angles of 7.4 degrees and 21.2 degrees respectively in the transmission mode, which are also shown as two data points in Fig. 3.10, thus showing the simultaneous multiple RF beam receiving capability of our system. It can also be seen from Fig. 5.6 that there is no beam squint effect observed using the PCF-TTD technique. Since the wavelength on the tunable laser source can be tuned to within 0.01nm accuracy, the error in determining the angle is very small. For example, for a change in 0.01nm in the wavelength of the source at 1550nm, the error in determining the angle is less than 0.027 degrees which corresponds to 0.2% error in determining the angle at 1550nm. Although the peaks in Fig. 5.6 are moderately distinguishable, by incorporating more number of adjacent elements to receive the impinging RF signals, we can achieve sharper peaks and distinguish very closely spaced signals.

The above result is rather rudimentary with $N = 2$ elements due to hardware constraint in the laboratory. It is possible to scale the working principle to a larger array consisting of N antenna elements by using one modulator per antenna element and N TTD lines with the largest length of PCF equal to $(N-1)*3.5$ meters for PCF with dispersion coefficient of -600ps/nm/km at 1550nm. The easy scalability is due to the fact that a very long length of PCF can be fabricated in a single draw of the fiber and the required lengths can be cut in precise lengths from the spool. The cut lengths of PCF can then be spliced to single mode fibers in order to achieve the required TTD network

consisting of N delay lines. The cost of the PCF-TTD network is reduced as the number of delay lines is increased due to the shared cost of fiber fabrication. Such an ‘all-fiber’ TTD system does not require intermediate electro-optic conversion and provides a very large bandwidth extending to several hundred GHz with beam squint free operation. Apart from the above advantages, the PCF-TTD network can also provide continuous beam scanning capability.

Compared to other optical TTD techniques [5-12], this method provides a relatively compact and extremely low weight feature with tremendous scope for scalability and extendibility to two dimensions. Although conventional FPGA-based electronic counterparts are extremely dense, small in size and cheaper with respect PCF approach, they suffer from beam squint effect and their operation is limited to several tens of GHz. By utilizing very high dispersive PCFs, the length of PCF required, and hence the overall size and weight of the system can further be reduced.

The operation can also be easily extended to two dimensions for (a) X-Y separable case by using two sets of PCF-TTD networks, one for each dimension as shown in [13] (b) non-separable X-Y case by making use of TTD networks in two dimensions and choosing the lengths of the PCF in the individual delay lines according to the location of the antenna element in the array. The received signal can then be processed by the signal processing unit to give the angle of arrival.

We are limited by the available hardware to conduct multi-beam reception. In principle, the total number of RF beams that can be simultaneously detected is limited by

the bandwidth ($\Delta\lambda$) of the WDM. As a result, hundreds of RF beams are detectable in the same time domain.

5.5 Summary

In this chapter, the principle of operation of simultaneous multiple RF beam transmission and reception were described and the experimental results of the demonstration of simultaneous dual RF beam transmission and reception of the PCF TTD based X-band PAA system were presented. By tuning the optical wavelengths on two tunable laser sources, simultaneous transmission of two RF signals with frequencies 8.4GHz and 12GHz to 7.4 degrees and 21.2 degrees respectively was observed by tuning the wavelengths respectively to 1547.72nm and 1552.52nm. Simultaneous dual RF beam receiving capability was demonstrated by receiving two RF signals with frequencies 8.4GHz and 12GHz from -7.4 degrees and -21.2 degrees respectively by detecting peak in the received power by simultaneously tuning the optical wavelengths on two tunable laser sources to 1547.72nm and 1552.52nm respectively. Thus, the capability of the PAA system to simultaneously and independently transmit and receive dual RF beams using PCF TTD-based X-band PAA system was successfully demonstrated for the first time.

5.6 References

- [1] M. Y. Chen, H. Subbaraman, and R. T. Chen, "Photonic Crystal Fiber Beamformer for Multiple X-Band Phased-Array Antenna Transmissions," *IEEE. Photon. Technol. Letts.* vol. **20**, pp. 375-377 (2008)
- [2] H. Subbaraman, M. Y. Chen, and R. T. Chen, "Photonic Crystal Fiber-Based True-Time-Delay Beamformer for Multiple RF Beam Transmission and Reception of an X-Band Phased-Array Antenna," *J. Lightwav. Technol.* vol. **26**, pp. 2803-2809 (2008)

- [3] G. A. Koepf, "Optical processor for phased-array antenna beam formation," *Proc. SPIE*. vol. **477**, pp. 75–81 (1984)
- [4] H. Subbaraman, M. Y. Chen, and R. T. Chen, "Photonic dual RF beam reception of an X band phased array antenna using a photonic crystal fiber-based true-time-delay beamformer," *Appl. Opt.* vol. **7**, pp. 6448–6452 (2008)
- [5] L. H. Gesell, R. E. Feinleib, J. L. Lafuse, and T. M. Turpin, "Acousto-optic control of time delays for array beam steering," *Proc. SPIE*. vol. **2155**, pp. 194–204 (1994)
- [6] N. A. Riza, "Liquid crystal-based optical time delay units for phased array antennas," *J. Lightwave Technol.* vol. **12**, pp. 1440–1447 (1994)
- [7] R. Soref, "Optical dispersion technique for time-delay beam steering," *Appl. Opt.* vol. **31**, pp. 7395–7397 (1992)
- [8] R. D. Esman, M. J. Monsma, J. L. Dexter, and D. G. Cooper, "Microwave true time-delay modulator using fibre-optic dispersion," *Electron. Letts.* vol. **28**, pp. 1905–1907 (1992)
- [9] M. Y. Frankel, P. J. Matthews, and R. D. Esman, "Fiber optic true time steering of an ultrawideband receive array," *IEEE Trans. Microwave Theory Tech.* vol. **45**, pp. 1522–1526 (1997)
- [10] M. Y. Frankel, R. D. Esman, and M. G. Parent, "Phased-array transmitter/receiver controlled by a true-time-delay fiber optic beamformer," *IEEE Photon. Technol. Letts.* vol. **7**, pp. 1216–1218 (1995)
- [11] A. Moloney, C. Edge, and I. Bennion, "Fiber grating time delay elements for phased array antennas," *Electron. Letts.* vol. **31**, pp. 1485–1486 (1995)
- [12] J. E. Roman, M. Y. Frankel, P. J. Matthews, and R. D. Esman, "Time-steered array with a chirped grating beamformer," *Electron. Letts.* vol. **33**, pp. 652–653 (1997)
- [13] Y. Jiang, Z. Shi, B. Howley, X. Chen, M. Y. Chen, and R. T. Chen, "Delay time enhanced photonic crystal fiber array for wireless communications using 2-D X-band phased-array antennas," *Opt. Engineering*. vol. **44**, 125001 (2005)

Chapter 6 Characterization and RF performance evaluation of PCF-TTD analog subsystem

In the previous chapters, a true-time-delay module utilizing highly dispersive photonic crystal fibers was described. The TTD module was used to demonstrate single and simultaneous multiple RF beam transmission and reception. In this chapter, important RF performance characteristics of the PCF TTD-based phased array antenna system will be described. Noise performance and distortion characteristics of the system will be the primary focus. Experiments to measure the noise figure and different types of distortion will be performed and experimental results will be presented. An important parameter related to the performance of the system, namely the Spurious-Free Dynamic Range (SFDR) will be presented and a method on improving the SFDR of the system will also be explained.

6.1 Noise in analog links

Noise is a term used for any unwanted and undesired signal present in the system. Noise limits the performance of any system because if the signal power is sufficiently low, noise can dominate and over shadow the desired signal. Every component in an analog system contributes to the overall noise. For good performance, the desired signal should be well resolvable over noise, and hence, the ratio of signal to noise (S/N) should be as high as possible. Therefore, it is important to evaluate the noise performance of the PCF-TTD module based X-band PAA system. In this section, the different noise sources that affect the performance of the analog link are briefly discussed and an important parameter called the noise figure is introduced and measured for our system.

6.1.1 NOISE SOURCES

There are three major noise sources that adversely affect the performance of an analog link [1]

1. *Thermal noise*
2. *Shot noise*
3. *Relative intensity noise (RIN)*

Thermal noise:

Thermal noise is generated due to the random movement of charge carriers in conductors. The noise voltage $\langle v_t \rangle$ that appears across a resistor R at an absolute temperature T , measure in a bandwidth Δf is given by [1]

$$\begin{aligned}\langle v_t^2 \rangle &= 4kTR\Delta f \\ \langle v_t \rangle &= \langle i_t \rangle R \\ \therefore \langle i_t^2 \rangle &= \frac{4kT\Delta f}{R}\end{aligned}\tag{6.1}$$

where k is the Boltzmann's constant ($k = 1.38 \times 10^{-23}$ J/K). $\langle i_t^2 \rangle$ is the square of the average noise current.

The available power P_t can be obtained by dividing $\langle v_t^2 \rangle$ in equation (6.1) by $4R$. If we assume $\Delta f = 1\text{Hz}$, $T=290\text{K}$, then $P_t \approx -174\text{dBm}$. The thermal noise has a flat spectrum and most of the device's working bandwidth falls within this range. Therefore, thermal noise can be considered as 'flat' or 'white' for the evaluation of the performance of PCF-TTD network.

Shot noise:

Due to discrete nature of electrons and photons, there is a fluctuation in the current generated at the photodetector. Therefore, the current generated at the photodetector has an average value over which there is a random ‘noise like current’ superimposed in a statistical manner. Such a superimposed noise term is termed as shot noise. For example, in an optical link, photons do not reach the photodetector continuously, but in discrete packets. At some instants in time, there might be more photons reaching the photodetector than at other instants in time. An average photodetector current is established over which the randomness is added. This contributes to shot noise. The bandwidth of such a noise is not flat as was the case with thermal noise. However, for the frequencies used (8-12.5GHz), the spectrum can be considered flat because the shot noise spectrum is relatively flat in the small localized bandwidth considered. The shot noise current over a bandwidth Δf is given by [1]

$$\langle i_{sn}^2 \rangle = 2q \langle I_D \rangle \Delta f \quad (6.2)$$

where q is the charge of the carrier, $\langle i_{sn}^2 \rangle$ is the square of the average shot noise current and $\langle I_D \rangle$ is the average photodetector current.

From equation (6.2), we see that the shot noise term decreases as the average photodetector current is reduced. Therefore, by reducing the average photodetector current, it is possible to reduce the shot noise below thermal noise term. It is easy to determine which of the noise terms, shot or thermal, dominate in a system. By equating currents from equations (6.1) and (6.2), and using the values of various constants with $R = 50\Omega$ (most common matching impedance), $T=290K$, it can be seen that as long

as the average photodetector current is less than 1mA, shot noise is less than thermal noise, and thermal noise with the flat spectrum is the dominant term.

Relative intensity noise (RIN):

Relative intensity noise (RIN) is referred to the instability in the output from a laser source. There are several factors such as changes in laser pump current, fluctuations in laser gain medium, vibration of cavity, temperature etc that contribute to this fluctuation in the laser's output power. The effect of RIN is observed at the electrical output from a photodiode [1]. If $\langle i_{RIN} \rangle$ is the average RIN noise current in the system, then RIN in the system is given by [1]

$$RIN = 10 \log \left(\frac{2 \langle i_{RIN}^2(t) \rangle}{\langle I_D \rangle^2 \Delta f} \right) \quad (6.3)$$

where $\langle I_D \rangle$ and Δf are the average diode current and bandwidth respectively.

Unlike the shot noise and thermal noise spectra, the noise spectrum of *RIN* is not flat. For relatively low optical power (~1mW), shot noise increases linearly with average photodetector current and *RIN* power increases as average photodetector current squared. This means that at relatively low optical powers, the RIN decreases faster than the shot noise and it falls to a value below the shot noise level. For links that do not use a directly modulated laser source (links using external modulation in conjunction with a continuous-wave (CW) laser source), RIN is negligible compared to shot noise as long as average photodetector current is less than 100mA [1]. In our application, the average photodetector current is well below this limit and therefore, *shot noise dominates over RIN*.

6.1.2 NOISE FIGURE (NF) MEASUREMENT

A standard factor that measures the effect of noise on the system is given by the noise factor (f). The noise factor contains the most important information about the RF system noise performance. The noise factor is the ratio of the available output noise power per unit bandwidth to the fraction of the noise caused by the actual sources at the input or it is the ratio of the signal-to-noise ratio at the input to the signal-to-noise ratio at the output. Therefore, the noise factor gives a measure of additive noises in the system referred to the input.

Noise Factor (f) = Total Output Noise Power/Output Noise due to Input Source Only

$$f = \frac{P_{N,Output}}{(Gain * P_{N,Input})} \quad (6.4)$$

In the above definition, ‘Noise’ comes from two effects. In the first, undesired signals comes to the input of the RF system in the form of interference. In the second, random fluctuation of carriers introduces noise. The available noise power, $P_{N,Input}$ is given by [1]

$$P_{N,Input} = kT\Delta f \quad (6.5)$$

where, k is the Boltzmann’s constant which has a value of $1.38 \times 10^{-23} J / K$, T is the temperature in Kelvin and Δf is the bandwidth of the system. Therefore, for $\Delta f = 1Hz$ and $P_{N,Input} = -174dBm$, the noise spectral density at 290K is $-174dBm / Hz$.

The system Noise Figure (NF) is given by [1]

$$NF = 10 * \log_{10}(f) = \{P_{N,Output}(dB) + 174(dBm/Hz) - Gain(dB) - 10 * \log_{10}(BW)\} \quad (6.6)$$

where the bandwidth of the system is given by BW.

If output noise spectral density (in dBm/Hz) instead of output noise power is specified, then the above equation is modified to

$$NF(dB) = \{P_{N,Output}(dBm/Hz) + 174(dBm/Hz) - Gain(dB)\} \quad (6.7)$$

Therefore, a measurement of output noise spectral density and gain of the analog system can be used to determine the noise figure. Using the schematic of the experimental setup shown in Fig. 6.1, we measure the NF for our system.

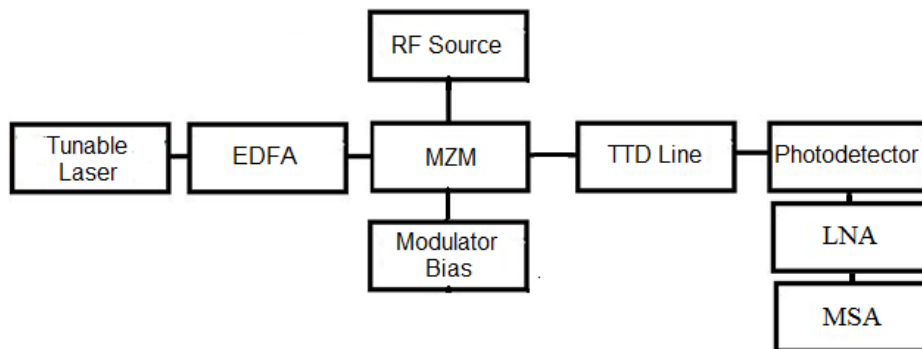


Fig. 6.1 Schematic of the setup used for noise figure measurement

The RF signal with a frequency of 8.0GHz and 0dBm power from the HP8510C network analyzer is modulated onto an optical carrier with a wavelength of 1550nm from the output of a combination of a tunable laser source (Santec ECL-100) and an Erbium-doped fiber amplifier which has an output optical power of 20mW. The modulated

optical carrier is passed through a TTD line comprising of 3.5m of NZ-DSF and 7.0m of high dispersion PCF. After passing through the TTD line, the optical signal is converted to electrical signal using a photodetector. This electrical signal is amplified using an X-band low noise amplifier (gain = 35dB). The RF output power and the output noise spectral density (in dBm/Hz) are measured on a microwave spectrum analyzer. For our system, under a set of given conditions, the gain is obtained by calculating the difference between the measured output RF power and input RF power (both expressed in dBm).

By changing the dc bias voltage of the modulator, it is possible to change the modulator bias angle between 90° (quadrature) at which the transmission is maximum and 180° at which the transmission is minimum. Usually, analog fiber-optic links are operated at quadrature in order to maximize RF gain and avoid even-order distortion (distortion characteristics will be explained in sections 6.3 and 6.4). As the bias angle is shifted towards 180° , the link gain is reduced due to a decrease in modulator slope efficiency and the average photodetector current decreases. Since the shot noise is proportional to the square of the average photodetector current, the shot noise term falls faster compared to the gain, and so, a minimum noise figure can be obtained as the bias is adjusted towards the transmission minimum modulator bias angle.

By changing the DC modulator bias, the gain and the output noise spectral density are obtained from the MSA. Using equation (6.7), the NF at each point is calculated and the result is shown in Fig. 6.2. It can be seen from the figure that the minimum noise figure is obtained close to 121° modulator bias.

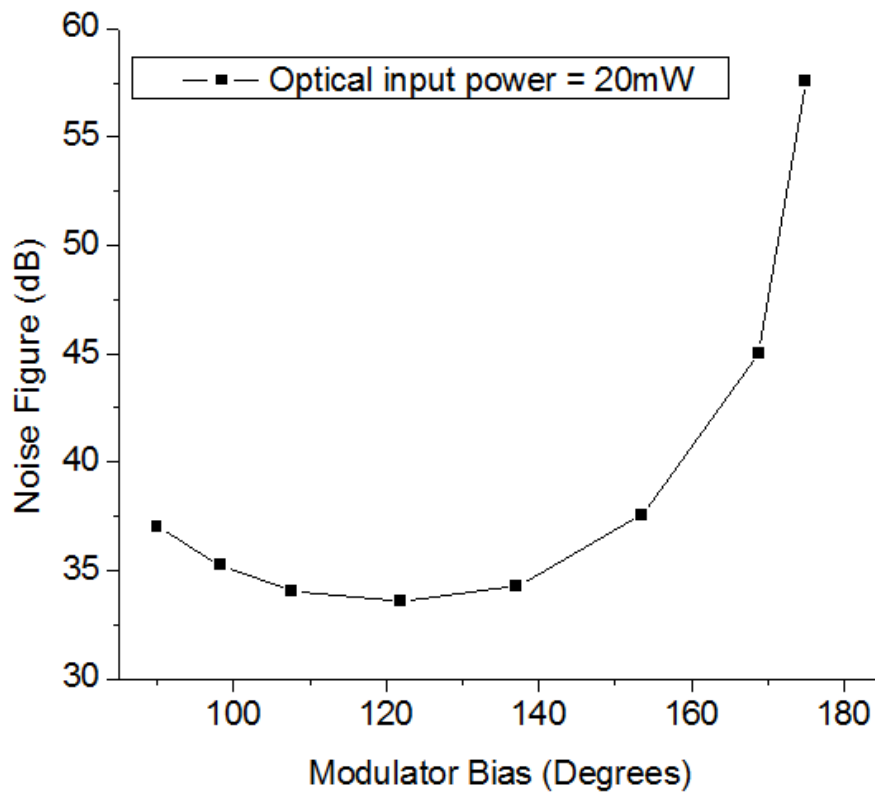


Fig. 6.2 Noise Figure versus Modulator bias measurement for PCF-TTD system at 20mW optical input power

The NF decreases from 37dB at quadrature (90 degrees bias angle) to 33.55dB at 121 degree bias angle.

6.2 Distortion in analog links

It is always reasonable to assume some nonlinearity in an analog system. The effect of this nonlinearity is to create extraneous signals which are otherwise not present in a linear system. These newly created frequencies are often undesirable and may even interfere with other frequencies used in the system. Fig. 6.3 shows a general picture of

different distortion terms that affect an analog system within a given working bandwidth (indicated by a yellow box).

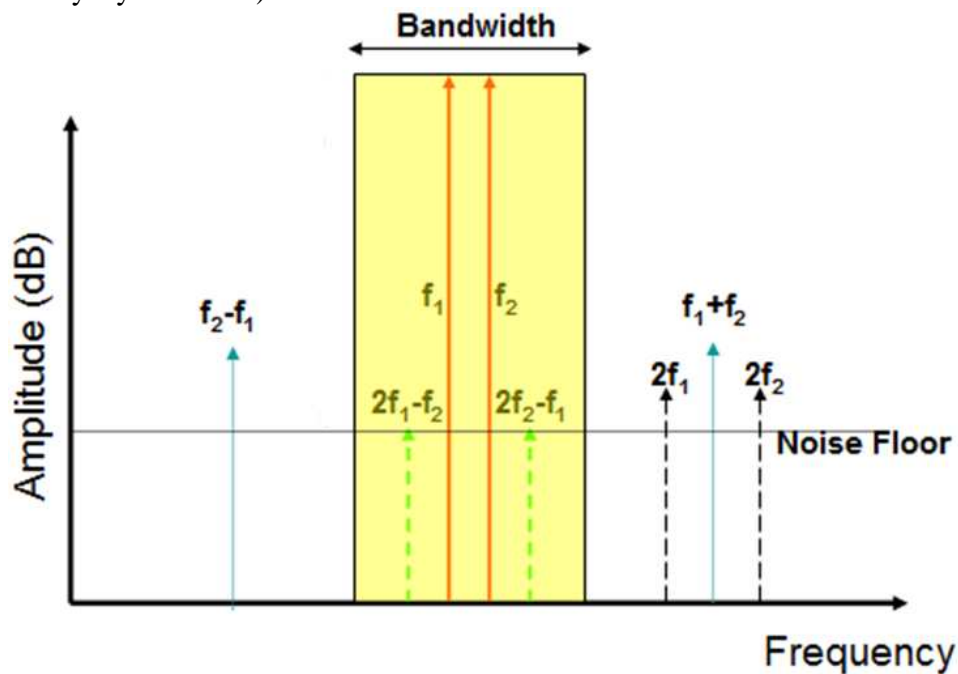


Fig 6.3 Spectrum plot of output RF signals from a component having a nonlinear transfer function

6.2.1 HARMONIC DISTORTION

Any transfer function $f(x)$ can be expanded in terms of a Taylor series as [2]

$$f(x) = 1 + \sum_{i=1}^{\infty} \frac{(x - \Delta h)^i}{i!} \left(\frac{d^i f}{dx^i} \right)_{x=\Delta h} \quad (6.8)$$

For a linear device, all derivatives of the transfer function, except $i=1$ are zero. Therefore, the output frequency follows the input frequency and no additional frequency terms are generated. In the case of a non-linear transfer function, the derivatives are non zero. Therefore, additional frequency components are generated in the output that differs

from the input frequency. If the additional components generated are such that they are integral multiples fundamental frequency, then these components represent harmonic (overtone) distortion. For example, if the fundamental frequency is f , then the harmonics occur at $2f, 3f, 4f \dots mf$ etc, where m is an integer. The harmonic distortion components are illustrated in Fig. 6.3 wherein two fundamental RF signals (represented with red arrows) with frequencies f_1 and f_2 respectively produce second harmonic distortion components $2f_1$ and $2f_2$ (represented with black dashed arrows). The higher order harmonic distortion components are not shown for clarity. The useful bandwidth of the analog system is also highlighted as a yellow box. If the bandwidth of the system is such that the harmonic distortion terms appear outside the bandwidth, then these components do not pose a problem for the system. If, however, the bandwidth of the system is large enough to accommodate these harmonic terms, then additional band-pass filters need to be used to eliminate these components. In practice, the bandwidth of systems is less than an octave, and therefore, the harmonic powers lie outside the bandwidth of the system and can be ignored.

6.2.2 INTERMODULATION DISTORTION

When two or more fundamental frequencies are present in the system, then apart from components generated at integral multiples of fundamental frequencies, additional components at the sum and difference of the any two fundamental frequencies also occur. These sum and difference frequencies (second order) can in turn generate additional sum and difference frequencies with other frequencies, providing components at sum and difference of twice one frequency and the other frequency (third order) and so on. These sum and difference frequency components are termed as intermodulation distortion components. It can be seen from Fig. 6.3 that the second order intermodulation

components for fundamental frequencies f_1 and f_2 occur at $(f_1 + f_2)$ and $(f_2 - f_1)$ (represented with blue arrows). These second order intermodulation terms usually lie outside the useful bandwidth of the system and can be filtered out. The third order intermodulation terms occur at $(2f_1 - f_2)$ and $(2f_2 - f_1)$ (represented with dashed green arrows). However, these third order intermodulation terms occur inside the useful bandwidth and can interfere with other useful signals at those frequencies. Therefore, it becomes necessary to evaluate third order intermodulation distortion and determine how these ‘spurious’ signals affect the working of the overall system.

6.3 Sources of distortion

Although noise in the system is present whether or not a signal source is present, distortion on the other hand is present only when at least one signal source is present. In our link, the optical signal from a CW laser source is modulated with the RF signal using an electro-optic modulator. The modulated optical carrier is then transmitted using the TTD lines and finally the optical signals are converted back to electrical signals at the photodetector. For the levels of optical power carried by the delay lines, they can be assumed to be linear devices. Therefore, the only sources of distortion in our link are the modulator and the photodetector. Usually, in such analog optical links, distortion due to modulator is more significant compared to that from the photodiode [1]. Therefore, distortion measurement based on modulator will be described in this chapter.

6.4 Harmonic distortion measurement

The schematic diagram of the setup shown in Fig. 6.1 can be used to measure the harmonic distortion in the highly dispersive photonic crystal fiber true time delay based phased array antenna system.

An RF signal at a frequency of 8.0GHz with a power of 1mW is generated using an HP 8510C network analyzer. Optical carrier from a tunable laser source with a wavelength of 1550nm is amplified using an Erbium-doped fiber amplifier (EDFA). The RF signal is modulated onto the amplified optical carrier using a Mach-Zehnder modulator. This modulated signal is passed through a TTD line comprising of 3.5m of NZ-DSF and 7.0m of highly dispersive PCF. After passing through the TTD line, the optical signal is converted to electrical signal using a photodetector and amplified using a low noise amplifier (LNA). The modulator bias is varied and the fundamental, second harmonic and the third harmonic powers are measured on the microwave spectrum analyzer and the measurement results are shown in Fig. 6.4.

It can be seen from the figure, that as the modulator bias is increased, the fundamental, second and third harmonic signal powers become oscillatory. This is because the transfer function of the modulator has a $(\cosine)^2$ relation. It can also be seen that at the bias points wherein the fundamental power is maximum, the second harmonic power is minimum. Therefore, by selecting the bias point as the maximum transmission point (quadrature), second harmonic terms can be minimized. However, the shape of the third order harmonic term follows that of the fundamental curve. It is possible to select a bias point to eliminate the second order term, but not the third

harmonic term as even the fundamental signal is minimum at the point of minimum third order power and is practically not useful.

In the PCF-TTD based phased array antenna system, the RF signals are in the X-band (8-12.5GHz). Therefore, the second and third harmonic components at 16GHz and 24GHz respectively lie outside the useful bandwidth of the system and hence can be neglected.

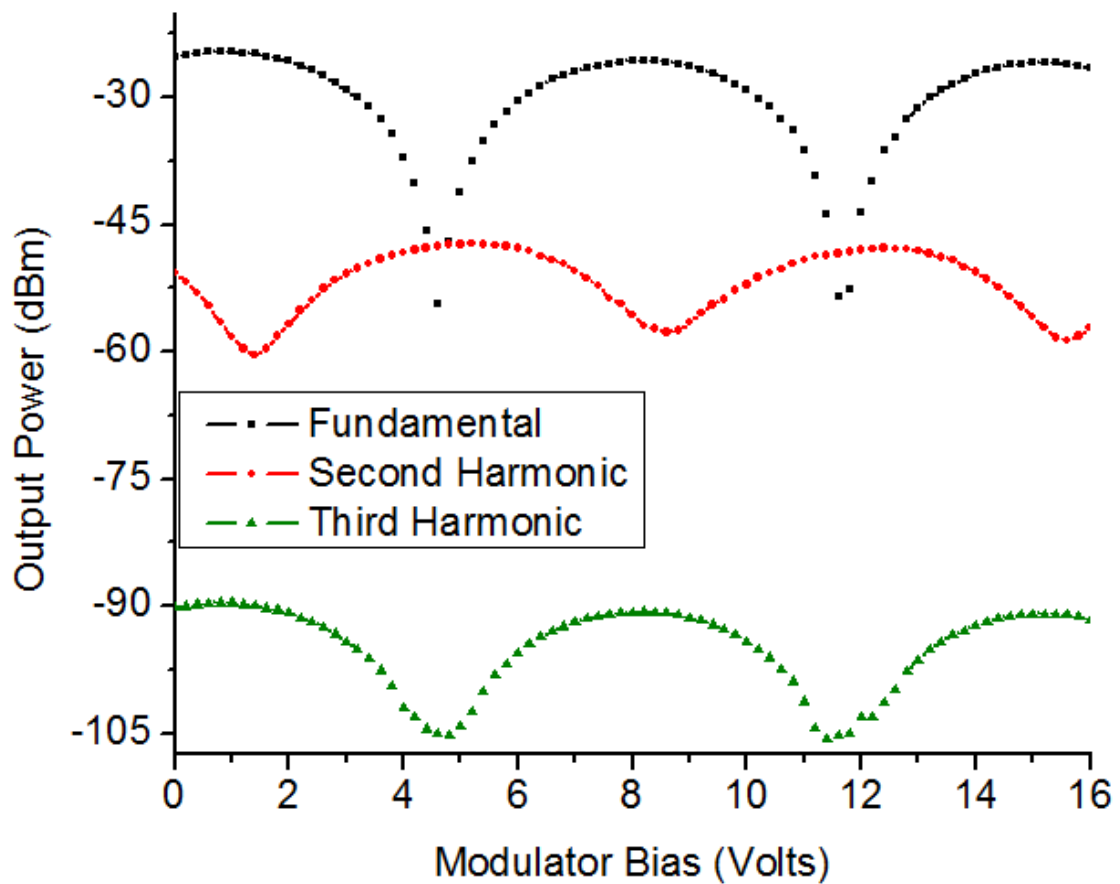


Fig. 6.4 Measured fundamental (black curve), second harmonic (red curve) and third harmonic (green) powers as a function of modulator bias

6.5 Intermodulation distortion measurement

It is clear from earlier discussion that the third order intermodulation distortion products are important in any system as they appear within the useful bandwidth of the system. For example, let us consider two closely spaced frequencies 9.0GHz and 9.1GHz respectively which are in the X-band. The third order intermodulation products occur at 8.9GHz and 9.2GHz. Both these terms also appear within the useful bandwidth of the system. If there are useful signals present at those frequencies, then these intermodulation terms can interfere with the useful signal. These intermodulation terms are also termed spurious as these are not the intended signals.

6.5.1 SPURIOUS-FREE DYNAMIC RANGE (SFDR)

A common way to measure distortion is to plot various output RF powers (fundamental, second order, third-order etc) as a function of input signal power on a log-log scale. The minimum power of the fundamental signal (P_{\min}) that the link can convey information is when the fundamental power is equal to the noise power. The maximum power of the fundamental signal (P_{\max}) that the link can convey information without producing intermodulation products is when the distortion power is equal to the noise power. Beyond this maximum input power, the distortion powers rise above the noise floor and become appreciable. A measure of the intermodulation distortion is given by the Spurious-Free Dynamic Range (SFDR) which is given by $P_{\max} - P_{\min}$. Since the SFDR is dependent on the noise power in the system, it is often convenient to provide the dynamic range in a 1-Hz bandwidth.

On the log-log plot, the slope of the fundamental signal is unity and that of the third-order IM is three. The slope of the lines gives the order of the output signal. A slope of unity indicates fundamental signal and a slope of three indicates third order terms. This means that the third-order intermodulation terms (IMD-3) rise or fall thrice as fast as the fundamental signal. Therefore, as the input power is increased, the intermodulation powers quickly rise above the noise floor. The point on the plot at which the fundamental and third order intermodulation output powers intersect is called the third-order intercept point (IIP3). The SFDR of an RF link limited by third-order intermodulation distortion is given by [3, 4]

$$SFDR = \frac{2}{3} * (IIP3 - (NF - 174)) \quad (6.9)$$

where IIP3 is the linearly extrapolated input power (in dBm) where the fundamental and third order curves intersect and NF is the link noise figure (in dB). The value of -174 refers to the noise power in dBm at a noise temperature of 290 K in a 1-Hz bandwidth.

6.5.2 SFDR MEASUREMENT

The experimental setup used to measure SFDR is shown in Fig. 6.5. An external cavity laser source emits an optical carrier with wavelength 1550nm with an output power of 5mW.

A high power Erbium-doped fiber amplifier (EDFA) from Amonics (which has a maximum output power of 1Watt) is used to amplify the optical input power as required and the amplified signal is passed through a polarization controller to the modulator. For the current measurement, the gain of the EDFA is set to provide an optical output power of 20mW. The closely spaced RF signals with frequencies 8GHz and 8.01GHz are

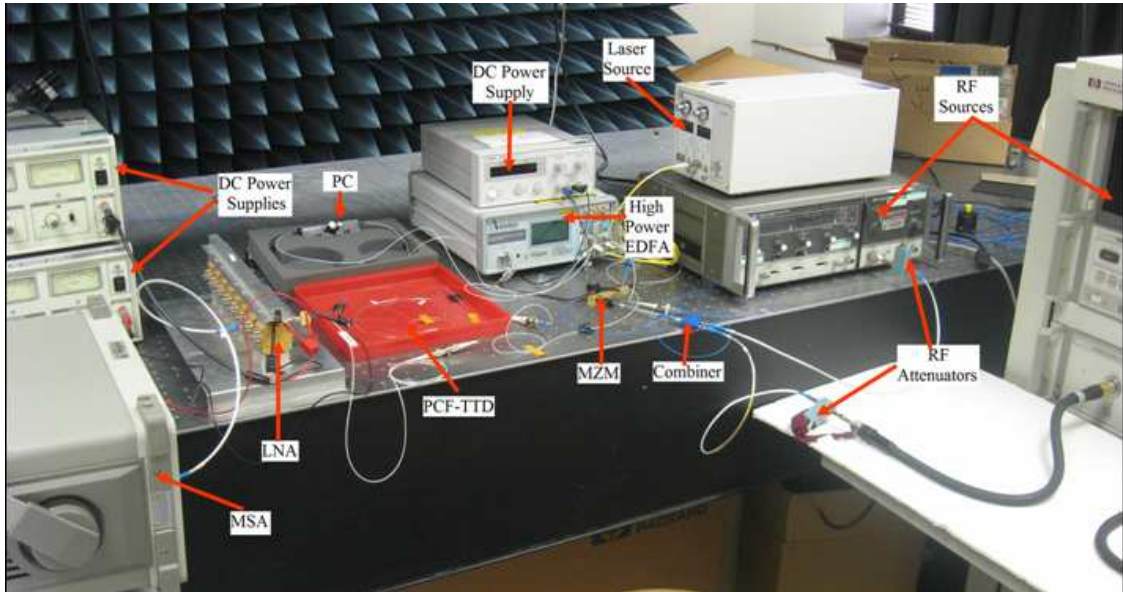


Fig. 6.5 Experimental setup for spurious-free dynamic range measurement. EDFA: Erbium-Doped Fiber Amplifier; MZM: Mach-Zehnder Modulator; TTD: True-Time-Delay; MSA: Microwave Spectrum Analyzer; LNA: Low-Noise Amplifier

generated by a HP 8620C sweep oscillator and HP 8510C network analyzer respectively. These signal powers are made equal and are combined using an RF combiner and modulated onto the optical carrier using a Lithium Niobate Mach-Zehnder modulator (MZM). The modulator bias is set for operation at quadrature. The modulated optical signal is then passed through the PCF-TTD line consisting of 3.5m of NZ-DSF and 7.0m of highly dispersive PCF.

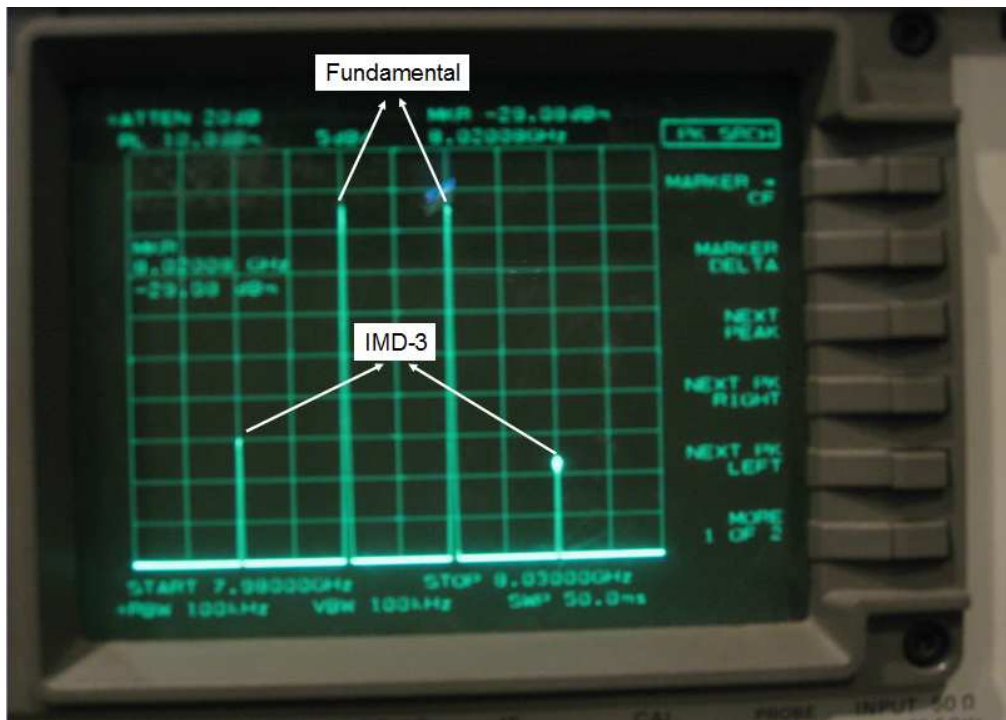


Fig. 6.6 Fundamental and IMD-3 output powers as observed on a microwave spectrum analyzer

A high speed photodetector is used to convert the optical signal to electrical signal. The electrical output signal is amplified using a low noise amplifier (LNA) and the various output RF powers are measured on a microwave spectrum analyzer (MSA). For the given fundamental frequencies, the third-order intermodulation products are generated at 7.99GHz and 8.02 GHz. The fundamental and IMD-3 products are shown in Fig. 6.6.

The fundamental input RF powers are changed and the corresponding fundamental and IMD-3 output RF powers are measured and the results are plotted in Fig. 6.7. The point of intersection of the fundamental RF output power line with the vertical axis at the point where the fundamental input RF power is 0dBm gives the RF

gain of the system. Therefore, the RF gain of our system is 11dB. The third-order intercept point (IIP3) is found to be 22dBm from the figure. The measured output noise spectral density is also shown in the figure as a horizontal line.

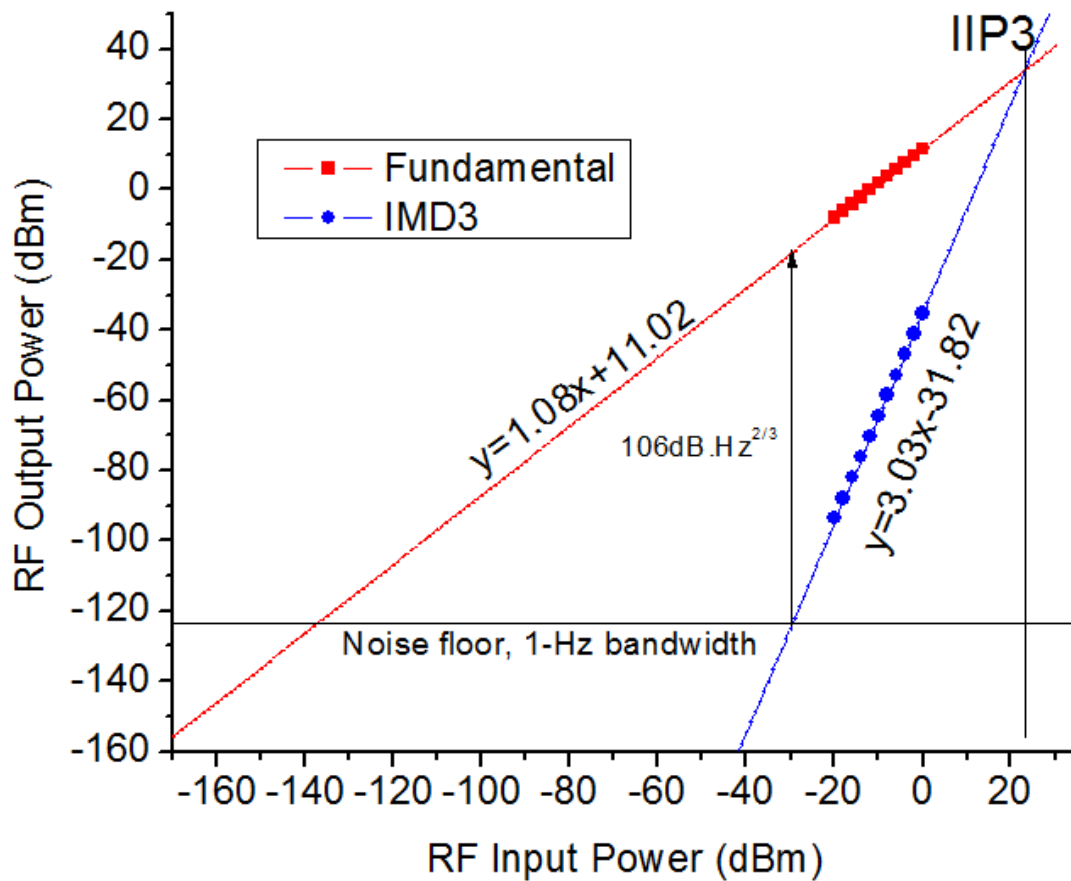


Fig. 6.7 Fundamental (red squares) and IMD-3 (blue circles) RF output powers as a function of input RF power. Optical input power of 20mW and modulator bias angle of 90 degrees are used. Extrapolated straight line fits to the data points are also shown. The extrapolated lines intersect at a point whose corresponding RF input power gives IIP3

For the operating conditions of 20mW input optical power and 90 degrees modulator bias, the noise figure of the system can be obtained from Fig. 6.2 as 37dB.

Using the values of IIP3 and NF, the SFDR of the system can be calculated using equation (6.9) as 106dB measured in a 1-Hz bandwidth ($106\text{dB}\cdot\text{Hz}^{2/3}$)

6.6 Improving SFDR using high power Erbium-doped fiber amplifier

In this section, the principle of operation and the experimental results of a method to improve the SFDR using a very high power EDFA and bias-shifted operation is demonstrated.

6.6.1 PRINCIPLE OF OPERATION

In section 6.1.2, it was stated that there is a decrease in the gain of the system as the modulator bias is changed from quadrature (90 degrees) to transmission minimum (180 degrees). However, this decrease in gain can be compensated by increasing the optical input power to the modulator. For example, in our system, an optical input power of 20 mW at a bias angle of 90° and an optical input power of 200mW at a bias angle of 165° both result in approximately the same gain. By operating close to 180° , the received photocurrent also reduces. This reduces the shot noise power density as it is proportional to the received photocurrent. The RIN and signal-spontaneous beat noise power densities are proportional to the square of the received photocurrent. Shot noise, RIN, and signal-spontaneous beat noise fall faster compared to the gain as the modulator bias angle is adjusted towards 180° [5]. At any given optical input power, there will be a modulator bias angle that minimizes the link noise figure and therefore, the optical input power can be increased and the bias angle shifted in order to minimize noise figure without reducing link gain.

6.6.2 EXPERIMENTAL RESULTS

The optical power from the EDFA is changed to 20mW, 100mW, 150mW and 200mW by adjusting the gain of the EDFA. The gain method described above is used to measure the Noise Figure at each of the four optical powers by changing the modulator bias voltage. The measured noise figures as a function of modulator bias angle for various optical input powers to the MZM are shown in Fig. 6.8 [6].

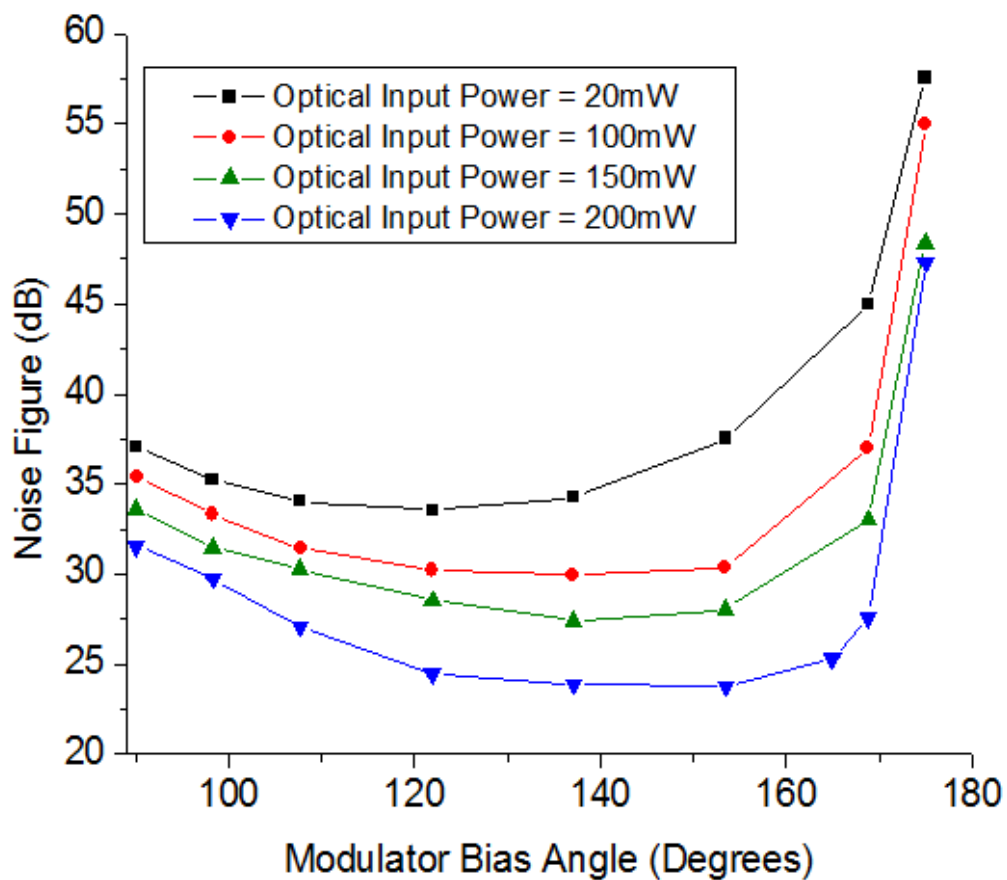


Fig. 6.8 Measured link noise figure as a function of modulator bias angle for different optical input powers

By increasing the optical input power to the modulator, the gain can be increased and this can be used to compensate for the reduction in gain due to shift in modulator bias angle. For example, in our system, an optical input power of 20 mW at a bias angle of 90° and an optical input power of 200mW at a bias angle of 165° both result in approximately the same overall gain. However, the NF can be reduced from 37 dB at quadrature for 20mW optical power input to 25.7 dB at a bias angle of 165° for 200mW optical input power.

For a modulator optical input power of 200mW, the link noise figure can be reduced from 31.55dB at quadrature to a minimum of 23.47dB at a bias angle of 153° . The experiment is performed with an optical input power to the modulator of 200mW and at a modulator bias angle of 153° , which provides the minimum NF. The fundamental frequencies used are at 8GHz and 8.01GHz. Therefore, the third order intermodulation products (IMD-3) are located at 7.99GHz and 8.02GHz respectively. Like in section 6.5.2, the fundamental input RF power is varied and the fundamental and IMD-3 output RF powers are measured on the MSA. The result is shown in Fig. 6.9. The IIP3 value from the graph is obtained as 22 dBm. The link gain is 13 dB and the link noise figure is 23.47 dB. The combination of IIP3, noise figure and equation (6.9) results in an SFDR of 115 dB, normalized to a 1-Hz bandwidth. For a system using Mach-Zehnder modulator, the IIP3 only depends on the half wave voltage of the MZM and is independent of the optical input power and the modulator bias voltage as the half wave voltage determines the ratio of the fundamental and third order products for a particular input signal value [1].

It can be seen that the improvement in the SFDR of the system from $106\text{dB}\cdot\text{Hz}^{2/3}$ to $115\text{dB}\cdot\text{Hz}^{2/3}$ can be achieved by simply controlling the dc modulator bias and using a very high power EDFA without using any other optical or electronic linearization schemes. Although the EDFA can provide up to 1W of optical power, the fundamental limitation in achieving very high SFDR is the optical power handling capacity of the modulator, which is 200mW for our device. Utilizing higher power handling MZMs, the SFDR can further be improved.

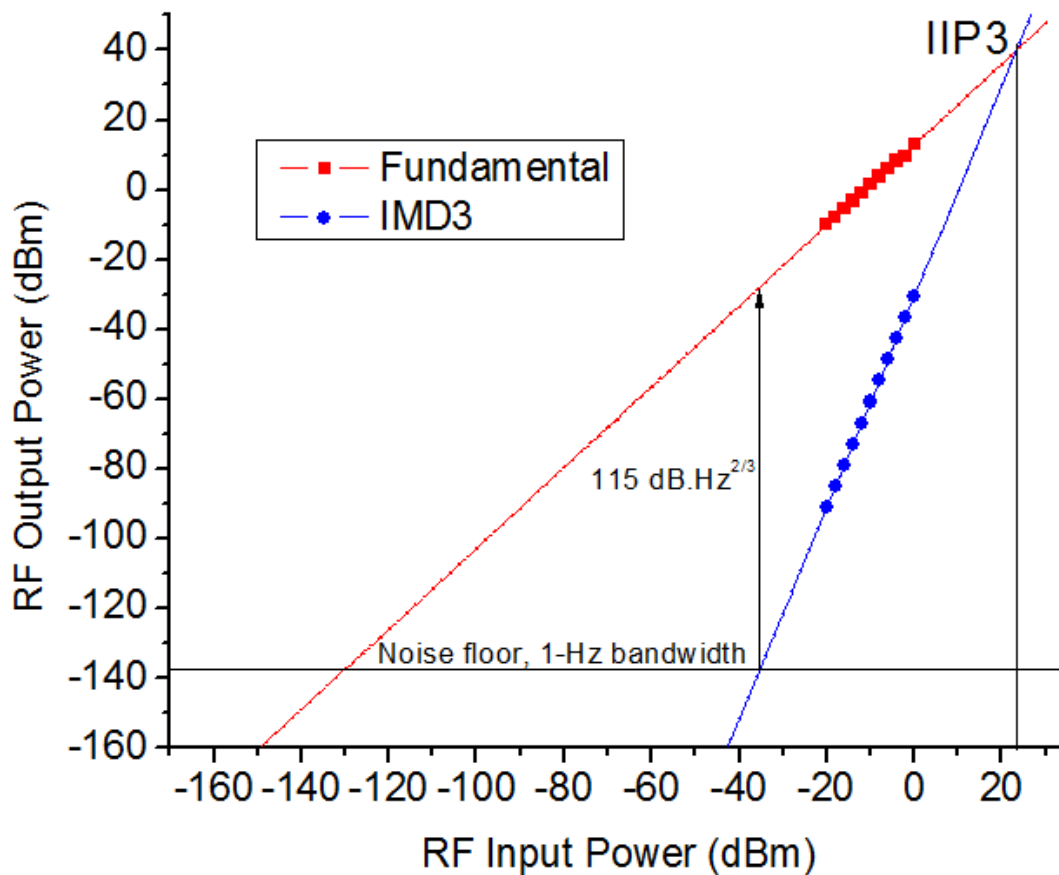


Fig. 6.9 Fundamental (red squares) and IMD-3 (blue circles) RF output powers as a function of input RF power. Optical input power of 200mW and modulator bias angle of 153 degrees are used. Extrapolated straight line fits to the data points are also shown. The extrapolated lines intersect at a point whose corresponding RF input power gives IIP3

6.7 Summary

In this chapter, RF performance characterization of the PCF TTD-based phased array antenna system was performed. Experiments were performed to evaluate the noise performance and distortion characteristics of the system by measuring the noise figure and harmonic distortion. An important parameter related to the performance of the system, namely the Spurious-Free Dynamic Range (SFDR) was presented and measured to be 106dB for the system with 20mW optical input power to the modulator at quadrature in a 1-Hz bandwidth. The SFDR of the system was improved using a high power EDFA and bias shifted operation. SFDR as high as 115dB in a 1-Hz bandwidth was achieved for an optical power input of 200mW and bias shifted to 153 degrees.

6.8 References

- [1] C. H. Cox, *Analog Optical Links: Theory and Practice*. Cambridge, U.K. Cambridge Univ. Press (2004)
- [2] P. Dienes, *The Taylor Series, An Introduction to the Theory of Functions of a Complex Variable*, Clarendon Press, Oxford (1931), reprint: Dover, New York (1957)
- [3] A. Karim and J. Devenport, "High Dynamic Range Microwave Photonic Links for RF Signal Transport and RF-IF Conversion," *J. Lightwave. Technol.* **26**, pp. 2718-2724 (2008)
- [4] A. Karim and J. Davenport, "Noise Figure Reduction in Externally Modulated Analog Fiber-Optic Links," *IEEE. Photon. Technol. Letts.* **19**, pp. 312-314 (2007)
- [5] G. E. Betts, J. P. Donnelly, J. N. Walpole, S. H. Groves, F. J. O'Donnell, L. J. Missaggia, R. J. Bailey, and A. Napoleone, "Semiconductor laser sources for externally modulated microwave analog links," *IEEE Trans. Microw. Theory Tech.* vol. **45**, pp. 1280-1287 (1997)
- [6] H. Subbaraman, M. Y. Chen, and R. T. Chen, "Spurious-Free Dynamic Range (SFDR) improvement in a true-time-delay system based on highly dispersive

photonic crystal fiber,” in IEEE/LEOS Winter Topical Meeting Series, pp. 58-59, Innsbruck, Austria (2009)

Chapter 7 X-band Sparse Array Antenna Demonstration

In this Chapter, the need to use a sparse array antenna for modern applications will be briefly discussed. Characteristic features of such antennas along with simulation results will be provided. Using the PCF-TTD module, experiment will be setup and preliminary beam steering results will be demonstrated for an X-band sparse array using 3 horn antennas which is equivalent to a 29 element standard array. Due to the limitation of the lengths of PCF in the TTD module, wider steering angles cannot be demonstrated. Therefore, another dispersive fiber module will be constructed using dispersion compensation fibers and the sparse array beam steering will be demonstrated.

7.1 Why do we require a sparse array?

A standard antenna array consists of antenna elements which are spaced half a wavelength apart according to the relation given in equation (1.11) in order to avoid grating lobes. In order to achieve a very narrow beam, a very large array needs to be used as the beam width is inversely proportional to the size of the array [1]. However, the weight and size of the antenna elements becomes extremely critical for applications such as phased array radar and satellite communications. Therefore, it becomes very important to be able to synthesize the required radiation pattern by using a minimum number of antenna elements. Also, the use of such a sparse array will eliminate complex computational capability that would otherwise be required in a standard array consisting of a large number of elements. The reduction in the number of elements also reduces the cost and the eases the construction of the array. It is possible to create an antenna array

with fewer elements to produce narrow beam widths. Such antenna arrays are called sparse antenna arrays.

7.1.1 SIMULATION RESULTS

The simulated array factor of a 100 element standard antenna array is shown in Fig. 7.1. The inter-element spacing is equal to half wavelength at 12.5GHz. The normalized pattern for a beam radiated broadside is shown. It can be seen from the figure that the large array provides a characteristic narrow ‘pencil’ like beam. However, such an array is not only cost prohibitive, but is also heavy and congested. Complex computation for large number of signals received from all the elements is also required.

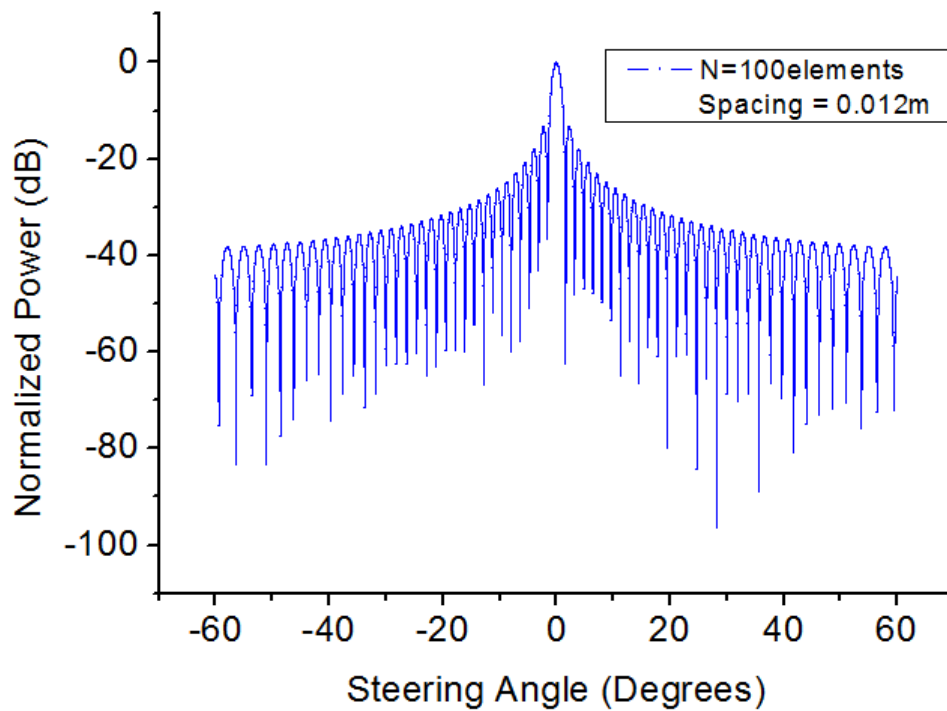


Fig. 7.1 Array factor simulation of a 100 element standard array with inter-element spacing $d = \frac{\lambda}{2}$ at 12.5GHz

In order to reduce the number of antenna elements in the array, we can either reduce the size of the array or increase the spacing between elements. By reducing the size of the array, we have a negative effect on the angular resolution, since a reduction in size shows up as a reduction in angular resolution (broader beam width). This is not desirable because high angular resolution is often required for various applications. Increasing the spacing between elements therefore becomes the only option available. However, by increasing the spacing between elements to values over half a wavelength, we introduce grating lobes. These grating lobes have the same amplitude as that of the desired main beam. The effect of increasing the spacing between elements on the array radiation pattern is shown in Fig. 7.2.

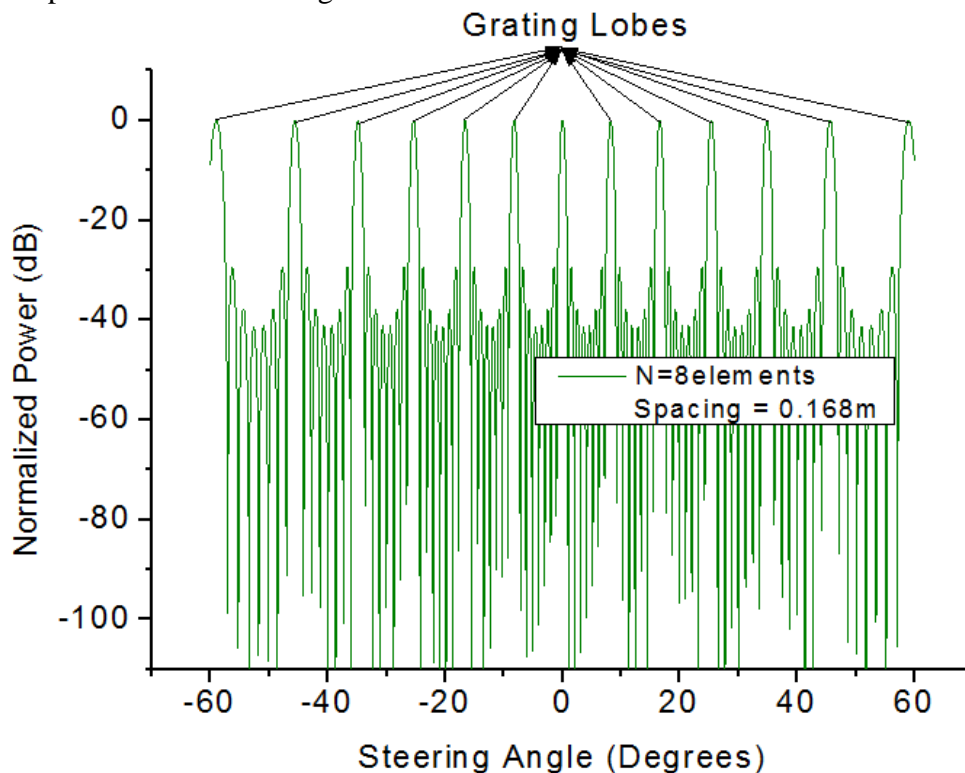


Fig. 7.2 Array factor simulation of an 8 element sparse array with inter-element spacing

$$d = 14 * \frac{\lambda}{2} \text{ at } 12.5\text{GHz}$$

The figure shows the normalized array factor of a sparse array consisting of 8 elements with inter-element distance equal to $14 * \frac{\lambda}{2}$. The overall dimension of the array is approximately equal to that of a standard 100 element array. It can be seen from the figure that although the beam width of the central beam at 0 degree steering angle is small, there are several lobes which have almost the same characteristics as that of the desired beam. These grating lobes or aliases occur at equal angle separations and are undesirable and hence need to be minimized or eliminated.

The overall far-field radiation pattern is obtained by multiplying the array factor with the antenna element pattern. If however, we choose an antenna element radiation pattern that has nulls at the places where there are grating lobes in the array factor, then the grating lobes can be totally eliminated. However, such an array antenna can only radiate broadside without grating lobes and the antenna head has to be rotated mechanically in order to steer the beam. This is because, if the beam is steered electronically, then the nulls do not exactly line up with the grating lobes, and the effect of grating lobes starts getting predominant. Mechanically moving the antenna array head defeats the purpose of a phased array antenna which has the advantage of beam steering without mechanical movement of the antenna array.

It is possible to form a sparse array wherein the antenna elements are aperiodically spaced [2-3]. Due to non-uniform antenna element spacing, the grating lobes no longer appear at equal angle separations. The grating lobes become wider and less sensitive. Many groups [4-7] have demonstrated sparse arrays designed with aperiodic spacing with reduced grating lobe levels.

In this chapter, preliminary work on the use of highly dispersive photonic crystal fibers and another highly dispersive fiber TTD module for a 3 element periodically spaced X-band sparse array are presented. The three elements are spaced to imitate a 29 element standard array. A three element sparse array is chosen because of the limitation of availability of minimum far-field distance in the laboratory.

7.2 Sparse Array Antenna

The X-band sparse antenna array constructed using 3 horn antenna elements is shown in Fig. 7.3. The base plate is fixed on a precision rotation stage.

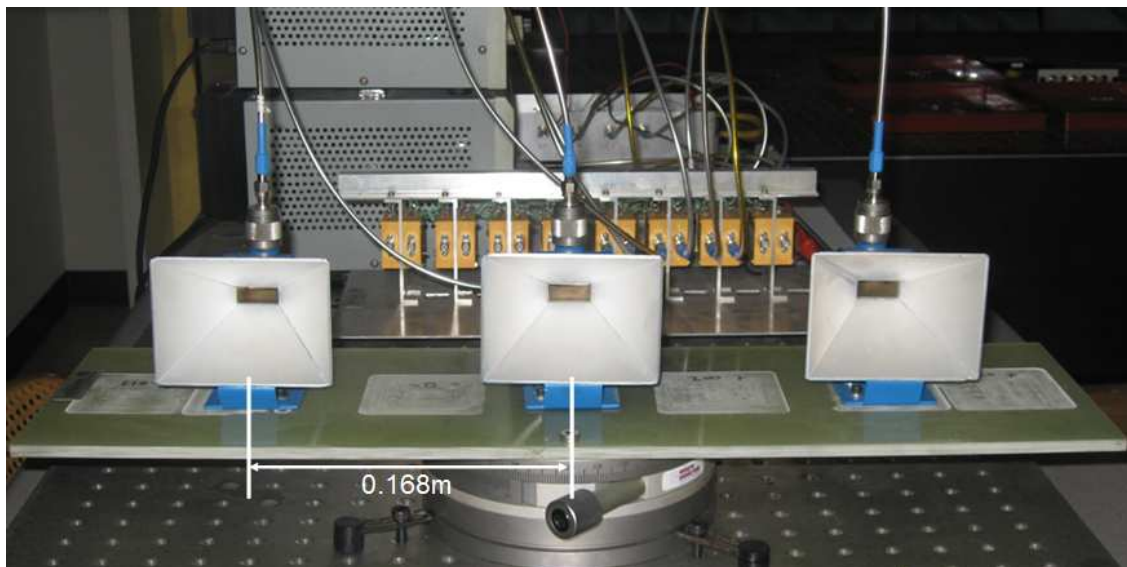


Fig. 7.3 X-band sparse array antenna consisting of three periodically spaced horn antennas spaced 0.168m apart, equivalent to a 29-element standard array (precision rotation stage is also shown)

The antenna element has a gain of 6dB. The three horn antennas are spaced 0.168m apart, and this is equivalent to a 29 element standard array. In order to ascertain the frequency of maximum transmission, the reflection coefficient (S_{11}) of 3 antenna

elements as a function of frequencies is measured using the network analyzer. The measured result is shown in Fig. 7.4. It can be seen from the figure that minimum reflections (minimum S_{11}) occur near 9GHz and 10GHz. Therefore, all experiments are performed at these two frequencies.

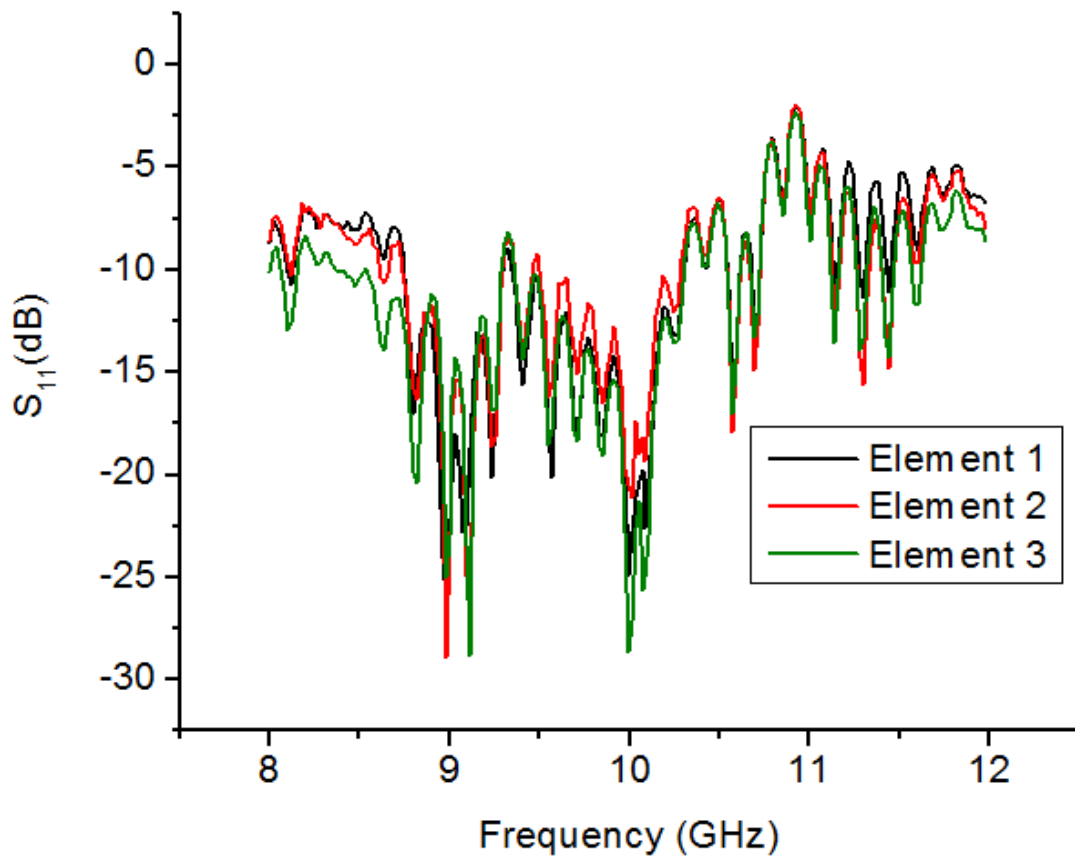


Fig. 7.4 Measured S_{11} parameter of three antenna elements

In order to simulate the far-field radiation pattern, the element pattern needs to be incorporated into the simulation. By multiplying the simulated array factor with a measured element pattern, the far-field radiation pattern of the sparse array can be simulated. In order to measure the element pattern of the antenna element, the antenna is

placed on a precision rotation stage and the radiated power is measured using the MSA at a distance greater than the antenna's far-field as a function of angle. The element patterns of the antenna element are measured at 9GHz and 10GHz and are shown in figures 7.5(a) and 7.5(b) respectively.

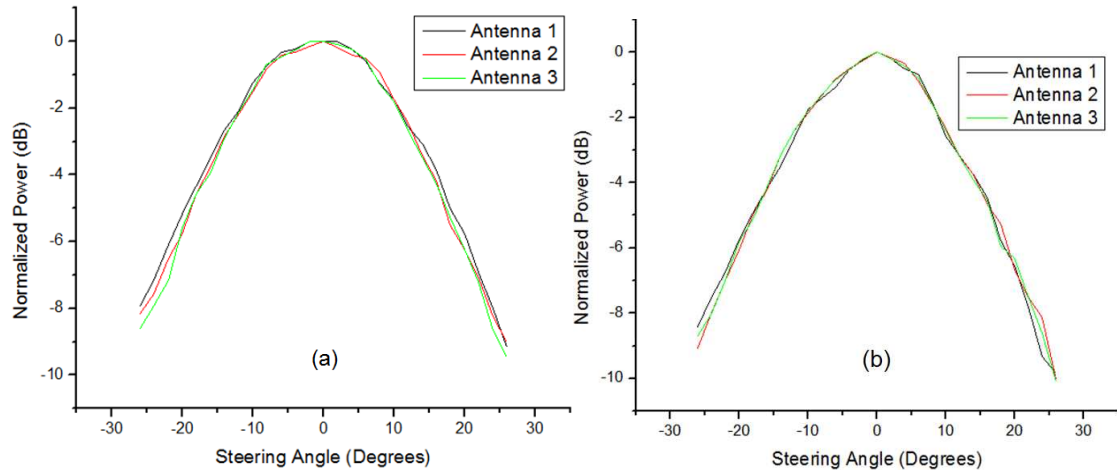


Fig. 7.5 Measured normalized patterns of 3 antenna elements at a frequency of (a) 9GHz and (b) 10GHz

Compared to the element pattern of the patch antenna that was shown in Fig. 4.3, the radiation pattern of the horn antenna has a strong dependence on the steering angle. Therefore, the beams at larger angles experience suppression compared to beams closer to broadside. This element pattern acts as a filter at larger angles and so, the desired beam at larger angles will have a lower power.

7.3 Highly dispersive PCF TTD based sparse array system

Since one of the primary objectives of a sparse array system is to reduce the size and weight of the system, the sparse array system can greatly benefit from highly dispersive photonic crystal fibers. In order to demonstrate the working of the sparse

array, the same schematic as shown in Fig. 4.1 can be used. The three adjacent delay lines consisting of 0m, 3.5m, and 7.0m PCF segments with 10.5m, 7.0m, and 3.5m NZ-DSF segments respectively are used. The standard X-band patch element antenna array is replaced with the X-band horn element sparse array of Fig. 7.3.

From the time-delay experiment results shown in Chapter 3, the PCF-TTD modules can provide continuous time delay differences (τ) from -28.3ps to 31.3ps by tuning the optical wavelength from 1530nm to 1560nm.

For the sparse array, antenna element spacing (d) is equal to 0.168meters and using equation (4.1) continuous steering angles (θ) from $\sim -3^\circ$ at 1530nm to $\sim +3^\circ$ at 1560nm can be obtained.

In the experiment, a 9GHz RF signal from HP8510C network analyzer is modulated on an optical carrier with a wavelength 1559.9nm. The transmitted RF signal from the X-band sparse antenna array is received by the receiving horn antenna, which is placed at a distance greater than the far-field distance (~ 24 meters). The antenna head is rotated on a precision micro-rotation stage and the received power at the horn antenna is measured as a function of the steering angle on the microwave spectrum analyzer. The measured power points (marked as red filled circles) of the 9GHz signal is shown in Fig. 7.6(a).

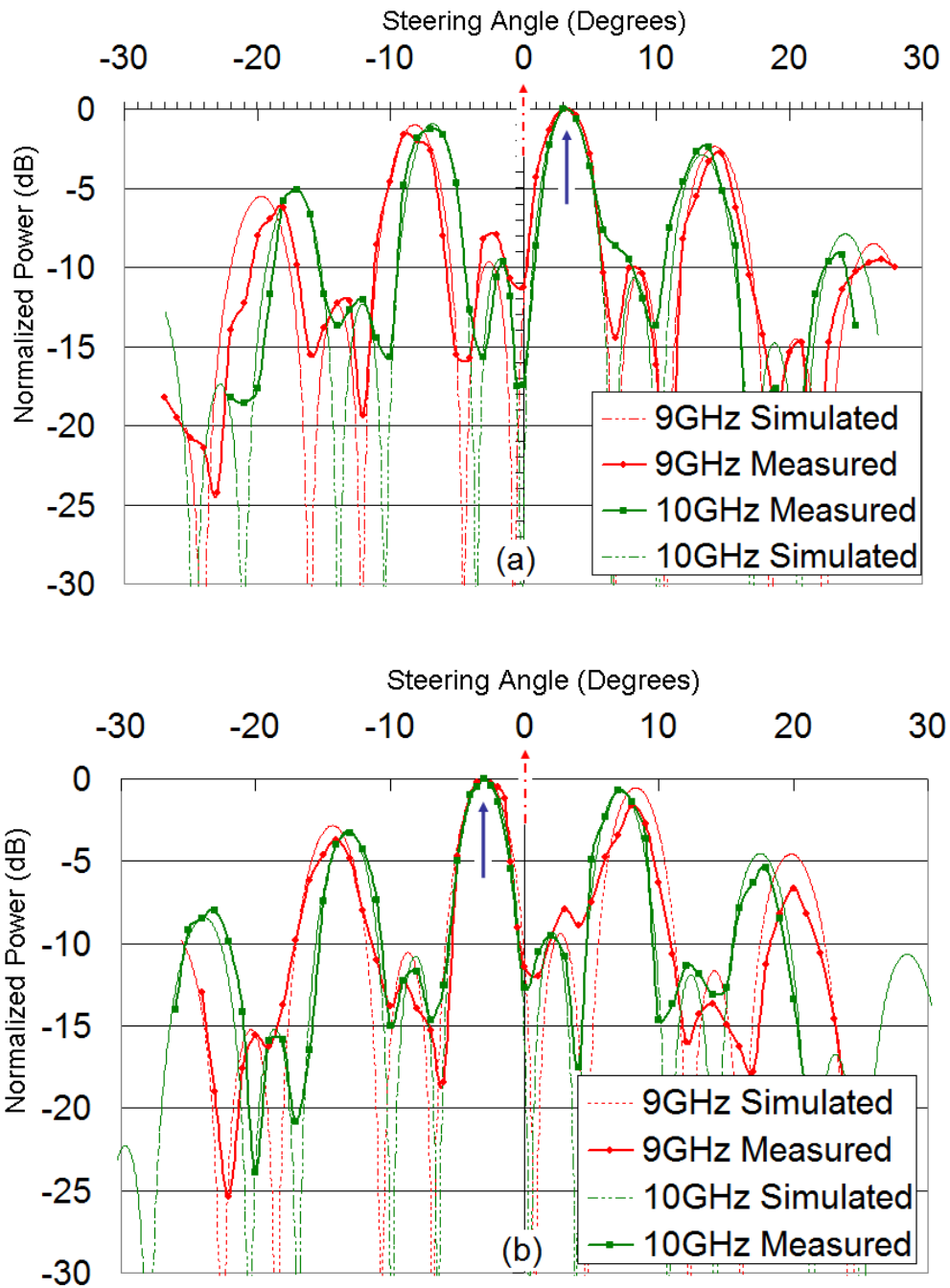


Fig. 7.6 Simulated and Measured far-field radiation patterns of the sparse array antenna at an optical wavelength of (a) 1559.9nm corresponding to +3degree beam steering and (b) 1529.9nm corresponding to -3degree beam steering (blue arrows indicate the desired beam, dashed red arrows at 0degree indicate the beam steering angle at center wavelength of 1545nm)

Similarly, the experiment is also performed for a 10GHz signal. The measured far field radiation pattern points (marked as green squares) of a 10GHz signal modulated on an optical carrier with wavelength 1559.9nm is shown in the same figure. The simulated far field radiation patterns are shown in figure as dashed curves. The far-field radiation patterns at the two frequencies are also measured by tuning the optical wavelength to 1529.9nm and the result is shown in Fig. 7.6(b). In both the figures, the desired beam is marked with a blue arrow. At the central wavelength of 1545nm, the desired beam would be directed at 0 degrees (indicated by dashed red arrows).

It can be seen from the figures that the maximum transmitted power occurs at +3 degrees at a wavelength of 1559.9nm and -3 degrees at a wavelength of 1529.9nm respectively, for 9GHz and 10GHz signals, thus showing a beam squint free operation. The different grating lobes that occur due to the spacing of the antenna elements are also evident. These lobes are lower in amplitude compared to the main lobe due to the filtering action of the horn element pattern. However, due to the limitation in the maximum achievable time delay due to the available length of PCF in the TTD modules, angles beyond 3 degrees from the sparse array system cannot be demonstrated using PCF-TTD module.

7.4 Highly dispersive fiber-based sparse array antenna system

In order to demonstrate angles greater than ± 3 degrees, we constructed another true-time-delay module with 4 delay lines, each consisting of a length of dispersion compensation fiber (Corning[®] Vast Dispersion Compensating Fiber) connected to a length of NZ-DSF (Corning[®] LEAF fiber). The total length of fibers (DCF and NZ-DSF)

in each delay line is equal to 720meters. The lengths of DCF in the 4 lines are 0m, 230m, 460m, and 690m. The dispersion coefficient of the DCF is equal to -120.5 ps/nm/km at 1545nm.

7.4.1 TIME DELAY MEASUREMENT

In order to obtain the chromatic dispersion of the DCF, the time delay difference (ΔT) between optical wavelengths of $\lambda \pm 0.1 \text{ nm}$ was measured at each wavelength according to the setup explained in [8]. The delay line consisting of 690m of DCF and 30m of NZ-DSF was used for this purpose. In order to measure the time delay difference, the phase difference as a function of microwave frequency is measured at optical wavelengths of $(\lambda + 0.1 \text{ nm})$ and $(\lambda - 0.1 \text{ nm})$. The slope of the phase versus frequency curve gives the time delay. The dispersion coefficient is calculated using

$$D = \Delta T / (\Delta \lambda \cdot L) \quad (7.1)$$

where $\Delta \lambda$ is the wavelength difference = 0.2 nm and L is the length of DCF = 690m (contribution to time delay difference from non-zero dispersion shifted fiber is negligible). The measured group velocity dispersion curve as a function of wavelength is shown in table 7.1.

Using the dispersion coefficient values and equations (1.14) and (1.20), the steering angles can be calculated at a central wavelength chosen as 1555nm. A TTD module consisting of 3 delay lines if formed by connecting different lengths of DSF with different lengths of NZ-DSF in each line.

Table. 7.1 Measured dispersion coefficient of the DCF

Wavelength (nm)	Measured dispersion coefficient (ps/nm/km)
1545	-120.724
1550	-121.6
1555	-125
1560	-127.8
1565	-129.7
1570	-134.4

7.4.2 EXPERIMENTAL SETUP

The experimental setup used to demonstrate sparse array antenna operation using the above fibers is shown in Fig. 7.7. Optical carrier from an external cavity tunable laser source (Santec ECL-200) is modulated with an X-band RF signal generated by HP 8510C vector network analyzer, using a high speed Lithium Niobate (LiNbO₃) modulator. The modulated optical signal is amplified using an Erbium-doped fiber amplifier (EDFA) and this amplified signal is split into 3 channels using a 1-to-3 optical power splitter and distributed to three TTD lines. The compositions of the three delay lines are: 720m NZ-DSF + 0m DCF; 490m NZ-DSF + 230m DCF; 260m NZ-DSF + 460m DCF.

The total length L , of each delay line is 720 meters. The lengths are chosen such that at a wavelength of 1555nm, the nominal delay through each TTD line is the same. This implies that at 1555nm, the RF signal is radiated broadside at the X-band (8-12.5GHz) antenna array. At any other wavelength, the beam is steered to a different

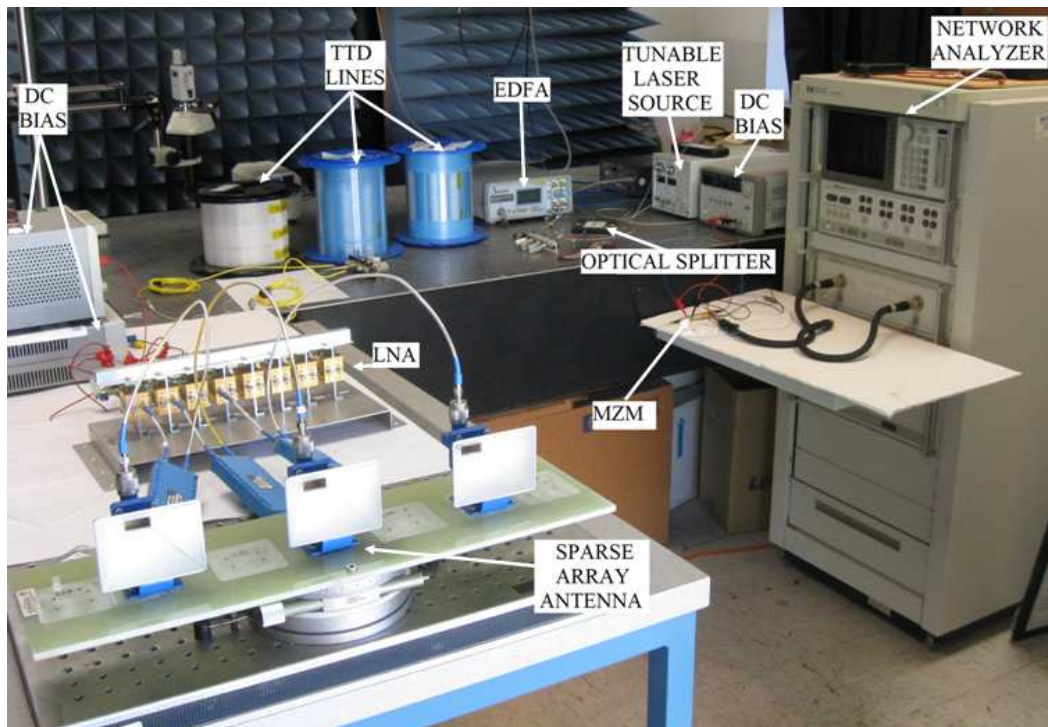


Fig. 7.7 Experimental setup for sparse array antenna demonstration, LNA: low-noise amplifier; MZM: Mach-Zehnder modulator; TTD: true-time-delay

direction depending on the time delay differences between adjacent delay lines. A photodetector bank converts the optical signals into electrical signals. Electrical tunable delay lines are used to fine tune the delays such that the delay through all TTD lines are equal at a wavelength of 1555nm. These signals are then amplified by an X-band low noise amplifier (LNA). After amplification, the electrical signals are fed to the 3 horn antenna elements of an antenna array, which has an element spacing of 0.168m. The far field radiation pattern of the X-band PAA is measured by fixing the antenna array on an accurate positioner and measuring the received power by a fixed standard horn antenna connected to a microwave spectrum analyzer (MSA) at a distance greater than the far-field distance.

7.4.3 FAR-FIELD RADIATION PATTERN

In the experiment, a 9GHz RF signal from HP8510C vector network analyzer is modulated onto an optical carrier with a wavelength 1558.65nm. The transmitted RF signal from the X-band sparse antenna array is received by the receiving horn antenna, which is placed at a distance greater than the far-field distance (~ 24 meters). The antenna head is rotated on a precision micro-rotation stage and the received power at the horn antenna is measured as a function of the steering angle on the microwave spectrum analyzer.

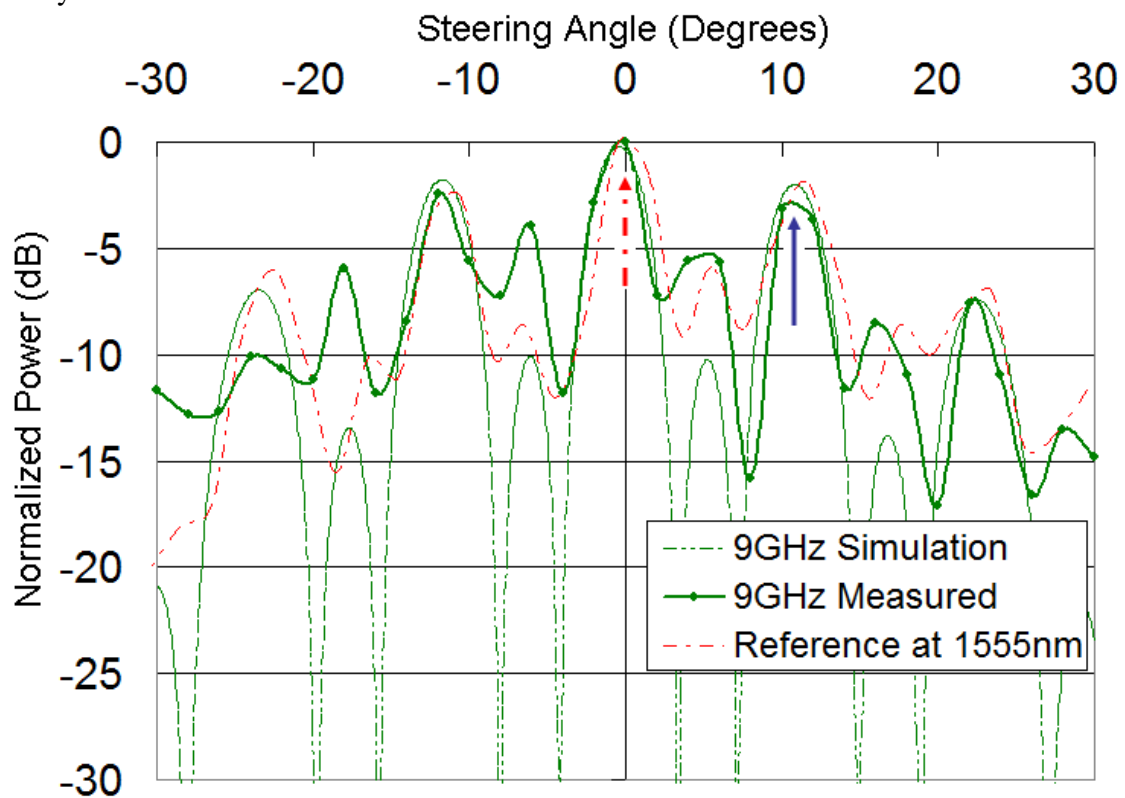


Fig. 7.8 Simulated (dashed curve) and Measured (curve marked with data points) far-field radiation patterns of the sparse array antenna at an optical wavelength of 1558.65nm corresponding to +11degree beam steering of a 9GHz RF signal (blue arrow indicates the desired beam). Measured pattern at central wavelength of 1555nm is also shown as a dashed red curve with peak at 0 degrees indicated by a red arrow

The far field radiation pattern of a 9GHz signal at the central wavelength of 1555nm is measured and the result is shown in Fig. 7.8 by a dashed red curve. It can be seen that the central wavelength, the beam is steered to 0° as indicated by a dashed red arrow. Next, the far field radiation pattern is measured by tuning the wavelength to 1558.65nm. It can be seen that the beam is steered to $+11^{\circ}$ (marked by a blue arrow). The simulated and measured patterns are shown by dashed and solid green patterns, respectively. Unequal levels of the intended main lobe (indicated by a blue arrow) and the grating lobes are due to the filtering action of the horn antenna radiation pattern. The individual horn element pattern is measured separately and included in the simulation. It can be seen from the figure that the measured and simulated curves agree well with each other. Beam squint-free operation is also demonstrated by steering 9GHz and 10GHz signals to -15° (with respect to 0° at 1555nm) by tuning the wavelength to 1550nm as shown in Fig. 7.9. The intended beam (indicated by blue arrow) has peak at -15° .

By employing highly dispersive photonic crystal fibers along with a properly designed aperiodic sparse array antenna, the size and weight of the system along with the levels of grating lobes can be reduced, thus providing a very useful system for air-borne and satellite applications. In this work, we designed a simple sparse array with periodic spacing between elements to show the working of the sparse array system.

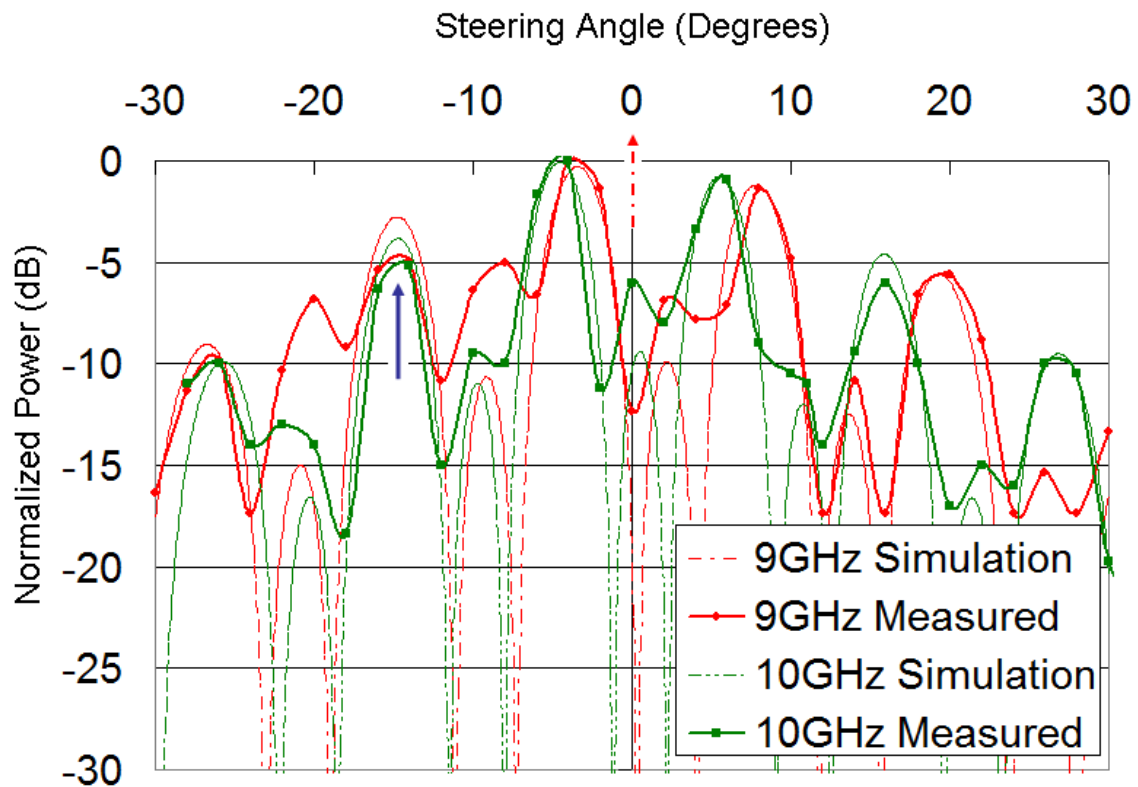


Fig. 7.9 Simulated (dashed smooth curves) and Measured (curves marked with data points) far-field radiation patterns of the sparse array antenna at an optical wavelength of 1550nm corresponding to -15degree beam steering of a 9GHz (red curves) and a 10GHz RF signal (green curves)

7.5 Summary

In this chapter, the need for a sparse array antenna was briefly discussed. An X-band sparse array antenna was constructed using 3 horn antenna elements with spacing such that the array was equivalent to a 29 element standard array. The working of the sparse array was shown by utilizing PCF-TTD module and demonstrating beam steering of two frequencies, 9GHz and 10GHz, to +3 degrees and -3 degrees by tuning the wavelength to 1559.9nm and 1529.9nm respectively. Another TTD module was created using dispersion compensation fibers and NZ-DSF fibers and beam steering results

beyond ± 3 degrees were demonstrated. 9GHz and 10GHz RF signals were steered to -15 degrees and +11 degrees by tuning the wavelength to 1550nm and 1558.65nm respectively. Such a sparse antenna array has the potential to reduce the size and weight of future systems.

7.6 References

- [1] H. J. Visser, *Array and Phased Array Antenna Basics*, John Wiley and Sons Ltd (2005)
- [2] Y. Liu, Z. Nie, and Q. Liu, "Reducing the number of elements in a linear antenna array by the matrix pencil method," *IEEE. Trans. Antennas. Propag.* vol. **56**, pp. 2955-2962 (2008)
- [3] B. P. Kumar and G. R. Branner, "Design of Unequally Spaced Arrays for Performance Improvement," *IEEE. Trans. Antennas. Propag.* vol. **47**, pp. 511-523 (1999)
- [4] R. L. Haupt, "Thinned arrays using genetic algorithms," *IEEE Trans. Antennas. Propag.* vol. **42**, pp. 993-999 (1994)
- [5] M. G. Bray, D. H. Werner, D. W. Boeringer, and D. W. Machuga, "Optimization of thinned aperiodic linear phased arrays using genetic algorithms to reduce grating lobes during scanning," *IEEE. Trans. Antennas. Propag.* vol. **50**, pp. 1732-1742 (2002)
- [6] T. G. Spence and D. H. Werner, "Design of Broadband Planar Arrays Based on the Optimization of Aperiodic Tilings," *IEEE. Trans. Antennas. Propag.* vol. **56**, pp. 76-86 (2008)
- [7] D. S. Goshi, K. M. K. H. Leong, and T. Itoh, "A Sparsely Designed Retrodirective Transponder," *IEEE. Antennas. Wireless. Propag. Letts.* vol. **5**, pp. 339-342 (2006)
- [8] B. Howley, Z. Shi, Y. Jiang, and R. T. Chen, "Thermally tuned optical fiber for true time delay generation," *Opt. Laser Technol.* vol. **37**, pp. 29-32, (2004)

Chapter 8 Other Important Achievements

In this chapter, other important achievements related to highly dispersive photonic crystal fibers will be discussed. In the first section, the fabricated design of an extremely high dispersion coefficient PCF will be presented and its drawbacks will be briefly discussed. The fabricated PCF exhibits the highest dispersion coefficient reported so far. In the second section, the principle of pulse compression will be described and using the PCF described in Chapter 3, the phenomenon of pulse compression will be demonstrated.

8.1 PCF with highest dispersion coefficient

The use of highly dispersive photonic crystal fibers as true-time-delay elements for phased array antenna application was demonstrated in the previous chapters. In section 2.2.3, a design of a highly dispersive photonic crystal fiber exhibiting dispersion coefficient of -5500ps/nm/km at 1553nm was presented. In this section, the fabricated design is explained and preliminary measurement results are presented.

8.1.1 STRUCTURAL DESIGN OF THE PCF

A schematic cross section of the PCF is shown in Fig. 8.1 in which the structural period (Λ) is $2.51\mu\text{m}$. The inner core (red region) is made of doped silica rod of diameter $d_1/\Lambda = 0.85$ with refractive index n_1 , surrounded by an inner cladding made of one air hole ring of diameter $d_2/\Lambda = 0.73$, followed by an outer core (green region) made up of 12 doped silica rods of refractive index n_2 ($n_2 < n_1$) with diameter $d_3/\Lambda = 0.8$. The rest of the air hole rings with diameters $d_4/\Lambda = 0.4$ form the outer cladding region. The

central core with refractive index n_1 is positively doped and has a doping concentration that raises its refractive index by 1.35% compared to background silica (yellow region). The outer core with refractive index n_2 is negatively doped and has a doping concentration that lowers its refractive index by -0.7% compared to background silica [1]. The values of the parameters are chosen in such a way that the phase matched wavelength is around $1.55 \mu\text{m}$.

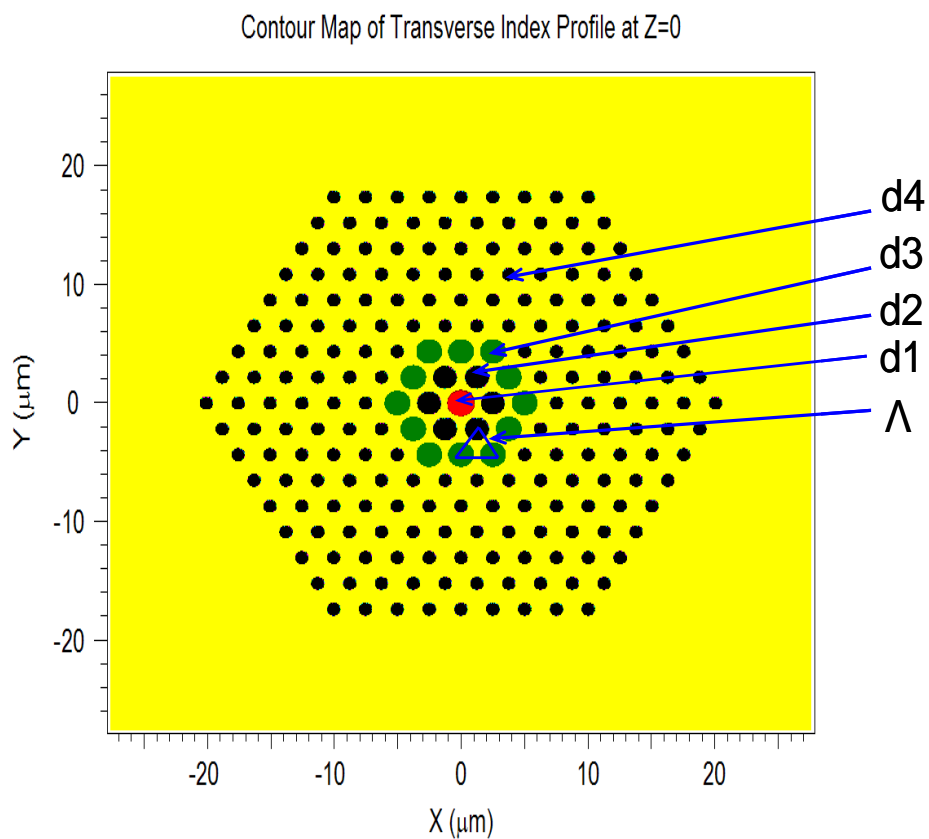


Fig. 8.1 Cross section of the designed photonic crystal fiber. The periodicity of the structure is given by Λ . A high index central core (d_1) is surrounded by an inner cladding (d_2) consisting of air holes. Outer core (d_3) has slightly lower refractive index compared to the central core. All other air holes (d_4) form the outer cladding region

The PCF is fabricated using stack and draw technique [2-4]. The scanning electron microscope (SEM) picture of the cross section of the fabricated PCF is shown in Fig. 8.2.

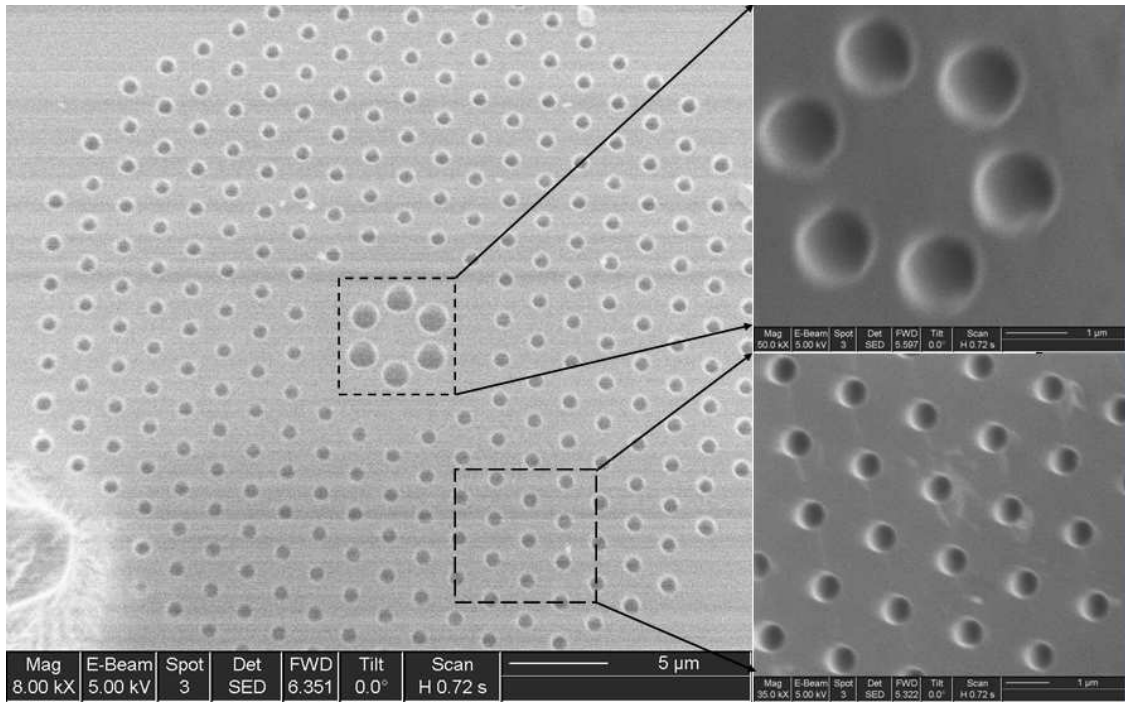


Fig. 8.2 Scanning electron microscope (SEM) picture of the cross section of the fabricated highly dispersive PCF (Enlarged views of the highlighted sections are also shown)

Since the fiber supports two supermodes – one in the inner core and other in the outer core, a necessary selective injection is needed to ensure that only one mode gets excited to support either negative or positive dispersion [5]. The characteristics of dispersion coefficient curves of the two supermodes are exactly identical, and they only differ in the sign. However in real application, both the modes are excited simultaneously.

Since in our experiments, we always connect the highly dispersive fiber to single mode fiber, we follow G er ome et al. [5] to use the phase delay method to simulate the dispersion value because this method is very accurate to describe the chromatic dispersion behavior. G er ome et al. have investigated the effect of launching conditions on the chromatic dispersion of a dual concentric core fiber. In the presence of both supermodes, the two oppositely signed dispersion coefficients do not cancel each other, but there exists a workable range of wavelengths in which there is still some high negative dispersion. Therefore, the dispersion of the two supermodes does not cancel each other, but the net dispersion depends on what fraction of energy is launched into each mode. The launching condition influences the dispersion coefficient value. The simulated dispersion curve under selective injection and random injection conditions are shown in Fig. 8.3.

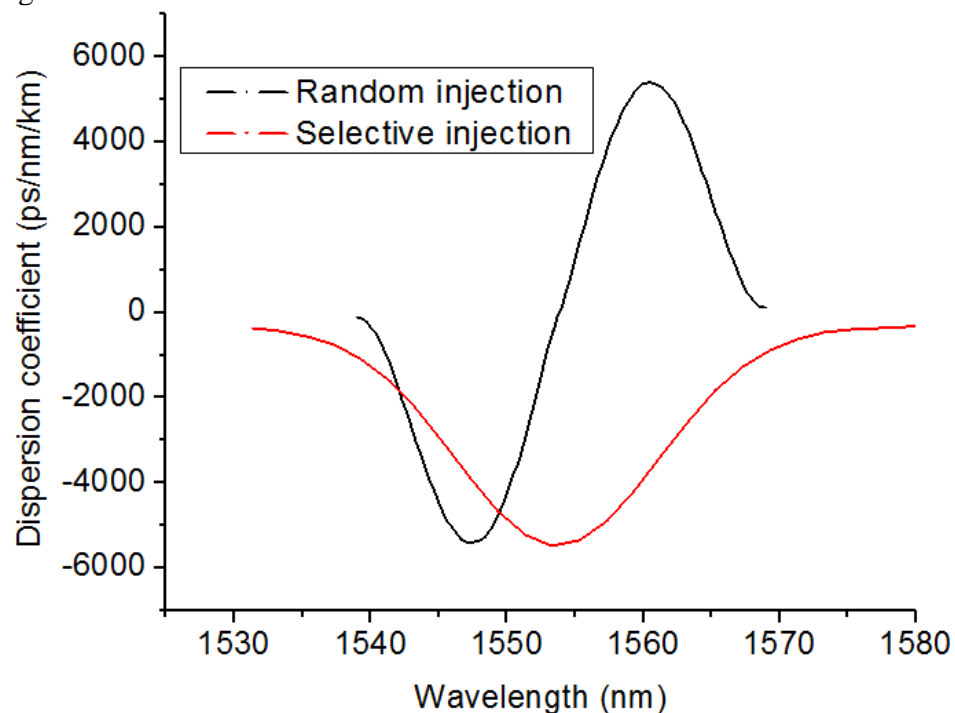


Fig. 8.3 Simulated dispersion coefficient for the designed high dispersion PCF with selective injecting into the inner core (red curve) and with random injection (black curve)

It can be seen that under random injection condition the dispersion coefficient goes from a high negative value to a very high positive dispersion value.

8.1.2 DISPERSION COEFFICIENT

The chromatic dispersion of the fabricated fiber is measured using a phase-shift method described earlier. The PCF is connected on each end with a SMF-28 single mode fiber. From our initial tests on the PCF, we found out that the signal output from the PCF is extremely sensitive to bending. Therefore, in all subsequent measurements, we consider the use of straight segments of PCF. The experimental setup is illustrated in Fig. 8.4 [1]. The X-band RF signal from the HP8510C vector network analyzer is modulated onto a tunable optical carrier using a LiNbO₃ electro-optic (EO) modulator. After the signal propagates through a 1.0m long straight segment of PCF, different phase shifts will be generated for different optical wavelengths. The signal is then detected by a photodetector and fed into the network analyzer to measure the RF phase.

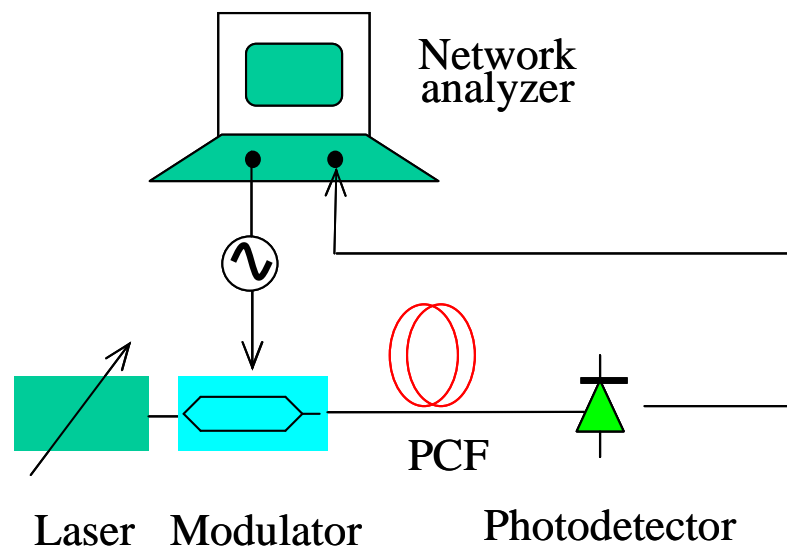


Fig. 8.4 System setup to measure dispersion value of PCF using phase-shift method

The time delay (t) generated when the wavelength is tuned from λ_1 to λ_2 is given by

$$t = L \cdot \int_{\lambda_1}^{\lambda_2} D(\lambda) d\lambda \quad (8.1)$$

where $D(\lambda)$ is the dispersion coefficient, λ is the optical wavelength, and L is the length of the PCF. The phase difference measured by the network analyzer at an RF frequency f is expressed as

$$\Delta\theta = 2\pi \cdot t \cdot f \quad (8.2)$$

Making use of the values of t derived from equation (8.2) into equation (8.1), the dispersion coefficient of the fiber is derived. The dispersion curve of the PCF thus derived is shown in Fig. 8.5 [1]. The simulation results with selective injection and random injection criteria are also drawn in Fig. 8.5 for comparison.

From the measurement it can be seen that the curve shows a negative peak around -5400 ps/nm/km at 1549nm. The dispersion becomes null almost halfway between the two peaks near 1555nm. There is a sudden change in the sign of the dispersion coefficient, and the value becomes highly positive $+3900 \text{ ps/nm/km}$ at 1560nm. The experimental data are in reasonably good agreement with simulation results. The fluctuations are attributed to the variation of the opto-geometrical parameters of the fiber during drawing. This is the highest reported dispersion coefficient thus far.

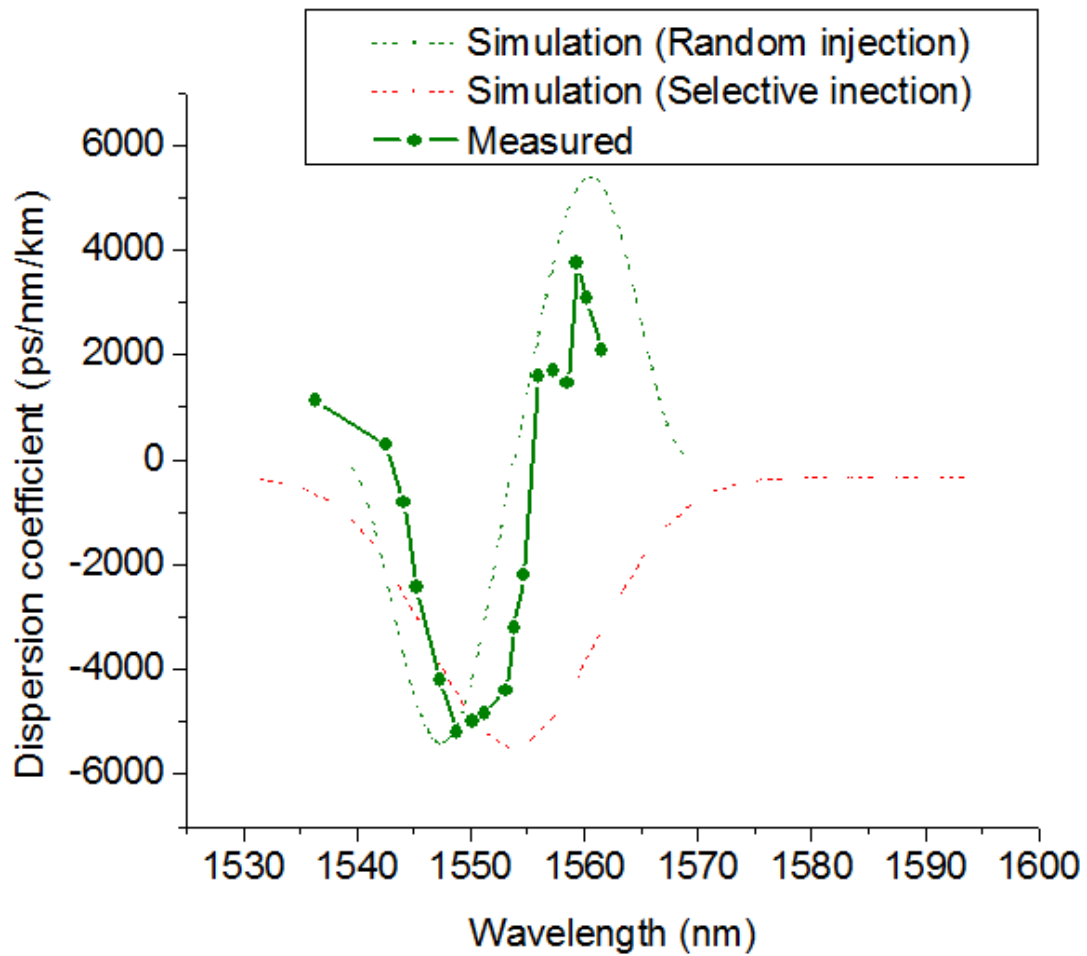


Fig. 8.5 Simulated dispersion curves for selective injection (dashed red curve), random injection (dashed green curve) and measured dispersion curve (green curve with marked circles) of the PCF

8.1.3 LIMITATIONS OF THE PCF

Since there is a strong coupling between the two super modes, a very high fluctuation in the mode energies in the two cores is observed due to bending. This bending induced fluctuation alters the dispersion coefficient appreciably. Therefore, straight segments of the fabricated PCF need to be used. Due to this limitation, TTD module required to steer RF beams could not be formed.

8.2 Pulse Compression

In this section, the principle of operation of pulse compression is explained. Using the PCF with a dispersion coefficient of $-600\text{ps}/\text{nm}/\text{km}$ at 1550nm, an experiment is performed to compress an input pulse with a pulse width of 1.848ps to an output pulse with of 0.402ps.

8.2.1 PRINCIPLE OF OPERATION

The dispersion parameter, D which is commonly used in fiber optics, is related to the group velocity dispersion (GVD) parameter β_2 given by [6]

$$D = \frac{-2\pi c}{\lambda^2} \beta_2 \quad (8.3)$$

Depending on the sign of β_2 parameter, the nonlinear effects in a fiber can be used to control the behavior of a pulse propagating through the fiber. If β_2 is positive, the fiber is said to exhibit normal dispersion, and if β_2 is negative, the fiber is said to exhibit anomalous dispersion [6].

In the normal dispersion region, the higher frequency components of an optical pulse travel slower compared to the lower frequency components of the pulse (blue components of the pulse travel slower compared to the red components). The opposite occurs in the case of anomalous dispersion (red components travel slower than the blue components). In the absence of non-linear effects and propagation through a dispersive fiber, both the regimes tend to broaden a pulse during the course of its propagation

through the fiber. Due to unequal speeds of the different frequency components, a frequency chirp is induced across the pulse. The chirp induced by normal dispersion is termed as positive and that induced by anomalous dispersion is termed as negative.

When the intensity of the light coupled into the fiber is very high, the refractive index of the fiber also begins to nonlinearly depend on the intensity of light inside the fiber. The general expression for the refractive index of the fiber is given by the relation [6]

$$n(\omega, |E|^2) = n(\omega) + n_2 |E|^2 \quad (8.4)$$

where, the first term on the right hand side of the equation gives the linear refractive index term, and the second term on the right hand side of the equation gives the intensity dependence of refractive index. E and n_2 are the electric field and non-linear refractive index coefficient respectively.

The phase of an optical pulse changes as it propagates through the fiber due to the dependence of the refractive index on the intensity of light. This dependence of phase on the optical intensity is termed as self phase modulation (SPM). The effect of SPM on a pulse is to red shift the wavelength at the leading edge and blue shift the wavelength at the trailing edge (positive chirp) [6].

Depending on the initial pulse power (P_0), the effective area of the fiber mode (A_{eff}) and initial width (T_0) of the pulse, the evolution of the pulse through the fiber based on the interplay between the dispersive and nonlinear effects can be studied. P_0 and T_0 determine whether the dispersive or the non linear effects play a predominant role. It

is customary to define two terms in order to understand the evolution of an optical pulse through a fiber. The two terms are the dispersion length (L_D), and the nonlinear length (L_{NL}) defined as [6]

$$L_D = \frac{T_0^2}{|\beta_2|} \quad (8.5)$$

$$L_{NL} = \frac{1}{\gamma P_0} \quad (8.6)$$

$$\gamma = \frac{n_2 \omega_0}{c A_{eff}} \quad (8.7)$$

If L_D is greater than L_{NL} , then the nonlinear effects dominate over the dispersive effects, and the opposite occurs if L_D is smaller than L_{NL} . When the fiber length (L) is comparable or longer than both L_D and L_{NL} , then the effects of both the dispersive and nonlinear terms on the pulse propagation become important. If the fiber exhibits normal dispersion, then the effect of SPM and normal dispersion tend to increase the existing positive chirp. SPM also broadens the spectrum of the pulse. If this positively chirped pulse is propagated through another medium which provides a negative chirp, such as a fiber exhibiting anomalous dispersion, then the positive chirp and negative chirp effects cancel each other and the pulse gets compressed.

8.2.2 EXPERIMENTAL SETUP AND RESULTS

The experimental setup to observe the effect of pulse compression is shown in Fig. 8.6. A pulse train from a femtosecond laser source from Calmar Optcom (pulse width ~ 0.08 ps, repetition rate = 17MHz, peak power = 1kW) is amplified using an EDFA. The amplified pulse is launched into the core of 3.5m of -600 ps/nm/km PCF

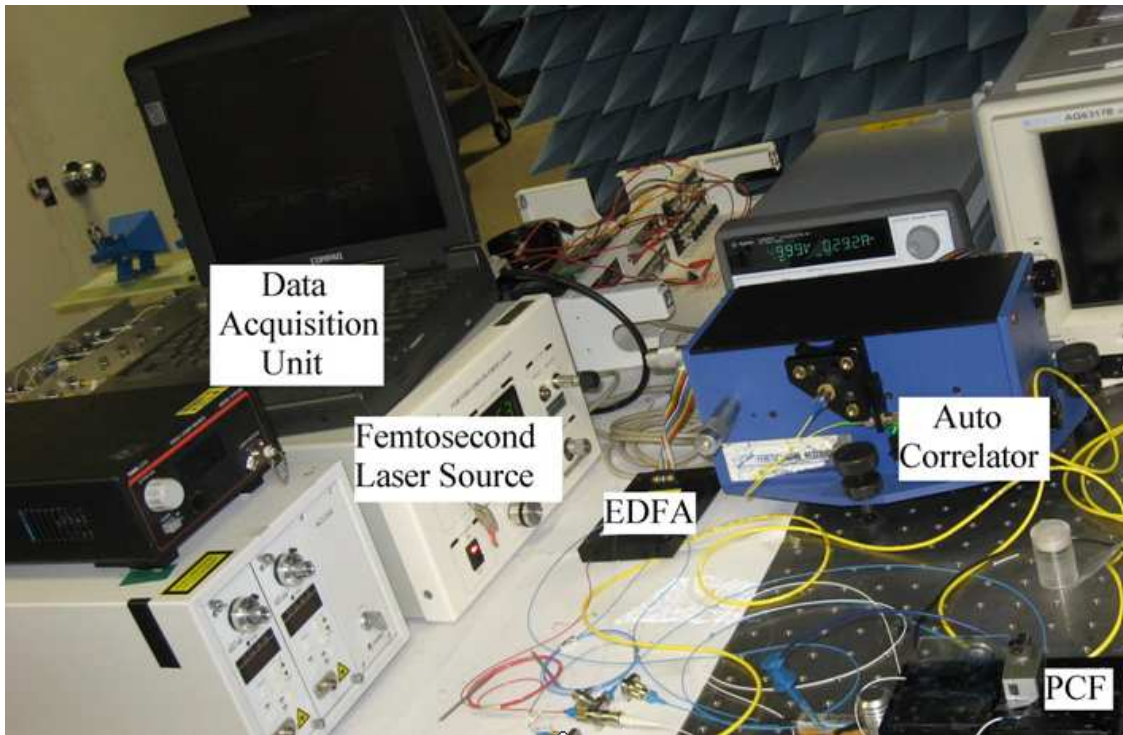


Fig. 8.6 Experimental setup for demonstrating pulse compression

using a manual 3-axis alignment stage. After passing through the PCF, the pulse propagates through another length segment of single mode fiber (SMF). The pulse traces are measured using an autocorrelator from Femtochrome, Inc which displays the pulse trace on a laptop screen connected to it. The trace of the pulse entering the EDFA and that exiting the SMF section after passing through the PCF are shown in Fig. 8.7. It can be seen from the figures that the input pulse (shown in Fig. 8.7(a)) with a pulse width of 1.848ps is compressed to a width of 401.94fs after passing through the PCF (shown in Fig. 8.7(b)). Since the chirp cancellation occurs effectively only in the linear portion (center of the pulse), compression takes place most

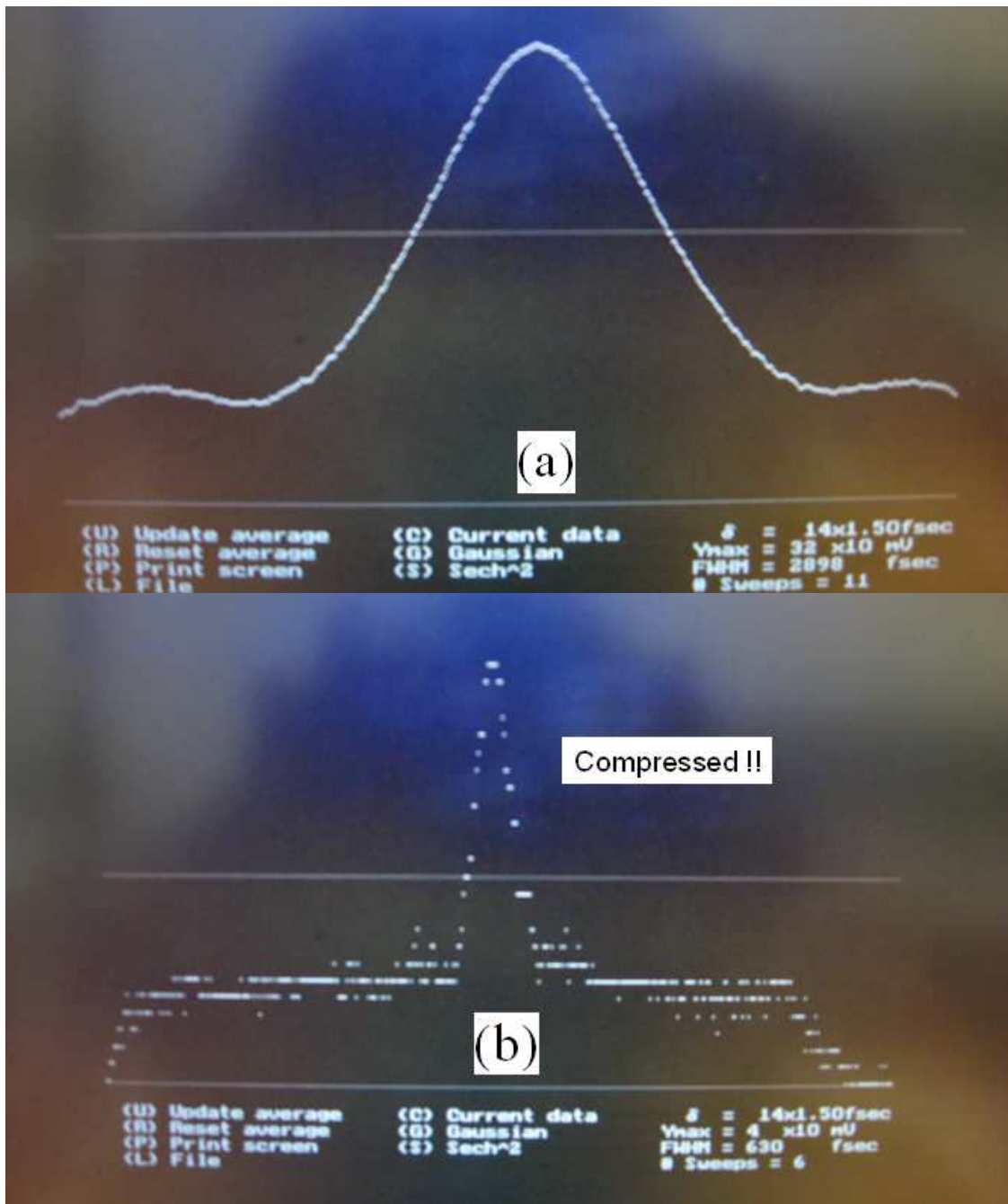


Fig. 8.7 Pulse compression demonstration with (a) Input pulse launched into the PCF (FWHM = 2898fs, pulse width = 1.848ps) (b) Output pulse as measured on the autocorrelator (FWHM = 630fs, pulse width = 401.94fs)

efficiently in the center of the pulse [6]. This creates a characteristic pedestal wherein the chirp cancellation is not complete.

8.3 Summary

In this chapter, the fabricated design of a highly dispersive photonic crystal fiber was presented. This photonic crystal fiber possessed the highest dispersion coefficient demonstrated so far. Application of highly dispersive PCF beyond its use in PAA systems was also demonstrated. For this purpose, the PCF with the dispersion coefficient of $-600\text{ps}/\text{nm}/\text{km}$ at 1550nm was used. A PCF-based compression system was setup and compression of a pulse with a pulse width of 1.848ps to a pulse with a pulse width of 401.94fs was demonstrated.

8.4 References

- [1] M. Y. Chen, H. Subbaraman, and R. T. Chen, "Dual-concentric-core Photonic Crystal Fiber with $-5400\text{ps}/\text{nm}/\text{km}$ Dispersion Coefficient," in OFC/NFOEC Technical Conference, 24-26 Mar 2009, San Diego (2009)
- [2] J. C. Knight, T. A. Birks, P. St J. Russell, and D. M. Atkin, "All-silica single-mode optical fiber with photonic crystal cladding," *Opt. Letts.* vol. **21**, pp. 1547–1549 (1996)
- [3] P. Kaiser and H. W. Astle, "Low loss single material fibers made from pure fused silica," *J. Bell Syst. Tech.* vol. **53**, pp. 1021–1039 (1974)
- [4] A. Bjarklev, J. Broeng, and A. S. Bjarklev, *Photonic crystal fibers*, Kluwer Academic Publishers (2003)
- [5] F. Gérôme, J. –L. Auguste, J. Maury, J. –M. Blondy, and J. Marcou, "Theoretical and Experimental Analysis of a Chromatic Dispersion Compensating Module Using a Dual Concentric Core Fiber," *J. Lightwav. Technol.* vol. **24**, pp. 442-228 (2006)

- [6] G. P. Agrawal, *Nonlinear Fiber Optics*, Academic Press (1995)

Chapter 9 Recommendations for Future Work

9.1 2-D continuously tunable photonic crystal fiber true-time-delay modules for phased array antenna systems

Using the photonic crystal fiber based true-time-delay modules; one dimensional beam steering can be easily extended to beam steering in two dimensions. The schematic of the TTD based 2-D phased array antenna system is shown in Fig. 9.1

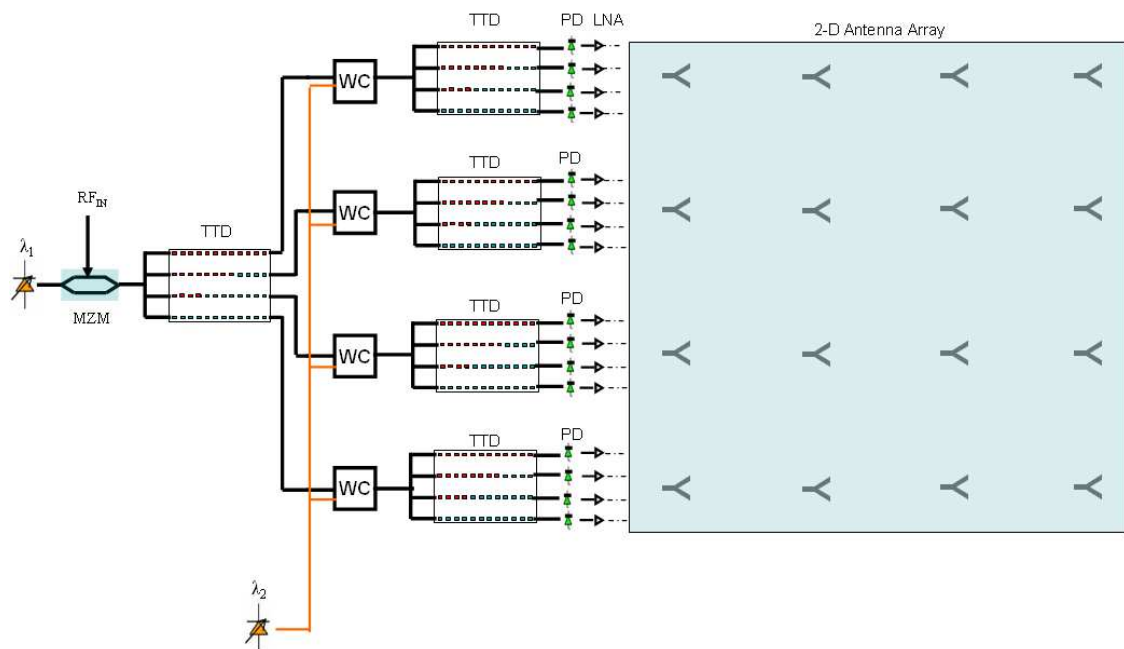


Fig. 9.1 Schematic setup of TTD based 2-D Phased Array Antenna, MZM: Mach-Zehnder modulator; TTD: true-time-delay; WC: wavelength converter; PD: photodetector; LNA: low-noise amplifier

Two tunable wavelength laser sources with output wavelength labeled λ_1 and λ_2 can be used to control the beam's azimuth and elevation angles respectively. The X-band RF signal is modulated onto the first optical carrier with wavelength λ_1 from one tunable

laser source using a Mach-Zehner modulator. This modulated carrier is split to the TTD lines, just as in the 1-D case. After passing through each TTD line comprising of different lengths of PCF and NZ-DSF lines, each of the outputs is passed through a wavelength convertor (WC). By feeding the WC with an optical carrier with wavelength λ_2 from a second tunable laser source, the phase information carrier by wavelength λ_1 can be transferred to λ_2 . Each of the four outputs from the WC device is further split into 4 channels using an optical power splitter and fed to the four delay lines of four respective TTD networks. The sixteen outputs from the four TTD modules are converted to electrical signals using photodetectors (PD) and amplified using low-noise amplifiers (LNA). These amplified signals feed corresponding antenna elements on a 4x4 antenna array. Thus, by changing λ_1 and λ_2 , the elevation and azimuth angles of the radiated beam can be changed continuously.

9.2 Other applications of highly dispersive PCF

Highly dispersive PCFs can be designed to achieve positive dispersion in the wavelength range of operation. An interplay between the nonlinearity and positive dispersion can be used to launch a pulse in the PCF that does not change its shape for a very long distance, thus finding great application in high speed optical communications.

9.2.1 SOLITON PROPAGATION

The dispersive and nonlinear lengths in a fiber are given by equations (8.5), (8.6) and (8.7). In order for an input pulse to retain its shape, L_D and L_{NL} should be equal. By equating equations (8.5) and (8.6) we get

$$L_D = L_{NL} = \frac{T_0^2}{|\beta_2|} = \frac{cA_{eff}}{n_2\omega_0 P_0} \quad (9.1)$$

In a hollow core photonic crystal fiber, the core is made of air. Therefore, the nonlinear refractive index coefficient is over 1000 times lower than that of silica. Therefore, for a fixed T_0 and β_2 , a hollow core PCF can support 1000 times higher peak power compared to a conventional single mode fiber. Even higher peak powers can be supported since the A_{eff} can also be tuned in PCF.

An input pulse with a pulse width of 2.5ps is launched into one end of a 2m long air core photonic crystal fiber from Crystal Fiber A/S (HC - 1550 - 02) with a dispersion coefficient of $100 \text{ ps} / \text{ nm} / \text{ km}$ at 1550nm and $A_{eff} = 44 \mu\text{m}^2$. The pulse from the other end of the PCF is observed using an autocorrelator connected to a laptop. The variation in the shape of the pulse as a function of the power of the pulse (by tuning the pump current of the pulse source) is also measured and the results are shown in Fig. 9.2. It can be seen that at a pump current of 110mA, the pulse output from the PCF has a width equal to the input pulse, thus showing a soliton. By further increasing the current, second order solitons start appearing at the output. The second order soliton can be clearly seen at a pump current of 210mA, wherein wings at the sides are prominent. The higher order solitons have pulse widths smaller than that of the fundamental soliton, which is also confirmed in Fig. 9.2

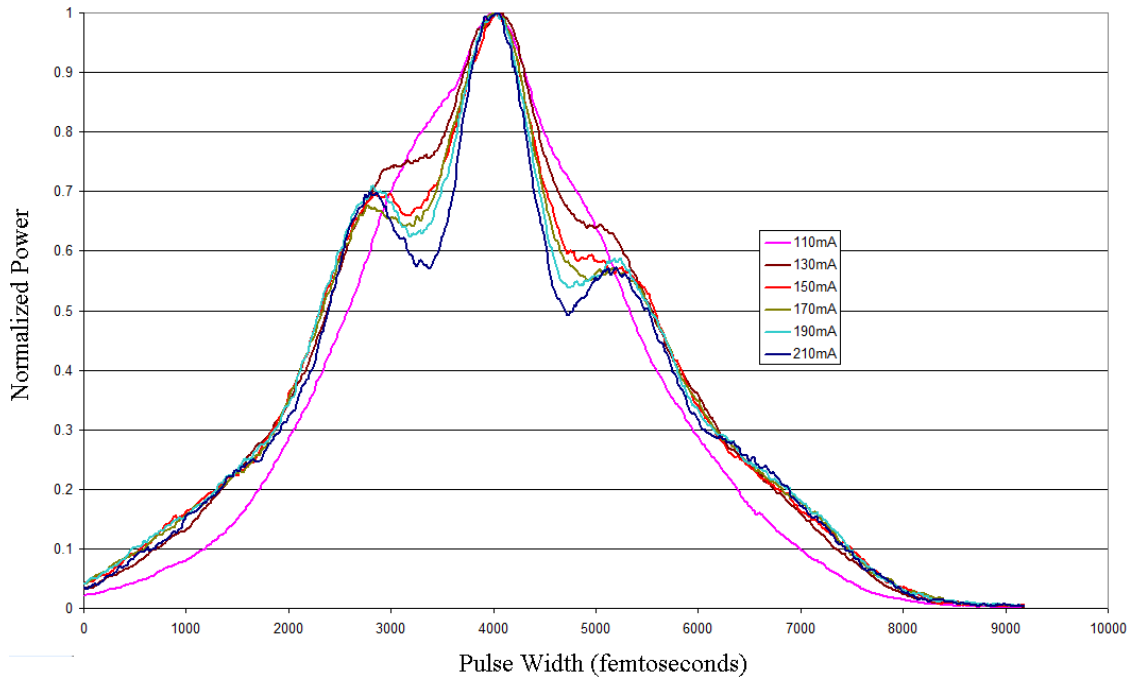


Fig. 9.2 Measured pulse traces of soliton from the PCF at different pump current levels

Therefore, by using a hollow core PCF with a dispersion coefficient of $100\text{ps}/\text{nm}/\text{km}$, a pulse with an energy of 0.1 microJoule and pulse width of 1ps, a soliton with a peak power of 44kW can be propagated. If, on the other hand, a pulse with an energy of 1microJoule and a pulse width of 1ps is launched into a hollow core PCF with a dispersion coefficient of $1000\text{ps}/\text{nm}/\text{km}$, 0.5MW peak power soliton can be propagated through the fiber. These results are impossible to achieve with a conventional fiber due to the limitation of damage threshold of silica core.

9.3 Summary

In this chapter, the architecture for a 2-D phased array antenna system employing highly dispersive photonic crystal fibers was presented. Two tunable laser sources, in

conjunction with wavelength convertors can be to control the elevation and azimuth angles of the radiated RF beam. Another application of highly dispersive photonic crystal fibers for use in soliton generation was also presented. A PCF with a dispersion coefficient of 100ps/nm/km at 1550nm was used to generate and support a soliton. With an increase in laser pump current, higher order solitons were also generated. By utilizing hollow core photonic crystal fibers, extremely high peak power solitons can be propagated without damaging the fiber.

Chapter 10 Summary

This doctoral research focused on the design and experimental use of highly dispersive photonic crystal fibers for use in single and simultaneous multiple RF beam transmission and reception. RF performance of the overall system was evaluated and other potential applications of highly dispersive photonic crystal fibers were also explored.

Designs of highly dispersive photonic crystal fibers for both index-guiding as well as photonic bandgap guiding PCFs showed that very high negative or positive dispersion coefficients could be achieved by proper design. In the case of index-guiding PCF based on dual concentric-core structure, dispersion coefficient as high as -9500 ps/nm/km at 1550nm with a full width at half maximum of about 55nm was obtained. Another highly dispersive fiber with a dispersion coefficient greater than -5400 ps/nm/km near 1550nm was designed and fabricated. The measured dispersion coefficient is the highest reported so far. In the case of a photonic bandgap PCF, dispersion coefficient greater than 4000 ps/nm/km at 1550nm was obtained. Such highly dispersive PCF designs show great promise in phased array antenna applications.

A true-time-delay module consisting of four delay lines was formed using the fabricated highly dispersive PCF with a dispersion coefficient of -600 ps/nm/km at 1550nm and non-zero dispersion shifted fibers (NZ-DSF) such that the overall length of each delay line was 10.5m with 3.5m length difference of PCF segments between adjacent delay lines. The delay lines were characterized and time delays through the delay lines as a function of wavelength were measured. The NZ-DSF sections in each

delay line were trimmed to produce zero time delay differences between adjacent delay lines at a central wavelength of 1545nm.

Using the PCF-TTD based X-band phased array antenna system, single RF beam transmission and receiving capability of the system was demonstrated first. Two RF signals were transmitted to and received from two different directions by tuning the wavelength on a tunable laser source. Single beam results were then extended to demonstrate simultaneous dual beam transmission and receiving capabilities of the PAA system by transmitting and receiving two RF beam simultaneously to/from two different directions by simultaneously controlling the wavelengths of two tunable laser sources for the first time. The X-band PAA system with an antenna array with inter-element spacing = 1.3cm is capable of transmitting and receiving single or multiple RF beams from -41° to $+46^{\circ}$ by tuning the wavelength on tunable laser sources from 1530nm to 1560nm.

The noise and distortion characteristics of the PCF-TTD based PAA system were evaluated. Noise figure (NF) and spurious-free dynamic range (SFDR) of the system with the modulator set to operate at quadrature were measured to be 37dB and $106\text{dB}\cdot\text{Hz}^{2/3}$ respectively at an input optical power of 20mW. Using a high power Erbium-doped fiber amplifier (EDFA) at the input of the modulator, the NF and SFDR are improved to 23.47dB and $115\text{dB}\cdot\text{Hz}^{2/3}$ by setting the modulator bias at 153° and optical power to 200mW.

The feasibility of a sparse antenna array based PAA system employing highly dispersive fibers was demonstrated by building a sparse array with 3 horn antenna elements spaced 0.165m apart, mimicking a 29 element standard antenna array and

measuring the far-field radiation patterns to -3° and $+3^{\circ}$ due to PCF length limitation in the TTD module. In order to demonstrate beam steering at larger angles, another TTD module was constructed using dispersion compensation fibers (DCF) with a dispersion coefficient of -100ps/nm/km . Using the DCF-based sparse antenna array system, RF beams were able to be transmitted to -45° and $+45^{\circ}$ by tuning the laser wavelength.

The fabricated photonic crystal fiber structure exhibiting the highest dispersion coefficient reported so far was presented. This PCF exhibited a very high dispersion coefficient of -5400ps/nm/km at 1549nm and $+3900\text{ps/nm/km}$ at 1560nm. Other interesting applications of highly dispersive PCFs were also explored and pulse compression effect and soliton propagation effects were demonstrated. The PCF with the dispersion coefficient of -600ps/nm/km at 1550nm was used in conjunction with an EDFA and a femtosecond laser source to compress a 1.848ps pulse to a pulse width of 401.94fs. A hollow core PCF with a dispersion coefficient of 100ps/nm/km at 1550nm respectively was used to demonstrate soliton propagation.

Appendix

Publications of Harish Subbaraman

- [1] M. Y. Chen, X. Lu, and **Harish Subbaraman**, “Conformal Ink-jet Printed C-band Phased-Array Antenna Incorporating Carbon Nanotube Field-effect Transistor Switch based True-time Delay Line,” submitted to IEEE. *Trans. Antenna. Propag.* (2009)
- [2] M. Y. Chen, X. Lu, **Harish Subbaraman**, and R. T. Chen, “Fully printed phased-array antenna for space communications,” in *Proc. SPIE*. vol. **7318**, pp. 731814-1 (2009)
- [3] M. Y. Chen, **Harish Subbaraman**, and R. T. Chen, “Dual-concentric-core Photonic Crystal Fiber with -5400ps/nm/km Dispersion Coefficient,” in *OFC/NFOEC Technical Conference*, 24-26 Mar 2009, San Diego (2009)
- [4] **Harish Subbaraman**, M. Y. Chen, and R. T. Chen, “Packaging and system demonstration of an X-band phased array antenna utilizing highly dispersive photonic crystal fiber based true-time-delay,” in *Proc. SPIE*, vol. **7221**, pp. 722107-1 (2009)
- [5] **Harish Subbaraman**, M. Y. Chen, and R. T. Chen, “Spurious-Free Dynamic Range (SFDR) improvement in a true-time-delay system based on highly dispersive photonic crystal fiber,” in *IEEE/LEOS Winter Topical Meeting Series*, pp. 58-59, 12-14 Jan 2009, Innsbruck, Austria (2009)
- [6] J. Vaillancourt, H. Zhang, P. Vasinajindakaw, H. Xia, X. Lu, X. Han, D. C. Janzen, W.-S. Shih, C. S. Jones, M. Stroder, M. Y. Chen, **Harish Subbaraman**, R. T. Chen, U. Berger, and M. Renn, “All ink-jet-printed carbon nanotube thin-film transistor on a polyimide substrate with an ultrahigh operating frequency of over 5 GHz,” *Appl. Phys. Letts.* vol. **93**, pp. 243301 (2008)
- [7] **Harish Subbaraman**, M. Y. Chen, and R. T. Chen, “Photonic Dual RF Beam Reception of an X-band Phased Array Antenna using Photonic Crystal Fiber based True-Time-Delay Beamformer,” *Appl. Opt.* vol. **47**, pp. 6448-6452 (2008)
- [8] **Harish Subbaraman**, M. Y. Chen, and Ray. T. Chen, “Photonic Crystal Fiber Based True-Time-Delay Beamformer for Multiple RF Beam Transmission and Reception of an X-Band Phased Array Antenna,” *IEEE/OSA J. Lightwav. Technol.* vol. **26**, pp. 2803-2809 (2008)

- [9] **Harish Subbaraman**, M. Y. Chen, Y. Jiang, and R. T. Chen, "Reply to Comment on Design of a broadband highly dispersive pure silica photonic crystal fiber," *Appl. Opt.* vol. **44**, pp. 3330-3332 (2008)
- [10] M. Y. Chen, **Harish Subbaraman**, and R. T. Chen, "Photonic Crystal Fiber Beamformer for Multiple X-band Phased-Array Antenna Transmissions," *IEEE. Photon. Technol. Letts.* vol. **5**, pp. 375-377 (2008)
- [11] **Harish Subbaraman**, M. Y. Chen, and R. T. Chen, "Simultaneous Dual RF Beam Reception of an X-Band Phased Array Antenna Utilizing Highly Dispersive Photonic Crystal Fiber Based True-Time-Delay," *AOE 2008 Technical Conference*, Oct 30 - Nov 2, Shanghai, China (2008)
- [12] **Harish Subbaraman**, T. Ling, Y. Jiang, M. Y. Chen, P. Cao, and R. T. Chen, "Design of a Broadband Highly Dispersive Pure Silica Photonic Crystal Fiber," *Appl. Opt.* vol. **46**, pp. 3263-3268 (2007)
- [13] M. Y. Chen, **Harish Subbaraman**, and R. T. Chen, "Highly dispersive photonic crystal fiber for beamforming," in *Proc. SPIE.* vol. **6838**, 683801, (2007) (Invited Paper)
- [14] **Harish Subbaraman**, P. Cao, M. Y. Chen, and R. T. Chen, "The Design and Fabrication of a Highly Dispersive Photonic Crystal Fiber for Phased Array Antenna Systems," *Proceedings of The OSA Topical Conference on Nanophotonics (NANO)*, pp. 92, Hangzhou, China, June 18-21, (2007)

Bibliography

Chapter 1

- [1] H. J. Visser, *Array and Phased Array Antenna Basics*, John Wiley and Sons Ltd (2005)
- [2] C. A. Balanis, *Antenna theory: Analysis and design, 3rd Edition*, John Wiley & Sons (2005)
- [3] R. C. Hansen, *Phased array antennas*, Wiley-Interscience (1998)
- [4] S. Barker and G. M. Rebeiz, "Distributed MEMS true-time delay phase shifters and wide-band switches," *IEEE. Trans. Microwav. Theory. Techniq.* vol. **46**, pp. 1881 - 1890 (1998)
- [5] W. Ng, A. A. Walston, G. L. Tangonan, J. J. Lee, I. L. Newberg, and N. Bernstein, "The first demonstration of an optically steered microwave phased array antenna using true-time-delay," *IEEE. J. Lightwav. Technol.* vol. **9**, pp. 1124- 1131 (1991)
- [6] R. D. Esman, M. Y. Frankel, J. L. Dexter, L. Goldberg, M. G. Parent, D. Stilwell, and D. G. Cooper, "Fiber-optic prism true time-delay antenna feed," *IEEE Photon. Technol. Letts.* vol. **11**, pp. 1347-1349 (1993)
- [7] R. Soref, "Optical dispersion technique for time-delay beam steering," *Appl. Opt.* vol. **31**, pp. 7395-7397 (1992)
- [8] Y. Chen and R. T. Chen, "A fully packaged true time delay module for a K-band phased array antenna system demonstration," *IEEE. Photon. Technol. Letts.* vol. **14**, pp. 1175 – 1177 (2002)
- [9] S. Yegnanarayanan and B. Jalali, "Wavelength-selective true time delay for optical control of phased-array antenna," *IEEE. Photon. Technol. Letts.* vol. **12**, pp. 1049 – 1051 (2000)
- [10] D. Dolfi, J. P. Huignard, and M. Baril, "Optically controlled true-time delays for phased array antenna," *Proc. SPIE.* vol. **1102**, pp. 152 (1989)
- [11] D. Dolfi, F. Michel-Gabriel, S. Bann, and J. P. Huignard, "Two-dimensional optical architecture for true-time-delay beam forming in a phased-array antenna," *Opt. Letts.* vol. **16**, pp. 255-257 (1991)

- [12] D. Dolfi, P. Joffre, J. Antoine, J. P. Huignard, D. Philippet, and P. Granger, "Experimental demonstration of a phased-array antenna optically controlled with phase and time delays," *Appl. Opt.* vol. **35**, pp. 5293-5300 (1996)
- [13] N. A. Riza, "Transmit/receive time-delay beam-forming optical architecture for phased-array antennas," *Appl. Opt.* vol. **30**, pp. 4594-4595 (1991)
- [14] N. A. Riza, "Liquid crystal-based optical time delay control system for wideband phased arrays," *Proc. SPIE.* vol. **1790**, pp. 171-183 (1992)
- [15] A. M. Levine, "Use of fiber optic frequency and phase determining element in radar," in *Proceedings of the 33rd Annual Symposium on Frequency Control*, IEEE, 436-443 (1979)
- [16] P. M. Freitag and S. R. Forrest, "A coherent optically controlled phased array antenna system," *IEEE. Microwav. Guided. Wav. Letts.* vol. **3**, pp. 293-295 (1993)
- [17] L. Xu, R. Taylor, and S. R. Forrest, "True-time delay phased array antenna feed system based on optical heterodyne techniques," *IEEE. Photon. Technol. Letts.* vol. **8**, pp. 160-162 (1996)
- [18] D. K. T. Tong, and M. C. Wu, "A novel multiwavelength optically controlled phased array antenna with a programmable dispersion matrix," *IEEE. Photon. Technol. Letts.* vol. **8**, pp. 812-814 (1996)
- [19] P. Goutzoulis and D. K. Davies, "Hardware-compressive 2-D fiber-optic delay line architecture for time steering of phased-array antennas," *Appl. Opt.* vol. **29**, pp. 5353-5359 (1990)
- [20] P. Goutzoulis and D. K. Davies, "All-optical hardware-compressive wavelength multiplexed fiber optic architecture for true-time delay steering of 2-D phased array antenna," *Proc. SPIE.* vol. **1703**, pp. 604-614 (1992)
- [21] P. Goutzoulis and D. K. Davies, J. Zomp, P. Hrycak, and A. Johnson, "Development and field demonstration of a hardware-compressive fiber-optic true time delay steering system for phased array antennas," *Appl. Opt.* vol. **33**, pp. 8173-8185 (1994)
- [22] Z. Fu and R. T. Chen, "Highly packing density optical true-time delay lines for phased array antenna applications," *Recent Research Developments Series*, pp. 1, Dec. 1998
- [23] S. Yegnanarayanan, P. D. Trinh, and B. Jalali, "Recirculating photonic filter: a wavelength-selective time delay for phased array antennas and wavelength code division multiple access," *Opt. Letts.* vol. **21**, pp. 740-742 (1996)

- [24] W. D. Jemison and P. R. Herczfeld, "Acousto-optically controlled true-time delay," *IEEE. Microwav. Guided Wav. Letts.* vol. **3**, pp. 72-75 (1993)
- [25] L. H. Gesell, R. E. Feinleib, J. L. Lafuse, and T. M. Turpin, "Acousto-optic control of time delays for array beam steering," *Proc. SPIE.* vol. **2155**, 194 (1994)
- [26] E. N. Toughlian and H. Zmuda, "A photonic variable RF delay line for phased array antennas," *IEEE. J. Lightwav. Technol.* vol. **8**, pp. 1824-1828 (1990)
- [27] E. H. Monsay, K. C. Baldwin, and M. J. Caucitto, "Photonic true-time delay for high-frequency phased array systems," *IEEE. Photon. Technol. Letts.* vol. **6**, pp. 118-120 (1994)
- [28] R. D. Esman, M. J. Monsma, J. L. Dexter, and D. G. Cooper, "Microwave True Time-Delay Modulator Using Fibre-Optic Dispersion," *Electron. Letts.* vol. **28**, pp. 1905-1907 (1992)
- [29] M. Y. Frankel and R. D. Esman, "True time-delay fiber-optic control of an ultra wideband array transmitter/receiver with multibeam capability," *IEEE. Trans. Microwav. Theory. Techniq.* vol. **43**, pp. 2387-2394 (1995)
- [30] S. T. Johns, D. A. Norton, C. W. Keefer, R. Erdmann, and R. A. Soref, "Variable time delay of microwave signals using high dispersion fibre," *Electron. Letts.* vol. **29**, pp. 555-556 (1993)
- [31] J. L. Cruz, B. Ortega, M. V. Andres, B. Gimeno, D. Pastor, J. Capmany, and L. Dong, "Chirped fiber gratings for phased array antenna," *Electron. Letts.* vol. **33**, pp. 545-546 (1997)
- [32] J. L. Corral, J. Marti, S. Regidor, J. M. Fuster, R. Laming, and M. J. Cole, "Continuously variable true time-delay optical feeder for phased-array antenna employing chirped fiber gratings," *IEEE. Trans. Microwav. Theory. Techniq.* vol. **45**, pp. 1531-1536 (1997)
- [33] Z. Shi, Y. Jiang, B. Howley, Y. Chen, F. Zhao, and R. T. Chen, "Continuously delay time tunable-waveguide hologram module for X-band phased-array antenna," *IEEE. Photon. Technol. Letts.* vol. **15**, pp. 972-974 (2003)
- [34] Z. Shi, L. Gu, B. Howley, Y. Jiang, Q. Zhou, R. T. Chen, M. Y. Chen, X. Wang, H. R. Fetterman, and G. Brost, "True-time-delay modules based on single tunable laser in conjunction with waveguide-hologram for phased-array antenna," *Opt. Engineering.* vol. **44**, 084301, (2005)
- [35] X. Chen, Z. Shi, L. Gu, B. Howley, Y. Jiang, and R. T. Chen, "Miniaturized Delay time-enhanced Photopolymer Waveguide Hologram Module for Phased-Array Antenna," *IEEE. Photon. Technol. Letts.* vol. **17**, pp. 2182-2184, (2005)

- [36] G. P. Agrawal, *Nonlinear Fiber Optics*, Academic Press (1995)
- [37] K. Thyagarajan, R. K. Varshney, P. Palai, A. K. Ghatak, and I. C. Goyal, "A Novel Design of a Dispersion Compensating Fiber," *IEEE. Photon. Technol. Letts.* vol. **8**, pp. 1510-1512 (1996)
- [38] J. -L. Auguste, R. Jindal, J. -M. Blondy, M. Clapeau, J. Marcou, B. Dussardier, G. Monnom, D. B. Ostrowsky, B. P. Pal, and K. Thyagarajan, "-1800ps/(nm.km) chromatic dispersion at 1.55 μ m in dual concentric core fibre," *Electron. Letts.* vol, pp. 1689-1690 (2000)
- [39] Y. Ni, L. Zhang, L. An, J. Peng, and C. Fan, "Dual-Core Photonic Crystal Fiber for Dispersion Compensation," *IEEE. Photon. Technol. Letts.* vol. **16**, pp. 1516-1518 (2004).
- [40] F. Gerome, J. -L. Auguste, and J. -M. Blondy, "Design of dispersion-compensating fibers based on a dual-concentric-core photonic crystal fiber," *Opt. Letts.* vol. **29**, pp. 2725-2727 (2004)
- [41] A. Huttunen, P. Torma, "Optimization of dual-core and microstructure fiber geometries for dispersion compensation and large mode area," *Opt. Express.* vol. **13**, pp. 627-635 (2005)
- [42] P. J. Roberts, B. J. Mangan, H. Sabert, F. Couny, T. A. Birks, J. C. Knight, and P. St. J. Russell, "Control of dispersion in photonic crystal fibers," *J. Opt. Fiber. Commun. Rep.* **2**, pp. 435-461 (2005)

Chapter 2

- [1] [1] J. C. Knight, T. A. Birks, P. St. J. Russell, and D. M. Atkin, "All-silica single-mode optical fiber with photonic crystal cladding," *Opt Letts.* vol. **21**, pp. 1547-1549 (1996); Also "errata," vol. **22**, 484 (1997)
- [2] J. Broeng, D. Mogilevstev, S. E. Barkou, and A. Bjarklev, "Photonic crystal fibres : A new class of optical waveguides," *Opt. Fiber. Tech.* vol. **5**, pp. 305-330 (1999)
- [3] Bjarklev, J. Broeng, A. S. Bjarklev, *Photonic crystal fibers*, Kluwer Academic Publishers (2003)
- [4] P. St J. Russell, "Photonic crystal fibers," *Science.* vol. **299**, pp. 358-362 (2003)

- [5] T. A. Birks, D. Mogilevtsev, J. C. Knight, P. St. J. Russell, "Dispersion compensation using single-material fibers," *IEEE Photon. Technol. Letts.* vol. **11**, pp. 674 – 676 (1999)
- [6] L. P. Shen, W. P. Huang, G. X. Chen, S. S. Jian, "Design and optimization of photonic crystal fibers for broad-band dispersion compensation," *IEEE. Photon. Technol. Letts.* vol. **15**, pp. 540-542 (2003)
- [7] A. Huttunen and P. Torma, "Optimization of dual-core and microstructure fiber geometries for dispersion compensation and large mode area," *Opt. Express.* vol. **13**, pp. 627-635 (2005)
- [8] Y. Ni, L. Zhang, L. An, J. Peng, and C. Fan, "Dual-Core Photonic Crystal Fiber for Dispersion Compensation," *IEEE. Photon. Technol. Letts.* vol. **16**, pp. 1516-1518 (2004)
- [9] K. Thyagarajan, R. K. Varshney, P. Palai, A. K. Ghatak, and I. C. Goyal, "A Novel Design of a Dispersion Compensating Fiber," *IEEE. Photon. Technol. Letts.* vol. **8**, pp. 1510-1512 (1996)
- [10] J. -L. Auguste, R. Jindal, J. -M. Blondy, M. Clapeau, J. Marcou, B. Dussardier, G. Monnom, D. B. Ostrowsky, B. P. Pal, and K. Thyagarajan, "-1800ps/(nm.km) chromatic dispersion at 1.55 μ m in dual concentric core fibre," *Electron. Letts.* vol. **36**, pp. 1689-1690 (2000)
- [11] F. G er ome, J. -L. Auguste, and J. -M. Blondy, "Design of dispersion-compensating fibers based on a dual-concentric-core photonic crystal fiber," *Opt. Letts.* vol. **29**, pp. 2725-2727 (2004)
- [12] P. J. Roberts, B. J. Mangan, H. Sabert, F. Couny, T. A. Birks, J. C. Knight, and P. St. J. Russell, "Control of dispersion in photonic crystal fibers," *J. Opt. Fiber. Commun. Rep.* vol. **2**, pp. 435-461 (2005)
- [13] R. Amezcua-Correa, F. G er ome, S. G. Leon-Saval, N.G. R. Broderick, T. A. Birks, and J. C. Knight, "Control of surface modes in low loss hollow-core photonic bandgap fibers," *Opt. Express.* vol. **16**, pp. 1142-1149 (2008)
- [14] J. D. Joannopoulos, R. D. Meade, and J. N. Winn, *Photonic Crystals*, Princeton University Press (1995)
- [15] J. D. Joannopoulos, S. G. Johnson, J. N. Winn, and R. D. Meade, *Photonic Crystals: Molding the flow of light*, Princeton University press, 2nd ed. (2008)
- [16] B. Jopson and A. Gnauck, "Dispersion compensation for optical fiber systems," *IEEE. Comm. Mag.* vol. **33**, pp. 96-102 (1995)

- [17] T. A. Birks, J. C. Knight, and P. St J. Russell, "Endlessly single-mode photonic crystal fiber," *Opt. Letts.* vol. **22**, pp. 961-963 (1997)
- [18] Z. Yusoff, J. H. Lee, W. Belardi, T. M. Monro, P. C. Teh, and D. J. Richardson, "Raman effects in a highly nonlinear holey fiber: amplification and modulation," *Opt. Letts.* vol. **27**, pp. 424-426 (2002)
- [19] K. Tajima, J. Zhou, K. Nakajima, and K. Sato, "Ultralow Loss and Long Length Photonic Crystal Fiber," *J. Lightwav. Technol.* vol. **22**, pp. 7-10 (2004)
- [20] M. Koshiba and K. Saitoh, "Simple evaluation of confinement losses in holey fibers," *Opt. Comm.* vol. **253**, pp. 95-98 (2005)
- [21] S. K. Varshney, K. Saitoh, and M. Koshiba, "A Novel Design for Dispersion Compensating Photonic Crystal Fiber Raman Amplifier," *IEEE. Photon. Technol. Letts.* vol. **17**, pp. 2062-2064 (2005)
- [22] S. K. Varshney, T. Fujisawa, K. Saitoh, and M. Koshiba, "Design and analysis of a broadband dispersion compensating photonic crystal fiber Raman amplifier operating in S-band," *Opt. Express.* vol. **14**, pp. 3528-3540 (2006)
- [23] B. J. Mangan, F. Couny, L. Farr, A. Langford, P. J. Roberts, D. P. Williams, M. Banham, M. W. Mason, D. F. Murphy, E. A. M. Brown, and H. Sabert, "Slope-matched dispersion-compensating photonic crystal fibre," *Lasers and Electro-Optics, 2004. (CLEO). (Conference on Vol. 2, 16-21 May 2004)*, pp. 1069-1070.
- [24] U. Peschel, T. Peschel, and F. Lederer, "A compact device for highly efficient dispersion compensation in fiber transmission," *Appl. Phys. Letts.* vol. **67**, pp. 2111-2113 (1995)
- [25] V. M. Schneider and J. A. West, "Analysis of wideband dispersion slope compensating optical fibres by supermode theory," *Electron. Letts.* vol. **38**, pp. 306-307 (2002)
- [26] H. Subbaraman, T. Ling, Y. Q. Jiang, M. Y. Chen, P. Y. Cao, and R. T. Chen, "Design of a broadband highly dispersive pure silica photonic crystal fiber," *Appl. Opt.* vol. **46**, pp. 3263 – 3268 (2007)
- [27] K. M. Ho, C. T. Chan, and C. M. Soukoulis, "Existence of a Photonic Gap in Periodic Dielectric Structures," *Phy. Rev. Letts.* vol. **65**, pp. 3152-3155 (1990)
- [28] RSoft Photonics CAD Suite, Version 5.1.7
- [29] R. Scarmozzino, A. Gopinath, R. Pregla, and S. Helfert, "Numerical Techniques for Modeling Guided-Wave Photonic Devices," *J. Selected Topics in Quantum Electronics.* vol. **6**, pp. 150-162 (2000)

- [30] R. Scarmozzino and R. M. Osgood, Jr, "Comparison of finite-difference and Fourier-transform solutions of the parabolic wave equation with emphasis on integrated-optics applications," *J. Opt. Soc. Amer. A*. vol. **8**, 724-731 (1991)
- [31] J. C. Knight, T. A. Birks, P. St J. Russell, and D. M. Atkin, "All-silica single-mode optical fiber with photonic crystal cladding," *Opt. Letts.* vol. **21**, pp. 1547–1549 (1996)
- [32] P. Kaiser, and H. W. Astle, "Low loss single material fibers made from pure fused silica," *J. Bell Syst. Tech.* vol. **53**, pp. 1021–1039 (1974)
- [33] M. van Eijkelenborg, M. Large, A. Argyros, J. Zagari, S. Manos, N. Issa, I. Bassett, S. Fleming, R. McPhedran, C. M. de Sterke, and N. A. Nicorovici, "Microstructured polymer optical fiber," *Opt. Express*. vol. 9, pp. 319–317 (2001)
- [34] K. Kiang, K. Frampton, T. Monro, R. Moore, J. Tucknott, D. Hevak, N. Broderick, D. Richardson, H. Rutt, "Extruded singlemode non-silica glass holey optical fibres," *Electron. Letts.* vol. **38**, pp. 546-547 (2002)
- [35] D. C. Allan et al. Photonic crystal fibers: effective index and band gap guidance. In *Photonic Crystals and Light Localization in the 21st Century* (ed. C. M. Soukoulis) pp. 305–320 (Kluwer, Netherlands, 2001).
- [36] R. Buczynski, "Photonic Crystal Fibers," *Acta Physica Polonica A*, vol. **106**, pp. 141-167 (2004)
- [37] D. Pysz, R. Stepien, P. Szarniak, R. Buczynski, and T. Szoplik, "Comparing characteristics and prospects of fabrication of multicomponent photonic crystal fibers with different lattice structures," *Proc. SPIE*, vol. **5576**, pp. 74-80 (2004)
- [38] T. Guo, S. Lou, H. Fang, and S. Jian, "Research on the fabrication of photonic crystal fiber," *Proc. SPIE*. vol. **6352**, 63523C (2006)
- [39] H. Subbaraman, M. Yihong Chen, Y. Jiang, and R. T. Chen, "Reply to Comment on Design of a broadband highly dispersive pure silica photonic crystal fiber," *Appl. Opt.* vol. **44**, pp. 3330-3332 (2008)

Chapter 3

- [1] Y. Jiang, B. Howley, Z. Shi, Q. Zhou, R. T. Chen, M. Y. Chen, G. Brost, C. Lee, "Dispersion-Enhanced Photonic Crystal Fiber Array for A True-Time-Delay Structured X-band Phased Array Antenna," *IEEE. Photon. Technol. Letts.* vol. **17**, pp. 187-189 (2005)

- [2] Y. Jiang, Z. Shi, B. Howley, X. Chen, M. Y. Chen, and R. T. Chen, "Delay Time Enhanced Photonic Crystal Fibers Array for Wireless Communications using 2-D X-band Phased Array Antennas," *Opt. Engineering*. vol. **44**, (2005)
- [3] U. Peschel, T. Peschel, and F. Lederer, "A compact device for highly efficient dispersion compensation in fiber transmission," *Appl. Phys. Letts*. vol. **67**, pp. 2111-2113 (1995)
- [4] RSoft Photonics CAD Suite, Version 5.1.7
- [5] K. M. Ho, C. T. Chan, and C. M. Soukoulis, "Existence of a Photonic Gap in Periodic Dielectric Structures," *Phys. Rev. Letts*. vol. **65**, pp. 3152-3155 (1990)
- [6] Harish Subbaraman, M. Y. Chen, and R. T. Chen, Packaging and system demonstration of an X-band phased array antenna utilizing highly dispersive photonic crystal fiber based true-time-delay, in *Proc. SPIE*, vol. **7221**, pp. 722107-1 (2009)
- [7] H. Subbaraman, M. Y. Chen, and R. T. Chen, "Photonic dual RF beam reception of an X band phased array antenna using a photonic crystal fiber-based true-time-delay beamformer," *Appl. Opt.* vol. **7**, pp. 6448-6452 (2008)
- [8] B. Howley, Z. Shi, Y. Jiang, and R. T. Chen, "Thermally tuned optical fiber for true time delay generation," *Opt. Laser Technol.* vol. **37**, pp. 29-32, (2004)
- [9] H. Subbaraman, M. Y. Chen, and R. T. Chen, "Photonic Crystal Fiber-Based True-Time-Delay Beamformer for Multiple RF Beam Transmission and Reception of an X-Band Phased-Array Antenna," *J. Lightwav. Technol.* vol. **26**, pp. 2803-2809 (2008)
- [10] M. Y. Chen, H. Subbaraman, and R. T. Chen, "Photonic Crystal Fiber Beamformer for Multiple X-band Phased-Array Antenna Transmissions," *IEEE. Photon. Technol. Letts*. vol. **5**, pp. 375-377 (2008)

Chapter 4

- [1] D. Dolfi, J. P. Huignard, and M. Baril, "Optically controlled true-time delays for phased array antenna," *Proc. SPIE*. vol. **1102**, pp. 152 (1989)
- [2] D. Dolfi, F. Michel-Gabriel, S. Bann, and J. P. Huignard, "Two-dimensional optical architecture for true-time-delay beam forming in a phased-array antenna," *Opt. Letts*. vol. **16**, pp. 255-257 (1991)

- [3] D. Dolfi, P. Joffre, J. Antoine, J. P. Huignard, D. Philippet, and P. Granger, "Experimental demonstration of a phased-array antenna optically controlled with phase and time delays," *Appl. Opt.* vol. **35**, pp. 5293-5300 (1996)
- [4] N. A. Riza, "Transmit/receive time-delay beam-forming optical architecture for phased-array antennas," *Appl. Opt.* vol. **30**, pp. 4594-4595 (1991)
- [5] N. A. Riza, "Liquid crystal-based optical time delay control system for wideband phased arrays," *Proc. SPIE.* vol. **1790**, pp. 171-183 (1992)
- [6] A. M. Levine, "Use of fiber optic frequency and phase determining element in radar," in *Proceedings of the 33rd Annual Symposium on Frequency Control*, IEEE, 436-443 (1979)
- [7] P. M. Freitag and S. R. Forrest, "A coherent optically controlled phased array antenna system," *IEEE. Microwav. Guided. Wav. Letts.* vol. **3**, pp. 293-295 (1993)
- [8] L. Xu, R. Taylor, and S. R. Forrest, "True-time delay phased array antenna feed system based on optical heterodyne techniques," *IEEE. Photon. Technol. Letts.* vol. **8**, pp. 160-162 (1996)
- [9] D. K. T. Tong, and M. C. Wu, "A novel multiwavelength optically controlled phased array antenna with a programmable dispersion matrix," *IEEE. Photon. Technol. Letts.* vol. **8**, pp. 812-814 (1996)
- [10] P. Goutzoulis and D. K. Davies, "Hardware-compressive 2-D fiber-optic delay line architecture for time steering of phased-array antennas," *Appl. Opt.* vol. **29**, pp. 5353-5359 (1990)
- [11] P. Goutzoulis and D. K. Davies, "All-optical hardware-compressive wavelength multiplexed fiber optic architecture for true-time delay steering of 2-D phased array antenna," *Proc. SPIE.* vol. **1703**, pp. 604-614 (1992)
- [12] P. Goutzoulis and D. K. Davies, J. Zomp, P. Hrycak, and A. Johnson, "Development and field demonstration of a hardware-compressive fiber-optic true time delay steering system for phased array antennas," *Appl. Opt.* vol. **33**, pp. 8173-8185 (1994)
- [13] Y. Chen and R. T. Chen, "A fully packaged true time delay module for a K-band phased array antenna system demonstration," *IEEE. Photon. Technol. Letts.* vol. **14**, pp. 1175 – 1177 (2002)
- [14] Z. Fu and R. T. Chen, "Highly packing density optical true-time delay lines for phased array antenna applications," *Recent Research Developments Series*, pp. 1, Dec. 1998

- [15] S. Yegnanarayanan, P. D. Trinh, and B. Jalali, "Recirculating photonic filter: a wavelength-selective time delay for phased array antennas and wavelength code division multiple access," *Opt. Letts.* vol. **21**, pp. 740-742 (1996)
- [16] W. D. Jemison and P. R. Herczfeld, "Acousto-optically controlled true-time delay," *IEEE. Microwav. Guided Wav. Letts.* vol. **3**, pp. 72-75 (1993)
- [17] L. H. Gesell, R. E. Feinleib, J. L. Lafuse, and T. M. Turpin, "Acousto-optic control of time delays for array beam steering," *Proc. SPIE.* vol. **2155**, 194 (1994)
- [18] E. N. Toughlian and H. Zmuda, "A photonic variable RF delay line for phased array antennas," *IEEE. J. Lightwav. Technol.* vol. **8**, pp. 1824-1828 (1990)
- [19] E. H. Monsay, K. C. Baldwin, and M. J. Caucuito, "Photonic true-time delay for high-frequency phased array systems," *IEEE. Photon. Technol. Letts.* vol. **6**, pp. 118-120 (1994)
- [20] R. Soref, "Optical dispersion technique for time-delay beam steering," *Appl. Opt.* vol. **31**, pp. 7395-7397 (1992)
- [21] J. L. Cruz, B. Ortega, M. V. Andres, B. Gimeno, D. Pastor, J. Capmany, and L. Dong, "Chirped fiber gratings for phased array antenna," *Electron. Letts.* vol. **33**, pp. 545-546 (1997)
- [22] J. L. Corral, J. Marti, S. Regidor, J. M. Fuster, R. Laming, and M. J. Cole, "Continuously variable true time-delay optical feeder for phased-array antenna employing chirped fiber gratings," *IEEE. Trans. Microwav. Theory. Techniq.* vol. **45**, pp. 1531-1536 (1997)
- [23] Z. Shi, Y. Jiang, B. Howley, Y. Chen, F. Zhao, and R. T. Chen, "Continuously delay time tunable-waveguide hologram module for X-band phased-array antenna," *IEEE. Photon. Technol. Letts.* vol. **15**, pp. 972-974 (2003)
- [24] Z. Shi, L. Gu, B. Howley, Y. Jiang, Q. Zhou, R. T. Chen, M. Y. Chen, X. Wang, H. R. Fetterman, and G. Brost, "True-time-delay modules based on single tunable laser in conjunction with waveguide-hologram for phased-array antenna," *Opt. Engineering.* vol. **44**, 084301, (2005)
- [25] X. Chen, Z. Shi, L. Gu, B. Howley, Y. Jiang, and R. T. Chen, "Miniaturized Delay time-enhanced Photopolymer Waveguide Hologram Module for Phased-Array Antenna," *IEEE. Photon. Technol. Letts.* vol. **17**, pp. 2182-2184, (2005)
- [26] Harish Subbaraman, M. Y. Chen, and R. T. Chen, Packaging and system demonstration of an X-band phased array antenna utilizing highly dispersive photonic crystal fiber based true-time-delay, in *Proc. SPIE*, vol. **7221**, pp. 722107-1 (2009)

- [27] W. Ng, A. A. Walston, G. L. Tangonan, J. J. Lee, I. L. Newberg, and N. Bernstein, "The first demonstration of an optically steered microwave phased array antenna using true-time-delay," *IEEE. J. Lightwav. Technol.* vol. **9**, pp. 1124-1131 (1991)

Chapter 5

- [1] M. Y. Chen, H. Subbaraman, and R. T. Chen, "Photonic Crystal Fiber Beamformer for Multiple X-Band Phased-Array Antenna Transmissions," *IEEE. Photon. Technol. Letts.* vol. **20**, pp. 375-377 (2008)
- [2] H. Subbaraman, M. Y. Chen, and R. T. Chen, "Photonic Crystal Fiber-Based True-Time-Delay Beamformer for Multiple RF Beam Transmission and Reception of an X-Band Phased-Array Antenna," *J. Lightwav. Technol.* vol. **26**, pp. 2803-2809 (2008)
- [3] G. A. Koepf, "Optical processor for phased-array antenna beam formation," *Proc. SPIE.* vol. **477**, pp. 75-81 (1984)
- [4] H. Subbaraman, M. Y. Chen, and R. T. Chen, "Photonic dual RF beam reception of an X band phased array antenna using a photonic crystal fiber-based true-time-delay beamformer," *Appl. Opt.* vol. **7**, pp. 6448-6452 (2008)
- [5] L. H. Gesell, R. E. Feinleib, J. L. Lafuse, and T. M. Turpin, "Acousto-optic control of time delays for array beam steering," *Proc. SPIE.* vol. **2155**, pp. 194-204 (1994)
- [6] N. A. Riza, "Liquid crystal-based optical time delay units for phased array antennas," *J. Lightwave Technol.* vol. **12**, pp. 1440-1447 (1994)
- [7] R. Soref, "Optical dispersion technique for time-delay beam steering," *Appl. Opt.* vol. **31**, pp. 7395-7397 (1992)
- [8] R. D. Esman, M. J. Monsma, J. L. Dexter, and D. G. Cooper, "Microwave true time-delay modulator using fibre-optic dispersion," *Electron. Letts.* vol. **28**, pp. 1905-1907 (1992)
- [9] M. Y. Frankel, P. J. Matthews, and R. D. Esman, "Fiber optic true time steering of an ultrawideband receive array," *IEEE Trans. Microwave Theory Tech.* vol. **45**, pp. 1522-1526 (1997)
- [10] M. Y. Frankel, R. D. Esman, and M. G. Parent, "Phased-array transmitter/receiver controlled by a true-time-delay fiberoptic beamformer," *IEEE Photonics Technol. Lett.* vol. **7**, pp. 1216-1218 (1995)

- [11] A. Moloney, C. Edge, and I. Bennion, "Fiber grating time delay elements for phased array antennas," *Electron. Letts.* vol. **31**, pp. 1485–1486 (1995)
- [12] J. E. Roman, M. Y. Frankel, P. J. Matthews, and R. D. Esman, "Time-steered array with a chirped grating beamformer," *Electron. Letts.* vol. **33**, pp. 652–653 (1997)
- [13] Y. Jiang, Z. Shi, B. Howley, X. Chen, M. Y. Chen, and R. T. Chen, "Delay time enhanced photonic crystal fiber array for wireless communications using 2-D X-band phased-array antennas," *Opt. Engineering.* vol. **44**, 125001 (2005)

Chapter 6

- [1] C. H. Cox, *Analog Optical Links: Theory and Practice*. Cambridge, U.K. Cambridge Univ. Press (2004)
- [2] P. Dienes, *The Taylor Series, An Introduction to the Theory of Functions of a Complex Variable*, Clarendon Press, Oxford (1931), reprint: Dover, New York (1957)
- [3] A. Karim and J. Devenport, "High Dynamic Range Microwave Photonic Links for RF Signal Transport and RF-IF Conversion," *J. Lightwave. Technol.* **26**, pp. 2718-2724 (2008)
- [4] A. Karim and J. Davenport, "Noise Figure Reduction in Externally Modulated Analog Fiber-Optic Links," *IEEE. Photon. Technol. Letts.* **19**, pp. 312-314 (2007)
- [5] G. E. Betts, J. P. Donnelly, J. N. Walpole, S. H. Groves, F. J. O'Donnell, L. J. Missaggia, R. J. Bailey, and A. Napoleone, "Semiconductor laser sources for externally modulated microwave analog links," *IEEE Trans. Microw. Theory Tech.* vol. **45**, pp. 1280–1287 (1997)
- [6] H. Subbaraman, M. Y. Chen, and R. T. Chen, "Spurious-Free Dynamic Range (SFDR) improvement in a true-time-delay system based on highly dispersive photonic crystal fiber," in *IEEE/LEOS Winter Topical Meeting Series*, pp. 58-59, Innsbruck, Austria (2009)

Chapter 7

- [1] H. J. Visser, *Array and Phased Array Antenna Basics*, John Wiley and Sons Ltd (2005)

- [2] Y. Liu, Z. Nie, and Q. Liu, "Reducing the number of elements in a linear antenna array by the matrix pencil method," *IEEE. Trans. Antennas. Propag.* vol. **56**, pp. 2955-2962 (2008)
- [3] B. P. Kumar and G. R. Branner, "Design of Unequally Spaced Arrays for Performance Improvement," *IEEE. Trans. Antennas. Propag.* vol. **47**, pp. 511-523 (1999)
- [4] R. L. Haupt, "Thinned arrays using genetic algorithms," *IEEE Trans. Antennas. Propag.* vol. **42**, pp. 993-999 (1994)
- [5] M. G. Bray, D. H. Werner, D. W. Boeringer, and D. W. Machuga, "Optimization of thinned aperiodic linear phased arrays using genetic algorithms to reduce grating lobes during scanning," *IEEE. Trans. Antennas. Propag.* vol. **50**, pp. 1732-1742 (2002)
- [6] T. G. Spence and D. H. Werner, "Design of Broadband Planar Arrays Based on the Optimization of Aperiodic Tilings," *IEEE. Transactions. Antennas. Propag.* vol. **56**, pp. 76-86 (2008)
- [7] D. S. Goshi, K. M. K. H. Leong, and T. Itoh, "A Sparsely Designed Retrodirective Transponder," *IEEE. Antennas. Wireless. Propag. Letts.* vol. **5**, pp. 339-342 (2006)
- [8] B. Howley, Z. Shi, Y. Jiang, and R. T. Chen, "Thermally tuned optical fiber for true time delay generation," *Opt. Laser Technol.* vol. **37**, pp. 29-32 (2004)

Chapter 8

- [1] M. Y. Chen, H. Subbaraman, and R. T. Chen, "Dual-concentric-core Photonic Crystal Fiber with -5400ps/nm/km Dispersion Coefficient," in *OFC/NFOEC Technical Conference*, 24-26 Mar 2009, San Diego (2009)
- [2] J. C. Knight, T. A. Birks, P. St J. Russell, and D. M. Atkin, "All-silica single-mode optical fiber with photonic crystal cladding," *Opt. Letts.* vol. **21**, pp. 1547-1549 (1996)
- [3] P. Kaiser and H. W. Astle, "Low loss single material fibers made from pure fused silica," *J. Bell Syst. Tech.* vol. **53**, pp. 1021-1039 (1974)
- [4] Bjarklev, J. Broeng, A. S. Bjarklev, *Photonic crystal fibers*, Kluwer Academic Publishers (2003)
- [5] F. Gérôme, J. -L. Auguste, J. Maury, J. -M. Blondy, and J. Marcou, "Theoretical and Experimental Analysis of a Chromatic Dispersion Compensating Module

Using a Dual Concentric Core Fiber,” J. Lightwav. Technol. vol. **24**, pp. 442-228 (2006)

- [6] G. P. Agrawal, *Nonlinear Fiber Optics*, Academic Press (1995)

Vita

Harish Subbaraman was born in Hyderabad, India on October 13, 1982. He is the son of Subbaraman Sundaresan and Dr. Anuradha Raman. He received the Bachelor of Engineering degree in Electronics and Communication Engineering from Chaitanya Bharathi Institute of Technology, India. He entered the graduate school at The University of Texas at Austin in 2004 and earned the degree of Master of Science in Engineering from Department of Electrical and Computer Engineering in 2006.

Permanent address: 1399, Street 20, Nagarjuna Nagar
Tarnaka, Secunderabad,
Andhra Pradesh, India.
500017

This dissertation was typed by the author